# NANOSCALE QUANTUM DYNAMICS AND ELECTROSTATIC COUPLING

A DISSERTATION PRESENTED TO
THE FACULTY OF
THE COLLEGE OF ARTS AND SCIENCES OF OHIO UNIVERSITY

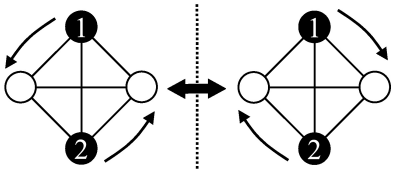


IN PARTIAL FULFILLMENT OF THE REQUIREMENTS
FOR THE DEGREE OF
DOCTOR OF PHILOSOPHY

Andreas Weichselbaum
June 2004

© 2004
Andreas Weichselbaum
All Rights Reserved

This dissertation entitled

# NANOSCALE QUANTUM DYNAMICS AND ELECTROSTATIC COUPLING

**by**

**Andreas Weichselbaum**

has been approved
for the Department of Physics and Astronomy
and the College of Arts and Sciences by

---

Sergio E. Ulloa
Professor of Physics and Astronomy

---

Leslie A. Flemming
Dean, College of Arts and Sciences

Andreas Weichselbaum, Ph.D. June 2004. Physics

Nanoscale Quantum Dynamics and Electrostatic Coupling (171 pp.)

Director of Dissertation: Sergio E. Ulloa

*Physical nanoscale systems have been analyzed both from an electrostatic point of view and quantum mechanically with respect to quantum computation. We introduce an elaborate code for the efficient numerical simulation of nanoscale electrostatics via a higher–order relaxation algorithm with a large variety of boundary conditions which then is applied to a set of physically relevant problems. Great emphasis is put on screening effects as well as capacitive coupling between spatially separated conducting regions. Specifically, we analyze the depletion of a two–dimensional electron gas using different methods. The effect of surface charges due to the pinning of the Fermi level at a semiconductor surface is shown to play an important role in that it can shift the whole system characteristics, underlining the importance of chemical potentials and work functions.*

*The capacitive coupling is further used to model the interactions in an interacting network of quantum dots, and the use of the capacitance formalism in the quantum mechanical context is explicitly justified. Quantum dot arrays are then analyzed on a general footing with respect to quantum computation and charge qubits based on an extended Hubbard Hamiltonian model. For systems with at most two operative electrons, general restrictions apply, introducing certain constraints on what realizations of this type of charge qubit may eventually look like. Furthermore, the interaction of the macroscopic world with the quantum dot network via quantum gates is discussed. Again, general arguments allow us to rule out certain scenarios of quantum gates. For example it turns out that capacitive coupling alone is not sufficient for full single qubit operation. Alternative ways are discussed, and finally, by using an external magnetic field and its resulting Aharonov–Bohm phases on the array, full single qubit operation based on charge is demonstrated.*

Approved _____

Sergio E. Ulloa
Professor of Physics and Astronomy

*To my parents and to my friends*
*I have been glad to meet.*

*SO ENTER THAT DAILY THOU MAYEST GROW*
*IN KNOWLEDGE WISDOM AND LOVE*

*Campus Gate (Ohio University, 1915)*

# Acknowledgments

It is not that long ago that I came to Athens, OH. It was a long way from home and things were not at all that clear then. Many new experiences were waiting for me, and looking back I am very grateful for it. I found the atmosphere here in the physics department very welcoming, and the very international group of students and grad students very enriching and appealing.

I want to thank the physics group here at the Ohio University for being this open to international students and giving them the opportunity to pursue their interests in physics. I really enjoyed many of the classes I took along the way, and also the teaching I did along my grad studies. Of course, it was not always easy but I think we were all learning from each other one way or the other.

I want to thank my advisor Sergio Ulloa for his continuous support and mentorship. It has been a joy being in his group and a good opportunity to meet many many new people, not to mention the always interesting get–togethers besides the physics schedule. Furthermore, I have really appreciated the many discussions on physics with other faculty here at OU. Especially, I want to mention in this context Sasha Govorov and Daniel Phillips whose expertise and experience I would not have liked to miss.

I am very grateful for the friends I have found here at OU, some of whom have already left for other places. I wish we could have spent more time together. You will always be on my mind.

Andreas

Ohio University, June 2004

# Table of Contents

# List of Figures

# List of Tables

# Glossary

| | |
|---|---|
| $\circ$ | as in $a \circ b$ - tensor product of the two (complex) vectors $a$ and $b$ such that $(a \circ b)_{ij} \equiv (\|a\rangle \langle b\|)_{ij} \equiv a_i b_j^*$. |
| ■ | marks the end of a proof. |
| $\equiv$ | equivalent, i.e. by definition. |
| 2DEG | two–dimensional electron gas - an abundance of charges (electrons) in a solid state system that is confined into a 2D plane in the sense that due to its nanoscopic thickness the wavefunction perpendicular to the plane is quantized such that only the lowest few discrete quantum levels are occupied. |
| 2D, 3D | two and three dimensional space. |
| AB | Aharonov–Bohm (e.g. related to AB phase [AB59]). |
| C | as in C matrix, capacitance matrix with coefficients $C_{(ij)}$. |
| *h.c.* | hermitian conjugate, e.g. indicating the lower triangular part of a Hermitian matrix with the upper triangular part given. |
| $c^+$, $c$ | quantum mechanical creation and annihilation operators in second quantization. |
| e | single electron, or equivalently single–electron charge where for convenience units are mostly chosen such that $e = 1$. |
| ee | electron–electron, as in ee–interaction. |
| e.g. | Lat. *exempli gratia*, for example (Merriam Webster) |
| FFT(3) | fast Fourier transform (in three dimensions). |
| $G$ | full Green's function in the quantum mechanical context including perturbative terms. |

| | |
|---|---|
| $G_0$ | free Green's functions similar to $G$ but without the perturbative terms. |
| GS | ground state, e.g. of a quantum mechanical system. |
| $h$, $\hbar$ | Planck's constant, where $\hbar \equiv h/2\pi$ - for convenience units are mostly chosen such that $\hbar = 1$. |
| i.e. | Lat. *id est*, that is (Merriam Webster) |
| LHS | left hand side, of an equation. |
| NB!, N.B. | Lat. *nota bene*, note well (Oxford Engl. Dictionary). |
| NN | nearest neighbor, e.g. on a grid. |
| $P$ | projector into $\mathcal{P}$ of the total Hilbert space with $P + Q = 1$. |
| $\mathcal{P}$ space | low dimensional subspace of interest in Feshbach formalism with its projector $P$ in Hilbert space such that $P + Q = 1$. |
| p(p) | page reference, p references quoted page only, while pp also includes the following pages (e.g. p. 12 is page 12, while pp. 12 includes the following pages in context). |
| PG, pg | plunger gate, with respect to an SET or quantum dot. |
| $Q$ | projector into $\mathcal{Q}$ of the total Hilbert space with $P + Q = 1$. |
| $\mathcal{Q}$ space | remainder of interacting Hilbert space in Feshbach formalism with its projector $Q$ such that $P + Q = 1$. |
| q.e.d. | Lat. *quod erat demonstrandum*, which was to be demonstrated (Merriam Webster). |
| QPC | quantum point contact, two Fermi seas connected through a quantum mechanically narrow constriction in the sense that only a very few quantum states down to a single quantum channel are left to couple between the two Fermi seas. |
| qu2LS | quantum two–level system, well decoupled from the remainder of the spectrum and preferentially in the ground state of the quantum mechanical system. |

qubit — quantum bit, quantum mechanical generalization of a classical two–state system (bit). The quantum mechanics manifests itself in the fact that the qubit can be set into a linear superposition of potentially classical states (e.g. in the macroscopic regime, this is sometimes referred to as a *(Schrödinger) cat state*).

qudot — quantum dot, nanometer size object (semiconductor or metallic) which strongly confines the electron wave function for a set of bound states.

qugate — quantum gate, an intended coherent interaction from the exterior with a quantum mechanical two–level system (qu2LS) for a short period in time which changes the state of the qu2LS in a unitary manner; these gates are conveniently described by Pauli matrices.

RHS — right hand side, of an equation.

RT — room temperature (= 300K).

SET — single electron transistor, formed from a quantum dot coupled to leads.

$\sigma_{\{x,y,z\}}$ — Pauli spin matrices.

SOR — successive overrelaxation - commonly used for numerical relaxation algorithms.

STM — scanning tunneling microscope, a conducting tip with a very sharp end point ($50 - 100\,\mathrm{nm}$) that is brought into very close proximity of a condensed matter surface via piezoelectric means. The sample surface is conducting in general, such that tunnel current provides important local information about the electronic charge density. On the other hand, with the sample surface being isolating or the tip far enough away from the surface, no tunnel current flows or is measured. Yet still, by applying a voltage onto the sample tip, this tip interacts capacitively with the electronic system of the sample which for example has fabricated quantum dots on it formed via local electrostatic fields.

vs. — versus, in dependence of, e.g. in a graph - y data versus x data.

X–gate — quantum gate acting on a single quantum bit as a time–dependent $\sigma_x$ term in the Hamiltonian.

xxx

| | |
|---|---|
| Y–gate | similar to X–gate, but related to $\sigma_y$ instead |
| Z–gate | similar to X–gate, but related to $\sigma_z$ instead |

# Chapter 1

# Introduction

Quantum systems on the nanometer scale have become common place in recent years and a wide variety of application and devices exists. This is evident insofar for example as the industrial semiconductor lithography itself is already at the 100 nm smallest feature size. Going to ever smaller dimensions down to molecular size opens up a whole new avenue towards testing and understanding of quantum mechanical effects and its highly complex structure in the many–body condensed matter world. Efforts to isolate quantum mechanical subspaces from their solid–state environment are clearly desirable, as they significantly reduce the quantum mechanical complexity so that eventually they can be well described and understood by simple physical models. The macroscopic environment, on the other hand, always perturbs any of these systems and this eventually destroys their quantum mechanical coherence over time. In this sense, full control of these systems in the real world over any time interval beyond any minute noise fluctuation will never be realizable as such. Nevertheless, the system may be brought into a sufficiently isolated situation to single out short–term quantum mechanical effects, as has been the case ever since quantum mechanics began. The interplay of photons with a local few level system is but one example. Increasing the time window where a system behaves quantum mechanically and thus coherently, requires that, first, the main sources of decoherence be identified and, second, that for a controlled quantum coherent interaction these sources are eliminated by appropriate means as far as is possible. In terms of thermal noise, for example, this clearly requires well below sub–Kelvin temperatures.

It is interesting to notice that even in the classical regime, or equivalently for decoherence times much shorter than typical observation times, there is still much to gain by making electrical devices much smaller still. In order to perform controlled processes at the single–electron scale such as logical operations, it means that one has to do work, and the minimum amount is determined by how much background fluctuation there exists to perturb the system. In other words, one has to overcome thermal

noise such that at least a few $k_BT$ of energy must be supplied for a controlled operation. This argument is used in [HKSW98] then, to estimate an order of magnitude limit on simple computational tasks such as the addition of two 10–digit numbers. According to [HKSW98], a rough estimate of the typical energy cost in 1971 gave rise to about $5 \cdot 10^2$ additions per Joule ( add/J), while nearly three decades later, in 1998 this number had improved to $3 \cdot 10^6$ add/J (e.g. equivalent to additions at the frequency of 0.1 GHz with a power consumption of 30 W) resulting in a factor of 1.90 every two years, yet another manifestation of Moore's law [Moo65]. The interesting point, however, is the comparison to the thermodynamical limit. Taking room temperature and roughly 10 $k_BT$ for every one of the 34 bits needed to implement a 10-digit number, then this amounts to about $10^{18}$ add/J which still leaves *plenty of room at the bottom* [Fey59] even in the classical sense.

In this work, the main emphasis is on electronic systems realized at the nanoscale. The primary realizations to be held in mind are on the basis of metallic nanoparticles as well as on chemically synthesized semiconductor quantum dots (qudots). For more easily tailorable and accessible systems, lithographically fabricated metallic quantum dots with fixed tunnel barriers in between are considered. Either one of these objects still contains at least hundreds of atoms, and in general clearly more than one and up to hundreds of electrons. In this sense, shifting a single electron between interacting qudots, leaves the overall charge configuration approximately the same and, consequently, the description of the electrodynamic interactions between quantum dots and their environment in terms of classical capacitances appears to be appropriate.

The dynamics within the quantum dot network is considered to be primarily controlled from the exterior by electrostatically coupled gates, such as the fixed top gates fabricated with the sample as well as gates adjustable in position such as an STM tip brought in close and set to some potential. Since the leads eventually are of macroscopic dimensions and highly conducting with a large number of participating electrons, the charge distribution within the leads primarily follows the classical charge distribution for the specific geometry. In the case of a dynamically driven potential, the electrons in the leads can be thought to behave as a group such that the rearrangement of the individual charge is minuscule and consequently, charge fluctuations in the leads are negligible. However, local rearrangements of single charges near the area where the quantum dot network resides will trigger a comparable amount of rearrangement of charge in the leads due to screening effects, with a likely very short but finite time scale. Dynamical effects like these may eventually become the dominant dephasing mechanism once all the other dephasing mechanisms such as temperature are sufficiently reduced. The major concern in this work, however, is different. Namely, we are concerned with the general case of any condensed matter system where many quantum mechanical states are available inherently and yet, one

only wants to have a certain number of relevant states. For example, a two level system for a quantum bit is embedded and "interacting" with the remaining states, while we would prefer that they do not interfere with the state space (Hilbert space) of interest. The construction of state spaces like these is primarily concerned with the more basic energetics. At the initial stage, screening effects themselves play an essential and potentially nontrivial role. In the later analysis then, the quantum mechanical influence of the higher lying states must be accounted for.

With this in mind, the outline of this dissertation is as follows: Chap. 2 introduces the total capacitance matrix for a typical network of quantum dots coupled electrostatically to a set of external leads. Several explicit examples to demonstrate its typical applicability are provided. Moreover, the energetics of these types of systems is explained in detail. The discreteness of the electron and therefore of charge is reflected in the Coulomb blockade of quantum dots which is also reviewed briefly. Finally, also with respect to the electrostatic simulations in the following chapter, the behavior of major physical variables such as the electric field or the charge distribution of an electrostatic system is reviewed with respect to scaling.

Chap. 3 describes in detail the package on electrostatic simulations that was developed on the basis of a higher–order relaxation algorithm. Plenty of different boundary conditions implemented into the program are motivated and derived such as the electrostatic depletion of a two–dimensional electron gas (2DEG). Moreover, the outer boundary of the 3D grid is calculated self–consistently via an efficient fast Fourier transform algorithm. Test examples clearly underline the usefulness and accuracy of this program package whose major applications are then presented with respect to a parabolically shaped (STM) tip interacting with a set of nanosized islands, quantum dots or quantum rings right underneath the tip. The quantum dots under consideration, for example, are formed via depletion in a 2DEG buried right below the surface. The interplay of these nanoelectronic devices with the capacitively coupled tip provides interesting and important information on charge accumulation or depletion in the presence of electrostatic screening as well as on the polarization and distortion of the *nano–puddles* of electronic charges. We compare our calculations with beautiful results from the experimental group at ETH Zürich.

Chap. 4 then changes gears towards the quantum mechanical treatment of energetically separated quantum subspaces that arise from specific quantum dot arrangements. This chapter introduces the general language of the Feshbach formalism together with the straightforward recipe on how to construct an effective Hamiltonian for the subspace of interest. Since this formalism has very close resemblance to the alternative route through Green's functions, a section on Green's functions is added. From a perturbative point of view, the probabilities of transitions mediated by different sorts of pulses in the gate voltages of arbitrary systems are discussed. In

the case of a step–like perturbation, it is seen that the more intuitive results from the Feshbach formalism are indeed exactly in agreement with the results from the Green's function approach. For this it should be noted that strictly speaking the Feshbach formalism is by construction for static analysis and as such has no real dynamical power.

The last chapter then, Chap. 5, fully describes quantum dynamics on a network of quantum dots modeled via the Hubbard Hamiltonian. The main emphasis in this chapter is on charge qubits and possible realizations thereof. General statements on the geometry as well as on the properties of the ground state quantum two–level system (qu2LS) are shown to put clear constraints on the answer to what a charge qubit may look like. The systems are considered with at most two operative excess electrons throughout. The interactions between the dots are modeled using a capacitor network based on the capacitance matrix formalism introduced in Chap. 2. The main simulations are implemented for a $2 \times 2$ array (cellular automata geometry) as well as on a larger $3 \times 3$ array. The construction of the Hamiltonian matrix for this type of system is described in detail using the notation of second quantization. The resulting Hamiltonian is then analyzed with respect to its ground state qu2LS and full single qubit operation via external gates. Electrostatically coupled voltage gates alone do not provide the necessary second quantum gate for single qubit operation in an efficient way. With the constraints of a constant tunneling amplitude and on the basis of the preceding arguments, the effectiveness of a real magnetic field to realize the necessary second quantum gate is demonstrated.

The appendix, App. A, contains a few notes on the source codes developed throughout these studies. Finally, also a complete list of papers, conferences attended and talks given in context with this dissertation is presented.

Overall, this dissertation starts with classical considerations with respect to electrostatic energy and equilibrium charge distributions in nanoscale systems. This analysis provides the major energy scales and parameters for the system, which then determine the primary energetics of the resulting quantum mechanical systems.

# Chapter 2

# Electrostatics on the Nanoscale

## 2.1 Capacitance Matrix

Any classical electrodynamic problem is described completely by the Maxwell equations which are linear in structure [Jac99]. This linearity automatically implies the superposition principle which says that two solutions with different charge distributions and potentials but with the same boundary conditions and thus the same geometrical arrangement can just be added together to get the combined solution. This principle is strongly reflected in describing the electrostatics of a fixed geometrical arrangement of conductors via the capacitance matrix formalism [Jac99]. For a single capacitor of charge $Q$ held at a potential $U$, this is $Q = CU$ while for a set of $n$ interacting metallic objects this generalizes to the linear vector–matrix algebra

$$q = CV \tag{2.1}$$

with $q_i$ and $V_i$ the total charge and the overall potential on the metallic object $i$, respectively. The capacitance matrix $C$ with its constant coefficients $C_{ij}$ relates the charges and the potential linearly ($i,\ j \in \{1 \dots n\}$). Within this formalism, the total energy is given as

$$E_{tot} = \frac{1}{2} VCV = \frac{1}{2} qC^{-1}q \tag{2.2}$$

with the implicit notation for vector–matrix–vector multiplication $aMb \equiv \vec{a}\hat{M}\vec{b} \equiv \sum_{i,j} a_i M_{ij} b_j$. The vector and matrix nature of $q$, $V$ and $C$ must be kept in mind, but for readability, it will not be written out explicitly.

The capacitance matrix (C–matrix) clearly represents a physical quantity and must be real as such. Since it directly relates to the total energy of the system, this implies certain properties and constraints, and as such the C–matrix cannot be modeled arbitrarily. These properties are as follows:

- The C–matrix is symmetric, and so is its inverse (a short proof is given at the end of this section, see p. 28) and
- therefore all eigenvalues $\lambda_i \equiv \mathrm{eig}(C)$ are real with $i = 1 \ldots n$ and $n$ the dimension of the C–matrix.
- The total energy must be bounded from below. From Eq. (2.2) this implies that the eigenvalues of the C–matrix need to be positive and from a physical point of view also unequal zero, therefore $\mathrm{eig}(C) \equiv \lambda_i > 0$ with $i = 1 \ldots n$.

Since the eigenvalues of $C^{-1}$ are just $\lambda_i^{-1}$, the same criteria also holds for the inverse of the C–matrix. $C$ and $C^{-1}$ are therefore positive definite matrices. In conclusion, it is again emphasized that by whatever approximation the C–matrix may be constructed, the above criteria are essential constraints that must be fulfilled.

### 2.1.1 Constructing the C–Matrix from a Capacitor Network

Consider a sample layout for a uniform array of metallic quantum dots as shown in Fig. 2.1B. All the islands are considered to be of the same geometry and sharing the same set of capacitive connections with their neighbors. Note that between the quantum dots only nearest neighbor capacitances are considered, which appears to be a reasonable approximation although by no means essential. The nearest neighbor capacitances clearly capture the largest contributions, where the extension to capacitive coupling beyond nearest neighbor would be possible straightforwardly within the C matrix formalism. The values of the individual capacitances connecting the objects with each other are simple numbers, referenced to by $\mathcal{C}_{ij}$ as the generic capacitance between site $i$ and site $j$; islands $i$ and $j$ are considered *connected* only if there is a capacitive coupling in between them, i.e. $\mathcal{C}_{ij} \neq 0$. The different sets of capacitors that appear in that context are summarized in Tbl. (2.1). Note that all of these are physical parameters which are not the direct entries into the C–matrix $(C)_{ij} \equiv c_{ij}$; they are the capacitances from the capacitor network which simulates the physical system. Notice also the difference in the notation, $\mathcal{C}_{ij}$ versus $c_{ij}$. In the case of nano–structures, the physical parameters $\mathcal{C}_{ij}$ to be specified are in the pF to aF range.

The total charge accumulating on island $i$ can now be calculated by summing up all contributions of the capacitors *connected* to island $i$ ($\mathcal{C}_{ij} = 0$ otherwise)

$$q_i = C_{0i} \cdot (V_i - 0) + \sum_j \mathcal{C}_{ij} \cdot (V_i - V_j) \tag{2.3}$$

$$= \Big(C_{0i} + \sum_{j(\neq i)} \mathcal{C}_{ij}\Big) V_i + \sum_{j(\neq i)} (-\mathcal{C}_{ij})\, V_j \tag{2.4}$$

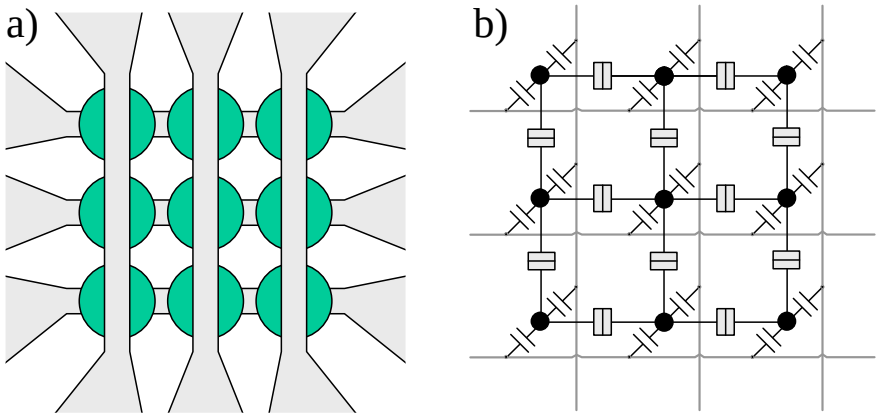


Figure 2.1: Model system - 3×3 array: (a) schematic layout: circles represent quantum dots and the three horizontal and the three vertical bars represent the gates which are connected to the outside macroscopic world. (b) same as panel (a) but drawn as a capacitor and tunnel junction network, where black circles represent the qudots and the horizontal and vertical lines the capacitively coupled voltage gates with the capacitors denoted as ⊣⊢ . The box symbols in between the dots ( ⊣▯⊢ ) represent capacitive tunnel junctions.

| | |
|---|---|
| $C_{0i}$ | self and stray capacitance of island $i$ |
| $C_{ij}$ | capacitance between nearest neighbor islands $i$ and $j$ |
| $C_{ig}$ | island $i$ to gate $g$ capacitance |

Table 2.1: Capacitance parameters that enter the total capacitance matrix via the generalized capacitances $\mathcal{C}_{ij}$ between object $i$ and object $j$, and therefore $\mathcal{C}_{ij} \in \{C_{0i}, C_{ij}, C_{ig}, 0\}$.

If for example the potential on island $i$ is larger than on some *connected* island $j$, the induced charge on island $i$ is positive which explains the signs in the previous equation. The parameter $C_{0i}$ contains both the self–capacitance of the $i$–th island as well as stray capacitance to ground as indicated in Eq. (2.3). Moreover, Eq. (2.4) already provides the C–matrix for the system through its linear structure of the type $q = CV$; the $i$–th element in the diagonal contains the sum over all the capacitances *connected* to island $i$ ($\mathcal{C}_{ij} = 0$ otherwise) while the off–diagonal elements are the negative of these capacitances, therefore

$$\begin{aligned} c_{ii} &= C_{0i} + \sum_{j(\neq i)} \mathcal{C}_{ij} \\ c_{ij} &= -\mathcal{C}_{ij} \end{aligned} \tag{2.5}$$

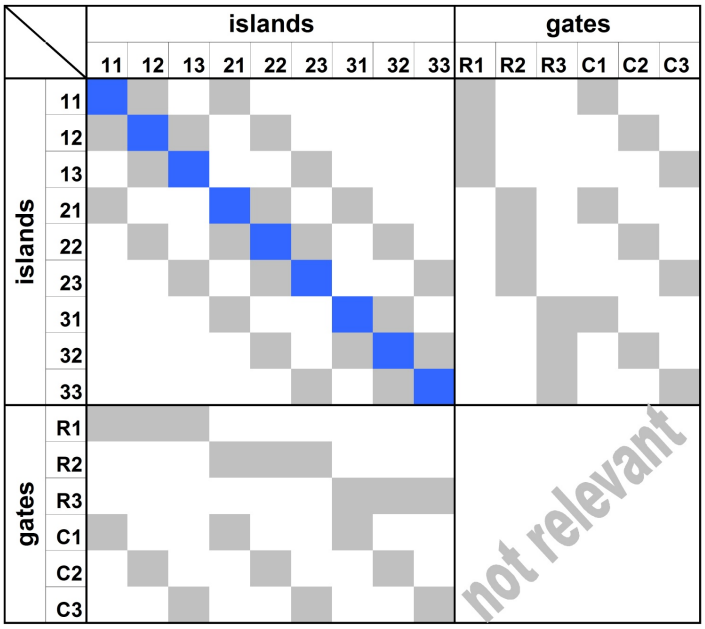


Figure 2.2: Schematic representation of the C–matrix for the network given in Fig. 2.1B: the grey entries are all negative and may differ in value, while the blue entries in the diagonal are all positive as described in the text. The islands are indexed by row and column as $ij$ with $i, j = 1 \ldots 3$, and similarly the gates along the rows as $Ri$ and along the columns as $Cj$ again with $i, j = 1 \ldots 3$.

Note that the parameters $C_{0i}$ are essential for the C–matrix to have an inverse (otherwise every row adds up to zero, and the matrix is singular! see also Sec. 2.3). This makes perfect sense, however, since squeezing charge together in space immediately rises the potential with respect to the environment. A proof of the physicality of the constructed C–matrix is given in Sec. 2.3 (p. 27).

### 2.1.2 Sample Networks

A sample network of capacitors modeling a $3 \times 3$ array of quantum dots linked to voltage gates has been shown in Fig. 2.1B. Now to be more specific, the C–matrix for this system is visualized in Fig. 2.2. As can be seen, the C–matrix will be highly sparse in general and represents the connectivity of the capacitor network. Further, by distinguishing between islands and gates, the C–matrix can be conveniently outlined into blocks. This essentially simplifies the notation as can be seen from the next section. Note in this context, that the lower right block (gate–gate interaction) will never be used and is therefore irrelevant.

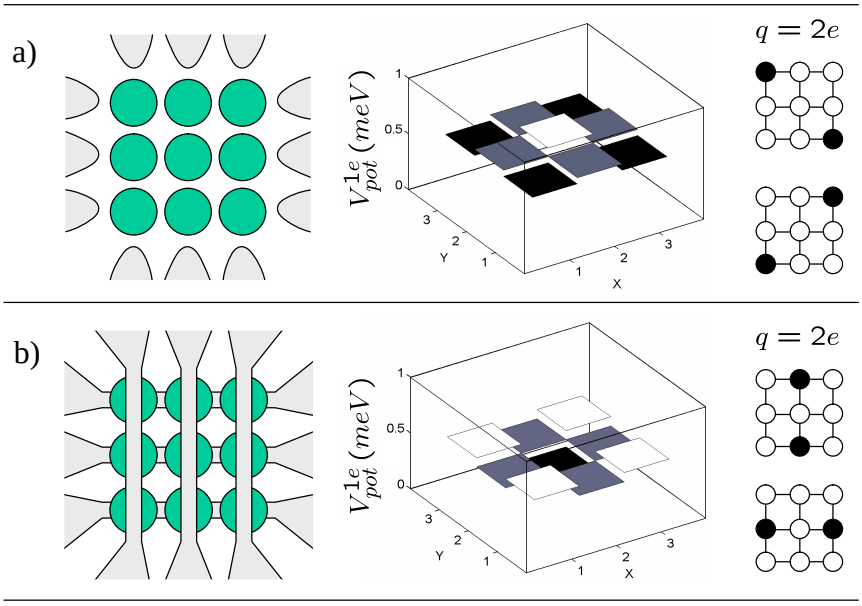


Figure 2.3: Comparison of two similar 3×3 arrays with very distinct single charge behavior - (a) 3×3 array with voltage gates coupling to the outer dots only. (b) the voltage gates extend over the whole array interacting with entire rows or columns of the array. The center panels in (a) and (b) show the potential of a single charge located on either one of the $3 \times 3$ islands resulting in a potential barrier like shape in case (a) while in case (b), the potential has the very distinct shape of a well. The potential on the gates is kept at $0V$ throughout. Adding another electron to the system, the lowest energy configurations with the two electrons localized to any of the dots are shown in the right panel of (a) and (b).

The capacitance matrix formalism allows us to get the main idea of the charge distribution on the system. Especially when considering single charges well localized to individual quantum dots, the question of which dots are most favorable in being occupied can be answered by classical electrostatic considerations. And the answer can be surprisingly different from system to system. As an example, consider the two quite similar setups in Fig. 2.3. In a handwaving argument, a single charge on the qudot array is attracted to its image charge in the voltage gates in the capacitor network of panel (a), such that for a single electron it is preferential to be on the outside of the $3 \times 3$ array, and especially on the corners of the array. For a second electron added to the system, its energetically favorite position is at the opposite corner with respect to the first electron, as shown in the right panel of Fig. 2.3a. Finally it should be noted, that for this effect of an attractive image charge in the voltage gates to

work, the capacitive coupling to the gates must have a certain (critical) strength. Choosing the coupling of the outer dots to the gates similar to the interdot capacitive coupling, as done in the simulation of Fig. 2.3, this requirement is clearly met.

For Fig. 2.3b, however, this image charge effect on the outer qudots is not present since the voltage gates act on entire rows or columns of the array. This inverts the single–electron potential landscape as shown in the center panel of Fig. 2.3b. Moreover, if a second charge is added to the system in the same fashion as in the panel (a), then these two charges repel each other. However, it turns out for the system under consideration that this repulsion is not strong enough to push the two electrons on opposite corners of the array as in Fig. 2.3a, and neither is it weak enough to leave both electrons in the center dot of the array. The energetic compromise is, that both charges move midway outside, as is shown in the right panel of Fig. 2.3b. Finally, due to the 90° symmetry of the system, in both cases (a+b), the minimum energy configuration is two fold degenerate by construction which is essential for the quantum bit setup on the basis of charge distribution later on.

### 2.1.3 Optimal Charge Configuration on Set of Islands

The energy for a certain charge or voltage configuration on an interacting set of conductors is given by Eq. (2.2). Considering a certain total amount of charge $Q$, the optimal static distribution of this charge on the given geometry is easily expressed using the C–matrix formalism. Using a Lagrange multiplier $\lambda$, the expression to be minimized is

$$\frac{1}{2}qC^{-1}q - \lambda\left(\sum_i q_i - Q\right) \rightarrow Min$$

Taking derivatives and setting them equal to zero gives (note that since $C$ is symmetric, so is $C^{-1}$ as shown in Eq. 2.43, p. 29)

$$C^{-1}q - \lambda u = 0 \tag{2.6a}$$

$$\sum_i q_i - Q \equiv uq - Q = 0 \tag{2.6b}$$

with $u \equiv (1, 1, \ldots, 1)$ being a vector with coefficients of 1 throughout. The last equation just reflects the constraint of charge conservation. Eq. (2.6a) is solved for $q$

$$q = C\lambda u$$

Since this equation has the form $q = CV$, it follows that the optimal charge configuration has uniform potential on all islands, namely $V = \lambda u$ with $\lambda$ determined from

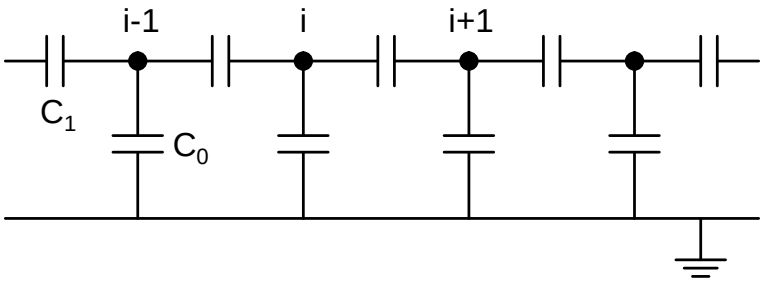


Figure 2.4: 1D capacitor network - the *islands* are indicated as $\ldots,\ i-1,\ i,\ i+1, \ldots$. The capacitors ( ⊣⊢ ) are considered to be identical throughout the chain, namely $C_1$ in between the islands and $C_0$ from the island to ground where latter $C_0$ includes self–capacitance as well as *stray capacitances* .

Eq. (2.6b)

$$u \cdot C\lambda u = Q \ \Rightarrow\ \lambda = \frac{Q}{uCu}$$

In summary, the optimal charge configuration implies the same potential $V_i \equiv V = Q/(uCu)$ for every island as expected from intuition and the overall charge distribution is given by

$$q = Q\frac{Cu}{uCu} \tag{2.7}$$

This is but one of the numerous examples of the convenience of the C–matrix formalism.

### 2.1.4 Screened Coulomb Potential in 1D Capacitor Network

Consider the network of capacitors given in Fig. 2.4 with the island index $i \in \{1,\ \ldots, n\}$. With an excess charge $q$ on one of the islands, i.e. island $i = i_0$, with all the other islands neutral, the question arises what is the corresponding potential distribution along the network. It is straightforward to write down the C–matrix for this system which is a highly sparse banded matrix. With the limit of the length of chain being very large, however, an alternative approach for solving the system is chosen here, such that an analytical solution can be derived for the simple geometry given in Fig. 2.4.

In the same fashion as for Eq. (2.3), the charge on island $i$ is the sum over the contributions from all the capacitors connected to it

$$q_i \ = \ C_0\,(V_i - 0) + C_1\,(V_i - V_{i-1}) + C_1\,(V_i - V_{i+1})$$

$$= C_0 V_i - C_1 \left(V_{i-1} + V_{i+1} - 2V_i\right) \tag{2.8}$$

$$\equiv C_0 V_i - C_1 \frac{\Delta^2 V_i}{\Delta x^2} \ . \tag{2.9}$$

The last term in Eq. (2.8) resembles the (discrete) Laplacian and has been indicated as such in Eq. (2.9) with the spacing between two consecutive islands on the chain being $\Delta x \equiv 1$. Furthermore, since by assumption $q_i = q \cdot \delta_{i,i_0}$, the $q_i$ at $i = i_0$ acts as a *point source* in this differential equation. In *free* space, namely where $q_i = 0$, the solution to Eq. (2.9) is closely related to the solution of the Laplacian for continuous functions. For the continuous case, the solution to $V''(i) = -\left(C_0/C_1\right) V(i)$ would be an exponential decay of $V\left(x\right)$ on the length scale of $\ell = \sqrt{C_1/C_0}$ islands [Lik99]. The exact solution for the *discrete* case looks slightly different, yet the main feature, the exponential decay of the potential, stays intact. With the ansatz $V_m = A\ e^{\kappa m}$ where $A$ and $\kappa$ are constants and where $m$ refers to a region of *free space* along the chain, i.e. a continuous set of islands with $q_m = 0$, Eq. (2.9) becomes

$$0 = C_0 A\ e^{\kappa m} \left(1 - \frac{C_1}{C_0}\left(e^{+\kappa} + e^{-\kappa} - 2\right)\right)$$

and thus with $A \neq 0$

$$1 - \frac{2C_1}{C_0}\left(\cosh\left(\kappa\right) - 1\right) = 0$$

$$\kappa = \pm \cosh^{-1}\left(1 + \frac{C_0}{2C_1}\right) \tag{2.10}$$

The ansatz motivated by the continuous solution is thus correct and two solutions of the sort $e^{\pm\kappa m}$ do exist with the coefficient $\kappa$ given by Eq. (2.10). This pair of *free–space* solutions must be matched to the boundary conditions of the specific problem. Consequentially, for the point source on island $i_0$, the potential induced by this extra charge will decay off exponentially to the left and to the right of it. The resulting object (excess charge of one electron + induced localized potential) can be thought of as a soliton which may move along the array. For $n$ large enough, this object is well localized within the array, and so there may be several of these *solitons* on the 1D array. And furthermore, this soliton does not have to originate in an extra electron on the array, but it can also originate in an extra hole, i.e. an electron taken out of the array. The resulting object is then referred to as an *antisoliton* [SKKL01]. If two of these solitons are far away from each other (distance $> (C_1/C_0)$ sites) they will not interact. However, when they come closer to each other, they will repel each other if they are of the same sort. Soliton and antisoliton, however, will attract and can eventually annihilate each other.

Finally, the continuous limit of the linear chain can be regained by considering $C_0 \ll C_1$, i.e. weak screening such that the potential modulations are weak from one island to the other. In this case, Eq. (2.10) becomes

$$1 + \frac{1}{2}\kappa^2 \approx 1 + \frac{C_0}{2C_1}$$

with the evident solution

$$\kappa \approx \sqrt{\frac{C_0}{C_1}} \text{ for } \frac{C_0}{C_1} \ll 1 \tag{2.11}$$

which is identical to the solution of the continuous case already indicated above. In the general case, since the cosh increases much faster than a simple quadratic term, it holds that $\kappa < \sqrt{C_0/C_1}$ which tells us that the continuous case puts a *lower* limit to the localization length, such that $\ell \gtrsim \sqrt{C_1/C_0}$. For small $C_0$ and therefore for small $\kappa$, $\ell \approx \sqrt{C_1/C_0}$ is a good approximation. The deviation becomes pronounced only for larger $\kappa$ and thus for $C_0/C_1 \gtrsim 1$. For larger $C_0$ there will be still a small spread of the soliton around its originating island yet it is essentially localized to one island, i.e. $\ell \lesssim 1$.

As an application of the soliton on a linear chain, its coupling to leads will be discussed in the following. Suppose the capacitor network shown in Fig. 2.4 is terminated to the left with a gate at a potential $V_L$ and coupled via a capacitor $C_L$ and similarly to the right ($V_R$, $C_R$). If there is a single soliton in the 1D network that reaches out still to the gates at the left and at the right, under the assumption of weak tunneling, where is it going to move? Is it energetically preferential to stay in the middle of the array, or will it be attracted towards the closest gate? If the extra charge is at island $i_0$, then the question will be answered to where the lowest potential $V_0 \equiv V(i_0)$ occurs in dependence of the $i_0$ limited to the array. The boundary conditions for this problem are the potentials $V_L$ and $V_R$ together with a charge $q$ on island $i_0$ with each of the other islands potentially polarized yet neutral as a whole. The arrays to the left and to the right of $i_0$ are described by the *free* solutions $e^{\pm\kappa m}$ but with unknown amplitudes at this point. Thus one has two sections (left/right of $i_0$) of the following sort

$$\begin{aligned} V_m &= A_1 e^{-\kappa m} + B_1 e^{+\kappa m} \text{ for } 1 < m < i_0 \text{ (left side)} \\ V_m &= A_2 e^{-\kappa m} + B_2 e^{+\kappa m} \text{ for } i_0 < m < n \text{ (right side)} \end{aligned} \tag{2.12}$$

where $n$ stands for the length of the string of islands considered. For $1 < i_0 < n$, the

boundary conditions are

$$\begin{aligned} 0 &= C_0 V_1 + C_1 (V_1 - V_2) + C_L (V_1 - V_0) && \text{at the left and} \\ 0 &= C_0 V_n + C_1 (V_n - V_{n-1}) + C_R (V_n - V_{n+1}) && \text{at the right and} \\ q &= C_0 V_{i_0} - C_1 (V_{i_0-1} + V_{i_0+1} - 2V_{i_0}) && \text{at } i = i_0. \end{aligned} \tag{2.13}$$

The potentials $V_0 \equiv V_L$ and $V_{n+1} \equiv V_R$ are considered given. The general approach of solving Eq. (2.12) with the boundary conditions in Eq. (2.13) is skipped. However, in order to answer the questions posed above, the following two situations are compared: (a) the soliton in the middle of a long string of islands, and (b) the soliton very close to the right end say, such that there is no neutral island left to the right of $i_0$, i.e. $i_0 = n$. In case (a), the left and the right side of $i_0$ are symmetric, and thus the last equation in Eqs. (2.13) turns out to be

$$q = C_0 V_{i_0} - C_1 V_{i_0} \left( e^{-\kappa} + e^{-\kappa} - 2 \right)$$

This is solved for $V_{i_0}$

$$V_{i_0} = \frac{q}{C_0 + 2C_1 (1 - e^{-\kappa})} \tag{2.14}$$

Similarly, for case (b) the last equation in Eqs. (2.13) needs some modification

$$q = C_0 V_{i_0} + C_1 \left( V_{i_0} - V_{i_0} e^{-\kappa} \right) + C_R (V_{i_0} - V_R)$$

which again is solved for $V_{i_0}$

$$V_{i_0} = \frac{q + C_R V_R}{C_0 + C_1 (1 - e^{-\kappa}) + C_R} \tag{2.15}$$

So in comparing Eq. (2.14) for case (a) and Eq. (2.15) for case (b), the following statements can be made

- since the potential $V_{i_0}$ can be thought of as an addition energy, the lowest potential of either Eq. (2.14) or Eq. (2.15) will determine which of the cases (a) or (b) is energetically favorable.
- for $V_R = 0$, the array is *ideally terminated* if and only if $C_R = C_1 (1 - e^{-\kappa})$ in the sense that the soliton can stay equally well anywhere because of the existing equipotential. For $C_R < C_1 (1 - e^{-\kappa})$, the soliton prefers to stay away from the border, while for $C_R > C_1 (1 - e^{-\kappa})$ the soliton is attracted to it. Specifically, this means that solitons are not attracted to open borders while on the other hand the possibility of *image charges* in the leads is attractive to them.

- since $V_{i_0}$ depends directly, namely linearly, on the external potential $V_R$ of the lead, this *external knob* can be used to repel or to attract a soliton of a certain charge at will. Therefore the lead can act as a source of solitons (or antisolitons) depending on the voltage applied to the lead [SKKL01].

In conclusion it is emphasized that the screening of the Coulomb potential is by no means restricted to the 1D array of islands. Considering the limit of the continuous case above, it is easy to generalize the capacitor network to more than one dimension. In free space, Eq. (2.9) still would have the similar structure $0 = C_0 V_i - C_1 \frac{\Delta^2 V_i}{\Delta x^2}$ resulting in the exponential screening of any excess charge.

### 2.1.5 Quantum Dots and Voltage Gates

For a set of quantum dots interacting with a set of external leads, two evidently distinct groups of islands enter the total C–matrix of the system: first, the *internal* islands (quantum dots), where the voltage is floating and thus unknown. The charge can be rearranged between the dots and is determined by minimizing the total *internal* energy (the free energy). On the other hand, the set of external leads is kept at fixed voltages by an external source (voltage gates). The C–matrix is conveniently grouped into blocks with respect to these two groups and is shown schematically for example in Fig. 2.2. The two groups with its related nomenclature are summarized in the Tbl. (2.2) such that Eq. (2.1) is rewritten as follows

$$\begin{pmatrix} q_1 \\ q_2 \end{pmatrix} = \begin{pmatrix} C_{11} & C_{12} \\ C_{21} & C_{22} \end{pmatrix} \begin{pmatrix} V_1 \\ V_2 \end{pmatrix} \tag{2.16}$$

The $q_i$ and $V_i$ are real vectors of dimension $n_i$ as indicated in the Tbl. (2.2). Here, the $C_{ij}$ are the corresponding block matrices of dimension $n_i \times n_j$. Note that for convenience and readability, the vector sign has been dropped; it should be still clear, however, that one is dealing with (sub) vectors and (block) matrices. $V_2$ is the known vector of potentials (voltages) applied to the gates, while $q_1$ and $V_1$ are unknown vectors determined by minimization of the free energy as already indicated. This fixes the charge configuration on the internal islands $q_1$. In the praxis, $q_1$ and $V_2$ are known and the missing pieces $q_2$ and $V_1$ can be calculated (notice the opposite roles of $q$ and $V$ with respect to the indices 1 and 2). Eq. (2.16) can now be expanded into two equations again being reminded that the $q$'s and $V$'s are vectors and the $C_{ij}$ block matrices

$$q_1 = C_{11} V_1 + C_{12} V_2 \tag{2.17a}$$
$$q_2 = C_{21} V_1 + C_{22} V_2 \tag{2.17b}$$

| index | represents | with | variables |
|---|---|---|---|
| 1 | internal islands | floating voltage and charge transfer | $q_1,\ V_1 \in \mathbb{R}^{n_1}$ |
| 2 | gates | voltage provided externally | $q_2,\ V_2 \in \mathbb{R}^{n_2}$ |

Table 2.2: Index convention on internal islands (quantum dots) and voltage gates

Since the *known* quantities are $q_1$ and $V_2 \equiv V_g$, the $V_1$ can be calculated (similarly, $q_2$ is determined but is actually not needed and will therefore be dropped)

$$V_1 = C_{11}^{-1}\left(q_1 - C_{12}V_g\right) \equiv V_1\left(q_1, V_g\right) \tag{2.18}$$

With this, the free energy of the internal islands is motivated as the work that must be done to change the charge distribution by the small amount $dq_1$

$$dW = V_1\left(q_1, V_g\right)\ dq_1$$

and thus up to a constant

$$\begin{aligned} W &= \int^{q_1} V_1\left(q_1', V_g\right)\ dq_1' && (2.19a)\\ &= \int^{q_1} C_{11}^{-1}\left(q_1' - C_{12}V_g\right)\ dq_1' \\ &= \frac{1}{2}q_1 C_{11}^{-1} q_1 - q_1 C_{11}^{-1} C_{12} V_g && (2.19b) \end{aligned}$$

With the definition

$$q_x \equiv C_{12}V_g, \tag{2.20}$$

this $q_x$ corresponds to the induced charge on the islands due to the presence of the voltage gates. The free energy then becomes

$$\begin{aligned} W &= \frac{1}{2}q_1 C_{11}^{-1} q_1 - q_1 C_{11}^{-1} q_x && (2.21a)\\ &= \frac{1}{2}\left(q_1 - q_x\right) C_{11}^{-1}\left(q_1 - q_x\right) - \frac{1}{2}q_x C_{11}^{-1} q_x && (2.21b) \end{aligned}$$

The last term in this equation is dependent on the gate voltages only and thus independent of $q_1$; therefore, it is irrelevant for the minimization of $W$ with respect to $q_1$

and the optimal charge distribution with minimum energy $W$ is given as

$$q_{1,min} = q_x = C_{12}V_g \tag{2.22}$$

All that is needed to calculate the free energy of the island system is the island–island capacitance submatrix $C_{11}$ and the island–gate coupling block $C_{12}$ (which is the conjugate of $C_{21}$). The gate–gate capacitance submatrix $C_{22}$ does not show up and is therefore not needed; in other words, the coupling amongst the gates and the coupling of the gates to rest of world is irrelevant to the problem as also indicated in Fig. 2.2. Furthermore, when Eq. (2.21a) is rewritten using Eq. (2.18)

$$W = \frac{1}{2}q_1V_1 - \frac{1}{2}q_1C_{11}^{-1}q_x \tag{2.23}$$

the influence of the environment, namely the voltage gates, is most clearly expressed. In a free system without interaction to an environment, the last term vanishes since $q_x = 0$ and the usual expression for the electrostatic energy $W = \frac{1}{2}q_1V_1$ is obtained. However, for a system interacting with an external environment, work is done also by the environment when rearranging charges on the islands while keeping the voltages on the gates constant. This essential physical interplay is taken care of by the last term in Eq. (2.23). Alternatively, this last term can also be interpreted as a local drag of the potential for every individual island in dependence of the external voltages.

For nanosized structures the quantization of charge becomes an essential ingredient to the overall behavior of the system [Lik99]. When localized by weak tunneling to small puddles, charge becomes quantized by $e$, the fundamental charge of the electron, i.e. charge configurations change in units of $e$. Then a certain charge arrangement can represent the lowest energy distribution for a small *range* of gate voltages and is thus a *rigid* charge configuration. But even so, for very specific voltages, two or more charge configurations can have exactly the same free energy. This degeneracy point in configuration space can then be utilized for controlled charge transfer through quantum dots. This is well–known as the Coulomb blockade regime with spikes in the interdot conductance for very specific gate voltage configurations [MWL91].

### 2.1.6 Change of Free Energy for Small Charge Variations

From a typical numerical simulation of the electrostatic problem, the data for $q$ and $V$ can be retrieved from the output. However, as mentioned above, for the Coulomb blockade regime the charge has to be constrained to integer multiples of the charge of the electron $e$. This is an extra constraint when minimizing the total energy of the system. When shifting single charges between the islands, it is natural to ask

which one of two such configurations is lower in energy. Therefore one must be able to estimate $\Delta W$ explicitly comparing the $(q_1, V_1)$ data while the gate voltages are considered constant.

Consider a specific setup of metallic islands as in the previous section with some set of voltage gates. The work done by the exterior when accounted for by the second term in Eqs. (2.21), requires the knowledge of the capacitance matrix. In this section, however, the capacitance matrix is considered unknown. Instead what is given is a set of gate voltages $V_2 \equiv \vec{V}_g$ fixed by the exterior, and two sets of data, set one $(q_1, V_1) = (q_a, V_a)$ for the first configuration of charges and the corresponding voltages and set two $(q_b, V_b)$ for some slightly altered configuration. Note that here this may also include a slight change of the regions which contain charges, thus a change of the geometry and consequently of the capacitance matrix. Now what is the change in the free energy when comparing the two systems (a) and (b)? To tackle this problem, the appropriate starting point is Eq. (2.19a). With the vectors $\Delta q_1 \equiv q_b - q_a$ and $\Delta V_1 \equiv V_b - V_a$ and Taylor expansion of $V_1(q_1, V_g)$ around $q_1 = q_a$, it then follows

$$\begin{aligned}
\Delta W_{ab} &= \int_{q_a}^{q_b} V_1(q_1', V_g = const)\, dq_1' \qquad (2.24)\\
&= (\text{with } q_1' \to q_1' - q_a)\\
&\equiv \int_0^{\Delta q_1} V_1(q_a + q_1')\, dq_1'\\
&\simeq \int_0^{\Delta q_1} \left( V_a + \left( q_1' \frac{\partial}{\partial q_1'} \right) V_a + \mathcal{O}\left( {q_1'}^2 \right) \right) dq_1'\\
&= \int_0^{\Delta q_1} \frac{\partial}{\partial q_1'} \underbrace{\left( q_1' V_a + \frac{1}{2} q_1' \left( \frac{\partial}{\partial q_1'} \circ V_a \right) q_1' \right)}_{\equiv F\left(q_1'\right)} dq_1' \qquad (2.25)
\end{aligned}$$

with the tensor product of two vectors denoted by $(a \circ b)_{ij} \equiv a_i b_j$. In the last equation, the path integral in $q_1'$ is written as a single gradient term which is easily integrated by taking the effective potential $F(q)$ at the limits of the integral $F(q) \equiv q_i V_i^a + \frac{1}{2} q_i \left( V_{i,j}^a \right) q_j$ with $V_{i,j}^a \equiv \partial V_i / \partial q_j$ evaluated at $q_a$ and with implicit summation over the double indices. Since $F(0) = 0$,

$$\Delta W_{ab} = F(\Delta q_1)$$

$$
\begin{aligned}
&= \Delta q_1 \; V_a + \frac{1}{2} \underbrace{\Delta q_1 \, (\nabla \circ V_a)}_{\equiv \frac{\partial V_a}{\partial q_1} \Delta q_1 \simeq \Delta V_1 = V_b - V_a} \Delta q_1 \\
&= \Delta q_1 \; V_a + \frac{1}{2} \Delta q_1 \; \Delta V_1
\end{aligned}
$$

with the final result

$$
\Delta W_{ab} \simeq \Delta q_1 \; \frac{1}{2} \left( V_a + V_b \right) \tag{2.26}
$$

Note that the approximate sign in the last equation becomes an equal sign for a rigid geometry and thus for a constant capacitance matrix for which the analytical expression for $F(q)$ *is* parabolic in its argument. To see this, the last equation is rewritten with the substitutions $(q_a, V_a) \rightarrow (0, V_0)$ and $(q_b, V_b) \rightarrow (q_1, V_1)$, such that $\Delta W = \frac{1}{2} q_1 \left( V_0 + V_1 \right)$. In the notation of the previous section, the potential is given as $V_1 = C_{11}^{-1} \left( q_1 - q_x \right)$. Thus with $V_0 \equiv -C_{11}^{-1} q_x$, the change in the free energy becomes $\Delta W = \frac{1}{2} q_1 \left( -C_{11}^{-1} q_x + C_{11}^{-1} \left( q_1 - q_x \right) \right) = \frac{1}{2} q_1 C_{11}^{-1} q_1 - C_{11}^{-1} q_x$, exactly the same as in Eq. (2.21a). For cases, however, where certain regions of space are depleted of charge due to Coulomb interaction, the potentials directly define an effective geometry which may change over the course of time. For small variations in the voltages, the resulting small changes also in the geometry are included in the expression given by Eq. (2.26).

### 2.1.7 Example: Coupled Two Dot System with SET

A setup of two interacting quantum dots (dots #1 and #2) is shown in Fig. 2.5. These two dots are capacitively coupled to a third dot, the single electron transistor (SET) shown at the bottom of Fig. 2.5. This SET when tuned into resonance with the chemical potential in the leads is highly sensitive to charging effects in the local environment and can therefore be used to measure the state in the double–dot system. For this, the SET leads $V_L$ and $V_R$ have a very small asymmetric voltage applied indicated by the infinitesimal $0^{\pm}$. All three dots are considered to have the same shape and therefore the same self–capacitance $C_0$. Furthermore, the gate capacitances of the first two dots are considered the same, i.e. $C_{g_1} = C_{g_2} \equiv C_g$, and also the gate capacitances for the SET, $C_L = C_R$.

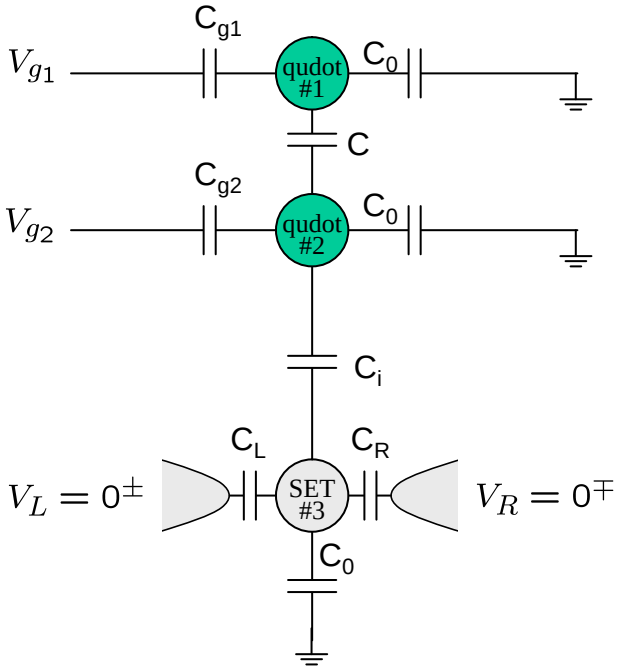


Figure 2.5: Sample system of two capacitively coupled quantum dots (dots #1 and #2) whose charge state is measured by the single electron transistor (SET) which includes quantum dot #3. Every dot has a self capacitance $C_0$ which includes the stray–capacitances to ground as indicated.

Then the capacitance matrix for the system under consideration is

$$\left(\begin{array}{c} q_1 \\ q_2 \\ q_3 \\ \hline q_{g_1} \\ q_{g2} \\ q_L \\ q_R \end{array}\right) = \left(\begin{array}{ccc|cccc} C_0{+}C_g{+}C & -C & 0 & -C_g & 0 & 0 & 0 \\ -C & C_0{+}C_g{+}C{+}C_i & -C_i & 0 & -C_g & 0 & 0 \\ 0 & -C_i & C_0{+}C_i{+}C_{L+R} & 0 & 0 & -C_L & -C_R \\ \hline & & & & & & \\ & & & & & & \\ & h.c. & & & (irrelevant) & & \\ & & & & & & \end{array}\right) \left(\begin{array}{c} V_1 \\ V_2 \\ V_3 \\ \hline V_{g_1} \\ V_{g2} \\ V_L \\ V_R \end{array}\right) \tag{2.27a}$$

or in short

$$\left(\begin{array}{c} q \\ q_g \end{array}\right) \equiv \left(\begin{array}{cc} C_{11} & C_{12} \\ C_{12}^{+} & C_{22} \end{array}\right) \left(\begin{array}{c} V \\ V_g \end{array}\right) \tag{2.27b}$$

written in the same block notations as indicated in Fig. 2.2. The block $C_{22}$ is irrelevant to the problem and therefore not written out. Note further that for a symmetrically applied voltage for the SET system, namely $V_L = -V_R$, the net contribution to the charge $q_3$ will be zero. An eventual plunger gate to tune the quantum dot on the SET has the effect of a slight shift of $V_3$, and would be easily introduce by adding another column to the right of the capacitance matrix shown above. The free energy for the $q$ subsystem is given by Eq. (2.21a)

$$W = \frac{1}{2} q C_{11}^{-1} q - q C_{11}^{-1} C_{12} V_g \tag{2.28}$$

Now, one may ask, starting from an initial charge configuration which minimizes the energy $W$, how must the gate voltages be altered so that the new charge configuration differs from the initial one only in that one electron was transferred from dot 1 to dot 2 or vice versa, i.e. $dq_1 = -dq_2 = \pm 1$ and therefore $dq = m\,(1, -1, 0)$ with $m = \pm 1$ or some other non–zero integer value (in terms of units, the electron charge $e$ is set to $-1$ for convenience, i.e. $|e| = 1$). The energetically optimal charge configuration is given by Eq. (2.22), $q = C_{12} V_g$, from which it follows that $dq = C_{12} dV_g$. Because of the linearity of this equation, the discrete changes in the charge configurations made by transferring one charge after another are directly related to equally spaced changes in the individual voltage gates. Together with a plunger gate (pg) for the SET, this equation becomes

$$\begin{pmatrix} dq_1 \\ dq_2 \\ dq_3 \end{pmatrix} = m \begin{pmatrix} 1 \\ -1 \\ 0 \end{pmatrix} = \begin{pmatrix} -C_g & 0 & 0 & 0 & 0 \\ 0 & -C_g & 0 & 0 & 0 \\ 0 & 0 & -C_L & -C_R & -C_{pg} \end{pmatrix} \begin{pmatrix} dV_{g_1} \\ dV_{g2} \\ dV_L \\ dV_R \\ dV_{pg} \end{pmatrix} \tag{2.29}$$

Since by assumption $dV_L = -dV_R$ and $C_L = C_R$, these drop out of this system of equations, as intuitively expected since their effect on the qudot #3 cancels out. With this, Eq. (2.29) reduces to the trivial result

$$dq = m \begin{pmatrix} 1 \\ -1 \\ 0 \end{pmatrix} = \begin{pmatrix} -C_g & 0 & 0 \\ 0 & -C_g & 0 \\ 0 & 0 & -C_{pg} \end{pmatrix} \begin{pmatrix} dV_{g_1} \\ dV_{g2} \\ dV_{pg} \end{pmatrix} \tag{2.30}$$

with the interpretation that when the extra charge on a specific island counter balances the induced charge due to a drag of its capacitively coupled voltage gate, then

the net effect on the remaining system is zero. In other words, the individual gates do not couple to each other if they are related to different dots. This assumption is somewhat ideal, however, but with this procedure it is straightforward to calculate the effects of more interconnected structures. If it happens that in the final system $V_{12}$ has more columns than rows, as initially in the above case, then the resulting freedom in the gate voltages can be used to constrain some of these gate voltages further, e.g. to constant value.

With the example problem at hand, it is also easy to demonstrate the consequences of the discreteness of the electronic charge. Looking back at Eq. (2.28), the hop of one electron from one dot to another is energetically favorable if $W(q_0) = W(q_0 + dq)$ with $dq$ being discrete as for example in Eq. (2.30). The charge configurations $q_a \equiv q_0$ and $q_b \equiv q_0 + dq$ are considered to be the minimal charge configurations for the voltage configurations $V_a$ and $V_b$ such that

$$q_a = C_{12} V_a \quad \text{and} \quad q_b = C_{12} V_b. \tag{2.31}$$

Starting at either $V_a$ or $V_b$, the voltages are tuned and the charges stay put at $q_a$ or $q_b$, respectively, until the discrete change between the charge configuration $q_a \longleftrightarrow q_b$ is energetically favorable, i.e. a cross–over happens at the gate voltages $V_g$ such that $W(q_a, V_g) = W(q_b, V_g)$ or equivalently

$$\frac{1}{2} q_a C_{11}^{-1} q_a - q_a C_{11}^{-1} C_{12} V_g = \frac{1}{2} q_b C_{11}^{-1} q_b - q_b C_{11}^{-1} C_{12} V_g \tag{2.32}$$

The first point to notice is that the last equation is fulfilled for $V_g = \langle V_g \rangle \equiv \frac{1}{2}(V_a + V_b)$ and is shown easily using Eqs. (2.31). This solution for $V_g$ corresponds to an optimal charge configuration exactly half–way between $q_a$ and $q_b$ since $\frac{1}{2}(q_a + q_b) = C_{12}\ \langle V_g \rangle$. This is a completely general result and for simple systems a well–known statement [Lik99] that is summarized as follows

> For two 'nearest neighbor valleys' in the energy spectrum due to the discreteness of charge with their minima at $V_a$ and $V_b$, there is always a crossover at exactly half–way in between these gate voltages, and there the optimal charge configuration is exactly the average of $q_a$ and $q_b$ where $q_a$ and $q_b$ are the optimal charge configurations at $V_a$ and $V_b$, respectively.

The effect of the discreteness of charge is shown visually in Fig. 2.6, for simplicity for one gate voltage and one dot, i.e. $q$ and $V_g$ are scalars. According to Eq. (2.28), $W(q; V_g)$ is a linear function of the gate voltage, and thus the left panel of Fig. 2.6 consists of a set of lines. The one line with the lowest energy for a given $V_g$ corresponds to the charge configuration with lowest energy. For the right panel, consider Eq. (2.28)

again

$$\begin{aligned} W(q;V_g) &= \frac{1}{2}qC_{11}^{-1}q - qC_{11}^{-1}C_{12}V_g \\ &= \underbrace{\frac{1}{2}\left(q-q_x\right)C_{11}^{-1}\left(q-q_x\right)}_{\equiv\tilde{W}(q;V_g)} - \frac{1}{2}q_xC_{11}^{-1}q_x \end{aligned} \tag{2.33}$$

with $q_x \equiv C_{12}V_g$. The last term only depends on the gate voltages and thus is irrelevant for the decision which charge configuration has the lowest energy configuration for a certain $V_g$ and thus can be dropped which is equivalent to subtracting that term. Now, the right panel of Fig. 2.6 shows exactly the same data as the left panel except that at every $V_g$ all the curves are shifted by the energy $\frac{1}{2}q_xC_{11}^{-1}q_x = \frac{1}{2}V_gC_{21}C_{11}^{-1}C_{12}V_g \sim (V_g)^2$. The lines from panel (a) thus bend into a set of equally spaced parabolas. It is easily seen that the transition from one discrete charge configuration to the next is related to equal intervals in change of the gate voltages. This is not surprising since it was already mentioned earlier. Consequently notice that if one were to draw vertical lines for every crossover in the groundstate of Fig. 2.6a then the result would also be a set of equally spaced lines. Finally, the graphical result in 1D also confirms the general result above, that the cross–over between charge configurations takes place exactly half–way in between the 'nearest neighbor valleys' in the energy spectrum.

Finally, for the case that more than one voltage gate is present ($n_g \equiv \dim(V_g) > 1$), a whole variety of different $V_g$ configurations are possible that result in a crossover of the sort $W(q_a, V_g) = W(q_b, V_g)$. This equation for $V_g$ is then most simply expressed by introducing the reference voltages with respect to $\langle V_g\rangle \equiv \frac{1}{2}(V_a + V_b)$, namely $\tilde{V}_g \equiv V_g - \langle V_g\rangle$, such that Eq. (2.32) becomes $0 = (q_b - q_a)\,C_{11}^{-1}C_{12}\tilde{V}_g$ which describes an $n_g - 1$ dimensional flat surface in the space of the gate voltages. Yet by construction of the two 'nearest neighbor valleys' $a$ and $b$ as introduced above, the energetic crossover in the charge configurations $q_a \leftrightarrow q_b$ is the energetic minimum for $\tilde{V}_g = 0$ while for solutions $\tilde{V}_g \neq 0$ and fixed $q_a$ and $q_b$ quite probably it is not. Therefore, only the first case with $\tilde{V}_g = 0$ and thus $V_g = \frac{1}{2}(V_a + V_b)$ is of physical interest since this transition takes place in the groundstate in contrast to all the other cross–overs that happen at excited energies as seen for example in Fig. 2.6.

## 2.2 Interaction Potential and Power Laws

The interaction between a point charge (electron) and a metallic object (island or voltage gate) as a function of their distance was used to test the numerical EST3D package developed by the author (see Chap. 3, pp. 31). The analytical asymptotic

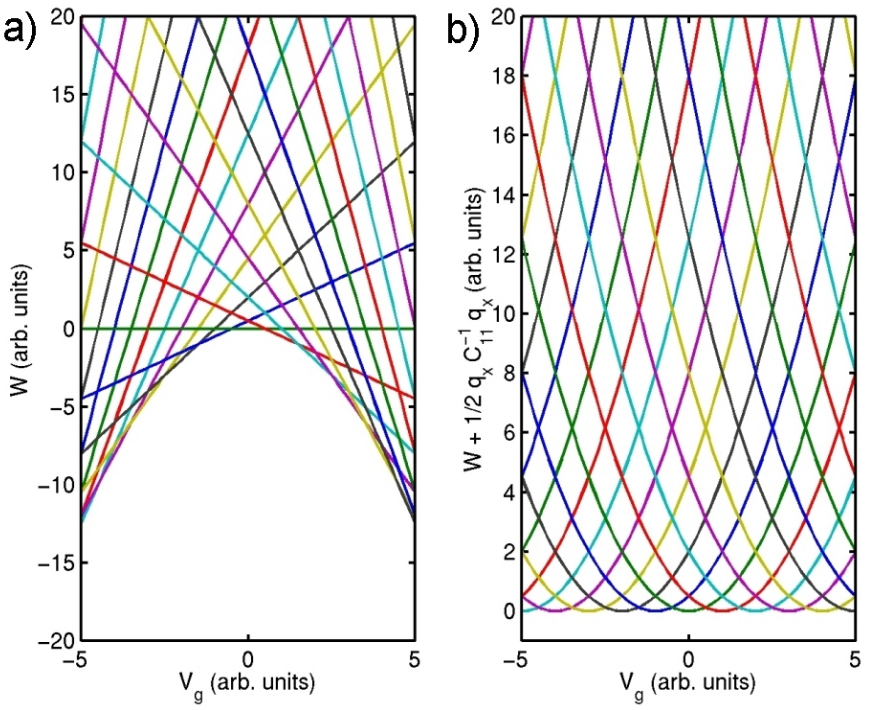


Figure 2.6: The effect of discrete charges on the charge configurations on a simplified model with one dot and one interacting gate - a) $W(V_g; q)$ as in Eq. (2.33) plotted with $q = \ldots, -2, -1, 0, 1, +2, \ldots$ as a parameter. The horizontal green line corresponds to $q = 0$. b) Same as panel (a) except that the energy is shifted as a function of $V_g$ (see text).

behavior that is expected from the numerical data is analyzed in this section. Fig. 2.7 shows the geometrical setup under consideration. A point charge with fixed charge $q$ is interacting with an extended metallic object at varying distance $z$. The potential $V$ and the charge $Q$ of the extended object are subject to different boundary conditions. Consider the following three cases:

1. minimum energy of the total system and therefore unknown $V$ and $Q$
2. isolated object and therefore $Q = const$
3. grounded object ($V = 0$) or more general, $V = const$.

In the first case, the charge on the extended object is constrained by the minimum of the total energy for this two–body system

$$E_{tot} = \frac{Q^2}{2C_0} + V_{int} \tag{2.34a}$$

$$\text{with } V_{int} \equiv \frac{qQ}{z} \tag{2.34b}$$

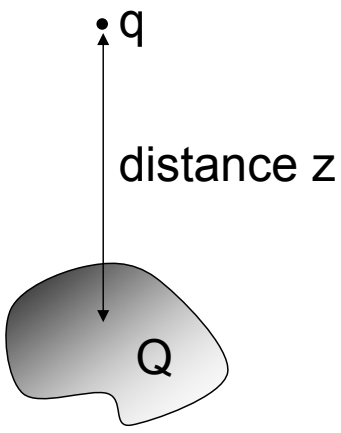


Figure 2.7: Schematic drawing of a point charge $q$ interacting with an extended conducting object with total charge $Q\,(V)$, where $V$ is the potential on the extended object.

All constant prefactors have been dropped for simplicity. The capacitance $C_0$ is related to the geometry of the larger object such that the first term in Eq. (2.34a) describes the self–energy of putting a total of a charge $Q$ onto the extended object. Since the charge on the point charge is considered constant, the self–energy thereof is constant and therefore irrelevant. The second term in Eq. (2.34a) is the interaction energy written as the monopole Coulomb interaction assuming large enough distances. Minimizing Eq. (2.34a) with respect to the charge $Q$ on the extended object, this results in $Q_{\min} = -\frac{q}{z}C_0$, i.e. the optimum induced charge on the extended object due to the presence of the point charge $q$ falls off like $1/z$. Consequently, the minimum interaction energy is

$$V^{int}_{E\to min} = -\frac{1}{2}\left(\frac{q}{z}\right)^2 C_0 \tag{2.35}$$

which falls off like $1/z^2$ and is negative, therefore attractive.

In the second case, where $Q = const$, the interaction energy is simply given by the lowest multipole of the extended object unequal zero, i.e. the $n$–th multipole where $n = 0$ refers to $Q \neq 0$, $n = 1$ is the dipole, $n = 2$ is the quadrupole and so on. With this, the interaction energy becomes $\mathcal{O}\,(1/z^{n+1})$, e.g. for $n = 0$ the standard Coulomb potential $\mathcal{O}\,(1/z)$. However, for $Q = const \neq 0$, this charge is independent of the point source. Therefore, for large distances, the interaction simply has a $1/z$ dependence. For $Q = 0$, however, the interacting dipole or quadrupole or higher are induced by the point charge $q$. The remaining procedure is very similar to the first case above, but here the charge is replaced by a generic $X$ which stands for the

strength of the lowest moment $n$ unequal zero. Also since this moment of order $n$ is induced, the strength $X$ is determined by the minimum of the total energy. In this sense, the total energy

$$E_{tot} = \frac{X^2}{2} + V_{int} \tag{2.36a}$$

$$\text{with } V_{int} \equiv \frac{qX}{z^{n+1}} \tag{2.36b}$$

when minimized with respect to $X$ gives $X_{min} = -q/z^{n+1}$ and therefore

$$V_{n\geq 1}^{int} = -\frac{1}{2}\left(\frac{q}{z^{n+1}}\right)^2. \tag{2.37}$$

The interaction potential falls off like $\mathcal{O}\left(1/z^{2(n+1)}\right)$, e.g. like $1/z^6$ if the lowest moment unequal zero is the quadrupole moment. Note also that the $n = 0$ case excluded here exactly corresponds to the first case considered above.

For the third case, again the point charge induces the dipole or quadrupole and so on in the extended object, but now, in order to fix the potential at given value, an extra contribution to the charge $Q$ from the exterior must exist. For $V \neq 0$, the case simplifies since for a large enough $z$ the potential $V$ induces a charge $Q$ which will saturate (or become independent of $z$) once the $z$ is large enough. Therefore the interaction energy will eventually have a $1/z$ dependence. The case $V = 0$ (grounded object), the potential on the extended object for large $z$ is given as $V \simeq \frac{Q}{C_0} + \frac{q}{z} = 0$. This immediately implies that the induced charge decays as $1/z$ as the point charge moves away to infinity, so that the interaction energy becomes

$$V_{grounded}^{int} = -\frac{1}{2}\left(\frac{q}{z}\right)^2 C_0 \tag{2.38}$$

which is exactly the same result as for the first case.

### 2.2.1 Note on Scaling

For the numerical simulation of electrostatics on a grid with a fixed lattice constant, it is natural to ask, how the solution scales with certain parameters. Due to the linearity of Maxwell's equations it is clear that for example scaling of sources of charge for a given geometry relates linearly to the generated potentials and vice versa. The scaling with respect to the grid spacing is discussed in the following.

A static charge distribution in space is related uniquely to a potential up to constant through Maxwell's equations [Jac99]. Now if one were to rescale space in the sense $\vec{r} \to \alpha\vec{r}$ with $\alpha$ being some scaling constant, then the electric potential $\phi$, the

electric field $\vec{E} = -\vec{\nabla}\phi$ and the charge distribution $\rho = \varepsilon\ \vec{\nabla}\vec{E} = -\varepsilon\ \nabla^2\phi$ scale as follows. Considering $\varepsilon = const$, then the dimensions of space entering into each of these variables are

| | spatial dimension | scaling with $\alpha$ |
|---|---|---|
| $\phi$ | $[-1]$ | $\alpha^{-1}$ |
| $\vec{E}$ | $[-2]$ | $\alpha^{-2}$ |
| $\rho$ | $[-3]$ | $\alpha^{-3}$ |

So for example, if a certain physical solution were scaled down spatially to half the size (e.g. $\alpha = 1/2$), then the potential would modulate $2\times$ as strong as in the original case, the electric field $4\times$ and the charge density $8\times$ as strong. Furthermore, reducing the size together with scaling up the charge density by $\alpha^{-3}$ implies that the overall charge is kept constant such that for example a point charge of $q = 1e$ remains the same point charge. Shrinking the dimensions by $\alpha$ thus increases the electrical field quadratically by $\alpha^{-2}$ and the potential linearly by $\alpha^{-1}$.

## 2.3 Appendix: Positive Definitness of C Matrix from Capacitor Network

The C–matrix as constructed in Eq. (2.5) is now shown to be physically relevant as outlined in Sec. 2.1 (p. 5). Specifically, it is symmetric and it is also positive definite. The symmetry immediately follows from the construction of the C–matrix, so all that remains to be shown is its positive definiteness. All the capacitor values are positive ($C_{0i} \geq 0$, $\mathcal{C}_{ij} \geq 0$), and so it follows that for an arbitrary vector $\vec{x}$

$$\begin{aligned} x\,C\,x &= \sum_{ij} x_i c_{ij} x_j \\ &= \sum_i c_{ii} x_i^2 + \sum_{i\neq j} x_i c_{ij} x_j \\ &= \sum_i \Big( C_{0i} + \sum_{j(\neq i)} \mathcal{C}_{ij} \Big) x_i^2 + \sum_{i\neq j} x_i \left(-\mathcal{C}_{ij}\right) x_j \\ &= \sum_i C_{0i} x_i^2 + \sum_{i\neq j} \left( x_i^2 \mathcal{C}_{ij} - x_i \mathcal{C}_{ij} x_j \right) \end{aligned} \tag{2.39}$$

Since in last part of the last equation an $i = j$ term would be zero anyway, the restriction $i \neq j$ is lifted

$$\begin{aligned} x\,C\,x &= \sum_i C_{0i}x_i^2 + \sum_{i,j}\left(x_i^2\mathcal{C}_{ij} - x_i\mathcal{C}_{ij}x_j\right) \\ &= \sum_i C_{0i}x_i^2 + \frac{1}{2}\sum_{i,j}\left(x_i - x_j\right)^2\mathcal{C}_{ij} \end{aligned}$$

where in the last step the symmetry of the mutual capacitances was used, specifically $\mathcal{C}_{ij} = \mathcal{C}_{ji}$. With all the terms being positive, the positive definiteness of above C–matrix follows, namely $x\,C\,x \geq 0$ for an arbitrary vector $\vec{x}$. ■

From Eq. (2.39) it also follows, that $x\,C\,x = 0$ for finite $x$is only possible, if some of the $C_{0i}$ are equal to 0 which again underlines the connection of the singularity of the C–matrix to some of the $C_{0i}$ being equal to 0. Thus the capacitances towards the environment $C_{0i}$, including both stray– as well as self–capacitance, represent an essential physical quantity for every single island under consideration.

## 2.4 Appendix: Symmetry of C Matrix and Green's Reciprocation Theorem

The symmetry of the C–matrix will be proven in the following using the *Green's reciprocation theorem* [Jac99, p. 52] which is restated as follows: consider two completely independent charge distributions $q_1(\vec{x})$ and $q_2(\vec{x})$ within a conducting surface $S$ and total volume $V$; each of these charge distributions $q_i$ is related to a unique surface charge $\sigma_i$ on the surface $S$ and derives from a potential $\phi_i$ such that $\nabla^2\phi_i = -q_i$ and $\frac{d\phi_i}{d\hat{n}} = \sigma_i$ with $i = 1, 2$ and $\varepsilon_0 = 1$ and where $d/d\hat{n}$ is the derivative perpendicular to the surface. Then from *Green's second identity* for arbitrary functions $\phi$ and $\psi$[Jac99, p. 36]

$$\int_V \left(\phi\ \nabla^2\psi - \psi\ \nabla^2\phi\right) d^3x = \oint_S \left(\phi\frac{d\psi}{dn} - \psi\frac{d\phi}{dn}\right) dS \tag{2.40}$$

rewritten as

$$\int_V \phi\left(-\nabla^2\psi\right) d^3x + \oint_S \phi\frac{d\psi}{dn}dS = \int_V \psi\left(-\nabla^2\phi\right) d^3x + \oint_S \psi\frac{d\phi}{dn}dS$$

it follows with the substitutions $\phi \to \phi_1$ and $\psi \to \phi_2$

$$\int_V \phi_1 q_2 d^3x + \oint_S \phi_1\sigma_2 dS = \int_V \phi_2 q_1 d^3x + \oint_S \phi_2\sigma_1 dS$$

This is called Green's reciprocation theorem.

Now taking the surface $S$ in free space out to infinity, the surface terms eventually drop out for physical reasons (i.e. with $Q_i \equiv \int_V q_i d^3x$, the potential $\phi_i$ goes like $\mathcal{O}(1/r)$ for large $r$, and so its derivative for the surface charge $\sigma_i$ goes like $\mathcal{O}(1/r^2)$; the surface term becomes $\mathcal{O}(1/r \cdot 1/r^2 \cdot 4\pi r^2) = \mathcal{O}(1/r)$ and vanishes as $r \to \infty$). Thus in open space, Green's reciprocation theorem reduces to

$$\int_V \phi_1 q_2 d^3x = \int_V \phi_2 q_1 d^3x \tag{2.41}$$

for two completely independent solutions $(q_i, \phi_i)$. In the language of a set of conductors and the related capacitance formalism with the vectors $q_i$ and $V_i$, this translates into

$$V_1 q_2 = V_2 q_1$$

and because $q_i = CV_i$,

$$V_1 C V_2 = V_2 C V_1$$

By construction, the latter equation has to hold for arbitrary vectors $V_1$ and $V_2$, and therefore also for $(V_1)_k = \delta_{ki}$ and $(V_2)_k = \delta_{kj}$. With this specific set of potentials, the symmetry of the capacitance matrix $C$ follows

$$C_{ij} = C_{ji} \ . \tag{2.42}$$

Moreover, with $C$ being symmetric, it follows with $1 = (C^{-1}C)^T = C^T (C^{-1})^T$ that

$$\left(C^{-1}\right)^T = \left(C^T\right)^{-1} = C^{-1} \tag{2.43}$$

that also $C^{-1}$ is symmetric. ■

# Chapter 3

# Numerical Electrostatic Simulation in 3D (EST3D)

In this chapter I introduce the software package EST3D © 2002 written during my Ph.D. project. The basic algorithm of the relaxation was published in [WU03c]. Slightly modified excerpts out of this paper are given in the following, followed by an extended section on boundary conditions.

The electrostatic landscape experienced by electrons in ever smaller structures, down to the scale of scanning–tunneling microprobes and single–electron devices, is crucial for many device applications. The presence of conducting leads for manipulating and measuring local potentials influences the quantum–mechanical behavior of electrons in a complex manner. In polarizable media, for example, charged "conglomerates" which include free as well as polarization charges in the neighborhood, behave as quasi–particles which can live for a comparatively long time and interact with the conducting leads via Coulomb interaction. Knowledge of the potential landscape describing this interaction for the case of a quasi–particle, is an interesting and important element in the better understanding of these systems. Electrons in single electron transistors [Lik99], or moving in the neighborhood of lithographically defined gate arrangements (see for example [WRM+91]), or tunneling through STM scanning tips, are but a few examples of the pervasiveness of electrostatic potentials in realistic structures.

## 3.1 EST3D Primer

The solution of the Laplace or Poisson equation to obtain electrostatic potential landscapes is a well defined boundary value problem, typically requiring the discretization of space on a convenient grid. Relaxation techniques are well known [TVPF93, Dem97, Jac99] and widely used in the solution of these problems, as they

provide convenient and efficient algorithms [Coa80]. For dimensions lower than three, simple second order algorithms are used together with common speedup features such as successive overrelaxation (SOR) and Gauss–Seidel (GS) iteration schemes [TVPF93, Dem97]. In three dimensions, however, due to the poor scaling with grid dimensions, more efficient routines are desirable. In this context a generalized $O(h^6)$ algorithm for 3D is presented and used to calculate the potential landscape of several physical systems of interest.

The boundary conditions most easily built into relaxation algorithms are fixed voltage surfaces, with the voltage known and provided by an external battery, for example. This does not apply, however, to cases with a *floating* potential, such as metallic islands which are isolated from the environment (like metallic quantum dots), or for open boundary problems. In the case of isolated islands, the value of the potential at a metallic boundary, even though constant, is not known. On the other hand, the overall charge on the island is determined at the outset and can be considered to be known. The solution to the problem taken here is that once one has access to the linear relationship between the charge on the island and the island potential derived from the relaxation algorithm, one can invert this relationship and calculate the potential with every relaxation cycle such that the overall charge is maintained at a fixed value, e.g. zero for an overall neutral island. Incorporation of this idea in the iteration procedure yields the appropriate floating potentials.

Notice moreover that the outer boundary is open in general in most nanosized geometries. If the size of the calculated cell could be chosen large enough, of course, one could assume that the potential would drop to zero there; however, this is operationally forbidden by the vast number of grid points needed in that case. The only feasible way is to determine the non–uniform potential on the outer boundary self–consistently within the algorithm. The approach taken here is that the knowledge of the total charge distribution (external *and* induced charges) allows for the calculation of the potential on the outer boundary via the standard free–space electrostatic Green's function, $1/4\pi r$. This is a straightforward procedure even though computationally very expensive if not done appropriately. Tabulating the inverse distances on the grid somewhat improves the performance of the algorithm, yet the implementation of a three–dimensional FFT (thus the name of the package, EST3D) vastly improves the speed by two orders of magnitude to obtain the potential on the outer boundary as will be described in more detail below. It is also important to emphasize that once the charges and potentials in the system are available numerically, it is straightforward to evaluate the capacitance matrix for the geometries of interest, regardless of the geometrical complexity of the participating objects.

### 3.1.1 Algorithm

With the standard Taylor expansion of a smooth function $f(x, y, z)$ in 3D around any grid point, the *center average* and the *square average* are defined as follows assuming uniform grid spacing $h$ in all three dimensions

$$\begin{aligned}
\langle f \rangle_C &\equiv \frac{1}{6}\left(\sum_{i,j,k}^{NN} f_{ijk}\right) = \\
&= f^{(000)} + \frac{h^2}{6}\vec{\nabla}^2 f + \frac{h^4}{72}\left(f^{(400)} + f^{(040)} + f^{(004)}\right) \\
&\quad + O\left(h^6\right) \qquad (3.1a) \\
\langle f \rangle_S &\equiv \frac{1}{8}\left(\sum_{i,j,k}^{TNN} f_{ijk}\right) = \\
&= f^{(000)} + \frac{h^2}{2}\vec{\nabla}^2 f + \frac{h^4}{24}\left(f^{(400)} + f^{(040)} + f^{(004)}\right) \\
&\quad + \frac{h^4}{4}\left(f^{(220)} + f^{(202)} + f^{(022)}\right) + O\left(h^6\right) , \qquad (3.1b)
\end{aligned}$$

with the derivatives evaluated at the grid point under consideration and where $(T)NN$ stands for (third) nearest neighbors and

$$f^{(rst)} \equiv \frac{\partial^r}{\partial x^r}\frac{\partial^s}{\partial y^s}\frac{\partial^t}{\partial z^t} f\,(i, j, k) \qquad (3.2a)$$

$$f_{\mathbf{i}} \equiv f_{ijk} \equiv f(i, j, k) \equiv f(i \cdot h, j \cdot h, k \cdot h)\,, \qquad (3.2b)$$

with $i,\ j,\ k$ and $r,\ s,\ t$ being integers. The averages in Eqs. (3.1) are shown graphically in Fig. 3.1. Notice that the odd–order derivatives in Eqs. (3.1) cancel due to the symmetric combinations around the grid points included in the averages. Notice also that *second* (or next) nearest neighbors are considered in the "checkered lattice" sweeps of the points making the simple cubic grid. (The relaxation sweeps are done sequentially over the face–centered cubic array of neighbors which form effectively a dual lattice.)

Taking the linear combination of the averages (3.1a) and (3.1b)

$$\langle\langle f \rangle\rangle \equiv \alpha\ \langle f \rangle_C + (1 - \alpha)\,\langle f \rangle_S\ , \qquad (3.3)$$

then with $\alpha \equiv \alpha_{3D} = 6/7$ the *overall average* becomes

$$\langle\langle f \rangle\rangle_{3D} \quad = \quad f_{\mathbf{i}} + \frac{3}{14}h^2\,\vec{\nabla}^2 f_{\mathbf{i}} + \frac{1}{56}h^4\ \vec{\nabla}^2\,\vec{\nabla}^2 f_{\mathbf{i}}$$

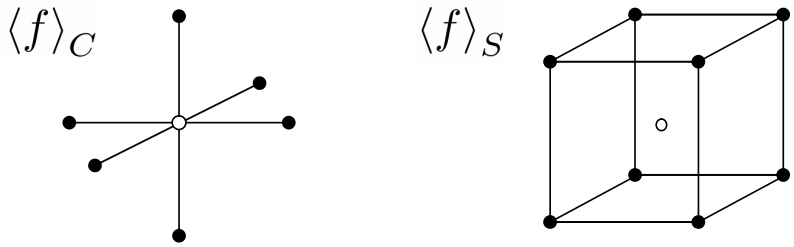


Figure 3.1: Visualization of averages taken on the grid: average $\langle f \rangle_C$ as in Eq. (3.1a) is over nearest neighbors (NN); average $\langle f \rangle_S$ as in Eq. ( 3.1b) is over third nearest neighbors (TNN). The grid points included in the sum are shown as filled symbols; solid lines joining these have length of two grid spacings, $2h$.

$$+O\left(h^6\right) . \tag{3.4}$$

Since we are solving for the Poisson equation

$$\vec{\nabla}^2 f = -g\,, \tag{3.5}$$

Eq. (3.4) can be rewritten as

$$\begin{aligned} f_{\mathbf{i}} &= \langle\langle f \rangle\rangle_{3D} + \frac{3}{28} h^2 \left(g_{\mathbf{i}} + \langle g \rangle_C\right) \\ &\quad +O\left(h^6\right) , \end{aligned} \tag{3.6}$$

where $\langle g \rangle_C$ is the *center average* for the *source term* at a given grid point. Equation (3.6), together with (3.4), serves as the basis for the iterative scheme: the potential $f$ is *relaxed to its minimum* considering external sources $g$ and the potential of the (third and) nearest neighbor sites through the linear 3D average. In order to calculate charges on the grid, Eq. (3.4) is employed again and gives a straightforward way for calculating *real* (i.e. free) and *induced* charges on the grid on an equal footing. Thus using Poisson's equation (3.5), the charge contribution of each grid point can be calculated as follows

$$\begin{aligned} q_{\mathbf{i}} &\equiv h^3 g_{\mathbf{i}} = h \left(-h^2 \vec{\nabla}^2 f_{\mathbf{i}}\right) = \\ &= \frac{14}{3} h \left(f_{\mathbf{i}} - \langle\langle f \rangle\rangle_{3D} + O\left(h^4\right)\right) . \end{aligned} \tag{3.7}$$

For convenience, the following convention on units is taken: The charge of an electron is one, $e = 1$, and the Coulomb energy is written in units of eV, i.e. $E =$

$q_1\,[e] \cdot q_2\,[e]\,/\,(4\pi r)$; note that this implies a unit for the distance of $[r] = 18.1$ nm. In short, the units chosen are

$$[energy] = \text{eV};\ [charge] = \text{e};\ [distance] = 18.1\ \text{nm} \tag{3.8}$$

This choice of units brings one naturally into the realm of nanostructures.

### 3.1.2 Successive Over–Relaxation and Iteration Scheme

The general method for successive over–relaxation (SOR) is described for 2D in [TVPF93, Dem97] for a $N \times N$ array and is generalized here to 3D as follows

$$f_{\mathbf{i}}^{(i+1)} = f_{\mathbf{i}}^{(i)} + \omega \left( f_{\mathbf{i}}^{(new)} - f_{\mathbf{i}}^{(i)} \right), \tag{3.9a}$$

where

$$\omega = \frac{2}{1 + \pi / \min(N_x, N_y, N_z)}, \tag{3.9b}$$

$N_j$ is the grid size in the $j$th direction, and $f_{\mathbf{i}}^{(new)}$ is calculated according to Eq. (3.6). The SOR parameter $\omega$ is in the range $1 < \omega < 2$ as required for the algorithm to converge. The basic idea behind $\omega$ is that if one is heading in the *right* direction (i.e. towards the solution), why not go a bit further. An $\omega$ too large ($\omega > 2$), however, results in instability of the algorithm and the relaxation process overshoots and diverges. Equation (3.9b) was tested for different $N_x$, $N_y$ and $N_z$ values and it was indeed this specific combination that gave the optimal value for $\omega$ (note that the window for a *good* $\omega$ is quite narrow in general). The specific structure of (3.9b) can be intuitively understood as follows: the SOR algorithm introduces perturbations in the system that propagate during the relaxation cycles and eventually die out if the grid is large enough; however, for finite grid sizes, the perturbations are reflected at the boundaries and so they interfere and pile up. In this sense, the minimum extension within the three grid dimensions constrains the optimal magnitude of $\omega$, consistent with Eq. (3.9b).

For further optimization of the algorithm, the Gauss–Seidel iteration scheme was adopted, as well as the alternating relaxation on the two checkerboard like subgrids that in sum span the whole grid [TVPF93, Dem97]. According to Coalson [Coa80], multigrid methods can be applied to account for the slowly converging long wavelength portions of the solution. This was not done here, since the variation of the potential on the isolated islands and especially the calculation of the outer boundary already introduced long range correlations over the grid that presumably already made the algorithm converge faster in given case.

A note about efficiency: As we use a successive overrelaxation method to iterate the potential on the grid, the total relaxation time for this in 2D is proportional to $\sim n^{3/2}$, where $n$ is the *total* number of grid points [Dem97], and is thus clearly comparable to algorithms like conjugate gradient. Notice also that SOR has known further improvements that may also be implemented and would thus make this algorithm superior to the former [Dem97]. Our relaxation over the bipartite lattices composing the simple cubic 3D grid preserves the spirit of the 2D algorithms, but obtains an accuracy of $O(h^6)$, as discussed above.

### 3.1.3 Test Cases for EST3D

In the following, basic test cases for the EST3D program are presented. The outer boundary is calculated self–consistently within the relaxation formalism according the free–space open boundary condition.

The first case is a single point charge localized on one grid point in the middle of the three–dimensional $128 \times 128 \times 128$ grid block. The output potential is shown in Fig. 3.2 and is plotted on a log–log scale such that the source $q$ and the expected $r^\alpha$ power law as a function of the distances can be easily extracted from line fits to this data. The source calculated from the line fits is $q = 1.00$ and the power law coefficient is $\alpha = -1.00$ to an excellent approximation. Thus the expected potential of a free points source $V(r) = q/4\pi r$ is well reproduced.

The second case is a wire localized in the middle of elongated $64 \times 64 \times 256$ block and has a length $L = 246h$. The charge density per unit length of the wire $\lambda$ is taken to be $\lambda = 1$. The expected potential away from the wire is

$$V(r) = -\lambda/2\pi \ \ln(r) + const \tag{3.10}$$

Since this only holds for an infinitely long wire, it is expected to be a good analytical approximation only far away from either one of the ends of a finite wire, hence in the middle section of the grid in given setup. The constant in Eq. (3.10) turns out to be essential since the length of the wire is a constant. An analytic expression for the potential of a finite wire is easily obtained in the plane perpendicular to the wire and intersecting with the wire in its middle:

$$V(x) = \frac{\lambda}{4\pi} \ln\left(\frac{\sqrt{\frac{1}{4} + x^2} + \frac{1}{2}}{\sqrt{\frac{1}{4} + x^2} - \frac{1}{2}}\right) \tag{3.11}$$

where $x \equiv r/L$ is the distance from the wire $r$ scaled to its length $L$. For $x \ll 1$, i.e. very close to the finite wire, the potential asymptotically approaches $V(x) \simeq$

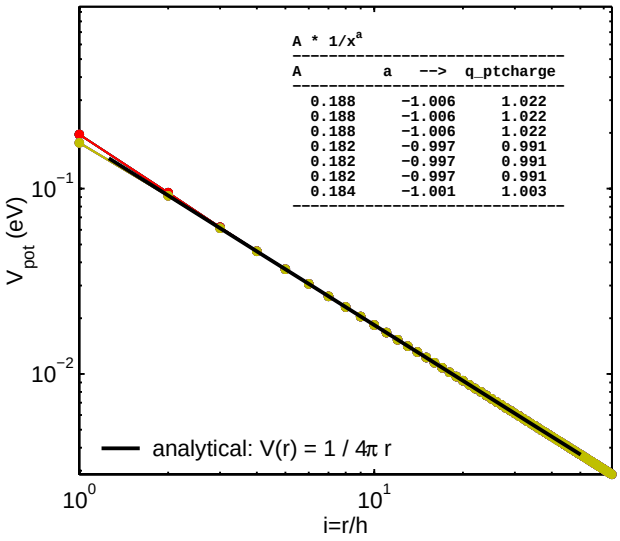


Figure 3.2: Test case for the EST3D program - a single point source with $q = 1.(e)$ in the middle of the $128 \times 128 \times 128$ block considered. The final output of the potential is shown along lines through the point charge in the directions [100], [010], [001], [110], [101], [011], [111] in crystallographic notation. The grid spacing $h = 7.84\,\mathrm{nm}$ was adjusted by factors of $\sqrt{2}$ and $\sqrt{3}$ for the [110], ... diagonals and the [111] diagonal, respectively, in order to map the data onto each other. The data stretches from distances of $r = 1 \ldots 62h$ where the data points right next to the delta point source not surprisingly show some slight deviation from the analytical result, they converge rapidly towards the analytical result (note the double log scale!). The inset shows the parameters for the best line fits to the log–log data.

$\frac{\lambda}{4\pi}\left(-2\ln x + \mathcal{O}\left(x^2\right)\right) \simeq -\lambda/2\pi \ \ln(r) + \lambda/2\pi \ \ln(L)$. Therefore the constant in Eq. (3.10) is determined to be related to the length of the wire and would diverge to infinity if the length $L$ were to go to infinity. On the other hand, far away from the wire, $x \gg 1$, the potential becomes $V(x) \simeq -\frac{\lambda}{4\pi}\left(1/x + \mathcal{O}\left(1/x\right)^3\right) \simeq -\lambda L/4\pi r$ which is the potential of a point charge at distance $r$ and overall charge $\lambda L$. In summary, the asymptotic form for the potential at distance $r$ from the middle of the wire is

$$V(r) = \begin{cases} -\frac{\lambda}{2\pi}\ln(r) + \frac{\lambda}{2\pi}\ln(L) & \text{if } r \ll L, \\ \frac{\lambda L}{4\pi r} & \text{if } r \gg L. \end{cases} \tag{3.12}$$

With this, it is straightforward to extract the charge density $\lambda$ and the length $L$ of the wire by analyzing the data in close proximity to the center of the wire in terms of a lin–log plot of the calculated potential. This is exactly what is shown in Fig. 3.3. The diameter of the grid block was chosen such that mostly the case $r \ll L$ is covered. The data is shown in a lin–log plot because of the expected potential

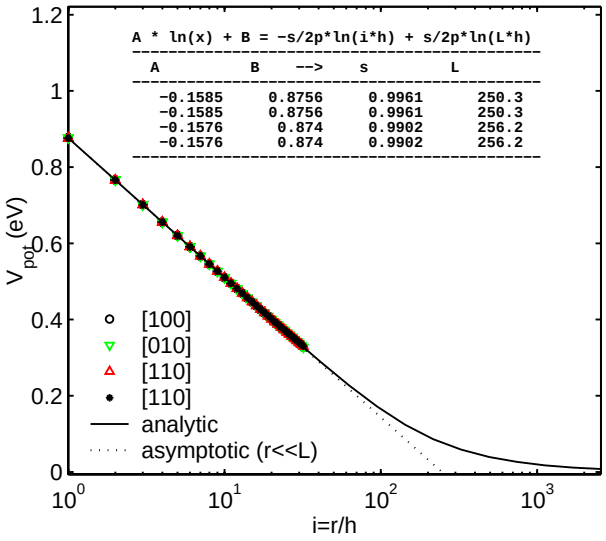


Figure 3.3: Test case for the EST3D program - a wire with charge density $\lambda = 1.e$ per unit length in the middle of the $64 \times 64 \times 256$ block considered. The calculated potential is shown along lines intersecting with the wire in a normal angle in the middle of the grid block point in the directions [100], [010], [110], [$\bar{1}$10] in crystallographic notation. The grid spacing $h = 15.8\,\mathrm{nm}$ was adjusted by a factor $\sqrt{2}$ for the diagonals in order to map the data onto each other. The curves (solid magenta line(s)) lie very well on top of each other then and are close to perfectly topped by the asymptotic fit for $r \ll L$. The data stretches over distances of $r = 1 \ldots 31h$.

$V(r) = -\lambda/2\pi \ \log(r/L)$. The inset shows the parameters for the best line fits to the lin–log data where $r \ll L$ together with the charge density on the wire and its length extracted from these parameters which are to be compared to the input values $\lambda = 1.$ and $L = 246\ h$. The line fits in the lin–log data give an average charge density $\lambda = 1.0$ and a length of the wire of about 253 $h$ which is in good agreement with the expected values. The fact that $r$ already approaches the length of the wire by a factor 1/8, the $\sim 1\%$ error of these extracted values is not very surprising.

## 3.2 Electrostatic Boundary Conditions on the Grid

In the following, a whole range of different boundary conditions are introduced. The outer boundary is considered open throughout the different applications and therefore it must be calculated self–consistently within the algorithm. In the interior of the grid space allocated, very commonly used boundary conditions such as dielectric boundary or depletion of a two–dimensional electron gas (2DEG) are implemented.

### 3.2.1 Solving for the Electrostatic Potential Using FFT3

In the numerical analysis of electrostatic problems, space has to be sampled into a grid of finite dimensions and of finite grid spacing. Thus sampling the three–dimensional space into a rectangular grid with lattice constant $h$ just means that any function specified on the grid necessarily represents averages over a volume $h^3$ around each grid point.

Consider the charge distribution on a grid indexed by some index $i$. Furthermore, assume the charge distribution $q_i$ is given and is entirely located within the grid. With free space outside the grid, the outer boundary of the grid block therefore is an open boundary. Using the electrostatic Green's function for the open 3D case, the potential at every grid point $r_i$ can be obtained from

$$V(r_i) = \sum_j \underbrace{\frac{1}{4\pi}\frac{1}{|\vec{r}_j - \vec{r}_i|}}_{\equiv g_{ij} \equiv g(i-j)} q_j \tag{3.13}$$

with the symbolic notation $g(i-j) \equiv g(|\vec{r}_j - \vec{r}_i|)$ emphasizing the translational invariance of the Green's function. With this, the total electrostatic energy of the system is given by

$$E_{tot} = \frac{1}{2}\sum_{i,j}\frac{1}{4\pi}\frac{q_i q_j}{|\vec{r}_j - \vec{r}_i|} = \frac{1}{2}\sum_{i,j} q_i g_{ij} q_j \tag{3.14}$$

The Green's function $g_{ij}$ introduced in Eq. (3.13) appears to be straightforward, but needs some reconsideration in terms of self–energy, i.e. for the term $i = j$: it is costly to squeeze lots of charge onto one grid cell but it is possible, and therefore $g_{ii} \equiv g(0)$ must be introduced at some finite value. In order to get an estimate, consider a uniform charge distribution on a sphere of radius $R$. The electrostatic (self–)energy of this system can be easily calculated as $E_\Sigma \equiv \frac{3}{5}\frac{Q^2}{4\pi R}$ with $Q$ being the total charge of the sphere. In the discretized version with all the charge $Q$ located around the grid cell $k$, and therefore $q_i = Q\delta_{ik}$, the energy calculated from Eq. (3.14) is

$$E_\Sigma = \frac{1}{2}Q^2 g_{kk}$$

Taking the smallest sphere that encloses one unit cell in the grid, then with $R \simeq \frac{\sqrt{3}}{2}h$ it follows $g_{kk} \gtrsim \frac{6}{5}\frac{2}{\sqrt{3}}\frac{1}{4\pi h} = 1.39\frac{1}{4\pi h}$, while fitting the sphere exactly into the cubic unit cell of the grid results in $R = h/2$ and therefore $g_{kk} \lesssim \frac{6\cdot 2}{5}\frac{1}{4\pi h} = 2.4\frac{1}{4\pi h}$. In practice, a prefactor of 2 was picked. Note that for the calculation of the potential as in Eq. (3.13), $g(0)$ is irrelevant when the potential is calculated at a grid point where there is no charge ($q_i = 0$), which specifically holds for the calculation of the potential

in free space such as on the outer boundary of the considered grid block. In summary, the 3D free space Green's function that has been employed in the calculations is

$$g_{ij} = \begin{cases} \frac{1}{4\pi h} \frac{1}{|\vec{r}_j - \vec{r}_i|/h} & \text{if } i \neq j, \\ \frac{1}{4\pi h} 2 & \text{if } i = j. \end{cases} \tag{3.15}$$

Equation (3.13) appears to be a rather straightforward approach to calculate the potential at a specific grid point. But this comes with a big caveat with respect to explicit numerical calculation since this naive way of calculating the potential on surfaces or on the whole grid is expensive. In this work, for example, the potential had to be calculated on the outer boundary of the grid block under consideration. Thus, for an $N \times N \times N$ block of a rectangular grid the number of grid points on the outer surface of the grid is about $6N^2$, and consequently the cost for the calculation of the outer boundary scales as $6N^2 \times N^3 = N^5$ which is *very* expensive with increasing $N$ and it is easy to have one's program spend by far the largest amount of time in calculating the potential this way. So are there more efficient ways to calculate the potential on the grid? For a rectangular grid, the answer is a clear yes and involves the fast Fourier transform in 3D (FFT3) [HE88], which was kindly suggested to me by the local astronomy group. FFT3 is known to scale close to linearly with respect to the number of grid points included (here $N^3$), specifically it scales as $N^3 \log N^3$ compared to the $N^5$ scaling in the ad hoc initial solution.

FFT, on the other hand, is intrinsically linked to periodic boundary conditions. Yet, there is a well–known trick to avoid periodic boundary conditions even though one is using FFT3. The basic idea is doubling the grid in each dimension. This does not sound very efficient at first glance, but numerically the overall speed up of the potential on the outer boundary for a typical grid size of $64 \times 64 \times 64$ was amazingly more than two orders of magnitude (e.g. clearly a factor 100 faster). The drawback is a significantly increased memory consumption on the computational facility (factor 8 for a 3D matrix), but with current standards, a $64 \times 64 \times 64$ array was handled with ease.

The FFT based algorithm relies on a rectangular grid such as the cubic grid under consideration. Since Fourier transform is basically a unitary transformation from the spatial basis ($r$ space) to the plane wave basis ($k$ space), the mutual completeness relations hold

$$\frac{1}{N} \sum_i e^{i(k-k')r_i} = \delta_{k,k'} \tag{3.16a}$$

$$\frac{1}{N} \sum_k e^{i(r-r')k} = \delta_{r,r'} \tag{3.16b}$$

where $k$ and $k'$ refer to vectors in the reciprocal $k$–space, while $r$ and $r'$ are vectors in real space constrained to the grid points and $N$ is the total number of grid points. Employing Eqs. (3.16), transforms Eq. (3.13) into

$$V(r_i) = \sum_j g(i-j)\, q_j \tag{3.17a}$$

$$= \frac{1}{N} \sum_k e^{ikr_i} \underbrace{\sum_j q_j e^{-ikr_j}}_{\equiv q_k} \underbrace{\sum_{i'} g(i'-j) e^{-ik(r_{i'}-r_j)}}_{\equiv g_k^{(j)}} \tag{3.17b}$$

The summation over $k$ will provide a $N \cdot \delta_{ii'}$ and thus eliminates the $i'$ summation. Note that the Eqs. (3.16) are strict mathematical identities and have no direct physical implication, i.e. no assumption on periodicity had to be made so far. The only restriction is that $V$ is calculated on the grid, i.e. on a grid point $r_i$ *within the grid considered*. If there was no $j$ dependence in the last term, the second term of Eq. (3.17b) is equal to $q_k$, the usual Fourier transform of $q_j$. The third term, however, is in general dependent on the vector $r_j$ which makes it a more complex object, i.e. it is not the Fourier transform of $g(i-j)$ as it stands.

For the sake of simplicity, only one of the three dimensions is considered in the following with $i = 0, \ldots, (n-1)$, with $n$ the number of grid points in that dimension. Consequently, the index $i-j$ in $g(i-j)$ in the original sum, Eq. (3.17a), spans the range $-(n-1)$ to $+(n-1)$ which is about *double* the size of the range of $i$, namely $2n-1$. Therefore for the second sum, Eq. (3.17b), to be correct, $g(m)$ must have the correct values as in Eq. (3.15) for that index range $m = -(n-1), \ldots, +(n-1)$. This is where the doubling of the original grid block comes in. For better illustration, consider Fig. 3.4 which shows an equivalent 2D setup. In panel (a), the area in green shows the initial grid data array $\Omega_0$ where $q_i \neq 0$ is given. Now $\Omega_0$ is doubled in every dimension towards the negative indices, and the resulting large area, labeled $\Omega$, includes the areas $2+3+4$ in Fig. 3.4a. In the entire new region $2+3+4$, the charge $q_i$ must be zero, while $g(m)$ is given as in Eq. (3.15). Furthermore, notice that $g(m)$ only needs to be defined correctly for $m = -(n-1), \ldots, +(n-1)$ in the above sense. If for example $\Omega$ were expanded further than its required minimum size of $2n-1$, then the values for $g(m)$ in the resulting extra space could be chosen arbitrarily! This for example includes one column and one row if the space is exactly doubled in size $(2n)$.

The freedom of what values to pick for $g(m)$ outside the $m = -(n-1), \ldots, +(n-1)$ region, is now exploited to require that $g(m)$ is continued in a periodic boundary kind of fashion outside $\Omega$. This is the essential step to make the last term in Eq. (3.17b) become independent of $j$. The resulting sum is the Fourier transform of

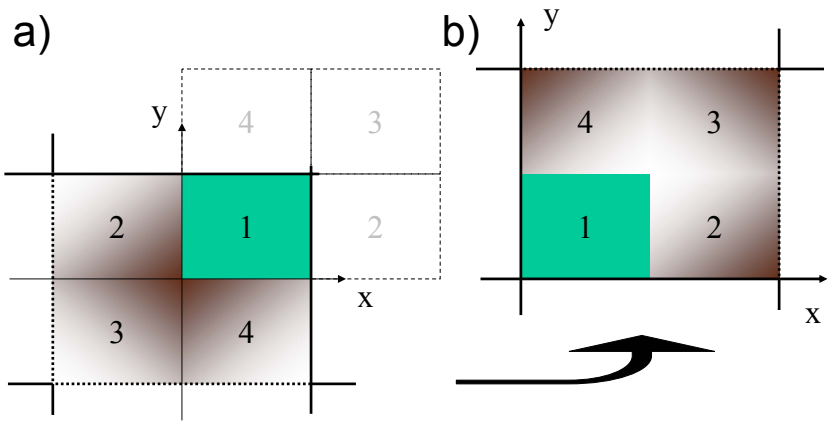


Figure 3.4: *Doubling the grid size* for the calculation of electrostatic potentials via FFT on a rectangular grid for simplicity shown in 2D. a) The initial grid block $\Omega_0$ (the green area of region 1) is increased by a factor of two in every dimension resulting in the block $\Omega$ (super cell) which includes all four shaded regions. b) Same as a) but making use of the periodic boundary conditions for the super cell to move the regions 2–4 with negative index by the super cell period to the $x, y \geq 0$ range. The doubling of the grid size is a trick in order to avoid the interference within the $\Omega_0$ block with otherwise periodically repeating charge configurations when using FFT. For this, regions 2–4 must be free of charge (zero padding, see text).

$g\,(i-j)$ and as such can be carried out over any region $\Omega$ floating in this periodic real space configuration. This freedom is used to move the negative index regions to *all positive* indices as indicated in Fig. 3.4b. The regions $2+3+4$ shifted to their new places are labeled accordingly and together with region 1 is now labeled $\Omega'$. Note that the largest values of $g$, namely around $g(0)$ initially in the center of $\Omega$, are now moved to the corners of $\Omega'$. This is also indicated by the color shading of the areas in Fig. 3.4.

The important result is that proper doubling of the size of the grid makes the last sum of Eq. (3.17b) independent of the index $j$. So the total expression for the potential becomes

$$V\,(r_i) = \frac{1}{N} \sum_k e^{ikr_i} \underbrace{q_k \cdot g_k}_{\equiv V_k} \tag{3.18}$$

which is the inverse Fourier transform from $V_k$ to $V\,(r_i)$ where $V_k$ is the simple element by element product of the corresponding Fourier transforms in $q_k$ and $g_k$. It is exactly this simple folding in Fourier space, this direct element–by–element product which enormously speeds up the computational process compared to the original excessive

summation over products $g_{ij}q_j$ that was present in the original folding in Eq. (3.13). The direct product clearly scales linearly in computational cost as $N^3$ similarly to the FFT algorithm already mentioned previously. Note that this scaling of $\sim N^3$ for the cost of calculating the potential on the *entire* grid should be compared to the original ad–hoc algorithm for that very task which scales as $N^3 \cdot N^3$. Even for calculating the potential on surfaces as in given case, the FFT based algorithm still calculating the potential on the whole grid scales much better than the $N^2 \cdot N^3$ in the original version.

Now in order to calculate $V(r_i)$ from a given charge distribution $q_i$, five steps are necessary. The Fourier transform $g_k$ of the Green's function as constructed above is calculated once in the beginning of the algorithm and is stored for later use. It is therefore not considered part of the steps necessary to calculate $V(r_i)$ later on. These five steps are then as follows

1. zero pad $q_i$ to double its size in every dimension
2. FFT forward transform $(q_i)$
3. element–by–element product of $q_k \cdot g_k =: V_k$
4. FFT back transform of $V_k$
5. skip all data of $V_i$ outside $\Omega_0$

The last step is important since one must keep in mind that the potential $V(r_i)$ calculated in the original equation (3.17a) refers to a grid point in $\Omega_0$. This still holds in the new expanded configuration, namely that $r_i$ must refer to a grid point in $\Omega_0$ (the green area marked as space 1 in Fig. 3.4). In other words, the potential $V(r_i)$ is numerically exact in $\Omega_0$ only! In the remaining space of $\Omega'$ (i.e. the areas $2 + 3 + 4$ in Fig. 3.4) the values for the potential are non–physical since there the potential eventually yields to the (non–physical) periodic boundary conditions.

Finally note that the potential $V_i$ has thus been calculated within $\Omega_0$ and therefore on the *entire* grid under consideration. However, in given case, only the values on the outer boundary are needed and the rest is skipped. Nevertheless and as already mentioned previously despite all these extra hurdles and actually all the data wasted, for a typical grid size of $64 \times 64 \times 64$ the FFT based algorithm still turned out to be more than amazing two orders of magnitude faster than the initial naive summation of the Coulomb potential.

### 3.2.2 Dielectric Boundary

Typical materials such as Ga(Al)As or $Al_2O_3$ have dielectric constants of order $\varepsilon = 12$ and thus the dielectric constant plays an important role especially in the sense that all charges are screened significantly. The numerical implementation is motivated first for the one–dimensional case since the resulting algorithm has a strong similarity to the 3D case. More literature and background on this topic can be found in [KHF+86, DM91, HS93, BIM97, Bec80].

A typical numerical spatial grid is shown in Fig. 3.5a for 2D which through its flat surface is similar to the 1D case. Considering the indices $i$ first and therefore neglecting the index $j$ at this stage, the numerical treatment for this boundary is derived from the *local* minimization of the electrostatic energy. The starting point is therefore [Jac99]

$$Energy = \frac{\varepsilon_0}{2} \int d^3r \; \vec{E}\vec{D}$$

with the electric displacement vector $\vec{D} \equiv \varepsilon_0 \vec{E} + \vec{P} \equiv \varepsilon\varepsilon_0 \vec{E}$ and therefore a linear optical media with $\varepsilon = const.$ In the discretized version in 1D with uniform grid spacing $h$, the electrostatic energy then becomes

$$E \simeq \frac{\varepsilon_0}{2} \sum_{i'} \frac{V_{i'} - V_{i'-1}}{h} \bar{\varepsilon}_{i'} \frac{V_{i'} - V_{i'-1}}{h}$$

Here by construction, $\bar{\varepsilon}_i$ refers to (the average of) the dielectric constant *between* the two grid points $i' - 1$ and $i'$, and as a reminder it is marked with a bar, therefore $\bar{\varepsilon}_i$. Assuming the boundary grid point is at $i' = i$, the optimal value for the potential $V_i$ at that grid point is derived from minimizing the total energy with respect to this $V_i$

$$\frac{\partial E}{\partial V_i} = \frac{\varepsilon_0}{h} \left( \bar{\varepsilon}_i \left( V_i - V_{i-1} \right) + \bar{\varepsilon}_{i+1} \left( V_{i+1} - V_i \right) \right) \stackrel{!}{=} 0$$

resulting in

$$V_i^{opt} = \frac{\bar{\varepsilon}_i V_{i-1} + \bar{\varepsilon}_{i+1} V_{i+1}}{\bar{\varepsilon}_i + \bar{\varepsilon}_{i+1}} \tag{3.19}$$

This is a weighted linear average of the neighboring potential values with the weights determined by the dielectric constants. In the case $\bar{\varepsilon}_i = \bar{\varepsilon}_{i+1}$, the dielectric constant cancels out, and the expression simplifies to the simple average $V_i^{opt} = \frac{1}{2} \left( V_{i-1} + V_{i+1} \right)$ shown as the straight line between the $V_{i-1}$ and $V_{i+1}$ in Fig. 3.5b. On the other hand, if $\bar{\varepsilon}_i \gg \bar{\varepsilon}_{i+1}$, then $V_i^{opt} \simeq V_{i-1}$, e.g the optimal $V_i$ gets closer to an equipotential with the side with the larger dielectric constant as shown in Fig. 3.5b.

For systems with dimension larger than one, the situation turns out to be quite similar. Whatever local minimization approximation is taken, e.g. by some specific

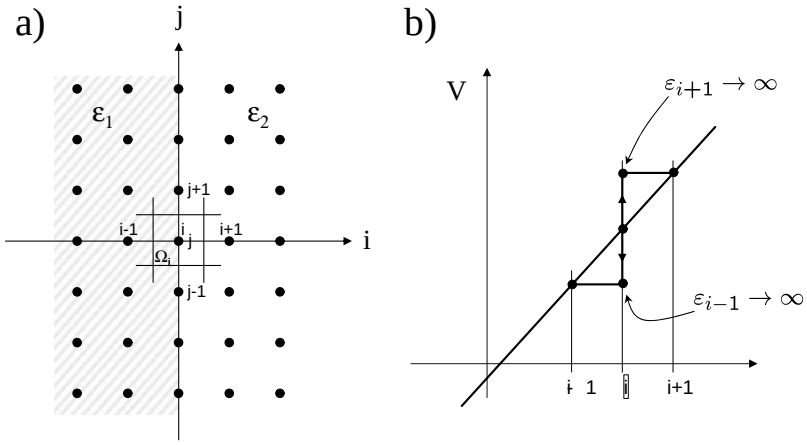


Figure 3.5: Dielectric grid boundary - Panel a) for simplicity the grid is shown in 2D. The dielectric constants to the left and to the right are $\varepsilon_1$ and $\varepsilon_2$, respectively. The boundary is considered flat with the grid points passing right through it. Panel b) reduced 1D grid and the effect of a jump in the electrostatic constant.

interpolation of the data for $V_i$ and $\varepsilon_i$ within the neighboring unit cells, in the end the optimal potential of a grid point at a dielectric boundary will be a *local* average over the neighboring potentials, but weighted with the corresponding dielectric constants.

Consider the Maxwell equation for dielectric media $\vec{\nabla}\vec{D} = \rho_{free}$ with $\vec{D} = \varepsilon\varepsilon_0\vec{E}$ and $\vec{E} = -\vec{\nabla}V$ [Jac99], then the differential equation for the electric potential becomes

$$\vec{\nabla} \cdot \varepsilon \cdot \vec{\nabla}V = -\rho_{free} \tag{3.20a}$$

or equivalently

$$\varepsilon\vec{\nabla}^2 V = -\rho_{free} - \left(\vec{\nabla}\varepsilon\right)\left(\vec{\nabla}V\right) \ . \tag{3.20b}$$

where the usual constant $\varepsilon_0$ is set to 1 for convenience ($\varepsilon_0 = 1$). The last term in Eq. (3.20b) has a clear physical interpretation, namely it is the contribution due to polarization charges. To see this, consider a smooth interface with a change in the dielectric constant equal to $\Delta\varepsilon$ and the x–direction chosen perpendicular to the surface such that the surface normal $\hat{n}$ is just $\hat{n} = \hat{x}$. Then with the surface being at $x = 0$ and $\vec{E} = -\vec{\nabla}V$, the last term in Eq. (3.20b) becomes

$$\left(\vec{\nabla}\varepsilon\right)\left(-\vec{\nabla}V\right) = \Delta\varepsilon\ \hat{n} \cdot \frac{+1}{2}\left(\vec{E}_+ + \vec{E}_-\right) \cdot \delta\left(x\right) \tag{3.21}$$

with $\vec{E}_+$ and $\vec{E}_-$ being the electrical fields right below and above the surface. Defining the normal components $E_1 \equiv \hat{n}\vec{E}_-$, $E_2 \equiv \hat{n}\vec{E}_+$ and the dielectric constants $\varepsilon_1$ and $\varepsilon_2$ accordingly, then with the electrostatic boundary condition $\varepsilon_1 E_1 = \varepsilon_2 E_2$ [Jac99], Eq. (3.21) is rewritten as

$$\begin{aligned}\left(\vec{\nabla}\varepsilon\right)\left(-\vec{\nabla}V\right) &= (\varepsilon_2-\varepsilon_1)\,\frac{1}{2}\left(1+\frac{\varepsilon_2}{\varepsilon_1}\right)E_2\;\delta(x)\\ &= \frac{\varepsilon_1+\varepsilon_2}{2}\cdot\underbrace{\frac{\varepsilon_2-\varepsilon_1}{\varepsilon_1}E_2}_{\equiv\sigma_{dielectric}}\cdot\;\delta(x)\end{aligned}$$

and indeed exactly reflects the surface charge density $\sigma_{dielectric}$ from the dielectric interface considering that the prefactor $(\varepsilon_1+\varepsilon_2)/2$ just corresponds to the average dielectric constant of the grid point at the interface and thus cancels with the $\varepsilon$ on the RHS of Eq. (3.20b)! Summarizing, Eq. (3.20b) is rewritten in the form of the 'dielectric free' case with the dielectric boundary just entering as an additional term of localized charges

$$\vec{\nabla}^2 V = -\frac{\rho_{free}}{\varepsilon} - \left(\vec{\nabla}\varepsilon\right)\frac{\vec{E}_+}{\varepsilon_-} \tag{3.22}$$

with the symbolic notation that the electric field has to be taken above the surface and is divided by the dielectric constant from below. Note that the region where $\vec{E}$ and $\varepsilon$ are taken could also be flipped since $\frac{\varepsilon_2-\varepsilon_1}{\varepsilon_1}E_2 = \frac{\varepsilon_2-\varepsilon_1}{\varepsilon_2}E_1$ in above nomenclature. The delta function is absorbed into the gradient of the dielectric function such that the last term only contributes at interfaces with distinct $\varepsilon$.

The last term in Eq. (3.22) is exactly equivalent to the usual boundary condition on a dielectric interface. However, this type of expression is rather ill–suited for the discretization, since the $\varepsilon_-$ in above notation is hard to grasp on the grid with a surface normal $\hat{n}$ pointing in any arbitrary direction. Therefore, for the discretization of the Poisson equation in dielectric media, a step is taken backward to the original Eqs. (3.20). The alternative approach taken now is to integrate Eq. (3.20a) over the unit cell around grid point $i$ with volume $\Omega_i$ stretching from grid point $i$ midway to its nearest neighbors (NN) indicated in Fig. 3.5a [KHF+86]. Thus

$$\int_{\Omega_i} d^3\vec{r}\;\vec{\nabla}\left(\varepsilon\vec{\nabla}V\right) + \underbrace{\int_{\Omega_i} d^3\vec{r}\;\rho_{free}}_{\equiv h^3\rho_i^f} = 0$$

and since the first term is a complete divergence, that integral is converted to a surface

integral

$$\oint_{\Omega_i} \varepsilon \left(\vec{\nabla} V\right) d\vec{S} + h^3 \rho_i^f = 0 \tag{3.23}$$

This equation is discretized straightforwardly as follows [KHF+86]: since the surface bisects the distances to the nearest neighbor (NN) grid points, the gradient is written to a good approximation in terms like $(V_j - V_i)/h$ where $j$ is meant to be the index over the nearest neighbors of grid point $i$ in a cubic grid. The reference to the dielectric susceptibilities $\varepsilon_i$, however, again becomes slightly modified similarly to the previous case in 1D (see Eq. (3.19)): $\varepsilon_i$ is still the average of the dielectric susceptibility in the closest proximity of grid point $i$ as usual, but the values $\bar{\varepsilon}_j$ related to the nearest neighbors refer now to the average of $\varepsilon$ *not* around the NN grid point $j$ itself but the average of $\varepsilon$ in between the grid point $i$ and the NN point $j$. As a reminder, these $\bar{\varepsilon}_j$ are again labeled with the bar on top. With this nomenclature, the integral in the last equation becomes

$$\frac{1}{h^2} \sum_j^{NN} \bar{\varepsilon}_j \left(V_j - V_i\right) + \rho_i^f = 0 \tag{3.24}$$

Rewriting this equation in a slightly different form

$$\begin{aligned} \frac{1}{h^2} \sum_j^{NN} \left(\bar{\varepsilon}_j - \varepsilon_i + \varepsilon_i\right) \left(V_j - V_i\right) + \rho_i^f &= 0 \\ \underbrace{\varepsilon_i \frac{1}{h^2} \sum_j^{NN} \left(V_j - V_i\right)}_{\simeq \vec{\nabla}^2 V} + \frac{1}{h^2} \sum_j^{NN} \left(\bar{\varepsilon}_j - \varepsilon_i\right) \left(V_j - V_i\right) + \rho_i^f &= 0 \end{aligned} \tag{3.25}$$

then this identifies the discretized version of the contribution of the polarization charges in Eq. (3.20b), namely

$$\left(\vec{\nabla}\varepsilon\right)\left(\vec{\nabla} V\right) \simeq \frac{1}{h^2} \sum_j^{NN} \left(\bar{\varepsilon}_j - \varepsilon_i\right) \left(V_j - V_i\right) \ .$$

Equation (3.24) is easily solved now for $V_i$

$$V_i^{opt} = \sum_j^{NN} \underbrace{\frac{\bar{\varepsilon}_j}{\bar{\Sigma}_\varepsilon^{NN}}}_{\equiv \alpha_j} V_j + \frac{h^2}{\Sigma_\varepsilon^{NN}} \rho_i^f \tag{3.26}$$

where $\bar{\Sigma}_\varepsilon^{NN} \equiv \sum_j^{NN} \bar{\varepsilon}_j$. Note that the weights $\alpha_j$ on the voltages $V_j$ of the NN grid

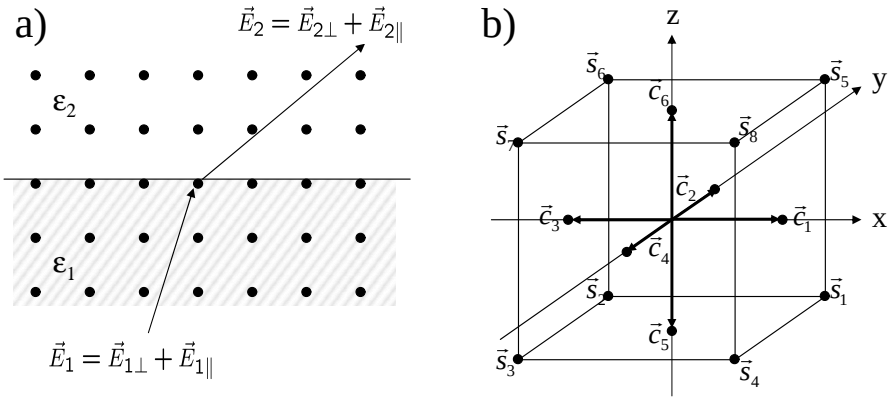


Figure 3.6: Test system for dielectric boundary - Panel a) dielectric boundary parallel to grid lines where the grid point on the boundary are still considered part of the $\varepsilon_1$ region where $\varepsilon_1$ and $\varepsilon_2$ are the lower and upper dielectric constant, respectively. The plane shown is considered the (x,z) plane with respect to the right panel. Panel b) Depiction of a grid point (center point) with its nearest up to next–next nearest neighbors - the $\vec{c}_i$ vectors point towards the nearest neighbors in this face centered cubic arrangement, while the $\vec{s}_i$ point towards the next–next nearest neighbors (the corners).

points are properly normalized in the sense $\sum_j^{NN} \alpha_j = 1$ and note also that this result is in direct analogy to initial result for the 1D case in Eq. (3.19). Finally, again a reminder that one must be aware that $\bar{\varepsilon}_j$ refers to the $\varepsilon$ halfway in between the grid point $i$ to the NN grid point $j$. However, for a piece–wise constant dielectric susceptibility and the boundaries passing through the grid along the grid lines as indicated in Fig. 3.5a, then in most cases, the dielectric constant will be the same midway as at the corresponding NN grid point and therefore this constraint can be relaxed, i.e. $\bar{\varepsilon}_j = \varepsilon_j$. Moreover, only the grid point at the boundary acquires charge due to surface polarization. This is properly taken care of by the $\bar{\varepsilon}_j$ but would not be if one were to use the $\varepsilon_j$ instead.

As a test example with respect to the averages as defined in Eq. (3.1) for the relaxation on the grid within a region of uniform dielectric constant, consider the setup as shown in Fig. 3.6a with a locally uniform electric field passing through a dielectric boundary parallel to grid as indicated. Furthermore for the optimization of the potential at grid point $i$, consider now that not only the nearest neighbor average ($V_c$, see also Eq. (3.1a)) is evaluated according to the *dielectric average* as in the previous section, but also the next–next nearest neighbor average ($V_s$, see also Eq. (3.1b)) in similar fashion. The overall new $V_i$ is calculated as some average between the two, i.e. $V_i^{opt} = \langle\langle V_i \rangle\rangle \equiv \alpha \langle V_c \rangle + (1-\alpha) \langle V_s \rangle$ with $0 \leq \alpha \leq 1$ as in

Eq. (3.3). Then with $\gamma \equiv \frac{\varepsilon_1}{\varepsilon_2}$, it follows for a grid point at the dielectric boundary

$$\begin{aligned}\langle V_c \rangle &= \frac{1}{5\gamma+1}\left(\sum_{i=1}^{5}\left(V_0 - \vec{c}_i\vec{E}_1\right)\gamma + \left(V_0 - \vec{c}_6\vec{E}_2\right)\cdot 1\right)\\ \langle V_s \rangle &= \frac{1}{4\gamma+4}\left(\sum_{i=1}^{4}\left(V_0 - \vec{s}_i\vec{E}_1\right)\gamma - \sum_{i=5}^{8}\left(V_0 - \vec{s}_i\vec{E}_2\right)\cdot 1\right)\end{aligned}$$

with the potential at point $\vec{r}$ with respect to the central point being $V_0 - \vec{r}E$. The vectors $\vec{c}_i$ and $\vec{s}_i$ are defined as in Fig. 3.6b. Due to the symmetry of this set of vectors $\vec{c}_i$ and $\vec{s}_i$, all components in the vector projections parallel to the surface vanish. This implies that for this case it does not matter what exact value for $\varepsilon$ is chosen for the other NN points in the boundary layer (i.e. the grid points specified by $\vec{c}_{1\ldots4}$). With the projections of the electric field $\vec{c}_5\vec{E}_1 \equiv -hE_{1n}$ and so, the overall average becomes

$$\begin{aligned}\langle\langle V_i \rangle\rangle &\equiv \alpha\langle V_c\rangle + (1-\alpha)\langle V_s\rangle\\ &= V_0\cdot 1 - \frac{\alpha}{5\gamma+1}\left(\vec{c}_5\vec{E}_1\gamma + \vec{c}_6\vec{E}_2\right) - \frac{1-\alpha}{4\gamma+4}\left(\sum_{i=1}^{4}\vec{s}_i\vec{E}_1\gamma - \sum_{i=5}^{8}\vec{s}_i\vec{E}_2\right)\\ &= V_0 - \frac{\alpha}{5\gamma+1}h\underbrace{(-E_{1n}\gamma + E_{2n})}_{=0} - \frac{1-\alpha}{4\gamma+4}4h\underbrace{(-E_{1n}\gamma + E_{2n})}_{=0}\\ &= V_0\end{aligned}$$

Thus applying the known boundary condition on the system ($\varepsilon_1 E_{1n} = \varepsilon_2 E_{2n}$) almost all of the terms cancel and $V_i^{opt}$ becomes $V_i^{opt} = \langle\langle V_i\rangle\rangle = V_0$, indeed, as expected. It is therefore permissible to still use the double average as defined in Eq. (3.3) but now with the modified weights depending on the dielectric constants $\bar{\varepsilon}_j$.

### 3.2.3 Depletion of 2DEG

In today's electronic devices, the two–dimensional electron gas (2DEG) is common place. In general, a 2DEG is an abundance of charges (electrons) in a solid state system which is confined onto a 2D plane in the sense that due to its nanoscopic thickness the wavefunction perpendicular to the plane is quantized such that only the lowest few discrete quantum levels are occupied.

In terms of classical electrostatic simulation, a 2DEG behaves like a metallic surface, i.e. equipotential for where there is charge. However, the charge density only comes in one flavor, namely with a negative sign due the charge of the electron. The charge density cannot become positive, since the 2DEG in general is offset spatially from the related donor layer and so its background is neutral. So once the 2DEG

is *depleted* of its charge through electrostatic interaction with the environment, that region of space has no charge left and the potential starts floating there. The donor layer has constant and uniform (positive) charge density throughout.

The numerical algorithm to simulate this depletion turns out to be surprisingly simple. It is straightforwardly built into the local update procedure of the potential as follows: when coming across a 2DEG grid point, say point $i$, with the 2DEG layer kept from the exterior at the potential $V_{2DEG}$ then

1. calculate the locally updated potential $V_i$ like in free space
2. if $V_i > V_{2DEG}$, take $V_i = V_{2DEG}$ instead, otherwise accept the calculated $V_i$.

The basic idea underlying this procedure is, that for the charges $q_i < 0$ in the 2DEG it is energetically favorable to go to a potential that is *higher* then $V_{2DEG}$. Therefore charges will gather in these regions until the potential reaches $V_{2DEG}$. q.e.d.

The remainder of this section is on different physical realizations of electrostatic depletion of a 2DEG system. All of them are rooted in the Coulomb interaction and thus in electrostatic concepts. The main examples are depletion via a negatively biased capacitively coupled gate electrode and shallow etching [HVH+98]. At first, however, an example is shown on how *not* to deplete a 2DEG.

### How Not to Deplete a 2DEG

Consider the setup in Fig. 3.7a. The donor layer at the top indicated in blue provides excess electrons which in a stack of sequentially grown materials are drained onto a layer slightly offset to it, the 2DEG. Suppose now the donor layer is etched away for $x \geq 0$ without damaging the 2DEG underneath as shown on the right–hand side of Fig. 3.7a. The question is, will the region where there are no donors ($x \geq 0$) be depleted of its electrons? If for example $x/d$ is just large enough with $d$ the distance of the donor layer to the 2DEG system then one may assume this could be the case. However, it is not.

The system in Fig. 3.7a can be solved analytically if one assumes an infinite plane for the 2DEG and an infinite extension of the donor layer in y–direction but with a finite or semi–infinite width in x–direction. Here, the donor charge density is considered constant and unequal to zero for $x < 0$ while it is zero for $x \geq 0$.

The electrostatic Green's function in 3D for a single wire of donors along the y–direction is

$$G\left(\vec{r}, \vec{r}\,'\right) = \frac{\lambda}{2\pi} \ln\left(\frac{\left|\vec{r} - \vec{r}_-'\right|}{\left|\vec{r} - \vec{r}_+'\right|}\right) \tag{3.27}$$

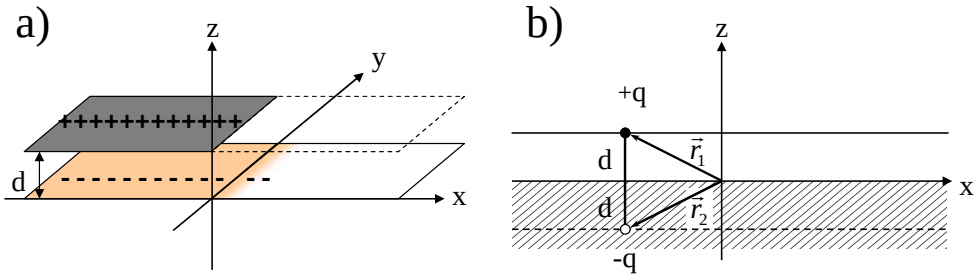


Figure 3.7: Effect of local removal of donor layer - Panel a) Schematic drawing of donor layer (grey area, top) on underlying conducting 2DEG (orange area, bottom) separated by a distance $d$ from the donors. Panel b) same as (a) but emphasizing the 2D infinite plane image charge setup.

where $\lambda$ is the charge density per unit length and $\vec{r}\,'_{+/-}$ point to the location of $+q/-q$ in the (x,z) plane, respectively, and therefore $\vec{r}\,'_{-} \equiv \vec{r}\,'_{+} - 2d\,\hat{z}$. Therefore for the problem as shown in Fig. 3.7a, the overall potential is the following integral over the Green's function in Eq. (3.27)

$$\begin{aligned} V(\vec{r}) &= \int_{-\infty}^{0} \sigma_0 dx' \, \frac{1}{4\pi} \ln\left(\frac{(x-x')^2 + (y-d)^2}{(x-x')^2 + (y+d)^2}\right) \\ &= \int_{-\infty}^{0} \sigma_0 dx' \, \frac{1}{4\pi} \ln\left(1 - \frac{4yd}{(x-x')^2 + (y+d)^2}\right) \end{aligned}$$

with $\sigma_0$ being the charge density in the donor layer and therefore, compared to Eq. (3.27), $\lambda \equiv \sigma_0 dx$ . The integral for $V(\vec{r})$ can be solved analytically. The induced charge density $\sigma_i(x)$ induced in the 2DEG is then calculated by employing the boundary condition that no static electric field will penetrate the metallic 2DEG [Jac99], i.e.

$$\sigma_i(x) = -\left(\vec{\nabla} V\right)\hat{n}$$

where for simplicity the usual constants are eliminated ($\varepsilon = \varepsilon_0 = 1$). With above expression for $V(r)$ and setting the length scale $d = 1$, the induced charge density follows as

$$\sigma_i(x) = -\frac{\sigma_0}{\pi} \tan^{-1}\left(\frac{1}{x}\right)$$

This is the specific case for the more general problem, where the donors only cover the region $x = [x_1, x_2]$ such that $\sigma_i(x) = \frac{\sigma_0}{\pi}\left(\tan^{-1}\left(\frac{1}{x-x_1}\right) - \tan^{-1}\left(\frac{1}{x-x_2}\right)\right)$. Care

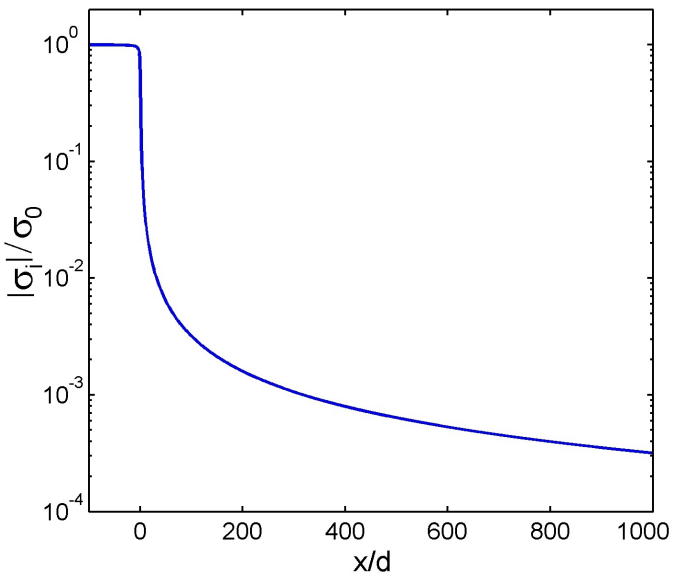


Figure 3.8: Induced (depleted) charge $\sigma_i$ in the 2DEG as a function of the distance $x/d$ for the geometry in Fig. 3.7.

must be taken of the fact that the $\tan^{-1}\left(\frac{1}{x}\right)$ has a seemingly non analytic structure at $x = 0$. However, $\tan^{-1}\left(\frac{1}{x}\right)$ can be chosen smoothly even at $x = 0$ considering the different branches of the tan function. In the end, the solution for $\sigma_i$ has to be physical and therefore has to be smooth. The result is shown on a semi–logarithmic plot in Fig. 3.8. Since eventually the $\sigma_i$ decays as $1/x$ for large $x$, there will always be an infinite amount of charge to the right of any $x > x_a > 0$. Consequently this is not what full depletion is supposed to be, namely the complete clearance of charge in a certain (finite) region of space. This has to be achieved by different electrostatic means then, where the underlying principle for the following examples of real depletion can be explained rather generally by a multiple parallel plate capacitor geometry which thus will be introduced next.

### Electrostatic Solution to Parallel Plate Geometry

Depletion through shallow etch [HVH+98] and the effect of surface charges can be well understood by considering a simple parallel plate geometry as shown in Fig. 3.9. Assume a given potential difference $V_0$ across the stack of layers which fixes the charge densities $\sigma_1$ and $\sigma_2$ uniquely. From electrostatics [Jac99], the charge density at a plane interface is related linearly to the difference in the normal component of the electric

field on both sides of that interface

$$\left(\vec{E}_+ - \vec{E}_-\right)\hat{n} = \frac{\sigma}{\varepsilon\varepsilon_0} \tag{3.28}$$

The constants $\varepsilon\varepsilon_0$ are eliminated by the following consistent change of variables

$$\tilde{\sigma} \equiv \frac{\sigma}{\sqrt{\varepsilon\varepsilon_0}} \iff \tilde{E} \equiv \sqrt{\varepsilon\varepsilon_0}E \tag{3.29}$$

where the tilde will be also dropped for convenience. With the boundary condition of no electric field to the left and to the right of the stack, the following equations follow

$$\sigma_1 d_1 + (\sigma_1 + \sigma_p)\, d_2 = +V_0 \tag{3.30a}$$

$$\sigma_1 + \sigma_p + \sigma_2 = 0 \tag{3.30b}$$

with the individual variables defined in Fig. 3.9. Alternatively, these equations can also be derived from an energetic point of view since the electrical field density is directly related to the electrostatic energy stored in the system $H \equiv \frac{1}{2}\int \varepsilon \left(\vec{\nabla}\phi\right)^2 d^3r$. Introducing the Lagrange multiplier $\lambda$ for the constraint of the overall voltage difference $V_0$, the energy functional becomes

$$\begin{aligned}\mathcal{H} &\equiv \frac{1}{2}\int \left(\vec{\nabla}\phi\right)^2 d^3r + \lambda\left[\sigma_1 d_1 + (\sigma_1+\sigma_p)\, d_2 - V_0\right] \\ &= \frac{A}{2}\left(\sigma_1^2 d_1 + (\sigma_1+\sigma_p)^2\, d_2\right) + \lambda\left[\sigma_1 d_1 + (\sigma_1+\sigma_p)\, d_2 - V_0\right]\end{aligned}$$

with $A$ being the area of the plates in (x,y) direction. Minimization of $\mathcal{H}$ with respect to $\sigma_1$, $\sigma_2$ and $\lambda$ again leads to exactly the same Eqs. (3.30) for $\sigma_1$ and $\sigma_2$.

The equations (3.30) are easily solved for the unknown $\sigma_1$ and $\sigma_2$

$$\sigma_1 = -\frac{d_2}{d_1+d_2}\sigma_p + \frac{V_0}{d_1+d_2} \tag{3.31a}$$

$$\sigma_2 = -\frac{d_1}{d_1+d_2}\sigma_p - \frac{V_0}{d_1+d_2}\,. \tag{3.31b}$$

Consequently, the closest conducting surface will carry most of the charge with the effect of screening the charges in the donor layer. Now, the metallic plate is used to drive the potential, and it is assumed that it can have both, positive or negative charge density (since depletion of the electrons brings forward the positive nuclei at the same region of space, i.e. the unsaturated dangling bonds at the surface of the stack). The 2DEG, however, can only have negative charge which originated from

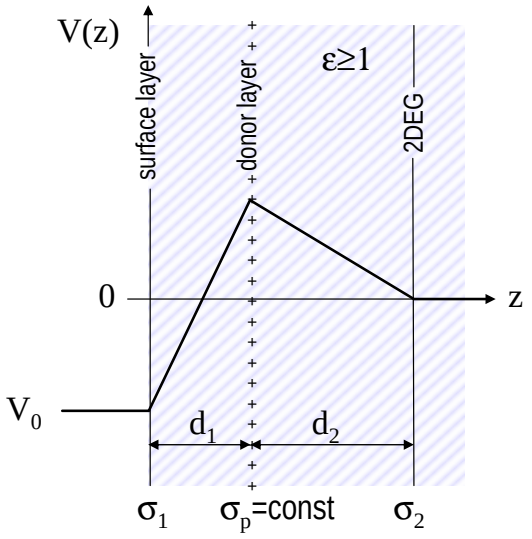


Figure 3.9: Parallel plate geometry to demonstrate depletion - the material in between the plates is considered uniform with a dielectric constant of $\varepsilon$. The charge densities on the three planes (plates) shown are $\sigma_1$, $\sigma_p$ (p for the *positive* charge of the donor layer) and $\sigma_2$, respectively. $V_0$ is the resulting potential difference across the whole stack.

the spatially separated donor layer in the first place. Thus the $\sigma_2$ of the 2DEG is constrained to $\sigma_2 \leq 0$. With the geometry kept constant, the critical voltage $V_0^*$ for $\sigma_2$ to be zero is

$$V_0^* = -\sigma_p d_1 \tag{3.32}$$

which is independent of $d_2$ (the distance of the 2DEG to the donor layer)! Making $V_0$ smaller, i.e. even more negative, would result in a positive $\sigma_2$ but since the latter is constrained to negative values, $\sigma_2$ is necessarily pinned to zero, i.e. the depletion is complete.

### Depletion Through Shallow Etch and Numerical Example

A different point of view on the depletion in the previous section is as follows: Consider $\sigma_1$ to be related to the surface of the sample followed by the donor layer and with the 2DEG buried underneath. The voltage $V_0$ is fixed as a consequence of the pinning of the Fermi energy at the surface. Moreover, the charges at the surface and in the 2DEG rearrange and equilibrate when the temperature is high enough, e.g. at room temperature (RT). Then the remaining variable is the distance $d_1$ which can be reduced, e.g. by etching. Then the critical distance $d_1^*$ for depletion is given as

$$-V_0 = \sigma_p d_1^* \tag{3.33}$$

in full analogy to Eq. (3.32). Similarly, $d_1^*$ is independent of $d_2$, the distance of the 2DEG to the donor layer. So making $d_1$ smaller than $d_1^*$ would result now in complete depletion.

As a specific example, consider a Ga(Al)As heterostructure with $\varepsilon = 12$. The 2DEG and the donor layer are considered extended (infinite) planes with a uniform charge density and a strong confinement in the vertical direction. The surface acquires extra charge due to dangling bonds which give rise to another layer of electronic (negative) charge. In semiconductors, this is equivalent to the pinning of the Fermi level at the surface. Specifically in the case of Ga(Al)As, the Fermi energy at the surface is pinned to the middle of the band gap, and therefore $V_0 \simeq -0.75\,\mathrm{V}$ where the sign automatically implies negative surface charges. In the semiconductor, the resulting field is eventually screened through unavoidable small doping of the bulk system on length scales that are much larger than the typical donor layer to 2DEG distance ( $\mu$m compared to nm).

Now typical size parameters for Ga(Al)As 2DEG systems are $d_1 = 15\,\mathrm{nm}$, $d_2 = 32\,\mathrm{nm}$ and $n_2 = 5 \cdot 10^{15}\,\mathrm{m}^{-2}$ where $n_j \equiv |\sigma_j/e|$ with $j = \{1, p, 2\}$. When returning back to SI units (see Eq. 3.29), Eq. (3.31b), becomes

$$n_2 = n_p \frac{d_1}{d_1 + d_2} + \underbrace{\frac{\varepsilon\varepsilon_0}{e} V_0 d_2}_{\equiv \tilde{V}} \frac{1}{d_2^2} \frac{d_2}{d_1 + d_2}$$

from which the calculated values follow, namely $n_p = 4.88 \cdot 10^{16}\,\mathrm{m}^{-2}$, i.e. $n_2/n_p = 0.102 \cong 10\%$. Thus out of pure electrostatic reasons, the majority of the electrons from the donor layer will actually gather at the surface ($\sigma_1 \simeq 90\%$ of $\sigma_p$). The critical distance of the surface to the donor layer $d_1^*$ turns out to be $d_1^* \simeq 10.2\,\mathrm{nm}$ which is only slightly smaller than the original $d_1 = 15\,\mathrm{nm}$. Consequently, a local shallow etch of about 5 nm depth is expected to completely deplete the 2DEG underneath! The obvious advantage of this procedure compared to *shaping* of the 2DEG via deep etch is that the quality of the 2DEG remains intact without introducing extra surface states laterally limiting the 2DEG, and so the mobility of the electrons therein can be expected to stay the same.

### 3.2.4 Electrostatic Effect of STM Tip Close to 2DEG

A typical setup with a two–dimensional electron gas (2DEG) and a donor layer buried underneath a semiconductor surface is shown again in Fig. 3.10, similar to the previous section.

At room temperature (RT), the charges on the surface as well as on the other planes are assumed to be in equilibrium. The conductivity on the surface may very

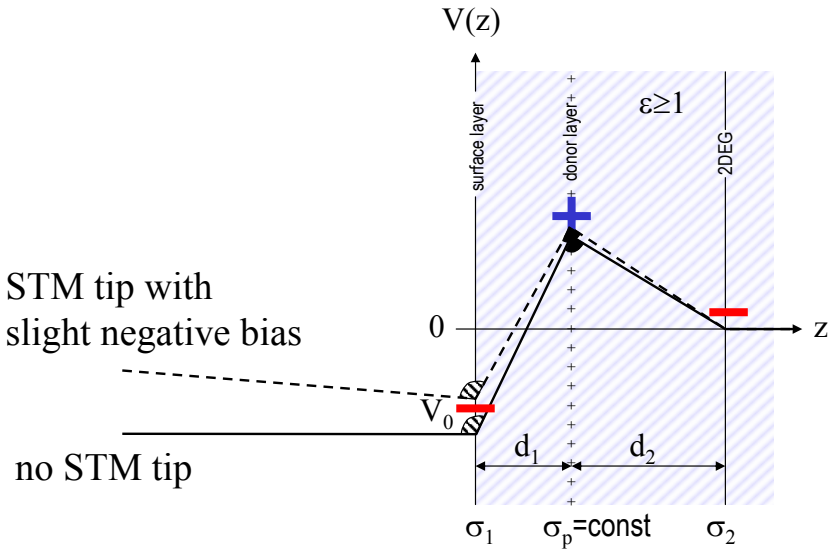


Figure 3.10: Schematic setup of 2DEG under influence of STM tip indicating the purely electrostatic potential with the STM tip at infinity (solid line, no STM tip) and at a slight negative bias voltage (dashed line).

well be small, yet on macroscopic time scales it allows for relaxation of the charges to a uniform potential over the entire surface. Now the optimal electrostatic charge distribution for the system in Fig. 3.10 has no electric field above the surface and below the 2DEG. This equilibrium distribution is given by Eqs. (3.31).

With the pinning of the potential $V_0 \simeq -0.75$ for GaAs, the donor doping density $\sigma_p$ and distances $d_{1,2}$ known, the resulting equilibrium charge densities at the surface ($\sigma_1$) and in the 2DEG ($\sigma_2$) can be calculated. Furthermore, with $V_0$ being constant along the entire surface, small variations in the $d_1$ or $d_2$ automatically translate into variations of the charge density in the 2DEG approximately described by Eqs. (3.31). For the remainder of the discussion, however, a perfectly flat surface is assumed.

Equations (3.31) describe the relationship between the equilibrium charge densities at RT with no other object present. Now cooling the system down to low temperatures eventually *freezes* the surface charge configuration, and consequently, $\sigma_1$ becomes constant to the value given by Eqs. (3.31). This fixes the relationship between the slopes of the potential on both sides of the surface. So in a sense, the joints of the potential curve in Fig. 3.10 become somewhat stiff as indicated for the surface and for the donor layer. Bringing close then another object, for example a voltage biased STM tip, will then neither change the surface charge configuration nor the donor charge density which is fixed all along, but act directly onto the 2DEG. However, and this is an important point, these intermediate layers of fixed charge density shift the voltage

reference. In the case of the GaAs system, this means that $V_{STM} \gtrsim V_0 = -0.75V$ acts like a positive voltage for the 2DEG and attracts further negative charge in the 2DEG plane even though the STM tip may be biased negatively, for example.

Two important notes as a corollary to the above: First, since the diameter of the STM tip is in general comparable to a typical distance from the surface (˜100 nm), the resulting nonuniform field distribution will alter the result somewhat. Yet qualitatively, the above observation still holds. In order to be more quantitative, the charge that gathers on the STM tip at a distance $d$ from the surface and at a potential $V$ is $Q_{STM} = C(d)(V - V_0)$ with $C(d) \sim (d + (d_1 + d_2)/\varepsilon)^{-1}$ describing the capacitive coupling between the tip and the 2DEG. This charge $Q_{STM}$ will be screened by an equal and opposite charge in the 2DEG, thus $\Delta Q_{2DEG} = -C(d)(V - V_0)$. The sign of the charge is still decided upon by the voltage reference $V_0$, and the total amount decreases like in the parallel plate case as $\mathcal{O}(1/d)$, yet the locally induced charge density in the 2DEG falls of more rapidly as $\mathcal{O}(1/d^2)$.

Second, the surfaces of the GaAs and of the STM are never perfectly clean and the way one would expect them to be. During the fabrication and also later on in the handling of either one of them, the surfaces may differ from sample to sample. The partially uncontrollable *dirt* on the surface thus further shifts the Fermi energies (chemical potentials) relative to each other, such that in the real experiment the reference of $V_0 = -0.75V$ is somewhat relative. In the experiment, the voltage offset $V_0$ can be found insofar, as the influence onto the 2DEG is minimized such as by Kelvin probe techniques. As in [VKI+03] for Ga(Al)As, the least invasive tip potential is close to the $-0.75\,\mathrm{V}$ as expected. Typical measured voltage off–sets, however, can vary significantly from sample to sample depending on the actual surface constitution of the individual samples.

### 3.2.5 Numerical Study on 2DEG Depletion - Ring Structure

The numerical study in the following section is based on a collaboration with the group of K. Ensslin, M. Sigrist, T. Ihn et al. in Zürich (ETH). The sample geometry of the Ga(Al)As system analyzed here was published by this group in recent papers [SFI+03a, SFI+03b].

A two–dimensional electron gas (2DEG) buried in close proximity to the surface of the host semiconductor has been already introduced in the previous section and was shown schematically in Fig. 3.10. We use the specific distances of 23.4 nm between the 2DEG and the donor layer, 15.6 nm between the donor layer and the surface, and 54.7 nm as separation of a parabolic conducting STM tip from the surface, together with a donor charge density of $n_p \equiv 4 \cdot 10^{16}\,\mathrm{m}^{-2}$ and a dielectric constant of $\varepsilon = 12.0$, and show the numerical results in Figs. 3.11 and 3.12. This calculation was done on

a $256 \times 256 \times 40$ 3D grid. With the grid constant of $h = 7.8\,\text{nm}$ this is equivalent to a total sample space of $2 \times 2 \times 0.3\,\mu\text{m}$ with open boundary conditions. The surface of the (GaAs) structure is considered partially shallow etched by 7.8 nm (i.e. one grid layer) through local oxidation via an STM tip at rather high negative voltage and humid atmospheric conditions [HVH+98]. This is enough to deplete the 2DEG right underneath consistent with the capacitive discussion in the previous sections.

The system is relaxed numerically without the (STM) tip present. The relaxed charge distribution on the surface is then considered frozen by cooling the system down to sub–Kelvin temperatures. Subsequently, a parabolically shaped tip with a curvature of about 100 nm is brought close to the surface (54.7 nm). The tip acts directly on the 2DEG underneath then, and the effects are shown in detail in Fig. 3.11. The oxide lines 'written' on the surface prior to the later analysis of the structure can be seen in panel (b). Due to the reduced distance of the surface to the donor layer, the 2DEG underneath is fully depleted (panel a). In the remaining regions with no shallow etch, the electrons provided from the donor layer split in a ratio of about 1 : 9 with respect to 2DEG and surface states, in agreement with the previous electrostatic considerations. Thus the charge density on the surface is much larger than in the 2DEG which is also reflected in the overall charge count provided in panels (a+b). Note in this context, that the color contrast changes between the panels in Fig. 3.11. For example, the charge density on the surface (panel b) is on average much larger than the charge density in the 2DEG, panel a.

One interesting thing to notice is that approaching a tip at zero or slightly negative potential *attracts* further electrons still in the 2DEG (panel c). Note that the color coding is such that red (blue) stands for negative (positive) charge density. This attraction of more electrons appears to be counter intuitive at first glance, but makes perfect sense in the light of the arguments of the preceding section. Lowering the potential to more negative potentials, eventually starts depleting the 2DEG when compared to the case without the tip (panel d). The numbers shown with each panel (c–d) give the total change of charge due to the tip. These changes in charge are huge and that is why in real experiment the voltages are swept over a much smaller range than the $0 \ldots -2\,\text{V}$ shown here. This also demonstrates why it is important to know which tip voltage will influence the 2DEG structure in the least possible way. Moreover, since the experiment has mostly access to transport data through the ring connected via the four narrow constrictions to the outside (leads), it is interesting to have an estimate of how many electrons there are in this ring. For the given setup, it turns out that with no STM tip present, there are about 150 electrons in the ring (not including the well–isolated ring at the very center). The change in the charge population in the ring due to the tip is about 25% of the total change which in the voltage range of $0 \ldots -2\,\text{V}$ translates to $+45 \ldots -70$ electrons.

The total charge accumulation in the 2DEG vs. applied tip voltage is shown in the last panel of Fig. 3.11(f). This clearly shows once more the accumulation of negative charge in the 2DEG for slightly negative tip voltages. The linear relationship in panel (f) for the total charge follows clearly from the fixed geometry in the given case where here the tip is at constant height and at a fixed lateral position slightly above the central region as indicated by the black circle in panel (a) in Fig. 3.11. In contrast to the initial accumulation of charge for a slightly negatively tip bias, the relative behavior on the tip bias is what one expects. More negative voltage implies

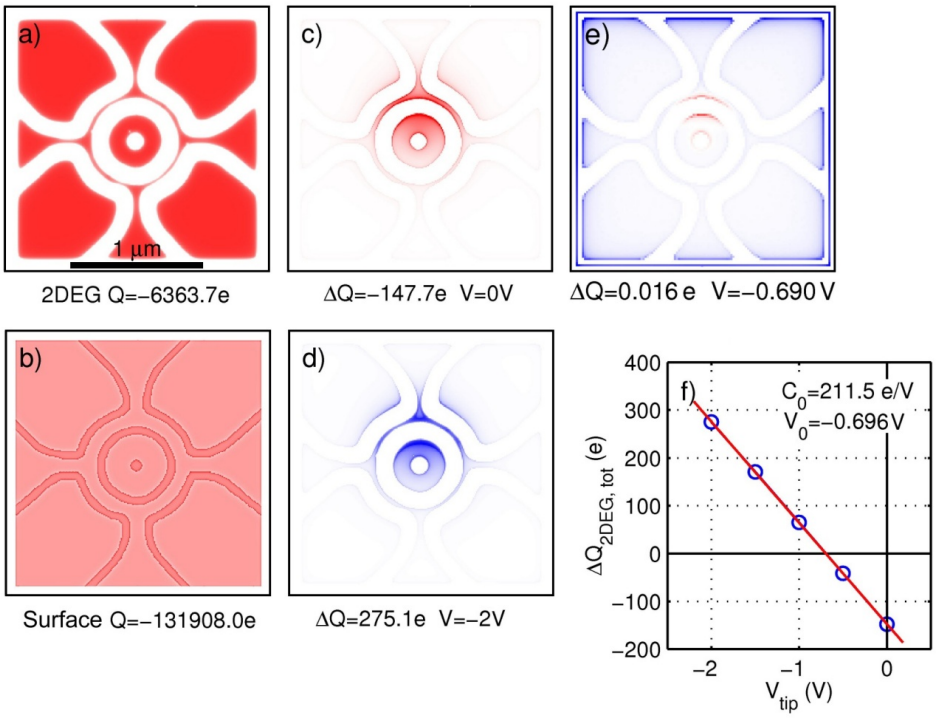


Figure 3.11: Numerical simulations on 2DEG system - ring structure. a) Charge distribution within 2DEG with regions depleted due to local oxidation on the surface. The 1 $\mu$m bar shows the scale of the system and the black circle the position and roughly the size of the subsequently introduced STM tip. b) Initially relaxed and then frozen charge distribution at the surface altered by local oxidation (shallow etch). c) Change in charge distribution due to the presence of a parabolic (STM) tip at a distance of 55 nm with $V_{tip} = 0\,\mathrm{V}$. d) Same as (c) but with $V_{tip} = -2\,\mathrm{V}$. e) Charge distribution in 2DEG with $V_{tip} = -0.69\,\mathrm{V}$, i.e. the least invasive potential with respect to the 2DEG. The color coding with respect to charge density in panels (a–e) is that red (blue) corresponds to negative (positive) charge, respectively. f) Dependence of the total change in the charge distribution in the 2DEG (e.g. panels c–e) vs. voltage on the STM tip at constant distance of 55 nm. The red line is a line fit to the data. From the linear relationship, the capacitive coupling between the tip and the 2DEG for this position of the tip follows as $C_0 = 211.5\,\mathrm{e/V} \equiv 33.9\,\mathrm{aF}$.

further increase in "positive" charge and thus depletion of the 2DEG (panel d). The capacitive interaction between the STM tip and the 2DEG extracted from the line fit to panel (f) turns out to be $C_0 = 211.5\,\mathrm{e/V} \equiv 33.9\,\mathrm{aF}$.

The transition point where the tip potential does neither accumulate nor deplete charges in the 2DEG is found to be at $V^0_{tip} \equiv -0.69\,\mathrm{V}$ close to the theoretically expected $-0.75\,\mathrm{V}$ (see Sec. 3.2.4, pp. 55). The difference stems from the finite size of the sample space as can be seen from panel (e). This panel shows the change in the charge distribution in the 2DEG with the STM tip at $V^0_{tip} = -0.69\,\mathrm{V}$ compared to the case with no STM tip present. Indeed, the tip influences the 2DEG structure underneath only slightly in the sense that the total charge variation is a tiny fraction of one single electron charge ($\sum q_i = 0.016\,\mathrm{e}$ or $\sum |q_i| = 0.031\,\mathrm{e}$). The tip at $V^0_{tip}$ thus only induces a slight polarization within the structure itself of a strength much smaller than a single–electron charge, i.e. the small slightly red shaded area in the center of panel (f). Here the main correction comes from the finite size of the sampled space, i.e. the charge accumulated on the outer regions of panel (f).

Studies on the electric field for the structure described above are presented in Fig. 3.12. With $n_p \equiv 4 \cdot 10^{16}\,\mathrm{m^{-2}}$ and $\varepsilon = 12.0$, the electric field from an equivalent parallel plate capacitor is $E_{ref} \equiv n_p e/\varepsilon\varepsilon_0 = 6.03 \cdot 10^7\,\mathrm{V/m}$. The maximum electric field in above structure with local oxidation slightly exceeds this value as intuitively expected from the charge accumulation due to the oxide line groove in the surface ($7.16 \cdot 10^6\,\mathrm{V/m}$ from panel a). The surface charge distribution remains in its equilibrium state without the tip. Consequently, the approaching STM tip at a certain potential induces an electric field parallel to the surface which may eventually rearrange charges on the surface if it becomes strong enough. This way the surface charge distribution can be altered permanently *by brute force*, so to speak, where $V_{tip} = -2\,\mathrm{V}$

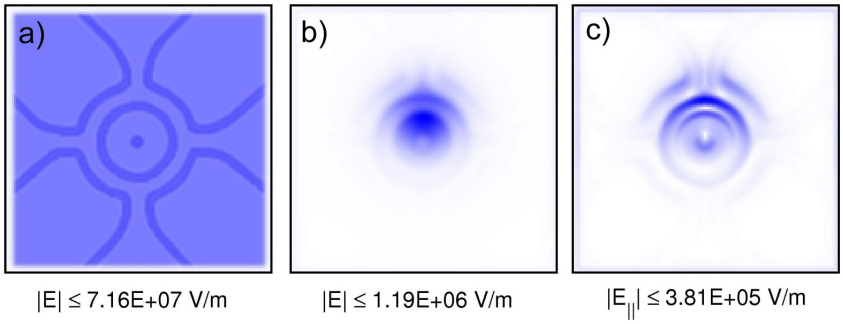


Figure 3.12: Electric field study for system in Fig. 3.11 - a) Strength of electric field right underneath the surface with a maximum electric field of $7.16 \cdot 10^7\,\mathrm{V/m}$. b) Change in the total electric field in (a) due to the presence of the tip at $V_{tip} = 0\,\mathrm{V}$. c) Same as (b) but showing the in–plane component of the change of the electric field only.

may already be clearly able to do so, as is also seen experimentally. In this sense it is interesting to have an estimate of the in–plane electric field induced by the STM tip. For the tip being held at $V_{tip} = 0\,\mathrm{V}$, the resulting changes in the electric field are shown in panel (b) for the total strength of the electric field, and in panel (c) for the in–plane component only. The maximum in–plane field that arises is about two orders of magnitude smaller than the typical total electric field strength, yet it is still of considerable strength in the sense that $V_{in--plane} = 3.81 \cdot 10^5\,\mathrm{V/m} = 0.381\,\mathrm{mV/nm}$ may very well be strong enough to induce in–plane hopping of charges between localized states within the surface. Note that at room temperature ($\sim 25\,\mathrm{meV}$) the charges on the surface are reasonably mobile to equilibrate but not so at the typical temperatures in experiments ($\sim$ mK).

### 3.2.6 Numerical Study on 2DEG Depletion - Double Dots

A rather different but very common approach to depletion is taken in the following example. Double dot systems are created in the 2DEG via depletion through negatively biased metallic top gates on the surface of the structure, e.g. fabricated by lithographic means. The system with its numerical results are shown in Fig. 3.13. The set of top gates chosen can be seen in panel (a). Every double dot system (qubit) has altogether six gates defining the dots, two of which are designed to be plunger gates, one for every dot, and a third one tunes the tunnel barrier between the two dots defining the qubit. The extra gate between the dots could be merged with one of the dot–defining gates. Yet it was introduced to allow for more flexible qubit spacing, e.g. as utilized for the results in panel (d). Panel (a) shows the charge distribution on the top gates (a red shading) resulting from the range of negative bias voltages applied, namely $-2.5 \ldots -4.5\,\mathrm{V}$. The individual gate voltages are directly related to the accumulated charge density on the top gates in the sense that the more negative the bias, the larger the accumulated negative charge on that gate.

The analysis of the qubit properties here is mainly concerned with the electrostatic interaction between the qubits. The coupling between the qubits that results from this analysis may be eventually used in a simple quantum mechanical two–level model describing the underlying charge qubit. Note that in order to tune the coupling dynamically, the geometry of the conducting regions must be altered. Otherwise, with the capacitance matrix being constant, the mutual interaction would remain the same. In the given example, however, the distance between qubits is altered which clearly can not be done dynamically in the experiment this way. However, it is still interesting to realize the dependence of the strength of the qubit screening on the qubit separation. For real dynamical tuning in the experiment, eventually it would be necessary to have an effective handle on the charge distribution in the area between

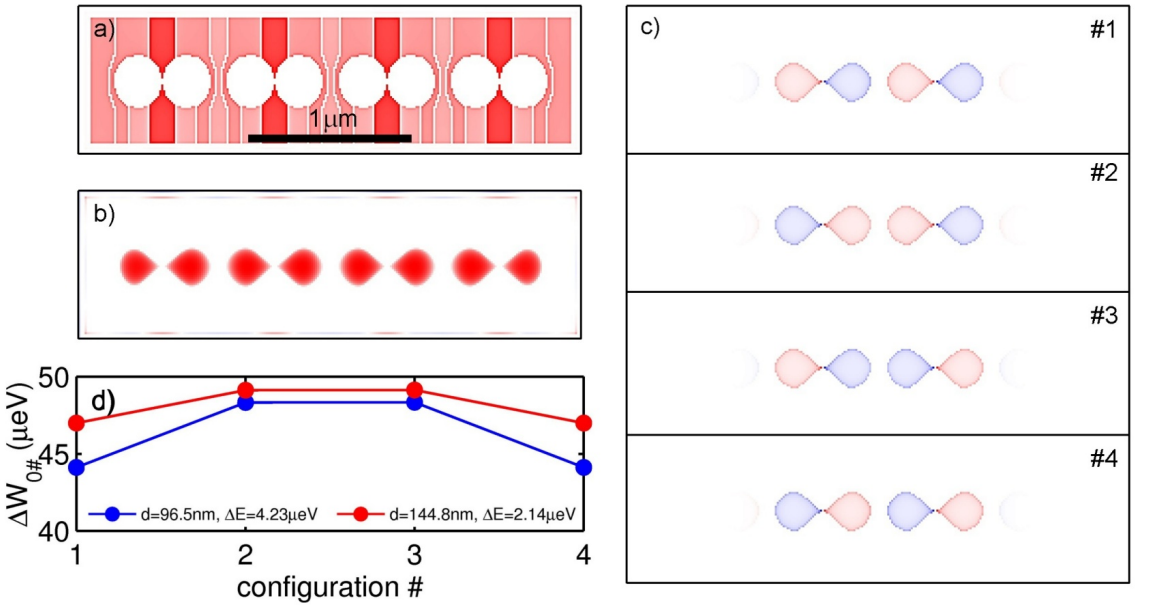


Figure 3.13: Numerical study - double quantum dots (charge qubit) formed by electrostatic depletion through top gates simulated on a $76 \times 256 \times 32$ cubic grid. The color coding in panels (a-c) is red (blue) for negative (positive) charge density, respectively. a) Setup of top gates defining four qubits. The color shading shows the charge distribution in the gates biased to different negative voltages. The $1\,\mu$m scale bar indicates the actual size of the simulated system. b) Charge distribution in 2DEG depleted by top gates with qubit separation of $8h = 96.5\,$nm. c.#1-4) Detuning of the charge distribution by one electron within the middle two qubits at constant gate voltages. Only the difference of the charge distribution with respect to initial distribution in panel (b) is shown such that the red (blue) areas in (c) indicates a total of $-1e$ ($+1e$), respectively. The resulting four combinations for the two central qubits are shown in panels #1 to #4. d) System energy for the different configurations in panels (c.#1-4). The red curve corresponds to a different geometry with the qubits slightly more separated ($12h = 144.8\,$nm).

the qudots which for example could be envisaged to be done on the basis of 2DEG depletion.

In the given case, the two basis states of the charge qubit are defined by looking at the topmost unpaired electron in every two–dot system. That single operative extra electron may reside in the left or the right dot, defining the corresponding two basis states of the system. In the initial stage the plunger gates for every dot are adjusted such that the total charge on the dot is a half–integer. Under this preconditioning, the transfer of the $e/2$ charge to either side generates two energetically equivalent and physically distinct states with integer occupation. We consider a distance of 36.2 nm for both the 2DEG – donor separation as well as the donor – top gates separation, a

dielectric constant of $\varepsilon = 12$ and a doping density of $n_p \equiv 4 \cdot 10^{16}\,\mathrm{m}^{-2}$, the charge density for the 2DEG is $1.31 \cdot 10^{16}\,\mathrm{m}^{-2} = 131.3/\,(100\,\mathrm{nm})^2 \simeq 1/3\; n_p$, for the case of an open surface with no top gate and an offset due to the surface states of $-0.75\,\mathrm{V}$ as in the previous sections. In this charges the charges of the donor layer split in a ratio of $\frac{1}{3} : \frac{2}{3} = 1 : 2$ between the 2DEG and the surface. With top gate voltages $V_g < -2.5\,\mathrm{V}$, the 2DEG becomes depleted. This leaves about 418 electrons in each dot area with approximately twice as many electrons (807 e) on the surface right above the dot, in agreement with the branching ratio of $1 : 2$. With this many participating electrons, the overall island configuration remains approximately constant under single–electron hops.

The qubit as outlined, clearly interacts with its nearest neighbor qubits in a "ferromagnetic" sense in spin terminology, as summarized in terms of the energetics in panel (d) based on the charge configurations #1-4 in panel (c). Since from the numerical simulation the overall charge accumulation and potentials are known, the relative energy cost due to the rearranging of charges can be easily calculated using Eq. (2.26), p. 19. Two neighboring qubits being in *antiparallel* states, as in the configurations #2-3, is clearly less favorable energetically. The energy difference is $4.23\,\mu\mathrm{eV}$ ($2.14\,\mu\mathrm{eV}$) for a qubit distance of $8h = 96.5\,\mathrm{nm}$ ($12h = 144.8\,\mathrm{nm}$), respectively (see Fig. 3.13, panel d). From a naive dipolar model for the charge configuration with the charge puddles of the quantum dots replaced by centered point charges and taking $\varepsilon = 12$, one would expect an energy scale of the order $\frac{1}{4\pi\varepsilon_0\varepsilon}\frac{(e/2)^2}{0.3\,\mu\mathrm{m}} = 400.1\,\mathrm{meV}$ and an energy difference between parallel and antiparallel state configurations of $126\,\mu\mathrm{eV}$ ($97\,\mu\mathrm{eV}$) for the blue (red) curve in Fig. 3.13d, respectively. The conclusion is clear - first, the presence of the top gate strongly screens the double–dot interaction, and second, this screening effect becomes more pronounced as the distance between the double–dot systems increases. For the two geometries analyzed, the interaction energy only reduces by a factor 1.30 in the dipolar picture while in the real physical system, it decreases by a factor of 1.97. This is very much plausible, since the top gate bridging the separation between two qubits prohibits electric field lines to penetrate to the side of the individual qubit.

# Chapter 4

# Feshbach Formalism

In this chapter we explore the Feshbach formalism. The formalism extracts an effective Hamiltonian for a subspace of the total system of interest. Since the resulting effective Hamiltonian is formally exact, it necessarily needs to be nonlinear in structure in order to contain still the entire set of eigensolutions. Furthermore, the formalism is especially suitable in a perturbative sense if the subspace under consideration is well decoupled energetically from the remainder of the spectrum, as we will see.

The Feshbach formalism is akin to perturbation theory for unperturbed states. The usual treatment there [MYS67, pp. 69] results in a perturbative expansion similar to here but is done with respect to one eigenstate only and is usually referred to as *Rayleigh–Schrödinger* theory. Historically, the Feshbach formalism traces back to the paper of Feshbach in nuclear theory [Fes62] which gave the formalism its name. For more recent references on that algorithm, see for example [So02].

I am very grateful to Prof. D. Phillips from the local nuclear theory group for pointing out this formalism to me.

## 4.1 Definitions

The projection operator $P$ defines a finite and likely small subspace isolated energetically from the remainder of the (possibly infinite) Hilbert space $Q$ such that $P + Q = 1$.

$$P \equiv \sum_{i \in \mathcal{P}} |i\rangle \langle i| \tag{4.1a}$$

$$Q \equiv \sum_{k \notin \mathcal{P}} |k\rangle \langle k| = 1 - P \tag{4.1b}$$

The Hamiltonian is written as

$$H = H_0 + V \tag{4.2a}$$
$$H_0 \left|\nu\right\rangle = \varepsilon_j \left|\nu\right\rangle \text{ with } \nu = i, k \tag{4.2b}$$

such that $\left|i\right\rangle \in \mathcal{P}$ together with $\left|k\right\rangle \in \mathcal{Q}$ form the complete orthonormal set of eigenstates of $H_0$. The term $V$ is then treated as a perturbation. The projection operators $P$ and $Q$ obey the following set of identities which are easily shown from their definition in Eqs. (4.1a).

$$P + Q = 1 \qquad \text{due to completeness} \tag{4.3a}$$
$$PQ = QP = 0 \quad \text{due to orthogonality of } \left|i\right\rangle \text{ and } \left|k\right\rangle \tag{4.3b}$$
$$P^2 = P,\ Q^2 = Q \tag{4.3c}$$
$$Q^+ = Q,\ P^+ = P \tag{4.3d}$$
$$[H_0, P] = 0,\ [V, P] \neq 0 \tag{4.3e}$$
$$[H_0, Q] = 0,\ [V, Q] \neq 0 \tag{4.3f}$$

## 4.2 Effective Hamiltonian

With the identities in Eq. (4.3), the Schrödinger equation $H\left|\psi\right\rangle = E\left|\psi\right\rangle$ is rewritten as

$$H\left(P + Q\right)\left|\psi\right\rangle = E\ \left|\psi\right\rangle \quad \text{since } P + Q = 1$$

Multiplying from the left with $P$ or $Q$ one gets

$$\begin{aligned} \left(PHP + PHQ\right)\left|\psi\right\rangle &= EP\left|\psi\right\rangle \\ \left(QHP + QHQ\right)\left|\psi\right\rangle &= EQ\left|\psi\right\rangle \end{aligned}$$

Latter equation can be cast into matrix notation using Eq. (4.3c)

$$\begin{pmatrix} PHP & PHQ \\ QHP & QHQ \end{pmatrix} \begin{pmatrix} P \\ Q \end{pmatrix} \left|\psi\right\rangle = E \begin{pmatrix} P \\ Q \end{pmatrix} \left|\psi\right\rangle$$

and in simplified notation

$$\begin{pmatrix} H_{PP} & H_{PQ} \\ H_{QP} & H_{QQ} \end{pmatrix} \begin{pmatrix} \left|\psi_P\right\rangle \\ \left|\psi_Q\right\rangle \end{pmatrix} = E \begin{pmatrix} \left|\psi_P\right\rangle \\ \left|\psi_Q\right\rangle \end{pmatrix}$$

equivalent to

$$\begin{pmatrix} H_{PP} - E & H_{PQ} \\ H_{QP} & H_{QQ} - E \end{pmatrix} \begin{pmatrix} |\psi_P\rangle \\ |\psi_Q\rangle \end{pmatrix} = 0 \; . \tag{4.4}$$

$H_{PP}$ only contains the matrix elements for states in $\mathcal{P}$ and is thus a matrix of dimension $\dim(\mathcal{P})$. Similarly, $H_{QQ}$ is interpreted as a matrix of dimension $\dim(\mathcal{Q})$, while $H_{PQ}$ and $H_{QP}$ have mixed dimensions. For non–trivial solutions, the determinant of the total matrix in Eq. (4.4) must be zero. However, it must be kept in mind that the determinant of this matrix written in terms of a $2 \times 2$ set of block matrices cannot be evaluated in terms of the determinants of the individual blocks. It is still a highly complex intermingled problem.

However, since we are interested in $|\psi_P\rangle \equiv P\,|\psi\rangle$, i.e. in the projection of $|\psi\rangle$ onto the subspace $\mathcal{P}$, we can formally solve for it. The two equations in the compact notation of Eq. (4.4) are

$$(H_{PP} - E)\,|\psi_P\rangle = -H_{PQ}\,|\psi_Q\rangle$$

and

$$\begin{aligned} (H_{QQ} - E)\,|\psi_Q\rangle &= -H_{QP}\,|\psi_P\rangle \\ |\psi_Q\rangle &= +\frac{1}{E - H_{QQ}} H_{QP}\,|\psi_P\rangle \end{aligned} \tag{4.5}$$

Then substituting $|\psi_Q\rangle$ in the first equation gives

$$\left( H_{PP} + H_{PQ} \frac{1}{E - H_{QQ}} H_{QP} - E \right) |\psi_P\rangle = 0 \; .$$

In the last step, what is done essentially, is eliminating the large number of coefficients (variables) of $|\psi_Q\rangle$. Thus this can be seen as an efficient elimination of variables on the grand scale. Reordering the last equation, gives the Schrödinger like equation

$$\boxed{H^P_{\mathit{eff}}\,|\psi_P\rangle \equiv \Big( H_{PP} + \underbrace{H_{PQ} \frac{1}{E - H_{QQ}} H_{QP}}_{\equiv \Sigma_{QQ}(E)} \Big) |\psi_P\rangle = E\,|\psi_P\rangle} \tag{4.6}$$

This is the resulting *nonlinear* form and provides the *effective* Hamiltonian for the subspace $\mathcal{P}$. The original Hamiltonian sub–matrix $H_{PP}$ acquires a correction due to the perturbation $V$. This correction is the so–called (generalized) self–energy $\Sigma(E)$ and will be discussed in more detail in a moment. Since every term in Eq. (4.6) is bracketed between a $P$ at the left and a $P$ at the right, this proves the statement

of an effective Hamiltonian in the subspace $\mathcal{P}$ which according to above notation is described by the states $|i\rangle$

$$H_{eff}^{P} \equiv P\left(H + HQ\frac{1}{E - H_{QQ}}QH\right)P \tag{4.7a}$$

$$H_{eff}^{P}\,|p_i\rangle = E_i\,|p_i\rangle \tag{4.7b}$$

where $|p_i\rangle \equiv \sum_{i'} c_{i'}^{(i)}\,|i'\rangle$ is an eigenstate in the reduced state space.

A few remarks on the structure of the effective Hamiltonian in the Feshbach formalism are given in the following.

**Remark 1.** The components $c_{i'}^{(i)}$ of an eigenvector for $H_{eff}^{P}$ as in Eq. (4.7b) are exactly the same as the corresponding components of the full eigenvector in the entire Hilbert space $\mathcal{P} + \mathcal{Q}$. This has to be true, since no approximations have been made and in that sense the above description is exact. In case of degeneracy, this mapping onto the full Hilbert space may not be unique, but that is a general feature of any set of degenerate states. So that causes no problems. A more important point, however, is the normalization of the wave function. If $\langle\psi_Q|\psi_Q\rangle \neq 0$, then when considering the full wavefunction $|\psi\rangle$ it follows that $\langle\psi_P|\psi_P\rangle < 1$. In the extreme case, $\langle\psi_P|\psi_P\rangle = 0$ such that this specific eigenstate of the total Hilbert space has no components in $\mathcal{P}$ space at all, and therefore $c_{i'}^{(i)} = 0$ for all $i \in \mathcal{P}$. Obviously, $|\psi_P\rangle = 0$ is a trivial solution of Eq. (4.7b) but as such does not couple into the $\mathcal{P}$ space. These states are taken care of by the self–energy term in Eq. (4.6). Also, since the $\mathcal{P}$ space is considered energetically well–separated from the reminder of the spectrum, the eigenstates of interest are the states of $\mathcal{P}$ *renormalized* by the self–energy $\Sigma\,(E)$. Working only in this space with the wave functions properly normalized is a consistent procedure. The remaining states outside $\mathcal{P}$ do gain a small contribution in $\mathcal{Q}$ due to the perturbation $V$ and thus $\langle\psi_Q|\psi_Q\rangle \ll 1$. But these states are not of interest, and from a perturbative point of view, are not among the relevant states of interest.

**Remark 2.** The inverse expression $(E - H_{QQ})^{-1}$ in Eq. (4.6) or (4.7a) has to be understood as the inverse of the *Hamiltonian projected onto the subspace* $\mathcal{Q}$ (first projection, then inversion), and therefore having reduced (but still possibly infinite) dimension $\dim(\mathcal{Q})$. Thus

$$\frac{1}{E - H_{QQ}} \equiv (E - H)_{Q}^{-1} \neq Q\frac{1}{E - H}Q \quad (!) \tag{4.8}$$

and the last inequality holds because the last expression represents the reverse operation of first inverting and then projecting; this equality becomes an equality only

if $[H, Q] = 0$, which corresponds to the trivial case of $[V, Q] = 0$ which has been excluded in Eq. (4.3f).

**Remark 3.** In Eq. (4.7a) the inverse appears to be quite ill–defined for the case that $E$ hits one of the eigenvectors of $H_{QQ}$. To circumvent this, quite generally a small imaginary part may be added to the energy and this will be roughly motivated in the following. The starting point for the derivation of Eq. (4.7a) was the stationary Schrödinger equation $\hat{H}|\psi\rangle = E|\psi\rangle$, which is a solution of the time–dependent Schrödinger equation $\hat{H}|\psi\rangle = i\frac{d}{dt}|\psi\rangle$ (for convenience, $\hbar$ is equal to 1). One may think about the stationary solution in a lightly different way: given an initial wave function at $t = 0$, say $|\psi_0\rangle$, one is interested in how it is going to evolve in time, specifically also for large $t$, i.e. $t \to \infty$. For this, the problem will be translated into Fourier space with respect to time. In space, it is recalled that every Hermitian operator has a complete set of orthonormal eigenstates which will be labeled here as $|k\rangle$ with eigenvalues $\omega_k$, such that any state $|\psi\rangle$ at a given time can be decomposed into these states

$$|\psi\,(t)\rangle = \sum_k c_k(t)\ \ |k\rangle$$

It is then the Fourier transform of the $c_k(t)$ which is of interest. Since $|\psi(t)\rangle$ has norm 1 at any time, there always must be some $c_k(t)$ unequal zero. Therefore, $\int^\infty c_k\,(t)\,dt$ is not necessarily finite, and so the Fourier transform appears to be ill–defined. So for the Fourier transform to exist, one conveniently introduces a time factor $e^{-\delta t}$ with $\delta = 0^+$ a positive infinitesimal. One thus makes the following replacement

$$|\psi\,(t)\rangle \longrightarrow e^{-\delta t}\,|\psi\,(t)\rangle$$

which for eigenstates translates to

$$H\,|k\rangle = (\omega_k + i\delta)\,|k\rangle\,.$$

Now it is convenient to associate the infinitesimal $\delta$ with the $\omega_k$ itself, which then represents an analytic continuation of $\omega$ (the energy) into the complex plane, for now just with an infinitesimal imaginary part. Note that the sign of $+i\delta$ is associated with the fact that one is interested in the future of $|\psi\rangle$ given a certain past (some initial $|\psi_0\rangle$). This admittedly rather heuristic approach gives, however, the right idea, namely that for particles propagating forward in time, the following substitution is common and meaningful

$$\omega \to \omega + i\delta \tag{4.9}$$

and has the physical interpretation of quantum eigenstates with infinite life time and no decay which would result from other mechanisms unaccounted for such as decoherence effects. So returning to Eq. (4.7a), the following substitution is justified

$$\frac{1}{E - H_{QQ}} \to \frac{1}{E - H_{QQ} + i\delta} = \frac{1}{(E + i\delta) - H_{QQ}} \; .$$

By associating the infinitesimal with the energy, one can conveniently drop the $i\delta$ again during most of the algebra. One must keep in mind, however, that the energies actually come with a positive imaginary infinitesimal.

---

There are several ways to look at Eq. (4.6). The part $Q(E - H_{QQ})Q$ is purely projected onto the subspace $\mathcal{Q}$, and there exists a set of vectors $|\tilde{k}\rangle$ which diagonalizes the projected Hamiltonian $H_{QQ}$ such that $H_{QQ}|\tilde{k}\rangle = \varepsilon_{\tilde{k}}|\tilde{k}\rangle$; note that the $|\tilde{k}\rangle$ in general are not necessarily the eigensolutions of neither $H_0$ nor $H$. Yet by construction, the set of vectors $|\tilde{k}\rangle$ provide a unitary representation within $\mathcal{Q}$ and thus it follows that $Q|\tilde{k}\rangle = |\tilde{k}\rangle$. Substituting $Q = \sum_k |k\rangle\langle k| = \sum_{\tilde{k}} |\tilde{k}\rangle\langle\tilde{k}|$, the matrix elements with respect to the states $i, j \in \mathcal{P}$ are

$$\langle i| \, H^P_{\mathit{eff}} \, |j\rangle \equiv \left(H^P_{\mathit{eff}}\right)_{ij} = H_{ij} + \sum_k H_{i\tilde{k}} \frac{1}{E - \varepsilon_{\tilde{k}}} H_{\tilde{k}j} \tag{4.10}$$

with $H_{ij} \equiv \langle i| \, H \, |j\rangle$. So what is gained by this transformation? The inverse operator in this correction is diagonalized by the $|\tilde{k}\rangle$, and so one is left with the inverse of numbers. However, the set of $\varepsilon_{\tilde{k}}$ values represent unknown eigenvalues of an (infinite) Hilbert space still, and thus the transformation Eq. (4.10) is not very useful yet.

However, one can expand the $\varepsilon_{\tilde{k}}$ around the $\varepsilon_k$ assumed to be known. This transformation is similar to the so–called *Rayleigh–Schrödinger theory* [MYS67, pp. 16] and will give an elegant derivation of generic perturbation theory. The case $\dim(\mathcal{P}) = 1$ can be found in most text books, e.g. [MYS67, pp. 16]. For $\dim(\mathcal{P}) > 1$, however, such as is the case for (close to) degenerate perturbation theory, the Feshbach formalism provides a very clearly structured procedure to obtain the effects of a perturbation onto the effective Hamiltonian of the subspace under consideration in terms of the self–energy term $\Sigma\,(E)$.

In order to obtain the expansion in the $\varepsilon_k$, one may return to the original operator equation (4.6)

$$P\left(H + HQ\frac{1}{Q\,(E - H)\,Q}QH - E\right) P \cdot P\,|\psi\rangle = 0 \; .$$

As by convention the states $|i\rangle$ span the subspace $\mathcal{P}$, the matrix elements of the effective Hamiltonian are

$$H_{ij}^{\mathit{eff}} \equiv \langle i| \left[ H + HQ \frac{1}{Q\,(E-H)\,Q} QH \right] |j\rangle \ .$$

Now when $H$ is decomposed into $H_0 + V$ as in Eq. (4.2a), then

$$\langle i| \left[ H_0 + V + (H_0+V)\,Q \frac{1}{Q\,(E-(H_0+V))\,Q} Q\,(H_0+V) \right] |j\rangle$$

By construction, $H_0$ is diagonal in the states $|i\rangle \in \mathcal{P}$ and $|k\rangle \in \mathcal{Q}$, such that $H_0\,|n\rangle = \varepsilon_n\,|n\rangle$ with $n \in \{i,k\}$ and therefore $[H_0, P] = [H_0, Q] = 0$. Consequently, terms such as $QH_0\,|i\rangle$ vanish since $PQ = 0$ and the last equation can be simplified to

$$\begin{aligned} H_{ij}^{\mathit{eff}} &= \varepsilon_i \delta_{ij} + V_{ij} + \langle i|\, VQ \frac{1}{Q\,(E-H)\,Q} QV\,|j\rangle \qquad (4.11a) \\ &= \varepsilon_i \delta_{ij} + V_{ij} + \sum_{k,k'} V_{ik}\,\langle k|\,(E-H)_Q^{-1}\,|k'\rangle\,V_{k'j} \\ &\equiv \varepsilon_i \delta_{ij} + \Sigma_{ij}\,(E) \end{aligned}$$

with

$$\Sigma_{ij}\,(\omega) \equiv V_{ij} + \sum_{k,k' \in \mathcal{Q}} V_{ik}\,\langle k|\,(\omega - H)_Q^{-1}\,|k'\rangle\,V_{k'j} \qquad (4.11b)$$

The last part in this equation $(\omega - H)_Q^{-1}$ directly resembles Green's functions in quantum mechanics and a short introduction is given later (see Sec. 4.3, pp. 74). The series expansion in Eq. (4.24) for example can then be used to rewrite Eq. (4.11b) where care needs to be taken since $(E-H)_Q^{-1}$ is defined in the $\mathcal{Q}$ space only

$$\begin{aligned} \Sigma_{ij}\,(\omega) &= V_{ij} + \sum_{k,k'} V_{ik}\,\langle k|\,\frac{1}{\omega - (H_0)_{QQ}} \sum_{n=0}^{\infty} \left( V_{QQ} \frac{1}{\omega - (H_0)_{QQ}} \right)^n |k'\rangle\,V_{k'j} \\ &= V_{ij} + \sum_{k,k'} V_{ik}\,\langle k|\,\frac{1}{\omega - H_0} \sum_{n=0}^{\infty} \left( QVQ \cdot Q \frac{1}{\omega - H_0} Q \right)^n |k'\rangle\,V_{k'j} \\ &= V_{ij} + \sum_{k,k' \in \mathcal{Q}} V_{ik}\,\langle k|\,\frac{1}{\omega - H_0} \sum_{n=0}^{\infty} \left( QV \frac{1}{\omega - H_0} \right)^n |k'\rangle\,V_{k'j} \qquad (4.11c) \end{aligned}$$

Note that the outer $Q$'s were dropped because the outer bracket $\langle k| \ldots |k'\rangle$ enforces the projection into the $\mathcal{Q}$ space. Moreover, $H_0$ is diagonal in the $k$ vectors so that

with $[H_0, Q] = 0$ and $k \in \mathcal{Q}$

$$\begin{aligned} \langle k| \frac{1}{\omega - (H_0)_{QQ}} |k'\rangle &= \langle k| Q \frac{1}{\omega - H_0} Q |k'\rangle \\ &= \langle k| \frac{1}{\omega - H_0} |k'\rangle \\ &\equiv \langle k| G_0 |k'\rangle = \frac{1}{\omega - \varepsilon_k} \delta_{kk'} \end{aligned} \tag{4.12}$$

The remaining $Q$ in Eq. (4.11c) is essential to ensure the projection of $V$ into the $\mathcal{Q}$ space in the power series where the actual order of $V$ and $Q$ in Eq. (4.11c) does not matter.

The self–energy $\Sigma_{ij}(\omega)$ from Eq. (4.11c) is a generalization of the well–known expression for self–energy due to a perturbation $V$. It is a generalization in the sense that it is also defined for any sub–space of (finite) dimension larger than one. The connection to the well–known self–energy of the states in $\mathcal{P}$ becomes clearer when according to Eq. (4.7b) $\left(E_i - H^{\mathit{eff}}\right)|p_i\rangle = 0$ one considers the operator (Green's function)

$$G^P(\omega) \equiv \frac{1}{\omega - H^{\mathit{eff}}} = \frac{1}{\omega - \varepsilon_i \delta_{ij} - \Sigma_{ij}(\omega)}$$

If $\omega$ hits one of the eigenvalues of $H^{\mathit{eff}}$, one has a pole in the Green's function $G^P(\omega)$. Arguing in reverse, the poles of $G^P(\omega)$ therefore define the correct eigenenergies of the system where the original $\varepsilon_i$ are corrected by the self–energy term which is generated by the perturbation $V$. This is the usual definition of the self–energy.

The structure of $\Sigma_{ij}(\omega)$ in Eq. (4.11c) becomes more apparent, when the $\mathcal{Q}$'s in the series expansion are replaced by their respective $\sum_k |k\rangle\langle k|$

$$\begin{aligned} \Sigma_{ij}(\omega) &= V_{ij} + \sum_k V_{ik} \frac{1}{\omega - \varepsilon_k} V_{kj} + \sum_{k,k'} V_{ik} \frac{1}{\omega - \varepsilon_k} V_{kk'} \frac{1}{\omega - \varepsilon_{k'}} V_{k'j} \\ &\quad + \sum_{k,k',k''} V_{ik} \frac{1}{\omega - \varepsilon_k} V_{kk'} \frac{1}{\omega - \varepsilon_{k'}} V_{k'k''} \frac{1}{\omega - \varepsilon_{k''}} V_{k''j} + \ldots \end{aligned} \tag{4.13}$$

Thus the sum in Eq. (4.13) is a *sum over all possible paths* from state $i$ to state $j$ in $\mathcal{P}$ over a set of intermediate states $k$ in $\mathcal{Q}$ only. This is shown schematically in Fig. (4.1). The perturbation $V$ *mediates these virtual transitions* and the energy denominator which enters through $G_0$ weighs them according to how far or close to some $\omega \equiv E$ in the energy spectrum the intermediate states are. Eq. (4.13) also exactly corresponds to the perturbative expansion, where order after order the path is elongated accordingly by another intermediate *step* in this path formulation.

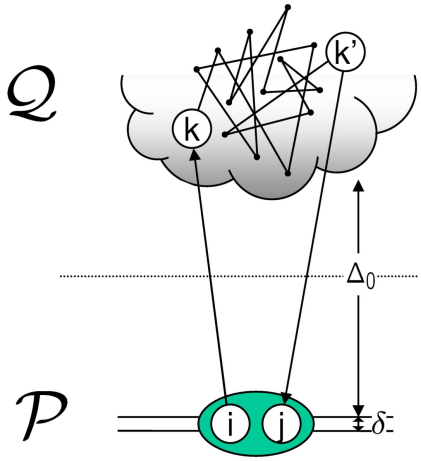


Figure 4.1: Feshbach algorithm - sum over all possible paths starting in the (finite) subspace $\mathcal{P}$ and proceeding to the remaining space $\mathcal{Q}$ for all intermediate states before coming back again the $\mathcal{P}$.

Moreover, if the $\mathcal{P}$ space is separated energetically from the $\mathcal{Q}$ space by at least $\Delta_0$ and if the perturbation $V$ is small enough in the sense $q \equiv |\max(\mathrm{eig}(V_{QQ}))| / \Delta_0 < 1$, then above series converges exponentially. And the better the decoupling of the two spaces $\mathcal{P}$ and $\mathcal{Q}$ on the energy scale (e.g the smaller the $q$), the faster is the convergence.

Summarizing, an effective finite dimensional Hamiltonian can be constructed from an initially much larger Hamiltonian using the Feshbach formalism as long as the subspace considered is sufficiently decoupled energetically from the remainder of the states. The price to pay for the formalism to be formally exact is that one gets a nonlinear system of equations to solve. This essentially is equivalent to the procedure of elimination of variables as can be seen in [PM01]. Finally, a perturbative expansion allows to construct a straightforward connection to Green's functions and their interpretation in terms of *all possible paths in Hilbert space* mediated by some perturbation $V$. The main contribution (lowest order) are determined by the shortest paths with lowest cost in energy in the intermediate states. Analyzing the resulting Green's functions with respect to their poles provides a procedure to extract the perturbed eigenenergies. For lowest order approximations, this gives a very simple and generic way to estimate the effects of a perturbation $V$ analytically. For higher order corrections and thus higher accuracy, the resulting (non–linear) eigensystem $H_P^{eff}(E)|i\rangle = E|i\rangle$ can be solved by numerical means.

## 4.3 Green's Functions

It should be noted that the Feshbach formalism introduced in the previous section does not have time–dependence in the interaction incorporated. Consequently that formalism applies to static but also adiabatic problems where a slowly turned on perturbation changes the eigenstates of the system which then can be calculated using the Feshbach formalism. For dynamical problems, where a perturbation induces transition between states, the Feshbach formalism is of limited use. However, Green's functions in quantum mechanical systems resemble very closely the structure of the Feshbach formalism where in addition, Green's functions allow to deal with time–dependent phenomena in a systematic way.

Of special interest is the transition amplitude between states for a step like perturbation where for example the external parameters of the quantum system are *switched* from one configuration to another. It turns out that the Feshbach formalism gives the correct answer for instantaneous transitions as will be shown at the end of this section (see pp. 4.3.4). On the other hand, in real physical systems transitions always happen in a finite time window. Consequently, a more rigorous formalism to treat dynamical behavior and transitions between states is desirable, and because of the structural similarity of the Feshbach formalism with Green's functions, the latter ones are the obvious choice at hand.

In the following, Green's functions will be briefly reviewed in the context of non relativistic quantum mechanics. Green's functions are formally introduced as the solution to a $\delta$ perturbation in a space and time point (a $\delta$ *source*) for a differential equation which in given case is the Schrödinger equation [Har79, pp. 217]

$$\left(i\frac{\partial}{\partial t} - H\right)\psi\left(r,t\right) = 0$$

in the sense

$$\left(i\frac{\partial}{\partial t} - H\right)G_{\pm}\left(r,r';t,t'\right) = \delta\left(r-r';t-t'\right) \tag{4.14}$$

For convenience, Planck's constant $\hbar$ is set to 1. Assuming the Hamiltonian $H$ is time independent, Eq. (4.14) becomes translational invariant in time and thus the Green's function $G_{\pm}$ must be a function of the difference $t-t'$ only. The Hamiltonian's complete set of eigenfunctions is $\psi_k\left(r\right) \equiv \langle r|k\rangle$ and so

$$H\left|k\right\rangle = \varepsilon_k\left|k\right\rangle$$

with the completeness relation $\sum_k |k\rangle\langle k| = 1$ or equivalently

$$\sum_k \psi_k^*(r')\,\psi_k(r) \equiv \sum_k \langle r|k\rangle\langle k|r'\rangle = \langle r|\left(\sum_k |k\rangle\langle k|\right)|r'\rangle = \langle r|r'\rangle = \delta(r-r')$$

where the sum extends over the whole Hilbert space. For a formal solution for the Green's function in Eq. (4.14), Eq. (4.14) is Fourier transformed in time ($t \to \omega$), while in space it is transformed into the set of eigenfunctions $|k\rangle$, into *k–space* so to speak ($|r\rangle \to |k\rangle$ where $k$ stands for a set of quantum numbers which not necessarily has to be the plane wave expansion in the usual terminology)

$$(\omega - \varepsilon_k \pm i\delta)\, G_\pm(k,k';\omega) = \delta_{kk'} \cdot 1$$

with the solution

$$G_\pm(k,k';\omega) = \frac{1}{\omega - \varepsilon_k \pm i\delta}\delta_{kk'} \tag{4.15}$$

and $\delta \equiv 0^+$ being a positive infinitesimal. Note that the $\pm i\delta$ in the last equation directly follows from the $\delta$ function in the time domain of Eq. (4.14) and consequently from a step in the Green's function. To see this, the last equation is back transformed into the time domain

$$\begin{aligned} G_\pm(k,k';t-t') &= \frac{1}{2\pi}\int_{-\infty}^{\infty} G_\pm(k,k';\omega)\; e^{-i\omega(t-t')}d\omega \\ &= \frac{1}{2\pi}\int_{-\infty}^{\infty} \frac{\delta_{kk'}}{\omega - \varepsilon_k \pm i\delta}\; e^{-i\omega(t-t')}d\omega \end{aligned}$$

Here, the only pole at $\omega^* \equiv \varepsilon_k \mp i\delta$ determines the integral using the residue theorem: for $t > t'$ ($t < t'$), the analytic continuation of $\omega$ into the complex plane is done in the lower (upper) half, respectively. Whether or not the integral gives a contribution is then determined by whether or not the upper (lower) half of the complex plane contains the pole $\omega^*$

$$\begin{aligned} G_\pm(k,k';t-t') &= \frac{-1}{2\pi}\delta_{kk'}e^{-i(\varepsilon_k \mp i\delta)(t-t')}2\pi i\vartheta_\pm(t-t') \\ &= -i\;\delta_{kk'}e^{-i(\varepsilon_k \mp i\delta)(t-t')}\vartheta_\pm(t-t') \end{aligned} \tag{4.16}$$

with the step functions

$$\vartheta\left(t-t'\right) \equiv \vartheta_{+}\left(t-t'\right) = \begin{cases} +1 & \text{if } t > t' \\ 0 & \text{if } t < t' \end{cases} \tag{4.17a}$$

$$\vartheta_{-}\left(t-t'\right) = \begin{cases} 0 & \text{if } t > t' \\ -1 & \text{if } t < t' \end{cases} \tag{4.17b}$$

Similarly, transforming back from $k$ space to $r$ space, one obtains

$$\begin{aligned} G_{\pm}\left(r,r';t-t'\right) &= \sum_{k,k'} \langle r|k\rangle \cdot G_{\pm}\left(k,k';t-t'\right) \cdot \langle k'|r'\rangle \\ &= -i\sum_{k} \psi_{k}^{*}\left(r'\right)\psi_{k}\left(r\right) e^{-i(\varepsilon_{k}\mp i\delta)(t-t')}\vartheta_{\pm}\left(t-t'\right) \\ &= -i\sum_{k} \psi_{k}^{*}\left(r'\right)\psi_{k}\left(r\right) e^{-i\varepsilon_{k}(t-t')}\vartheta_{\pm}\left(t-t'\right) \end{aligned}$$

From this, it follows straightforwardly that

$$\begin{aligned} \psi\left(r,t\right) &= \begin{cases} +i\int\limits_{-\infty}^{\infty} d^{3}r'\; G_{+}\left(r,r';t-t'\right)\psi\left(r',t'\right) & \text{if } t > t' \\ 0 & \text{if } t < t' \end{cases} \\ \psi\left(r,t\right) &= \begin{cases} 0 & \text{if } t > t' \\ -i\int\limits_{-\infty}^{\infty} d^{3}r'\; G_{-}\left(r,r';t-t'\right)\psi\left(r',t'\right) & \text{if } t < t' \end{cases} \end{aligned} \tag{4.18}$$

since the integral decomposes the $\psi$ at time $t'$ into the eigenstates of $H$ and adds the correct phase for the time evolution. Now Eq. (4.18) suggests the following intuitive interpretation of the Green's functions $G_{\pm}$: $G_{+}$ *propagates* the state $\psi$ at an earlier time $t' < t$ forward to time $t$; there is no *back–propagation* since $G_{+}$ is zero for $t < t'$. In this sense causality holds and $G_{+}$ is called the *retarded* Green's function. On the other hand, $G_{-}$ takes a state $\psi$ at a time $t'$ and propagates it back in time, and so is called the *advanced* Green's function. Overall, the Green's functions above *represent an integration of the Schrödinger equation over time* [Har79, pp. 217].

### 4.3.1 Resolvent Operator

The Green's function in Eq. (4.15) can be written as

$$G_{\pm}\left(k,k';\omega\right) = \langle k|\,\frac{1}{\omega - H \pm i\delta}\,|k'\rangle$$

The operator $(\omega - H \pm i\delta)^{-1}$ sandwiched between the $k$'s is called the *resolvent operator* [Hew93, pp. 173], but will be also referred to as the Green's function (operator) in the following discussion. The Hamiltonian is given as $H = H_0 + V$ being split into the unperturbed systems Hamiltonian $H_0$, whose eigenstates are known, and the non–trivial perturbation $V$ with $[H_0, V] \neq 0$. Then the Green's function operators are introduced as

$$G_0^{\pm}(\omega) \equiv \frac{1}{\omega - H_0 \pm i\delta} \equiv \frac{1}{\omega^{\pm} - H_0} \equiv G_0(\omega^{\pm}) \tag{4.19a}$$

$$G^{\pm}(\omega) \equiv \frac{1}{\omega - H \pm i\delta} \equiv \frac{1}{\omega^{\pm} - (H_0 + V)} \equiv G(\omega^{\pm}) \tag{4.19b}$$

with $\omega^{\pm} \equiv \omega \pm i\delta$ and $\delta \equiv 0^+$ a positive infinitesimal related to causality as indicated above (see also the remark on pp. 69, and Eq. (4.9) therein). Note that $G^+_{(0)}$ and $G^-_{(0)}$ are complex conjugates of each other since

$$\left[G^-_{(0)}\right]^+ = \left[\left(\omega - H_{(0)} - i\delta\right)^{-1}\right]^+ = \left[\left(\omega - H_{(0)} - i\delta\right)^+\right]^{-1} = G^+_{(0)}$$

since for any operator $A$, assuming that its inverse exists, the complex conjugate operation can be flipped with the inverse operation ($[A^+]^{-1} = [A^{-1}]^+$ since $A^+ (A^{-1})^+ = (A^{-1}A)^+ = 1$).

Furthermore, the operators $G$ and $G_0$ are related to each other by the following identities (Dyson equation)

$$G = G_0 + G_0 V G = G_0 + G V G_0 \tag{4.20}$$

Proof: Assuming $G$ and $G_0$ exist, then they have an inverse by construction, and so

$$\begin{aligned} G &= G_0 + G_0 V G \iff (1 - G_0 V)\, G = G_0 \iff \\ G &= (1 - G_0 V)^{-1} G_0 = \left[G_0^{-1} (1 - G_0 V)\right]^{-1} \\ &= \left(G_0^{-1} - V\right)^{-1} = \left(\omega^{\pm} - H_0 - V\right)^{-1} \end{aligned}$$

and similarly

$$\begin{aligned} G &= G_0 + G V G_0 \iff G\,(1 - V G_0) = G_0 \iff \\ G &= G_0\,(1 - V G_0)^{-1} = \left[(1 - V G_0)\, G_0^{-1}\right]^{-1} \\ &= \left(G_0^{-1} - V\right)^{-1} = \left(\omega^{\pm} - H_0 - V\right)^{-1} . \end{aligned}$$

■

Due to the equivalence of left–inverse and right–inverse operators ($AA^{-1} = A^{-1}A =$

1) and the definition of the Green's functions as inverse operators, it follows from Eqs. (4.19) that

$$\left(\omega^{\pm} - H_{(0)}\right) G^{\pm}_{(0)}(\omega) = G^{\pm}_{(0)}(\omega) \left(\omega^{\pm} - H_{(0)}\right) = 1 \ . \tag{4.21}$$

This can also be seen explicitly being aware that $G^{+}$ and $G^{-}$ are complex conjugates of each other

$$\begin{aligned} \left[\left(\omega - H_{(0)} \pm i\delta\right) G^{\pm}_{(0)}(\omega)\right]^{+} &= \left(G^{\pm}_{(0)}\right)^{+} \left(\omega - H_{(0)} \pm i\delta\right)^{+} \\ &= G^{\mp}_{(0)} \left(\omega - H_{(0)} \mp i\delta\right) = 1 \end{aligned}$$

Thus the order of the $G$'s to the left or to the right on the RHS of Eq. (4.21) does not matter. Furthermore, the '$\pm$' may thus me dropped safely and the infinitesimal $\pm i\delta$ is incorporated into the $\omega$

$$G_{(0)}(\omega) \left(\omega - H_{(0)}\right) = \left(\omega - H_{(0)}\right) G_{(0)}(\omega) = 1 \tag{4.22}$$

With this, a simple alternative proof of Eq. (4.20) can be given as follows:
Proof (2): multiplying Eq. (4.21) for $G$ with $G_0$ from the left

$$G_0 \left[\omega - (H_0 + V)\right] G = G_0 \ \Leftrightarrow \ G \cdot 1 - G_0 V G = G_0 \Leftrightarrow G = G_0 + G_0 V G$$

and similarly

$$G \left[\omega - (H_0 + V)\right] G_0 = G_0 \ \Leftrightarrow \ G \cdot 1 - G V G_0 = G_0 \Leftrightarrow G = G_0 + G V G_0$$

■.

Iterating $G$ in Eq. (4.20) results in the series

$$\begin{aligned} G &= G_0 + G_0 V G_0 + G_0 V G_0 V G_0 + \ldots && \text{(4.23a)} \\ &= G_0 \sum_{n=0}^{\infty} (V G_0)^n \equiv G_0 \frac{1}{1 - V G_0} && \text{(4.23b)} \\ &= \sum_{n=0}^{\infty} (G_0 V)^n G_0 \equiv \frac{1}{1 - G_0 V} G_0 && \text{(4.23c)} \end{aligned}$$

The formal solutions of the series provided in Eqs. (4.23b) and (4.23c) are again consistent with Eq. (4.20). The iterative series in Eq. (4.23a) can be written substituting for $G_0$

$$G = \frac{1}{\omega - H_0} \sum_{n=0}^{\infty} \left(V \frac{1}{\omega - H_0}\right)^n \tag{4.24}$$

### 4.3.2 Green's Function Operator

Consider again Eq. (4.14)

$$\left(i\frac{\partial}{\partial t} - H\right) G_{\pm}(x, x') = \delta^{(4)}(x - x')$$

which is obviously written in the specific representation of space and time with $x \equiv (t, r)$. In this basis, the differential operator is local including local derivatives in the sense

$$\langle x| \left(i\frac{\partial}{\partial \hat{t}} - \hat{H}\right) |x'\rangle = \delta^{(4)}(x - x') \left(i\frac{\partial}{\partial t} - H(x)\right)$$

and the Green's function $G_{\pm}(x, x') \equiv \langle x|G_{\pm}|x'\rangle$ is a number, namely the matrix element between the states $|x\rangle \equiv |r, t\rangle$ and $|x'\rangle \equiv |r', t'\rangle$. However, above differential equation can be written independent of any basis set in terms of a much more compact and convenient operator equation

$$\langle x| \Big( \underbrace{i\frac{\partial}{\partial \hat{t}}}_{\equiv T} - \hat{H} \Big) \Big( \underbrace{\sum_{x''} |x''\rangle \langle x''|}_{=1} \Big) G_{\pm} |x'\rangle = \langle x| \, 1 \, |x'\rangle$$

from which the operator equation follows

$$(T - H)\, G = 1 \tag{4.25}$$

where every term is an operator (a tensor) without explicitly marking it as such. Note that the operator $T$ is *not* hermitian, since with $|\psi\rangle = \sum_k c_k(t) |k\rangle$ the expectation value is given as $\langle \psi_1| T |\psi_2\rangle = \sum_k c_{1k}^* \left(i\frac{\partial}{\partial t}\right) c_{2k} \neq (T|\psi_1\rangle)^+ |\psi_2\rangle$ for arbitrary wavefunctions $|\psi_1\rangle$ and $|\psi_2\rangle$. Moreover, if one includes the integration over time, then

$$\int_{-\infty}^{\infty} dt \; \psi_1^* \left(i\frac{\partial}{\partial t}\psi_2\right) = i \; \psi_1^* \psi_2 |_{-\infty}^{\infty} - \int_{-\infty}^{\infty} dt \; \left(-i\frac{\partial}{\partial t}\psi_1\right)^* \psi_2$$

In contrast to the spatial case, however, where for localized wave packets the boundary term can has not contribution and vanishes, the wave function always has norm one in the time domain and therefore never vanishes. Consequently, the boundary term in the last equation from the partial integration does not vanish which would be necessary for the operator $T$ to be hermitian.

So with $T$ not being hermitian, $G = (T - H)^{-1}$ cannot be hermitian either. This becomes obvious, once the infinitesimal $\pm i\delta$ is introduced as has been done previously, $(T - H \pm i\delta)\, G^{\pm} = 1$. This makes $G^+$ and $G^-$ complex conjugates of each other but

not of themselves. Even though $\delta \equiv 0^+$ is an infinitesimal, this $\pm i\delta$ is crucial for the time dependence of $G$ and is consistently associated with the $T$ operator ($T \to T \pm i\delta$) which is consequently not hermitian.

### Time Independent Hamiltonian

If $H$ is independent of time, then the time–dependent definition of the Green's function

$$\left(i\frac{\partial}{\partial\tau} - H\right) G(\tau) = \delta(\tau) \tag{4.26a}$$

is also easily Fourier transformed

$$(\omega - H \pm i\delta)\, G(\omega) = 1 \tag{4.26b}$$

The term $\pm i\delta$ in the Fourier transform follows from the arguments already given previously (Sec. 4.3). Basically it comes from the way the boundary condition is chosen (e.g. retarded or advanced), as will be explicitly seen in a moment. In general, the Hamiltonian $H$ is a smooth function of its arguments and the only differential that occurs in it, is the second order derivative with respect to the coordinates $p^2 \sim \partial^2/\partial x_i^2$. This structure right away implies the following for the solution of the differential Eq. (4.26a): first, the Green's function must be smooth in the spatial coordinates, and second, it must have a discontinuity in the time domain at $\tau = 0$. The homogenous solution of the differential Eq. (4.26a) is $Ae^{-iH\tau}$ with $A$ being some constant. This solution holds for $\tau < 0$ and for $\tau > 0$. The two solutions must be matched at $\tau = 0$ due to the inhomogeneous term on the RHS of Eq. (4.26a)

$$\int_{-\varepsilon}^{+\varepsilon} d\tau \left(i\frac{\partial}{\partial\tau} - H\right) G(\tau) = \int_{-\varepsilon}^{+\varepsilon} d\tau \delta(\tau)$$

which leads to the discontinuity at $\tau = 0$

$$\begin{aligned} i\left(G\left(0^+\right) - G\left(0^-\right)\right) &= 1 \\ G\left(0^+\right) &= G\left(0^-\right) - i \end{aligned} \tag{4.27}$$

Finally, setting the constant $G(0^-) = 0$ out of causality considerations, the resulting solution for this Green's function is

$$G^+(\tau) \equiv -i\vartheta(\tau)\, e^{-iH\tau} \tag{4.28}$$

with the step function $\vartheta(\tau)$ as in Eq. (4.17a), consistent with Eq. (4.16). Thus the discontinuity in the time domain manifests itself as a step function at the origin $\tau = 0$. Applying Eq. (4.28) onto an arbitrary state vector $|\psi\rangle$ at time $t_1$, gives

$$iG^{+}(t_2 - t_1)|\psi(t_1)\rangle = \begin{cases} e^{-iH(t_2-t_1)}|\psi(t_1)\rangle = |\psi(t_2)\rangle & \text{if } t_2 \geq t_1 \\ 0 & \text{if } t_2 < t_1 \end{cases}$$

Again it makes sense to say that the Green's function $G^{+}(\tau)$ *propagates the solution forward in time*, as already indicated in the text following Eq. (4.18). Since the (retarded) Green's function contains the Hamiltonian, it already has all the information needed to predict the wave function.

Alternatively, one may choose $G(0^{+}) = 0$ in Eq. (4.27) instead. Then the Green's function becomes

$$G^{-}(\tau) \equiv +i\vartheta(-\tau)\, e^{-iH\tau} \equiv -i\vartheta_{-}(\tau)\, e^{-iH\tau} \tag{4.29}$$

consistent with Eq. (4.16). It represents the (advanced) Green's function $G^{-}(\tau)$

$$-iG^{-}(t_2 - t_1)|\psi(t_1)\rangle = \begin{cases} e^{-iH(t_2-t_1)}|\psi(t_1)\rangle = |\psi(t_2)\rangle & \text{if } t_2 \leq t_1 \\ 0 & \text{if } t_2 > t_1 \end{cases}$$

where special attention should be drawn to the alternating signs of the two solutions, namely the retarded and the advanced Green's functions.

### Time Dependent Hamiltonian

For a time–dependent Hamiltonian the situation becomes significantly more involved. Since the time–dependence is given explicitly from the exterior, this clearly is related to the interaction with an external system over time and thus the translational symmetry with respect to time is broken. Consequently, the Green's function does in general not depend just on the difference in the two times involved anymore. Equation (4.26a) reads

$$\left(i\frac{\partial}{\partial\tau} - H(\tau)\right) G(\tau) = \delta(\tau) \tag{4.30}$$

and the Fourier transform cannot be carried out as simple as in Eq. (4.26b). In order to obtain the homogenous solution for $\tau \neq 0$, Eq. (4.30) is written as

$$G^{+}(\tau) - G^{+}(0^{+}) = \int_{0^{+}}^{\tau} d\tau' \cdot \frac{\partial}{\partial\tau'} G^{+}(\tau') = -i\int_{0^{+}}^{\tau} d\tau' H(\tau')\, G^{+}(\tau')$$

which can be iterated using the initial condition $G^{+}\left(0^{+}\right)=1$

$$G^{+}(\tau)=1+\int_{0^{+}}^{\tau}d\tau'\left(-iH\left(\tau'\right)\right)+\int_{0^{+}}^{\tau}d\tau'\left(-iH\left(\tau'\right)\right)\int_{0^{+}}^{\tau'}d\tau''\left(-iH\left(\tau''\right)\right)+\ \ldots$$

Note that the terms on the RHS are time ordered, i.e. that the $n$–th term $H\left(\tau'\right)H\left(\tau''\right)\ldots H\left(\tau^{(n)}\right)$ has $\tau'\geq\tau''\geq\ldots\geq\tau^{(n)}$; this restriction can be lifted *symbolically* by taking all integrals up to $\tau$ and by introducing the time ordering operator $T$ and correcting for the consequent overcounting resulting from all permutations of $\tau',\tau'',\tau'''\ldots$ of $n$ variables which equals $n!$)

$$\begin{aligned}G(\tau) &= 1+\int_{0^{+}}^{\tau}d\tau'\left(-iH\left(\tau'\right)\right)+\frac{1}{2!}T\left[\int_{0^{+}}^{\tau}d\tau'\left(-iH\left(\tau'\right)\right)\int_{0^{+}}^{\tau}d\tau''\left(-iH\left(\tau''\right)\right)\right]+\ \ldots\\ &= T\left[\sum_{n=0}^{\infty}\frac{1}{n!}\left(-i\int_{0^{+}}^{\tau}d\tau' H\left(\tau'\right)\right)^{n}\right]\equiv T\left[\exp\left(-i\int_{0^{+}}^{\tau}d\tau' H\left(\tau'\right)\right)\right]\end{aligned}$$

For a non–trivial time dependence of the Hamiltonian, the time ordering $T$ is essential since the Hamiltonian does not commute with itself when taken at different times, i.e. $\left[H\left(\tau'\right),H\left(\tau''\right)\right]\neq 0$ for $\tau'\neq\tau''$.

### 4.3.3 Notes on Energies and Temporal Fourier Transform

The Green's function $G$ has been defined above in several different yet equivalent ways. Stripping off any basis representation, the pure operator equation is given by Eq. (4.25), $(T-H)\,G=1$ with $T\equiv i\frac{\partial}{\partial t}$. This section is meant to give a few interesting details on the change of the basis representation in the time domain to the temporal Fourier transform ($\omega$ space). One may start with the general operator case writing out the time–dependence explicitly assuming a time independent Hamiltonian first (see Eqs. 4.26)

$$\left(i\frac{\partial}{\partial t_2}-H\right)G(t_2-t_1)=\delta\left(t_2-t_1\right) \tag{4.31}$$

or explicitly term by term,

$$\begin{aligned}\langle t_2|\,TG\,|t_1\rangle &= i\frac{\partial}{\partial t_2}G(t_2-t_1)\\ \langle t_2|\,HG\,|t_1\rangle &= HG(t_2-t_1)\end{aligned}$$

$$\langle t_2|\, 1\, |t_1\rangle \;=\; \delta\left(t_2 - t_1\right)$$

In $\omega$ representation, Eq. (4.31) becomes

$$\left(\omega - H\right) G(\omega) = 1$$

derived from the individual terms

$$\begin{aligned}
\langle \omega_2|\, TG\, |\omega_1\rangle &= \omega_2 G\left(\omega_2\right) \cdot \delta\left(\omega_2 - \omega_1\right) \\
\langle \omega_2|\, HG\, |\omega_1\rangle &= HG\left(\omega_2\right) \cdot \delta\left(\omega_2 - \omega_1\right) \\
\langle \omega_2|\, 1\, |\omega_1\rangle &= \delta\left(\omega_2 - \omega_1\right)
\end{aligned}$$

after dropping the overall $\delta\left(\omega_2 - \omega_1\right)$ and replacing $\omega_2$ by $\omega$. These terms are derived explicitly as follows

$$\begin{aligned}
&\langle \omega_2|\, \hat{H} G\left(\hat{t}_2 - \hat{t}_1\right) |\omega_1\rangle = \\
&= H \int\limits_{-\infty}^{\infty} \frac{dt_1}{2\pi} \int\limits_{-\infty}^{\infty} \frac{dt_2}{2\pi} e^{+i\omega_2 t_2} \left( \int\limits_{-\infty}^{\infty} d\omega'' e^{-i\omega''(t_2 - t_1)} G\left(\omega''\right) \right) e^{-i\omega_1 t_1} \\
&= H \int\limits_{-\infty}^{\infty} d\omega'' G\left(\omega''\right) \delta\left(\omega_2 - \omega''\right) \delta\left(\omega'' - \omega_1\right) \\
&= HG\left(\omega_2\right) \cdot \delta\left(\omega_2 - \omega_1\right)
\end{aligned}$$

and similarly

$$\begin{aligned}
&\langle \omega_2|\, i \frac{\partial}{\partial \hat{t}_2} G\left(\hat{t}_2 - \hat{t}_1\right) |\omega_1\rangle = \\
&= \frac{1}{2\pi} \int\limits_{-\infty}^{\infty} dt_1 \frac{1}{2\pi} \int\limits_{-\infty}^{\infty} dt_2 e^{+i\omega_2 t_2} \left( i \frac{\partial}{\partial t_2} \int\limits_{-\infty}^{\infty} d\omega'' e^{-i\omega''(t_2 - t_1)} G\left(\omega''\right) \right) e^{-i\omega_1 t_1} \\
&= \int\limits_{-\infty}^{\infty} d\omega'' \omega'' G\left(\omega''\right) \delta\left(\omega_2 - \omega''\right) \delta\left(\omega'' - \omega_1\right) \\
&= \omega_2 G\left(\omega_2\right) \cdot \delta\left(\omega_2 - \omega_1\right)
\end{aligned}$$

$$\begin{aligned}
&\langle \omega_2|\, \delta\left(\hat{t}_2 - \hat{t}_1\right) |\omega_1\rangle = \\
&= \int\limits_{-\infty}^{\infty} \frac{dt_1}{2\pi} \int\limits_{-\infty}^{\infty} \frac{dt_2}{2\pi} e^{+i\omega_2 t_2} \left( \int\limits_{-\infty}^{\infty} d\omega'' e^{-i\omega''(t_2 - t_1)} \cdot 1 \right) e^{-i\omega_1 t_1}
\end{aligned}$$

$$= \int_{-\infty}^{\infty} d\omega'' \delta(\omega_2 - \omega'') \delta(\omega'' - \omega_1)$$
$$= 1 \cdot \delta(\omega_2 - \omega_1)$$

For a time–dependent Hamiltonian, Eq. (4.31) must be replaced by

$$\left( i\frac{\partial}{\partial t_2} - H(t_2) \right) G(t_2, t_1) = \delta(t_2 - t_1) \tag{4.32}$$

derived from

$$\langle t_2 | TG | t_1 \rangle + \int dt' \langle t_2 | H | t' \rangle \langle t' | G | t_1 \rangle = \langle t_2 | 1 | t_1 \rangle$$

Due to the explicit appearance of $t_2$ in the Hamiltonian, the translational invariance in time is broken and, therefore, $G$ can no longer be written just as a function of the difference of $t_1$ and $t_2$ as already mentioned. Subsequently, in Fourier space, $G$ is not diagonal anymore and one must also keep two frequencies, $G = G(\omega_2, \omega_1)$, with the interpretation that an initial state at $\omega_1$ can propagate into a final state at $\omega_2$ with the probability amplitude given by $G(\omega_2, \omega_1)$. Since $\omega_2$ in general is unequal to $\omega_1$, an excitation or relaxation due to the external interaction included in $H$ can take place.

For a time–dependent Hamiltonian, the exact Fourier transform of Eq. (4.32) does not have the simple structure of the time independent case, and so a convenient approach is to pack all time–dependence of the Hamiltonian related to the external interaction into a perturbation such that $H = H_0 + V(t)$. Stripping off all spatial and temporal representations, the *pure* operator expression for the Green's function is given by Eq. (4.25), $(T - H)\, G = 1$. With the definitions $(T - H_{(0)}) G_{(0)} = 1$ similar to Sec. 4.3.1 (p. 76) or Sec. 4.3.2 (p. 79), this leads to

$$G = G_0 + G_0 V G = G_0 + G V G_0$$

As outlined previously, the total Green's function $G$ can be evaluated by iteration using $G_0$ and $V$ only. The structure of $G_0$ is known and since it is based on the time independent $H_0$, its Fourier decomposition is given by

$$\langle \omega | G_0 | \omega' \rangle = G_0(\omega) \delta(\omega - \omega')$$

i.e. it is diagonal and therefore energy preserving. Moreover, since the potential $V(t)$ is a regular function in time, its exact operator form is $\langle t | V | t' \rangle = V(t) \delta(t - t')$ with its Fourier transform $V(\omega, \omega')$ equal to $V(\omega - \omega')$. This implies for the Fourier

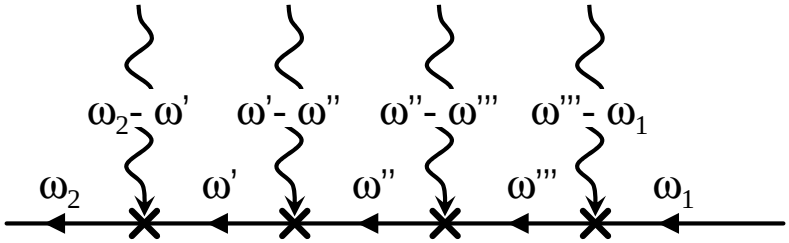


Figure 4.2: Green's function as propagator in time in Fourier representation.

decomposition of $G$

$$
\begin{aligned}
G(\omega',\omega) &= G_0(\omega)\,\delta(\omega'-\omega) + G_0(\omega')\int_{-\infty}^{\infty} d\omega'' V(\omega'-\omega'')\,G(\omega'',\omega) \\
&\equiv \quad \longrightarrow\!\!- \quad + \quad \longrightarrow\!\!\times\!\!\Longrightarrow\!\!- \\
&= G_0(\omega')\,\delta(\omega'-\omega) \;+\; G_0(\omega')\,V(\omega'-\omega)\,G_0(\omega) \\
&\quad + G_0(\omega')\int_{-\infty}^{\infty} d\omega'' V(\omega'-\omega'')\,G_0(\omega'')\,V(\omega''-\omega)\,G_0(\omega) \;+\; \ldots \\
&\equiv \quad \longrightarrow\!\!- \quad + \quad \longrightarrow\!\!\times\!\!\longrightarrow\!\!- \quad + \quad \longrightarrow\!\!\times\!\!\longrightarrow\!\!\times\!\!\longrightarrow\!\!- \quad + \ldots
\end{aligned}
\tag{4.33}
$$

The structure of Eq. (4.33) is very intuitive: every insertion of the potential $V$ can be considered a node in a linear diagram as indicated schematically by the diagrams in Eq. (4.33) and more visually in Fig. (4.2): at each node, the frequencies (energies) are conserved in the sense that the difference between incoming and outgoing frequency is accounted for by an external leg that is linked to the external interaction $V(t)$.

The transformation of Eq. (4.33) back to real time complicates things somewhat. Even though it may seem that the single pole of $G_0(\omega)$ would make integration simple using complex contour integration, the time–dependence of the perturbation $V(t)$ comes into play: only for a few very explicit cases for the shape of $V(\omega)$ the integrals can be done.

An example is the case $V(\omega) = const$, which is equivalent to applying the perturbation at one single point in time $V(t) = V_0\ \delta(t - t_0)$. This perturbation is maximally non–adiabatic in that it provides energy for all possible transitions in the system. Note, furthermore, that the strength $V_0$ of this $\delta$ perturbation is dimension-

less ($\hbar = 1$). The typical emerging integrals from Eq. (4.33) can be easily evaluated

$$\frac{1}{2\pi}\int_{-\infty}^{\infty} d\omega\; e^{\pm i\omega t}\frac{1}{\omega-\varepsilon_k+i\delta} = -i\vartheta\left(\mp t\right)e^{\pm i\varepsilon_k t} \tag{4.34a}$$

$$\int_{-\infty}^{\infty} d\omega\; \frac{1}{\omega-\varepsilon_k+i\delta} = -i\pi \tag{4.34b}$$

with the step function $\vartheta\left(\tau\right)$ as in Eq. (4.17a). The first integral was already calculated in Sec. 4.3 (pp. 74), and the last equation follows directly from the identity

$$\frac{1}{\omega-\varepsilon_k+i\delta} = P\left(\frac{1}{\omega-\varepsilon_k}\right) - i\pi\delta\left(\omega-\varepsilon_k\right) \tag{4.34c}$$

where $P\left(\;\right)$ stands for the principal value. With $t\to-\infty$ and $t'\to+\infty$, the propagator (Green's function) for this $\delta$ like perturbation becomes

$$\begin{aligned}
&G^{\delta}_{k'k}\left(t',t\right) \equiv -i\delta_{k'k}e^{-i\varepsilon_k(t'-t)} \\
&+\int_{-\infty}^{\infty}\frac{d\omega}{2\pi}\;e^{i\omega t}\int_{-\infty}^{\infty}\frac{d\omega'}{2\pi}\;e^{-i\omega' t'}\;* \\
&\frac{1}{\omega'-\varepsilon_{k'}+i\delta}\left(V^0_{k'k}+V^0_{k'k''}\left[\int_{-\infty}^{\infty}d\omega''\frac{1}{\omega''-\varepsilon_{k''}+i\delta}\right]V^0_{k''k}+\;\;\ldots\right)\frac{1}{\omega-\varepsilon_k+i\delta}
\end{aligned}$$

and consequently

$$\begin{aligned}
G^{\delta}_{k'k}\left(t',t\right) &= \left(-i\delta_{kk'}-V^0_{k'k}+i\pi\sum_{k''}V^0_{k'k''}V^0_{k''k}+\;\;\ldots\right)e^{-i(\varepsilon_{k'}t'-\varepsilon_k t)} \\
&= \langle k'|-i\mathbf{1}-V^0+i\pi V^0V^0+\;\;\ldots|k\rangle\;\;e^{-i(\varepsilon_{k'}t'-\varepsilon_k t)}.
\end{aligned} \tag{4.35}$$

From dimensional analysis, $V^0_{k'k''}$ has to be dimensionless, as is indeed the case. Starting with an initial state $k$, the perturbation will mediate transitions to other states $k'$ with probability amplitudes $G_{k'k}$. Thus the total conditional transition probability is given to lowest order by

$$P\left(k|k'\right) \equiv \left|G_{k'k}\right|^2 \approx \left|V^0_{k'k}\right|^2. \tag{4.36}$$

Since the perturbation is maximally non–adiabatic as mentioned above, all transitions

with any cost in energy are allowed, weighted only by the matrix elements $V^0_{k'k}$. The energy difference for every transition is provided by the external perturbation.

For an arbitrary smooth perturbation potential acting over a *finite* time, there is in general no analytic solution to above integrals. The integrands depend on the analytic function $V_{k'k}(\omega' - \omega)$ which itself has a set of unknown poles

$$G_{k'k}(t', t) \equiv \delta_{k'k}\varepsilon_k e^{-i\varepsilon_k(t'-t)} + \int_{-\infty}^{\infty}\frac{d\omega}{2\pi}e^{i\omega t}\int_{-\infty}^{\infty}\frac{d\omega'}{2\pi}e^{-i\omega' t'}\frac{1}{\omega - \varepsilon_k + i\delta}V_{k'k}(\omega - \omega')\frac{1}{\omega' - \varepsilon_{k'} + i\delta} + \ \ldots \tag{4.37}$$

Thus the application of the residue theorem depends on the very specific *shape* of the perturbation potential. The zeroth order term still is trivial, but already the first order term contains an integral which can not be solved right away. To lowest order, one may neglect the analytic structure of $V_{k'k}(\omega' - \omega)$ though and just consider the poles of the free Green's function. Then the Green's function becomes

$$G_{k'k}(t', t) \approx \delta_{k'k}\varepsilon_k e^{-i\varepsilon_k(t'-t)} + e^{-i(\varepsilon_{k'}t' - \varepsilon_k t)} * \left(V_{k'k}(\varepsilon_{k'k}) + \sum_{k''}\int_{-\infty}^{\infty} d\omega'' V_{k'k''}(\varepsilon_{k'k''})\frac{1}{\omega'' - \varepsilon_{k''} + i\delta}V_{k''k}(\varepsilon_{k''k}) + \ \ldots\right) \tag{4.38}$$

where $\omega_{k'k} \equiv \varepsilon_{k'} - \varepsilon_k$. What does it mean to *neglect the analytic structure of* $V_{k'k}(\omega)$ and what is the error one makes? For this, consider the specific example where the perturbation has the shape of a Lorenzian in $\omega$ space, i.e. $V_{k'k}(\omega) = V^0_{k'k}\omega_0/(\omega^2 + \omega_0^2)$ which corresponds to a perturbation $V_0$ first exponentially growing and then exponentially decaying in time. $V_{k'k}(\omega)$ has two poles at $\omega^* = \pm i\omega_0$ which have to be considered in the contour integral over $\omega$. Therefore, in above Eq. (4.38), additional terms such as

$$V^0_{k'k}\frac{1}{\omega_0 - \varepsilon_k}\frac{\omega_0}{2\omega_0}e^{-i\omega_0 t} \sim \frac{V^0_{k'k}}{\omega_0 - \varepsilon_k}e^{-i\omega_0 t}$$

have been neglected. If $\omega_0$ is much larger than the other relevant frequencies $\varepsilon_k$, then this just adds a small and rapidly oscillating term which, indeed, may be averaged and neglected. In the limit $\omega_0 \to \infty$, the frequency domain is infinitely spread and the perturbation becomes a $\delta$ function in real space again; in this limit, the previous case of Eq. (4.35) is recovered, yet with the more specific information for transition probabilities

$$P(k|k') \equiv |G_{k'k}|^2 \approx |V_{k'k}(\varepsilon_{k'k})|^2 \ . \tag{4.39}$$

This has the very intuitive interpretation, that the transition to state $k'$ given an initial state $k$ is provided by the matrix element $V_{k'k}$ evaluated at frequency $\omega_{k'k} \equiv$

$\varepsilon_{k'} - \varepsilon_k$ which is exactly the energy difference that needs to be supplied from the external perturbation for this transition. However, this only holds for very short *pulses* of perturbation that are short enough compared to typical system times. If the perturbation extends over a longer period in time, this no longer is valid. In the other extreme case of a very extended pulse shape in time, the so–called *adiabatic limit*, the perturbation $V_{k'k}(\omega)$ becomes a delta function, $V_{k'k}(\omega) = V^0_{k'k}\delta(\omega)$. However, the pole structure of $V_{k'k}(\omega)$ is essential, and the adiabatic limit must be taken at the end of the calculation. With the choice

$$\delta(\omega' - \omega) = \frac{\Delta}{\pi}\frac{1}{(\omega' - \omega)^2 + \Delta^2}$$

this introduces two poles, namely at $\omega^* = \omega' \pm i\Delta$. The width $\Delta$ is taken to zero eventually, but during the algebra it is considered much larger than the $\delta \equiv 0^+$ that appears in the (advanced) Green's functions, therefore $0^+ = \delta \ll \Delta \ll 1$. With this, Eq. (4.37) becomes

$$\begin{aligned} G_{k'k}(t',t) &\equiv -i\,\delta_{k'k}\,e^{-i\varepsilon_k(t'-t)} \\ &+ \int_{-\infty}^{\infty}\frac{d\omega}{2\pi}\int_{-\infty}^{\infty}\frac{d\omega'}{2\pi}\,e^{-i\omega' t'}\frac{1}{\omega' - \varepsilon_{k'} + i\delta}\frac{\Delta}{\pi}\frac{V^0_{k'k}}{(\omega' - \omega)^2 + \Delta^2}\frac{1}{\omega - \varepsilon_k + i\delta}e^{+i\omega t} \\ &+ \dots \\ &\simeq -i\,\delta_{k'k}\,e^{-i\varepsilon_k(t'-t)} \end{aligned} \tag{4.40}$$

The double integral vanishes in the limit $\Delta \to 0^+$ as is easily seen by applying the Residue theorem. Both integrals, over $\omega$ as well as over $\omega'$, are carried out by closing the integration contour in the lower complex plane. From the residue theorem, the $\omega$ integral has two relevant poles at $\omega^* = \omega' - i\Delta$ and $\omega^* = \varepsilon_k - i\delta$ and so

$$\begin{aligned} &\int_{-\infty}^{\infty}\frac{d\omega}{2\pi}\int_{-\infty}^{\infty}\frac{d\omega'}{2\pi}\,e^{-i\omega' t'}\frac{1}{\omega' - \varepsilon_{k'} + i\delta}\,\frac{\Delta}{(\omega' - \omega)^2 + \Delta^2}\frac{1}{\omega - \varepsilon_k + i\delta}e^{+i\omega t} \\ = &\int_{-\infty}^{\infty}\frac{d\omega'}{2\pi}\,e^{-i\omega' t'}\frac{-i}{\omega' - \varepsilon_{k'} + i\delta}\left(e^{(i\omega' + \Delta)t}\frac{1}{\omega' - \varepsilon_{k'} + i\delta}\frac{\Delta}{2i\Delta}\frac{1}{\omega' - \varepsilon_k - i\Delta}\right. \\ &\left. + e^{+i\varepsilon_k t}\frac{\Delta}{\omega' - \varepsilon_k + i\Delta}\frac{1}{\omega' - \varepsilon_k - i\Delta}\right). \end{aligned}$$

The first term vanishes, since $t \to -\infty$. Similarly taking $t' \to +\infty$, the only relevant

pole in the $\omega'$ integral is at $\omega' = \varepsilon_{k'} - i\delta$ such that the last equation becomes

$$\begin{aligned} & -e^{-i\varepsilon_{k'}t'} \frac{\Delta}{\varepsilon_{k'} - \varepsilon_k + i\Delta} \frac{1}{\varepsilon_{k'} - \varepsilon_k - i\Delta} e^{+i\varepsilon_k t} \\ = \; & -e^{-(i\varepsilon_{k'}t' - i\varepsilon_k t)} \frac{\Delta}{(\varepsilon_{k'} - \varepsilon_k)^2 + \Delta^2} \qquad (4.41a) \\ = \; & -e^{-(i\varepsilon_{k'}t' - i\varepsilon_k t)} \cdot \pi\delta(\varepsilon_{k'} - \varepsilon_k) \qquad (4.41b) \end{aligned}$$

Consequently, in the adiabatic limit of $\Delta \to 0$, the only possible contributions is mixing within degenerate states. There are no transitions to different energy levels due to this type of slowly varying perturbation. The higher order terms are suppressed by powers of $\Delta$ as can be seen for example in the second order term in Eq. (4.41a).[1]

### 4.3.4 Step–Like Perturbations and Induced Transitions

The Fourier transform of an external interaction potential has been assumed to exist ever since it was introduced. In order for this to be true, however, the perturbation must be finite in time, i.e.

$$\lim_{t \to -\infty} H(t) = \lim_{t \to +\infty} H(t) = H_0$$

For a transition to a different configuration, this appears to be problematic for $V_{kk'}(\omega)$ with $\omega \to 0$. However, the Fourier transforms of step functions are asymptotically well defined, such as in Eq. (4.17a), p. 76. In this sense, also step like transitions in potential configurations through the exterior can also be included equally well in above treatment. The step–like perturbation is included as it is, while the subsequent

[1] Note that if $\Delta$ had been taken to zero right away at the beginning of the calculation, then the integral

$$\int_{-\infty}^{\infty} \frac{d\omega}{2\pi} \int_{-\infty}^{\infty} \frac{d\omega'}{2\pi} \, e^{-i\omega' t'} \frac{1}{\omega' - \varepsilon_{k'} + i\delta} \delta(\omega - \omega') \frac{1}{\omega - \varepsilon_k + i\delta} e^{+i\omega t}$$

would be

$$\begin{aligned} & \int_{-\infty}^{\infty} \frac{d\omega'}{2\pi} e^{-i\omega'(t'-t)} \frac{1}{\omega' - \varepsilon_{k'} + i\delta} \frac{1}{\omega' - \varepsilon_k + i\delta} \\ = \; & e^{-i\varepsilon_{k'}(t'-t)} \frac{-i}{\varepsilon_{k'} - \varepsilon_k + i\delta} + e^{-i\varepsilon_k(t'-t)} \frac{-i}{\varepsilon_k - \varepsilon_{k'} + i\delta} \\ = \; & \frac{i}{\varepsilon_{k'} - \varepsilon_k + i\delta} \left( e^{-i\varepsilon_k(t'-t)} - e^{-i\varepsilon_{k'}(t'-t)} \right) \end{aligned}$$

where it is far from clear that the latter expression should vanish. Therefore it is essential to carry out the perturbative algebra first, and then to take the adiabatic limit at the end of the calculation.

constant time evolution is brought back on a long time scale (and thus adiabatically) to the original Hamiltonian in the sense

$$H = H_0 + V(t) \text{ with } V(t) = V_0 \vartheta(t) e^{-\Delta \cdot t} \tag{4.42}$$

With a constant operator $V_0$. The time scale $\Delta^{-1}$ for the adiabatic relaxation after the step–like perturbation is considered to be very large, and therefore much smaller then the characteristic transition frequencies of the system ($\Delta \ll \varepsilon_{k'k}$) but still much larger then the usual positive infinitesimal $\delta \equiv 0^+$ that appears in the free Green's function. The Fourier transform of the step–like perturbation in Eq. (4.42) is

$$\langle \omega_2 | V | \omega_1 \rangle = V(\omega_2 - \omega_1) = \frac{i}{\omega_2 - \omega_1 + i\Delta}$$

with the full operator form for the perturbation $V$ being $\langle t_2 | V | t_1 \rangle = V(t)\, \delta(t_2 - t_1)$.

The Green's function describes the propagation of the probability amplitude of the system over time. Transitions to different states are mediated by the time–dependent perturbation $V$. The expansion of the full Green's function in this perturbation $V$ is given in Eq. (4.33)

$$\begin{aligned} G(\omega', \omega) &= G_0(\omega')\, \delta(\omega' - \omega) + G_0(\omega')\, V(\omega' - \omega)\, G_0(\omega) \\ &\quad + G_0(\omega') \int_{-\infty}^{\infty} d\omega'' V(\omega' - \omega'')\, G_0(\omega'')\, V(\omega'' - \omega)\, G_0(\omega) + \dots \end{aligned}$$

Since we are interested in transitions, the first term on the RHS is irrelevant since it does not provide any transitions. To lowest order, the transitions are given by the second term. Being interested in the transition amplitude $T(t', t) \equiv \langle t' | G | t \rangle \equiv G(t', t)$ with $t \to -\infty$ and $t' \to +\infty$ with all the perturbation clearly located within the time interval $[t, t']$, this is evaluated to lowest order as

$$\begin{aligned} T(t', t) &\equiv \int_{-\infty}^{\infty} \frac{d\omega'}{2\pi} e^{-i\omega' t'} \int_{-\infty}^{\infty} \frac{d\omega}{2\pi} e^{+i\omega t}\, G(\omega', \omega) \\ &\simeq \int_{-\infty}^{\infty} \frac{d\omega'}{2\pi} e^{-i\omega' t'} \int_{-\infty}^{\infty} \frac{d\omega}{2\pi} e^{+i\omega t}\, G_0(\omega')\, V(\omega' - \omega)\, G_0(\omega) \\ &= \int_{-\infty}^{\infty} \frac{d\omega'}{2\pi} e^{-i\omega' t'} \int_{-\infty}^{\infty} \frac{d\omega}{2\pi} e^{+i\omega t} * \end{aligned}$$

$$\sum_{k,k'} |k'\rangle \underbrace{\langle k'| V_0 |k\rangle}_{\equiv V_{k'k}} \langle k| \frac{1}{\omega' - \varepsilon_{k'} + i\delta} \frac{i}{\omega' - \omega + i\Delta} \frac{1}{\omega - \varepsilon_k + i\delta}$$

with $\delta = 0^+ \ll \Delta$. Both integrals over $\omega$ as well as over $\omega'$ are done by contour integrals closing the path in the lower complex plane since $t < 0$ and $t' > 0$. The integral over $\omega$ only contains the pole of the last term, $\omega^* = \varepsilon_k - i\delta$, and so the last equation becomes

$$\sum_{k,k'} V_{k'k} \ (-i)\, e^{i\varepsilon_k t} \cdot |k'\rangle \langle k| \int_{-\infty}^{\infty} \frac{d\omega'}{2\pi} e^{-i\omega' t'} \frac{1}{\omega' - \varepsilon_{k'} + i\delta} \frac{i}{\omega' - \varepsilon_k + i\Delta}.$$

The $\omega'$ integral contains two poles which result in

$$e^{-i\varepsilon_{k'} t'} \frac{1}{\varepsilon_{k'} - \varepsilon_k + i\Delta} + e^{-i(\varepsilon_k - i\Delta)t'} \frac{1}{\varepsilon_k - \varepsilon_{k'} - i\Delta}$$

where the last term vanishes with the assumption that $t'$ is taken much larger than $\Delta^{-1}$, i.e. $t' \to +\infty$. To lowest order, finally, the matrix of the transition amplitudes $T(t', t)$ becomes

$$T(t', t) \simeq -i \sum_{k,k'} \frac{V_{k'k}\ e^{-i(\varepsilon_{k'} t' - \varepsilon_k t)}}{\varepsilon_{k'} - \varepsilon_k + i\Delta} |k'\rangle \langle k| \tag{4.43}$$

In the limit of exact adiabaticity after the step–like perturbation, $\Delta$ equals zero and drops out of the equation. The resulting transition probabilities are

$$|T_{k'k}(t', t)|^2 \simeq \left| \frac{V_{k'k}}{\omega_{k'k}} \right|^2 \tag{4.44}$$

with $\omega_{k'k} \equiv \varepsilon_{k'} - \varepsilon_k$.

For the sake of a double check, the previous results performed in the energy space, can also be obtained by staying in the time domain all along. Then

$$\begin{aligned} T(t', t) &\equiv G(t', t) \\ &\simeq \int_{-\infty}^{\infty} dt_1\ G_0(t', t_1)\, V(t_1)\, G_0(t_1, t) \\ &= \sum_{k,k'} \int_{-\infty}^{\infty} dt_1\ (-i)\, \vartheta(t' - t_1)\, e^{-i\varepsilon_{k'}(t' - t_1)} * \\ &\quad |k'\rangle \underbrace{\langle k'| V_0 \vartheta(t_1)\, e^{-\Delta \cdot t_1} |k\rangle}_{\equiv V_{k'k}\ \vartheta(t_1) e^{-\Delta \cdot t_1}} \langle k| (-i)\, \vartheta(t_1 - t)\, e^{-i\varepsilon_k (t_1 - t)} \end{aligned}$$

$$
\begin{aligned}
&= \sum_{k,k'} -V_{k'k} \left|k'\right\rangle \left\langle k\right| \; e^{-i(\varepsilon_{k'}t'-\varepsilon_k t)} \int_{-\infty}^{\infty} dt_1 \; e^{+i(\varepsilon_{k'}-\varepsilon_k+i\Delta)t_1} \vartheta\left(t_1\right) \\
&= \sum_{k,k'} -V_{k'k} \left|k'\right\rangle \left\langle k\right| \; e^{-i(\varepsilon_{k'}t'-\varepsilon_k t)} \frac{i}{\varepsilon_{k'}-\varepsilon_k+i\Delta}
\end{aligned}
$$

consistent with Eq. (4.43).

In above result for the transition amplitude, it is clear by definition of transition that one considers $k \neq k'$ and therefore $\varepsilon_{k'} \neq \varepsilon_k$. The case of degenerate states is not considered here. Nevertheless, the blow up of the transition amplitude for the transition into the same state as $1/\Delta$ for $\Delta \to 0$ can be easily understood from the following simple example. The trivial perturbation $V\left(t\right) = c \; \vartheta\left(t\right) \; \mathbf{1} e^{-\Delta t}$ with some strength scalar $c$ only shifts the energy reference but does not induce any transitions. The exact Green's function is written down easily

$$
\begin{aligned}
G\left(t',t\right) &= -i\delta\left(t'-t\right) \sum_k \left|k\right\rangle \left\langle k\right| \; \exp\left( -i\varepsilon_k \left(t'-t\right) \; - \; i\int_t^{t'} dt_1 \; c\vartheta\left(t_1\right) \; e^{-\Delta t_1} \right) \\
&= -i\delta\left(t'-t\right) \sum_k \left|k\right\rangle \left\langle k\right| \; \exp\left( -i\varepsilon_k \left(t'-t\right) \; - \; ic\frac{1-e^{-\Delta t'}}{\Delta} \right)
\end{aligned}
$$

where in the last equation, similar to the previous assumptions, $t < 0$ is taken negative and the time $t' \gg 1/\Delta$ is taken far beyond the subsequent adiabatic relaxation time scale $1/\Delta$, such that the $e^{-\Delta t'}$ term vanishes. Now expanding the Green's function with respect to the strength $c$ of the perturbation, gives

$$
G\left(t',t\right) = -i\delta\left(t'-t\right) \sum_k \left|k\right\rangle \left\langle k\right| \; e^{-i\varepsilon_k(t'-t)} \left(1 - \; i\frac{c}{\Delta} + \mathcal{O}\left(c^2\right)\right)
$$

which has exactly the same $1/\Delta$ correction as already encountered previously for the case of no transition. The *large* contribution $1/\Delta$ now makes sense, since the extra phase due to the potential step piles up over the time scale $1/\Delta$.

For the loss of probability from a subspace $\mathcal{P}$ to the remainder of the Hilbert space $\mathcal{Q}$, above derivation within the Green's function formalism can be linked to the Feshbach formalism in the beginning of this chapter: Equation (4.5, p. 67) states

$$
\left|\psi_Q\right\rangle = +\frac{1}{E-H_{QQ}} H_{QP} \left|\psi_P\right\rangle \; .
$$

For an eigenstate at energy $E$ completely localized in space $\mathcal{P}$ initially, a perturbation $V$ in the Hamiltonian introduces probabilities in space $\mathcal{Q}$. This can be interpreted

the following way that the perturbation $V$ when turned on instantaneously, induces transitions into space $\mathcal{Q}$ such that the total 'loss' of probability in space $\mathcal{P}$ is equal to

$$\begin{aligned}
\langle\psi_Q|\psi_Q\rangle &= \langle\psi_P| H_{PQ} \frac{1}{E - H_{QQ}} \frac{1}{E - H_{QQ}} H_{QP} |\psi_P\rangle \\
&= \langle\psi_P| V_{PQ} \left[ \frac{1}{E - H_0} \sum_{n=0}^{\infty} \left( QV \frac{1}{E - H_0} \right)^n \right]^2 V_{QP} |\psi_P\rangle \\
&= \langle\psi_P| V_{PQ} \frac{1}{E - H_0} \frac{1}{E - H_0} V_{QP} |\psi_P\rangle + \ \ldots \\
&= \sum_k |i\rangle \langle j| \left| \frac{V_{ik}}{E - \varepsilon_k} \right|^2 + \ \ldots
\end{aligned}$$

where the expansion of the term $(E - H_{QQ})^{-1}$ is the same as in Eq. (4.11c). If $V_{ik}$ is of order $\delta$ and the splitting in energy space of space $\mathcal{P}$ with respect to space $\mathcal{Q}$ is $\Delta$, then the loss of probability scales like $(\delta/\Delta)^2$. On the other hand, in the Green's function formalism above which deals with the time–dependent perturbation in a systematic way, to lowest order the same result is obtained (see Eq. 4.44).

# Chapter 5

# Quantum Dot Networks and Charge Qubits

This chapter is dedicated to the quantum mechanics of a set of quantum dots interacting via the Coulomb interaction and via the possibility of quantum mechanical tunneling. Throughout this discussion, the tunneling is considered weak, which turns out to be essential for the construction of an isolated two level space in the ground state. It will also be explicitly defined what is meant by weak tunneling.

Furthermore, the setup includes a set of external gates which allow us to dynamically interfere with this *network of quantum dots*. The gates are mainly thought to be capacitively coupled voltage gates, which are driven by an external potential. Only at the end of this chapter an external magnetic field is introduced.

The main interest in these type of systems is based on possible realizations of charge qubits. Being a two–level system, any qubit can be mapped onto the standard spin 1/2 Hamiltonian with its Pauli spin matrices. In this context the dynamics of two–level systems is reviewed in general.

The charge qubits constructed are all based on the fixed number of two electrons being thought of as the top–most particles in a Fermi sea with the single particle levels clearly split by the nanoscale confinement. With all the lower lying states filled, only these excess electrons are allowed to hop between the quantum dots. The two–electron Hamiltonian is constructed, and the dynamics for the resulting singlet and triplet states is discussed in detail starting with Sec. 5.5 (pp. 128). Before that, however, an extended section on the relevant qubit algebra is provided.

## 5.1 Hubbard Hamiltonian

The Hubbard Hamiltonian is commonly written in the notation of second quantization with its creation and annihilation operators $c_i^+$ and $c_i$ [Mah00]. The operator $c_i^+$

creates a particle in state $i$ where $i$ is meant to include all necessary quantum numbers in the specific context. An often used set of (anti)commutator relationships is given in the following

$$\left\{c_i, c_j^+\right\} = \delta_{ij}, \ \{c_i, c_j\} = 0 \tag{5.1a}$$
$$[\hat{n}_i, c_j] = -\delta_{ij} c_i, \ \left[\hat{n}_i, c_j^+\right] = \delta_{ij} c_i^+ \tag{5.1b}$$
$$[\hat{n}_i, \hat{n}_j] = 0, \ \left[c_i^+ c_{i'}, c_j^+ c_{j'}\right] = \delta_{i'j} c_i^+ c_{j'} - \delta_{ij'} c_j^+ c_{i'} \tag{5.1c}$$

where Eqs. (5.1b+5.1c) are derived equations from Eq. (5.1a).

### 5.1.1 (Extended) Hubbard Hamiltonian

The general form of the extended Hubbard Hamiltonian for a network of quantum dots with tunneling in the tight binding sense is given by

$$\begin{aligned} H \ = \ & \sum_{i,\sigma} \varepsilon_\sigma \, c_{i\sigma}^+ c_{i\sigma} - \sum_{i,j,\sigma} t_{ij}^\sigma (c_{i\sigma}^+ c_{j\sigma} + c_{j\sigma}^+ c_{i\sigma}) + \\ & \frac{1}{2} \sum_{i,j,\sigma,\sigma'} V_{ij} \, c_{i\sigma}^+ c_{j\sigma'}^+ c_{j\sigma'} c_{i\sigma} + \sum_i V_i \hat{n}_i \end{aligned} \tag{5.2}$$

where $c_{i\sigma}^+$ is the creation operator for a particle on site $i$ with spin $\sigma = \{\uparrow, \downarrow\}$ and $\hat{n}_i \equiv c_{i\uparrow}^+ c_{i\uparrow} + c_{i\downarrow}^+ c_{i\downarrow}$. The $\varepsilon_{(i)\sigma}$ refers to the local energy of the state $\sigma$ on the $i = \{1, \ldots, n\}$ identical dots and can be used to account for the Zeeman splitting of spins in an external magnetic field. For most cases, the $\varepsilon_\sigma$ are simply set equal and zero. The tunneling coefficients $t_{ij}^\sigma$ from dot $i$ to dot $j$ are considered independent of the spin orientation, thus $t_{ij}^\uparrow = t_{ij}^\downarrow \equiv t_{ij}$. The electrostatic energy in the last two terms of Eq. (5.2), i.e. the coefficients $V_{ij}$ and $V_i$, are derived from the (total) capacitance matrix of the system which is approximated by the capacitor network indicated in Fig. 5.1b. In summary, the simplified version of Eq. (5.2) as applied in the following is

$$H = -t \sum_{\langle i,j \rangle, \sigma} (c_{i\sigma}^+ c_{j\sigma} + c_{j\sigma}^+ c_{i\sigma}) + \frac{1}{2} \sum_{i,j} V_{ij} \, \hat{n}_i \hat{n}_j + \sum_i V_i \, \hat{n}_i \tag{5.3}$$

A justification for employing the classical capacitance matrix in this type of Hubbard Hamiltonian is given at the end of this section (see Sec. 5.1.3, pp. 98).

### 5.1.2 Weak Tunneling

Mentioned in various contexts of this work, weak tunneling often appears at the basis of an argument. So naturally one may ask, how weak is weak? There are at least three possible yet related answers to this question.

The first answer is based on the argument of quantum conductance. Consider, for example, a quantum point contact (QPC). Two Fermi seas are connected to each other through a quantum–mechanically small channel. By definition, this channel is 1D since only a few quantum states actually do couple through the QPC in a left–right and thus in a 1D sense, while all the other ones are reflected well before they reach the QPC. For two coupled 1D systems with perfect transmission through their contact point and negligible resistance in the leads, the conductance $g$ defined through Ohm's law $I = g \cdot \Delta V$ is a constant with respect to a single quantum channel, namely the *quantum of conductance* $g_0 \equiv h/2e^2$. This, however, is for a perfectly transmissive QPC so that the tunneling rate through the QPC is high. In this sense it is straightforward to define what one means by weak tunneling, namely that the conductance through the QPC is much smaller than $g_0$. In terms of the dimensionless transmission probability $T$, this means a large resistance $R = (T \cdot \frac{2e^2}{h})^{-1} \gg \frac{h}{2e^2} = 12.9\,\mathrm{k}\Omega$. Consequently, what is meant by weak tunneling in this context, is obviously $T \ll 1$.

On the other hand with respect to the Hubbard Hamiltonian in this section, for example, there is no parameter like the transmission probability $T$, but there is the tunneling or hopping amplitude $t$ instead where $t_{ij} \equiv \langle \psi_i | H | \psi_j \rangle$ which obviously has units of energy and can equally well be associated with kinetic energy or an effective mass in a periodic array. So what is meant by weak tunneling here? In a periodic 1D system with a single level per site $t$ and dot to dot separation $d$, the energy spectrum broadens to a band with width $4t$ and the eigenstates are plane waves over the whole array. However, applying an electric field $E$ with a strength such that $E \cdot d \geq 4t$, clearly causes the band model to break down since the electrostatic potential difference from one dot to the next is larger than the original bandwidth. Equivalently, if the electric field is replaced by disorder, then potential changes larger than $4t$ between neighboring dots clearly also destroy the band picture, and as a result, strongly localized states emerge. The important point is what the relevant energy scales in the system ($Ed$, disorder, ...) are and how the tunneling amplitude $t$ compares to them. If $t$ is small in that respect, then the picture of a localized electron hopping from dot to dot emerges.

Both of the answers above still do not quite answer the question to what is meant by weak tunneling in this work. The quantum dot networks considered only have a few dots with a very few operative electrons on them. The dots are considered identical,

and the arrangement is optimized towards certain properties. The connection between dots is not quite via a QPC, and so the first answer to the initial question posed is not relevant. The second answer is somewhat closer, but does still not quite capture what is meant by weak tunneling in this context. The energy scale here is set by the presence of higher lying excited states above the (degenerate) ground state system which become relevant if the system is perturbed too much. It is thus the energy splitting $\Delta_0$ between the ground state system and the nearest excited states that serves as a measure to whether the tunneling is weak or not. In this sense, weak tunneling in this work is to be interpreted as $t \ll \Delta_0$ in order to preserve the identity of *single–level tunneling*.

### 5.1.3 The C Matrix Formalism in a Quantum Mechanical Problem

The capacitance matrix formalism is rooted in classical electrodynamics. In the following, its relevance for the quantum mechanics of coupled quantum dots is shown, and the classical Coulomb two–body interaction is properly introduced into the quantum mechanical context. The derivation is similar to the motivation of the $tJV$–model in terms of the Hubbard Hamiltonian given in [JH96] which by itself is an interesting complementary paper to the following.

In the notation of the Hubbard Hamiltonian with its creation and annihilation operators, the classical potential is written with Eq. (2.21a) as

$$\begin{aligned} W_{classical} &= \frac{1}{2}\sum_{i,j} q_i \left(C_{11}^{-1}\right)_{ij} q_j - \sum_{i,g} q_i \left(C_{11}^{-1}C_{12}\right)_{ig} V_g \\ &\equiv \frac{1}{2}\sum_{i,j} \hat{n}_i V_{ij} \hat{n}_j + \sum_i \hat{n}_i V_i \end{aligned} \tag{5.4}$$

with $\hat{n}_i \equiv \sum_\sigma c_{i\sigma}^+ c_{i\sigma}$ counting the total number of electrons on site $i$ and the coefficients $V_{ij} \equiv e^2 \left(C_{11}^{-1}\right)_{ij}$ and $V_i \equiv +\sum_g e \left(C_{11}^{-1}C_{12}\right)_{ig} V_g$ with the voltages on the gates being $V_g$ and the charge of the particles (electrons) being $-e$. The gate–voltage dependent coefficients $V_i$ thus correspond to a local energy shift of the single–electron states and do not contribute to the ee–interaction *per se*. It will be taken care of later by the site energy terms, and will be dropped now for most of the discussion.

Quantum dots of typical sizes currently have 10s to a few 100s of electrons. Adding or removing a single electron does not alter the probability distribution of the total wavefunction much which is exactly the argument why the capacitance matrix formalism is still a valid approach for the potential in these quantum mechanical systems.

The interaction energy for free carriers based on the Coulomb potential

$$W = \frac{1}{2}\sum_{i,j} q_i \frac{1}{|\vec{x}_i - \vec{x}_j|} q_j$$

can be equivalently replaced as follows in the presence of finite size distinct objects each of which has a uniform potential across it. With $Q_i$ being the total charge on object $i$, it follows

$$\begin{aligned} W &= \frac{1}{2}\sum_{i,j} Q_i V_{ij} Q_j \\ &\equiv \frac{1}{2}\int d^3x \int d^3x' \; \rho(x)\, V(x,x') \rho(x') \end{aligned}$$

with the charge density $\rho(x)$ and where $V(x,x') = V_{ij} = \left(C_{11}^{-1}\right)_{ij}$ when $x$ is residing within the space of object $i$ and $x'$ within the space of object $j$, i.e. $V(x,x')$ is constant when $x \in \Omega_i$ and $x' \in \Omega_j$. Overall, the interaction potential is still given by the two–body function $V(x,x')$ which is not exactly a function of the difference $|x - x'|$ anymore, yet it is still symmetric under the exchange $x \leftrightarrow x'$ (since also $V_{ij} = V_{ji}$).

Now from a quantum mechanical point of view, the total energy of the ground state is minimized when the correct antisymmetry for Fermions (electrons) is taken into account. This is conveniently done within the second quantization formalism. With the definition of the integrals

$$V_{klmn} \equiv \int d^3x \int d^3x' \; \varphi_k^*(x)\, \varphi_l^*(x') \cdot V(x,x') \cdot \varphi_m(x)\, \varphi_n(x') \tag{5.5}$$

the typical matrix element for any pair of 2–particle wavefunctions, properly written as a Slater determinant to account for the correct Fermi statistics, follows as

$$\begin{aligned} \langle kl|\, V\, |mn\rangle &= \int d^3x \int d^3x' \frac{1}{\sqrt{2!}} \begin{vmatrix} \varphi_k(x) & \varphi_k(x') \\ \varphi_l(x) & \varphi_l(x') \end{vmatrix}^* V(x,x') \frac{1}{\sqrt{2!}} \begin{vmatrix} \varphi_m(x) & \varphi_m(x') \\ \varphi_n(x) & \varphi_n(x') \end{vmatrix} \\ &= \frac{1}{2}\left(V_{lknm} - V_{lkmn} - V_{klnm} + V_{klmn}\right) \\ &= \langle 0|\, c_l c_k \cdot \left(\frac{1}{2}\sum_{k'l'm'n'} V_{k'l'm'n'} \cdot c_{l'}^+ c_{k'}^+ c_{m'} c_{n'}\right) \cdot c_m^+ c_n^+ \,|0\rangle \end{aligned}$$

Thus the proper quantum mechanical expression for the two–particle interaction in

second quantization is motivated as [Mat76, p. 78, p. 91]

$$V = \frac{1}{2}\sum_{klmn} V_{klmn} c_l^+ c_k^+ c_m c_n \tag{5.6}$$

where besides the typical symmetry $V^*_{klmn} = V_{mnkl}$ there is also $V_{klmn} = V_{lknm}$. This identity follows from the simple interchange of $x \leftrightarrow x'$ in Eq. (5.5) and the symmetry in the interaction potential under this exchange, i.e. $V(x,x') = V(x',x)$. Now one must be careful with the interaction potential introduced in Eq. (5.6) since it purely describes the interaction between particles and does not take care of local self–energy terms (in the language of the capacitance matrix, the $V_{kl}$ with $k \neq l$ are taken care of, but not the $V_{kk}$). More on this below.

In the case of quantum dots the wave functions generated by $c^+_{i\sigma}$ are considered to be strongly localized at site $i$, now symbolically written as function $\varphi_k(x) \sim \delta_{kx}$ with $\delta_{kx}$ some smoothened $\delta$–function centered around the $k$–th dot. Therefore the integrals $V_{klmn}$ can be written out according their significance

$$\begin{aligned} V_{klmn} &\equiv \int d^3x \int d^3x' \; \varphi_k^*(x)\,\varphi_l^*(x') \cdot V(x,x') \cdot \varphi_m(x)\,\varphi_n(x') \\ &= \delta_{km}\delta_{ln} V_{kl} + \delta_{km} \langle l| V_k |n\rangle \big|_{l\neq n} + \delta_{ln} \langle k| V_l |m\rangle \big|_{k\neq m} && \text{(5.7a)} \\ &\quad + \delta_{kn}\delta_{lm} \langle (\varphi_k\varphi_m)(x)\, V(x-x')\, (\varphi_k\varphi_m)(x') \rangle && \text{(5.7b)} \\ &\quad + \text{small terms} && \text{(5.7c)} \end{aligned}$$

with $V_{kl} = \left(C_{11}^{-1}\right)_{kl}$ and the notation $\langle l| V_k |n\rangle \equiv \int d^3x' \varphi_l^*(x')\, V(x_k, x')\, \varphi_n(x')$ for $l \neq n$ only, since the $l = n$ case is already taken care of by the first term in line (5.7a). As already mentioned, the terms in Eq. (5.7) are sorted by their relevance, i.e. the largest terms are shown first followed by smaller and smaller contributions. Now, the contributions of the $V_{klmn}$ integrals in Eq. (5.7) to the matrix elements

$$\langle kl| V |mn\rangle = \frac{2}{2}\left(V_{klmn} - V_{lkmn}\right) = V_{klmn} - V_{lkmn}$$

are identified as follows: The first term in line (5.7a) is the *direct* term with the contribution

$$\langle kl| V |kl\rangle = V_{kl}$$

and its trivial counter part under particle exchange $\langle lk| V |kl\rangle = -V_{kl}$. The second and third term in line (5.7a) describe the hopping. The $\delta_{km}$ or $\delta_{ln}$ still leave one of the two particles residing on the same dot while the other one is hopping to another site. Some small spatial overlap of the wave functions is essential for this contribution to be $\neq 0$ and therefore only nearest neighbor hops are relevant. These last two

terms in line (5.7a) are thus by definition part of the hopping coefficients $t_{ij}$ and therefore included in these. Note that also the kinetic energy operator contributes to the tunneling coefficient in a very similar way. There, however, it is a single particle process. Together they form the tunneling coefficient which eventually enters as a parameter to the model [JH96].

The first term in line (5.7b), i.e. the overall fourth term Eq. (5.7), is the exchange contribution. In general, the exchange contribution is only relevant if there is significant spatial overlap of the wavefunctions. Thus it either refers to the two particles being on the same dot (which in given case are states high above the groundstate energy because of the strong Coulomb interaction and thus are negligible in this context), or at the very minimum on neighboring dots. In comparison, for the tunneling case above, one particle stays on its qudot while the other one hops to a neighboring dot. That involves only one overlap entering the overall magnitude. For the exchange term here, however, the overlap enters twice, and therefore it is a second order process compared to the first order process of the tunneling and can be neglected.

In terms of typical numbers used in the simulation, $V_{12} = 0.29\,\text{meV}$ and a relatively large $t = 5\,\mu\text{eV}$ (large in the sense to still have a ground state pair well isolated from the remainder of the states), the overlap becomes $s \approx t/V_{12} \approx 0.017$. Thus the exchange is estimated to be $V_{12} * s^2 = s * t = 0.086\,\mu\text{eV}$ which is significantly smaller than the tunneling $t$ in the first place and, in addition, because of the deltas $\delta_{kn}\delta_{lm}$ in line (5.7b), it enters in the diagonal of the Hamiltonian. The largest off–diagonal contributions are thus the tunnelings $t$, while the overwhelmingly largest terms on the diagonal are from the direct contribution, namely the first term in Eq. (5.7). The corrections due to the exchange energy, the fourth term in Eq. (5.7), are considerably smaller and therefore they can be safely neglected.

So this *regular* exchange contribution to the total Hamiltonian originating in the two–particle interaction potential is negligible [JH96]. However, this does not mean that exchange is completely irrelevant in this context. In the perturbative approach with respect to tunneling later on, the exchange of two particles on neighboring dots can still take place even if the *regular* exchange is neglected. This effective exchange appears from the multiple step processes that explicitly include intermediate states of likely higher energy. Processes with intermediate states with even higher energy such as double occupancy will still remain negligible. However, through the mechanism of tunneling of the electrons, eventually an exchange of two particles avoiding an intermediate state with double occupancy is possible and will be essential for some of the discussion later on.

The *pure* interaction potential is given by Eq. (5.5) which is now rewritten con-

sidering only the direct contribution

$$V_{direct} = \frac{1}{2}\sum_{kl} V_{kl} c_l^+ c_k^+ c_k c_l$$

with the constants $V_{kl} = \left(C_{11}^{-1}\right)_{kl}$. Then grouping the $c^{(+)}$ operators by the indices $k$ and $l$ using the commutator relations for the $c^{(+)}$ in Eqs. (5.1), it follows

$$\begin{aligned} V_{direct} &= \frac{1}{2}\sum_{kl} V_{kl} c_l^+ \left( -\underbrace{\left[c_k^+, c_l\right]_+}_{=\delta_{kl}} + c_l c_k^+ \right) c_k \\ &= \frac{1}{2}\sum_{kl} \hat{n}_k V_{kl} \hat{n}_l - \frac{1}{2}\sum_k V_{kk} \hat{n}_k \end{aligned} \tag{5.8}$$

The first term in Eq. (5.8) is the direct equivalent to the classical electrostatic energy *including* the 'self–energy' terms $V_{kk}$ and $V_{ll}$ which however are subtracted by the second term in Eq. (5.8). Thus above expression for the interaction potential $V$ does not contain the self–energy terms, and in this sense, it is a pure interaction potential of the two particles considered. On the other hand, the self–energy terms are related to a local potential of the individual qudots, and therefore must be accounted for as such. The $V_{kk}$ must be included in the energies $\varepsilon_{i\sigma}$ of the single particle energies, or alternatively, one can redefine the potential $V$ in Eq. (5.8) by simply dropping the last term on the RHS which otherwise cancels the important $V_{kk}$ terms.

In summary, the electrostatic potential due to the mutual capacitive coupling between the qudots and the voltage gates is justified in the quantum mechanical context. It is equivalent in the weak coupling regime to the classical analog in Eq. (5.4)

$$V_{QM} = \frac{1}{2}\sum_{i,j} \hat{n}_i V_{ij} \hat{n}_j + \sum_i \hat{n}_i V_i$$

with $V_{ij} \equiv e^2 \left(C_{11}^{-1}\right)_{ij}$ and $V_i \equiv \sum_g e \left(C_{11}^{-1} C_{12}\right)_{ig} V_g$, completely analogous to the classical expressions in terms of the capacitance matrix in Eq. (5.4). The hopping coefficients which enter the Hamiltonian in the off–diagonal can be modified by the two–body ee–interaction potential in above sense, which needs to be kept in mind when choosing these parameters.

## 5.2 Spin 1/2 and Quantum Two Level Systems

Any quantum mechanical two level system (qu2LS) can be mapped onto the spin 1/2 Hamiltonian. This surely applies for the spin 1/2 of the electron, but more generally also for systems that are energetically separated from the remainder of their spectra. The starting point for the spin 1/2 formalism are the three Pauli spin matrices. Together with the unity operator they form a complete set of Hermitian operators with two dimensions ($SU(2)$)

$$\sigma_0 \equiv \mathbf{1} = \begin{pmatrix} 1 & 0 \\ 0 & 1 \end{pmatrix} \tag{5.9a}$$

$$\sigma_1 \equiv \sigma_x = \begin{pmatrix} 0 & 1 \\ 1 & 0 \end{pmatrix} \tag{5.9b}$$

$$\sigma_2 \equiv \sigma_y = \begin{pmatrix} 0 & -i \\ i & 0 \end{pmatrix} \tag{5.9c}$$

$$\sigma_3 \equiv \sigma_x = \begin{pmatrix} 1 & 0 \\ 0 & -1 \end{pmatrix} \tag{5.9d}$$

where the non–index $i$ refers to the complex number $\sqrt{-1}$. The Pauli spin matrices obey the following relations as is easily shown using their definitions in Eqs. (5.9).

$$\mathrm{tr}\,\{\sigma_i\} = 0,\ \mathrm{tr}\,\{\sigma_i\sigma_j\} = 2\delta_{ij} \tag{5.10a}$$

$$\sigma_i^2 = \mathbf{1},\ \sigma_i\sigma_j = \delta_{ij} + i\varepsilon_{ijk}\sigma_k \tag{5.10b}$$

$$[\sigma_i, \sigma_j] = 2i\varepsilon_{ijk}\sigma_k \tag{5.10c}$$

$$(\vec{a}\vec{\sigma})\,(\vec{b}\vec{\sigma}) = \vec{a}\vec{b}\cdot 1 + i(\vec{a}\times\vec{b})\vec{\sigma} \tag{5.10d}$$

$$\left[\vec{a}\vec{\sigma}, \vec{b}\vec{\sigma}\right] = 2i(\vec{a}\times\vec{b})\vec{\sigma} \tag{5.10e}$$

for $i, j, k \in \{1, 2, 3\} \equiv \{x, y, z\}$ and with implicit summation over double indices.

The most general unitary operator in $SU(2)$ is given by $e^{i\mathbf{A}}$ with $\mathbf{A}$ a Hermitian matrix. Since the most general Hermitian operator can be expressed in terms of the Pauli matrices, $\mathbf{A}$ can be written as $\mathbf{A} \equiv \vec{a}\vec{\sigma}$ (up to a trivial additional term proportional to the unity matrix) with $\vec{a}$ being a real vector of three dimensions ($\vec{a} \in \mathbb{R}^3$). Using the series expansion of exponential function, it follows that

$$e^{i\mathbf{A}} = \mathbf{1}\cos a + i\hat{a}\vec{\sigma}\sin a$$

$\hat{a}$ being the unit vector in direction of $\vec{a}$. With this, it is straightforward to look at arbitrary unitary transformations of another unitary operator $B \equiv e^{i\vec{b}\vec{\sigma}}$ ($\vec{b} \in \mathbb{R}^3$), such as $UBU^+$ with the most general $U$ written as $e^{i\vec{a}\vec{\sigma}}$ ($\vec{a} \in \mathbb{R}^3$). For example,

$$\begin{aligned} & e^{i\vec{a}\vec{\sigma}} e^{i\vec{b}\vec{\sigma}} e^{-i\vec{a}\vec{\sigma}} = (\cos a + i\hat{a}\vec{\sigma}\sin a)\left(\cos b + i\hat{b}\vec{\sigma}\sin b\right)(\cos a - i\hat{a}\vec{\sigma}\sin a) \\ = \;& \cos b \cdot 1 + i\sin b\,\left(\hat{b}\vec{\sigma}\cos^2 a + i\cos a\sin a\,\left[\hat{a}\vec{\sigma},\hat{b}\vec{\sigma}\right] + \sin^2 a\;\hat{a}\vec{\sigma}\cdot\hat{b}\vec{\sigma}\cdot\hat{a}\vec{\sigma}\right) \\ = \;& \cos b + i\sin b\;\vec{\sigma}\,\left(\hat{b}\left(\cos^2 a - \sin^2 a\right) - 2\cos a\sin a\;\hat{a}\times\hat{b} + 2\left(\hat{a}\hat{b}\right)\hat{a}\sin^2 a\right) \\ = \;& \cos b\;\mathbf{1} + i\sin b\;\vec{\sigma}\underbrace{\left((1-\hat{a}\circ\hat{a})\,\hat{b}\cos 2a - \hat{a}\times\hat{b}\sin 2a + \left(\hat{a}\hat{b}\right)\hat{a}\right)}_{\equiv\mathbf{R}_{\vec{a}}\hat{b}} \end{aligned}$$

where the notation $\vec{x}\circ\vec{y}$ stands for the tensor product between the two vectors $\vec{x}$ and $\vec{y}$. The final result is thus given as

$$e^{i\vec{a}\vec{\sigma}} e^{i\vec{b}\vec{\sigma}} e^{-i\vec{a}\vec{\sigma}} = \cos b\;\mathbf{1} + i\sin b\;\left(\mathbf{R}_{\vec{a}}\hat{b}\right)\vec{\sigma} \tag{5.11}$$

with $\hat{e} \equiv \mathbf{R}_{\vec{a}}\hat{b} = (1-\hat{a}\circ\hat{a})\,\hat{b}\cos 2a - \hat{a}\times\hat{b}\sin 2a + \left(\hat{a}\hat{b}\right)\hat{a}$ being $\vec{b}$ rotated around $\hat{a}$ by an angle $a$ (see later, Eq. (5.25, p. 112)). Note that since the unitarily transformed unitary operator $e^{i\vec{b}\vec{\sigma}}$ is another unitary operator by construction, the vector $\hat{e}$ must be a unit vector, which is easily verified since it is just the rotated version of the unit vector $\hat{b}$.

Another useful identity, is the unitary transformation of an arbitrary hermitian object described by $\vec{b}\vec{\sigma}$ (with $\vec{b} \in \mathbb{R}^3$ as always)

$$\begin{aligned} e^{i\vec{a}\vec{\sigma}}\;\vec{b}\vec{\sigma}\;e^{-i\vec{a}\vec{\sigma}} &= (\cos a + i\hat{a}\vec{\sigma}\sin a)\,\vec{b}\vec{\sigma}\,(\cos a - i\hat{a}\vec{\sigma}\sin a) \\ &= (\text{similar derivation as for Eq. (5.11)}) \\ &= \vec{\sigma}\underbrace{\left((1-\hat{a}\circ\hat{a})\,\vec{b}\cos 2a - \hat{a}\times\vec{b}\sin 2a + \left(\hat{a}\vec{b}\right)\hat{a}\right)}_{=\mathbf{R}_{\vec{a}}\vec{b}} \\ e^{i\vec{a}\vec{\sigma}}\;\vec{b}\vec{\sigma}\;e^{-i\vec{a}\vec{\sigma}} &= \left(\mathbf{R}_{\vec{a}}\vec{b}\right)\vec{\sigma} \end{aligned} \tag{5.12}$$

with $\mathbf{R}_{\vec{a}}$ as in Eq. (5.25). Thus the unitary transformation of an operator $\vec{b}\vec{\sigma}$ in $SU(2)$ by $e^{i\vec{a}\vec{\sigma}}$ exactly maps into a rotation in the 3D space of the real vector $\vec{b}$ around the vector $\vec{a}$ by an amount $|\vec{a}|$. This equivalence of $SU(2)$ and $O(3)$ will become still more evident later on when considering the time dynamics of quantum two level systems.

### 5.2.1 Spin in Second Quantization

Second quantization is a very transparent formalism, and as such it is very convenient in coding numerical simulations. Since spin was considered in full, in the sense that there was no restriction to singlet/triplet in the program itself, even more, the particle number was given a parameter to the program, it is then interesting to extract information on the total spin for the eigenstates of the overall system. Since the Hubbard Hamiltonian as considered, does not include any spin flip processes, $S^2$ and $S_z$ commute with the Hamiltonian and as such the total spin $S$ is a good quantum number for the total system. It is therefore necessary, to cast the total spin operator into second quantization. This is trivial for $S_z$, but needs more careful algebra in the case of $S^2$ as will be shown.

The spin matrices in Eqs. (5.9) can be cast into the second quantization operators straightforwardly, using the standard recipe for single particle operators [Mat76] where an operator $A$ with the matrix elements $a_{ss'}$ has the following representation

$$A = \sum_{s,s'} a_{ss'} \cdot c_s^+ c_{s'}$$

where $s$ and $s'$ refer to the specific states in the corresponding Hilbert space. Thus for a set of particles, the Pauli matrices become

$$\sigma_x^{(i)} = c_{i\uparrow}^+ c_{i\downarrow} + c_{i\downarrow}^+ c_{i\uparrow} \tag{5.13a}$$
$$\sigma_y^{(i)} = -i\ c_{i\uparrow}^+ c_{i\downarrow} + i\ c_{i\downarrow}^+ c_{i\uparrow} \tag{5.13b}$$
$$\sigma_z^{(i)} = c_{i\uparrow}^+ c_{i\uparrow} - c_{i\downarrow}^+ c_{i\downarrow} \tag{5.13c}$$

The super index $i$ refers to the combined index of which particle in what spatial orbital, while the $s^{(\prime)}$ index above becomes the spin index $\{\uparrow, \downarrow\}$. By using the known commutator relationships for the $c_i^{(+)}$ only as in Eqs. (5.1), exactly the same spin matrix relationships as in Eqs. (5.10) can be derived from Eqs. (5.13) consistently for the case of a single particle. But for more than one particle, exchange and correlation effects contribute additional terms. The following examples will show this more clearly. The commutator relationships in Eq. (5.10c) still hold in the general case (with the index $i$ dropped for readability where convenient)

$$\begin{aligned}
[\sigma_x, \sigma_y] &= \left[c_\uparrow^+ c_\downarrow + c_\downarrow^+ c_\uparrow,\ -i\ c_\uparrow^+ c_\downarrow + i\ c_\downarrow^+ c_\uparrow\right] \\
&= -i\underbrace{\left[c_\uparrow^+ c_\downarrow,\ c_\uparrow^+ c_\downarrow\right]}_{=0} + i\left[c_\uparrow^+ c_\downarrow,\ c_\downarrow^+ c_\uparrow\right] - i\left[c_\downarrow^+ c_\uparrow,\ c_\uparrow^+ c_\downarrow\right] + i\underbrace{\left[c_\downarrow^+ c_\uparrow,\ c_\downarrow^+ c_\uparrow\right]}_{=0} \\
&= \text{(using Eq. (5.1c))} \\
&= 2 \cdot i\left(c_\uparrow^+ c_\uparrow - c_\downarrow^+ c_\downarrow\right)
\end{aligned}$$

$$= \quad 2i\ \sigma_z$$

or including the (particle+state) indices $i$ and $j$

$$\left[\sigma_x^{(i)}, \sigma_y^{(j)}\right] = 2i\ \delta_{ij}\ \sigma_z^{(i)}$$

consistent with Eq. (5.10c). For the square of the Pauli matrices, however, the result is as follows

$$\begin{aligned}
\left(\sigma_x^{(i)}\right)^2 &= \left(c_{i\uparrow}^+ c_{i\downarrow} + c_{i\downarrow}^+ c_{i\uparrow}\right)\left(c_{i\uparrow}^+ c_{i\downarrow} + c_{i\downarrow}^+ c_{i\uparrow}\right) \\
&= \underbrace{c_{i\uparrow}^+ c_{i\downarrow} c_{i\uparrow}^+ c_{i\downarrow}}_{=-c_{i\uparrow}^+ c_{i\uparrow}^+ c_{i\downarrow} c_{i\downarrow}=0} + \underbrace{c_{i\uparrow}^+ c_{i\downarrow} c_{i\downarrow}^+ c_{i\uparrow}}_{=+c_{i\uparrow}^+ c_{i\uparrow}\cdot c_{i\downarrow} c_{i\downarrow}^+} + c_{i\downarrow}^+ c_{i\uparrow} c_{i\uparrow}^+ c_{i\downarrow} + \underbrace{c_{i\downarrow}^+ c_{i\uparrow} c_{i\downarrow}^+ c_{i\uparrow}}_{=0} \\
&= (\text{using } c^+ c^+ = 0 \text{ since } \left\{c^+, c^+\right\} = 0) \\
&= c_{i\uparrow}^+ c_{i\uparrow} \cdot c_{i\downarrow} c_{i\downarrow}^+ + c_{i\downarrow}^+ c_{i\downarrow} \cdot c_{i\uparrow} c_{i\uparrow}^+ \\
&= c_{i\uparrow}^+ c_{i\uparrow}\left(\left\{c_{i\downarrow}, c_{i\downarrow}^+\right\} - c_{i\downarrow}^+ c_{i\downarrow}\right) + c_{i\downarrow}^+ c_{i\downarrow}\left(\left\{c_{i\uparrow}, c_{i\uparrow}^+\right\} - c_{i\uparrow}^+ c_{i\uparrow}\right) \\
&= c_{i\uparrow}^+ c_{i\uparrow} + c_{i\downarrow}^+ c_{i\downarrow} - 2\ c_{i\uparrow}^+ c_{i\uparrow} \cdot c_{i\downarrow}^+ c_{i\downarrow} \\
&= (\text{not that this is equal to } \left(\sigma_z^{(i)}\right)^2) \\
&\equiv \mathbf{1}^{(i)} - 2\ n_{i\uparrow} n_{i\downarrow}
\end{aligned} \tag{5.14}$$

In the simple single particle picture, the second term vanishes and thus the usual result Eq. (5.10b) is obtained. Here, the second quantization is just an alternative way of writing out the matrices. For the case of more than one particle, however, the arithmetic within the formalism of second quantization becomes a much more systematic way of describing the system including the correct physically and essential particle (Fermi) statistics. This is also reflected in the general case of multiplying two arbitrary operators $\mathbf{A}$ and $\mathbf{B}$

$$\begin{aligned}
\mathbf{A}\cdot\mathbf{B} &= \left(\sum_{ij} a_{ij}\ c_i^+ c_j\right)\cdot\left(\sum_{i'j'} b_{i'j'}\ c_{i'}^+ c_{j'}\right) \\
&= \sum_{ij,i'j'} a_{ij} b_{i'j'}\ c_i^+ c_j\ c_{i'}^+ c_{j'} \\
&= \sum_{ij,i'j'} a_{ij} b_{i'j'}\ c_i^+ \left(\underbrace{\left\{c_j, c_{i'}^+\right\}}_{=\delta_{ji'}} - c_{i'}^+ c_j\right) c_{j'} \\
&= (\text{equivalent to using Wicks theorem}) \\
&= \sum_{ij}\left(\sum_k a_{ik} b_{kj}\right)\ c_i^+ c_j - \sum_{ij,i'j'} a_{ij} b_{i'j'}\ c_i^+ c_{i'}^+ c_j c_{j'}
\end{aligned} \tag{5.15}$$

In the single particle picture, the matrix elements are evaluated by $\langle i|\,\mathbf{A}\cdot\mathbf{B}\,|j\rangle = \langle 0|\,c_i\cdot\mathbf{AB}\cdot c_j^+\,|0\rangle$ for which the second term vanishes. The remaining first term then represents exactly what one would expect from the matrix multiplication of $\mathbf{A}$ and $\mathbf{B}$. In the case of more than one particle, however, particle correlation comes into play. The first term in Eq. (5.15) corresponds to the *direct* term then, while the remaining *exchange* and *correlation* contributions are taken care of by the second term [Mat76, p. 131, 141].

With all this prerequisites at hand, the components of the total spin operator $\mathbf{S}\equiv(\mathbf{S}_x,\mathbf{S}_y,\mathbf{S}_z)$ are written as

$$\begin{aligned}
\mathbf{S}_x &\equiv \frac{1}{2}\sum_i \sigma_x^{(i)} \equiv \frac{1}{2}\sigma_x = \frac{1}{2}\sum_i \left(c_{i\uparrow}^+ c_{i\downarrow} + c_{i\downarrow}^+ c_{i\uparrow}\right)\\
\mathbf{S}_y &\equiv \frac{1}{2}\sum_i \sigma_y^{(i)} \equiv \frac{1}{2}\sigma_y = -\frac{i}{2}\sum_i \left(c_{i\uparrow}^+ c_{i\downarrow} - c_{i\downarrow}^+ c_{i\uparrow}\right)\\
\mathbf{S}_z &\equiv \frac{1}{2}\sum_i \sigma_z^{(i)} \equiv \frac{1}{2}\sigma_z = \frac{1}{2}\sum_i \left(c_{i\uparrow}^+ c_{i\uparrow} - c_{i\downarrow}^+ c_{i\downarrow}\right)
\end{aligned}$$

The square of the total angular momentum follows as

$$\begin{aligned}
\mathbf{S}^2 &\equiv \frac{1}{4}\left(\sigma_x^2+\sigma_y^2+\sigma_z^2\right)\\
&= \frac{1}{4}\left(\frac{1}{2}\left(\left(\sigma_x+i\sigma_y\right)\left(\sigma_x-i\sigma_y\right)+\left(\sigma_x-i\sigma_y\right)\left(\sigma_x+i\sigma_y\right)\right)+\sigma_z^2\right)\\
&= \frac{1}{2}\left(\sigma^+\sigma^- + \sigma^-\sigma^+\right)+\frac{1}{4}\sigma_z^2\\
&= (\text{separating } i=j \text{ from } i\neq j)\\
&= \frac{1}{4}\sum_i\left(\left(\sigma_x^{(i)}\right)^2+\left(\sigma_y^{(i)}\right)^2+\left(\sigma_z^{(i)}\right)^2\right)+\frac{2}{2}\sum_{i<j}\left(\sigma_{(i)}^+\sigma_{(j)}^- + \sigma_{(j)}^-\sigma_{(i)}^+\right)+\frac{2}{4}\sum_{i<j}\sigma_z^{(i)}\sigma_z^{(j)}
\end{aligned}$$

and finally

$$\boxed{\mathbf{S}^2 = \tfrac{1}{4}\sum_i\left(\left(\sigma_x^{(i)}\right)^2+\left(\sigma_y^{(i)}\right)^2+\left(\sigma_z^{(i)}\right)^2\right)+\tfrac{1}{2}\sum_{i<j}\sigma_z^{(i)}\sigma_z^{(j)}+\sum_{i<j}\left(\sigma_{(i)}^+\sigma_{(j)}^- + \sigma_{(j)}^-\sigma_{(i)}^+\right)} \tag{5.16}$$

where $\sigma^+\equiv\frac{1}{2}\left(\sigma_x+i\sigma_y\right)$ and $\sigma^-\equiv\frac{1}{2}\left(\sigma_x-i\sigma_y\right)$ such that $\left(\sigma^-\right)^+=\sigma^+$ and thus

$$\sigma_{(i)}^+ \equiv \begin{pmatrix}0 & 1\\ 0 & 0\end{pmatrix} \equiv c_{i\uparrow}^+ c_{i\downarrow}$$

$$\sigma^-_{(i)} \equiv \begin{pmatrix} 0 & 0 \\ 1 & 0 \end{pmatrix} \equiv c^+_{i\downarrow} c_{i\uparrow}$$

The first two terms in Eq. (5.16) enter in the diagonal of the $\mathbf{S}^2$ matrix when taken in the $c^+_i$ basis. The last term, generates off–diagonal terms and thus mixes the single particle spin states with the effect to generate eigenstates of the total spin operator for the system.

As an example, the case of two particles is worked out in detail. More specifically, the matrix elements $\langle i\sigma'', j\sigma'''| \mathbf{S}^2 |i\sigma, j\sigma'\rangle$ are evaluated. Note that since $\mathbf{S}^2$ only acts on the spin, the (particle+state) indices $i$ and $j$ must be the same on the left and on the right of $\langle \ldots | \mathbf{S}^2 | \ldots \rangle$. The first terms to be evaluated are of the sort

$$\begin{aligned}
\textstyle\sum_{i'} & \left(\sigma_x^{(i')}\right)^2 \cdot c^+_{i\sigma} c^+_{j\sigma'} |0\rangle = \text{(using Eq. (5.14))} \\
= & \sum_{i'} \left( \mathbf{1}^{(i')} - 2\, n_{i'\uparrow} n_{i'\downarrow} \right) \cdot c^+_{i\sigma} c^+_{j\sigma'} |0\rangle \\
= & \sum_{i'} \left( n_{i'\uparrow} + n_{i'\downarrow} - 2\, n_{i'\uparrow} n_{i'\downarrow} \right) \cdot c^+_{i\sigma} c^+_{j\sigma'} |0\rangle \\
= & \begin{cases} 2\, c^+_{i\sigma} c^+_{j\sigma'} |0\rangle & \text{if } i \neq j, \\ 0 & \text{if } i = j. \end{cases}
\end{aligned}$$

Thus, for the case $i \neq j$, one gets

$$\langle i\sigma'', j\sigma'''| \mathbf{S}^2 |i\sigma, j\sigma'\rangle = \left(\begin{array}{c|ccc|c} \frac{6}{4}+\frac{1}{2} & & & & \\ \hline & \frac{6}{4}-\frac{1}{2} & & 1 & \\ & & 1 & \frac{6}{4}-\frac{1}{2} & \\ \hline & & & & \frac{6}{4}+\frac{1}{2} \end{array}\right) = \left(\begin{array}{c|cc|c} 2 & & & \\ \hline & 1 & 1 & \\ & 1 & 1 & \\ \hline & & & 2 \end{array}\right)$$

with the empty places being equal to zero. This is the expected result for two coupled spin 1/2 particles and results in the usual singlet (triplet) eigenstates with the eigenvalues of 0 (2), respectively.

The case of $i = j$ is quite distinct. The two particles must have different spin (Pauli exclusion principle), so that the resulting space has only one dimension. Since by Eq. (5.14) $\mathbf{S}^2 |i\sigma, i\bar{\sigma}\rangle = 0$ with $\bar{\sigma}$ being defined as having the opposite spin of $\sigma$, the eigenvalue of $\mathbf{S}^2$ is 0. It is also easily shown that the eigenvalue of $\mathbf{S}_z$ is equal to 0, too, the resulting state is the well known singlet state for this particular case.

Summarizing, in second quantization the particle correlation plays an essential role which must be accounted for carefully. In the codes written for numerical analysis of

few particle states, it was finally Eq. (5.16) which was coded for the general case where the number of particles $n_e$ entered as a parameter. From Eq. (5.16) it is obvious that $\mathbf{S}^2$ will be highly sparse: for example, for an $\mathcal{N}$ dimensional Hilbert space without spin, the inclusion of spin results in an $N = \mathcal{N} \cdot 2^{n_e} + \mathcal{N}_{do}$ dimensional Hilbert space due to the folding in of the spin configuration space. The extra term $\mathcal{N}_{do}$ keeps record of the now possible double occupancy of every state. Most terms in $\mathbf{S}^2$ will be diagonal. The off–diagonal terms come from pairs of particles in different states $i$, and consequently the sparsity of $\mathbf{S}^2$ is determined by the maximum number of pairs in different states that can be formed which is $\binom{n_e}{2} = \frac{1}{2} n_e \left(n_e - 1\right)$ which in general is significantly smaller than the total dimension of the available Hilbert space.

### 5.2.2 Spin Representation and Spin Dynamics

Qubit systems are mapped conveniently into the spin 1/2 notation with its Pauli matrices (pseudo spin) where the potential is described by an effective magnetic field (pseudo field). Since the dynamics of a single qubit is considered only, this is a single particle description and the second quantization can be put aside in the following.

The pseudo–spin, in the following just called *spin*, can be oriented arbitrarily in its 3D quantum space. This orientation is most conveniently extracted by writing the general state $|\psi\rangle = (c_1,\ c_2)$ with the scalar coefficients $c_1$ and $c_2$ in the equivalent density matrix [Bal99, p. 171]. For the state $|\psi\rangle = (c_1,\ c_2)$, the density matrix $\rho$ is given by

$$\rho \equiv |\psi\rangle \langle\psi| = \begin{pmatrix} c_1 \\ c_2 \end{pmatrix} \begin{pmatrix} c_1^* & c_2^* \end{pmatrix} = \begin{pmatrix} |c_1|^2 & c_1 c_2^* \\ c_1^* c_2 & |c_2|^2 \end{pmatrix} \equiv \frac{1}{2}\left(1 + \vec{r}\vec{\sigma}\right) \tag{5.17}$$

where $\vec{\sigma} \equiv (\sigma_z, \sigma_y, \sigma_y)$ is the vector of the usual Pauli spin matrices in Eq. (5.9). The last step in Eq. (5.17) defines the *polarization* vector $\vec{r}$ which is equivalent to the Bloch vector [Bal99, p. 171] and defines the orientation of the spin in its 3D quantum space. For a pure state, $\vec{r}$ has its maximum length of one since

$$\begin{aligned}
1 &= \langle\psi|\psi\rangle^2 = \langle\psi|\,\rho\,|\psi\rangle = \mathrm{tr}\left\{\rho^2\right\} \\
&= \frac{1}{4}\mathrm{tr}\left\{\left(1 + \vec{r}\vec{\sigma}\right)\left(1 + \vec{r}\vec{\sigma}\right)\right\} = \frac{1}{4}\mathrm{tr}\left\{1 + 2\vec{r}\vec{\sigma} + \left(\vec{r}\vec{\sigma}\right)^2\right\} \\
&= \frac{1 + |\vec{r}|^2}{4}\underbrace{\mathrm{tr}\left\{\mathbf{1}\right\}}_{=2} + \frac{2}{4}\underbrace{\mathrm{tr}\left\{\vec{r}\vec{\sigma}\right\}}_{=0} \\
&= \text{(using Eqs. (5.10))} \\
&= \frac{1}{2}\left(1 + |\vec{r}|^2\right) \quad \Longleftrightarrow \quad |\vec{r}| = 1
\end{aligned}$$

while on the other hand in the opposite case of a completely statistical mixture of states, the length of $\vec{r}$ becomes zero. Here, we are dealing with (idealized) pure states, and thus $|\vec{r}| \equiv |\hat{r}| = 1$. The density matrix in Eq. (5.17) obeys its usual relation $\mathrm{tr}\{\rho\} = 1$ independent of $\hat{r}$ related to the proper normalization of $|\psi\rangle$ as can be seen by applying Eq. (5.10a). Eq. (5.10a) immediately also gives the recipe to extract the coefficients $r_i$ from the density matrix, namely

$$r_i = \mathrm{tr}\{\sigma_i \rho\} \tag{5.18}$$

noting that $\mathrm{tr}\{\mathbf{1}\} \equiv \mathrm{tr}\{\sigma_0\} = 2$. Therefore, the coefficients of the Bloch vector are given as

$$\begin{pmatrix} r_x \\ r_y \\ r_z \end{pmatrix} = \begin{pmatrix} \mathrm{tr}\{\sigma_x \rho\} \\ \mathrm{tr}\{\sigma_y \rho\} \\ \mathrm{tr}\{\sigma_z \rho\} \end{pmatrix} = \begin{pmatrix} c_1 c_2^* + c_1^* c_2 \\ i\left(c_1 c_2^* - c_1^* c_2\right) \\ |c_1|^2 - |c_2|^2 \end{pmatrix} = \begin{pmatrix} 2\mathrm{Re}\{c_1 c_2^*\} \\ -2\mathrm{Im}\{c_1 c_2^*\} \\ |c_1|^2 - |c_2|^2 \end{pmatrix} \tag{5.19}$$

The direction of the Bloch vector can also be described by two angles $\vartheta$ and $\varphi$ in typical spherical coordinates, such that for a pure state

$$\begin{pmatrix} r_x \\ r_y \\ r_z \end{pmatrix} = \begin{pmatrix} \sin\vartheta\cos\varphi \\ \sin\vartheta\sin\varphi \\ \cos\vartheta \end{pmatrix} = \begin{pmatrix} 2\mathrm{Re}\{c_1 c_2^*\} \\ -2\mathrm{Im}\{c_1 c_2^*\} \\ |c_1|^2 - |c_2|^2 \end{pmatrix}$$

from which it follows immediately that $c_1 c_2^* = \mathrm{Re}\{c_1 c_2^*\} + i\mathrm{Im}\{c_1 c_2^*\} = \frac{1}{2}(\sin\vartheta e^{-i\varphi})$ and thus $|c_1 c_2^*|^2 = |c_1|^2 |c_2|^2 = \frac{1}{4}\sin^2\vartheta$. From the equations $|c_1|^2 + |c_2|^2 = 1$ and $|c_1|^2 - |c_2|^2 = \cos\vartheta$, $|c_1|^2$ and $|c_2|^2$ are determined as $|c_1|^2 = \frac{1}{2}(1+\cos\vartheta) = \cos^2\left(\frac{\vartheta}{2}\right)$ and $|c_2|^2 = \frac{1}{2}(1-\cos\vartheta) = \sin^2\left(\frac{\vartheta}{2}\right)$. Finally, the state $|\psi\rangle$ in terms of the angles of the Bloch vector is given as

$$|\psi\rangle = e^{i\gamma}\left(\cos\frac{\vartheta}{2}, e^{i\varphi}\sin\frac{\vartheta}{2}\right)$$

with the arbitrary but irrelevant overall phase $\gamma$ [NC00, p. 15].

Now having the Bloch vector representation of the quantum two–level system (qu2LS), the Bloch vectors time evolution is governed by its Hamiltonian. The most general 2D Hamiltonian written in terms of the Pauli matrices is

$$H = \varepsilon_0 1 + \vec{B}\vec{\sigma} \tag{5.20}$$

where henceforth, $\varepsilon_0$ will be set to zero since it solely acts as an energy reference. The

time evolution for the density matrix is given by the equivalent of the Schrödinger equation [Bal99, p. 171]

$$i\frac{d}{dt}\rho = [H, \rho] \tag{5.21}$$

called the Liouville equation where for simplicity $\hbar$ is set to 1. Using Eq. (5.20), this translates into

$$\begin{aligned} i\frac{d}{dt}\vec{r}\vec{\sigma} &= \left[\vec{B}\vec{\sigma}, \vec{r}\vec{\sigma}\right] = 2i\left(\vec{B}\times\vec{r}\right)\vec{\sigma} \\ \frac{d}{dt}\vec{r} &= 2\vec{B}\times\vec{r} \end{aligned} \tag{5.22}$$

Now since the change in $\vec{r}$ is always perpendicular to $\vec{r}$, its length is preserved. The equivalent mathematical statement is $\frac{d}{dt}r^2 = 2\vec{r}\frac{d\vec{r}}{dt} = 4\vec{r}\left(\vec{B}\times\vec{r}\right) = 0$. The solution to Eq. (5.22) for constant $\vec{B}$ is trivial: the vector $\vec{r}$ rotates around the vector $\vec{B}$ with angular frequency $\omega = \left|2\vec{B}\right|$ since $\frac{d}{dt}r_{||} = 0$ and $\frac{d}{dt}r_{\perp} = 2Br_{\perp}$. This is in complete analogy with the solution of the spin rotating around a static magnetic field $\vec{B}$ [MW98, p. 194]. Now in order to rotate the spin to any orientation, it is clear from 3D analogy that subsequent rotations around two distinct axes are sufficient for doing so. Yet since the 3D space of $O(3)$ is mapped isomorphically into $SU(2)$, the generators for the rotations around $x$, $y$ and $z$ are the Pauli spin matrices. Every rotation in 3D is mapped into a unitary transformation in $SU(2)$. Moreover, every rotation can be decomposed into a sequence of rotations around two distinct axes [NC00, p. 175]

$$U = e^{i\alpha}R_{\hat{n}}(\beta)\,R_{\hat{m}}(\gamma)\,R_{\hat{n}}(\delta) \tag{5.23}$$

with $\hat{n}$ and $\hat{m}$ being non–parallel unit vectors and $a$, $\beta$, $\gamma$ and $\delta$ appropriately chosen angles. The rotation matrices $R_{\hat{n}}(\beta)$ are defined as rotations around the axis $\hat{n}$ by an angle $\vartheta$ which is mathematically represented in $SU(2)$ by $R_{\hat{n}}(\vartheta) \equiv \exp\left[-i\frac{\vartheta}{2}\hat{n}\vec{\sigma}\right]$. For the case of an effective magnetic field $\vec{B} \equiv B\hat{n}$ applied during a certain time interval with $\hat{n} = const$, the effective rotational operator for the qu2LS is $R_{\hat{n}}(\vartheta) \equiv \exp\left[-i\hat{n}\vec{\sigma}\cdot\beta\right]$ with $\beta = \int dtB(t)$.

Finally, the energy expectation value for a given $|\psi\rangle$ is easily evaluated in above spin notation

$$\begin{aligned} \langle\psi|H|\psi\rangle &= \mathrm{tr}\{H\rho\} = \frac{1}{2}\mathrm{tr}\left\{\vec{B}\vec{\sigma}\left(1+\hat{r}\vec{\sigma}\right)\right\} \\ &= \frac{1}{2}\mathrm{tr}\left\{\vec{B}\vec{\sigma}\cdot\hat{r}\vec{\sigma}\right\} = \frac{1}{2}\mathrm{tr}\left\{\vec{B}\hat{r} + i\left(\vec{B}\times\hat{r}\right)\vec{\sigma}\right\} \\ &= \frac{\vec{B}\hat{r}}{2}\mathrm{tr}\{\mathbf{1}\} = \vec{B}\hat{r} \end{aligned} \tag{5.24}$$

This implies straightforwardly, that an $\hat{r}$ parallel to $\vec{B}$ has the highest energy, while an $\hat{r}$ antiparallel to $\vec{B}$ has the lowest.

### 5.2.3 Short Review on Rotations in 3D

Let $\tilde{\mathbf{L}} \equiv \{\mathbf{L}_x, \mathbf{L}_y, \mathbf{L}_z\}$ be the vector of generator for the rotations in 3D [Jac99, p. 545], i.e.

$$\mathbf{L}_x = \begin{pmatrix} 0 & 0 & 0 \\ 0 & 0 & i \\ 0 & -i & 0 \end{pmatrix}, \; \mathbf{L}_y = \begin{pmatrix} 0 & 0 & -i \\ 0 & 0 & 0 \\ i & 0 & 0 \end{pmatrix}, \; \mathbf{L}_z = \begin{pmatrix} 0 & i & 0 \\ -i & 0 & 0 \\ 0 & 0 & 0 \end{pmatrix}$$

such that

$$\begin{aligned} \mathbf{R}_{\hat{n}}(\alpha \equiv \omega t) &\equiv \mathbf{R}(\vec{\omega} t) = e^{i\vec{\omega}\tilde{\mathbf{L}} \cdot t} \\ &= \hat{\omega} \circ \hat{\omega} + \cos \omega t \; (1 - \hat{\omega} \circ \hat{\omega}) + \sin \omega t \; i\hat{\omega}\tilde{\mathbf{L}} \\ \mathbf{R}(\vec{\omega} t) &= \hat{\omega} \circ \hat{\omega} + \cos \omega t \; (1 - \hat{\omega} \circ \hat{\omega}) + \sin \omega t \; \hat{\omega}\times \end{aligned} \tag{5.25}$$

These $\mathbf{R}_{\hat{n}}(\alpha)$ correspond to the usual rotation matrices in 3D. In this derivation, usage of the following identity is made

$$\begin{aligned} \left(\vec{\omega}\tilde{\mathbf{L}}\right)^2 &= \sum_{i,j} (\omega_i \mathbf{L}_i)(\omega_j \mathbf{L}_j) = \sum_{i,j} \omega_i \omega_j \mathbf{L}_i \mathbf{L}_j \\ &= \begin{pmatrix} \omega_2^2 + \omega_3^2 & -\omega_1\omega_2 & -\omega_1\omega_3 \\ -\omega_2\omega_1 & \omega_1^2 + \omega_3^2 & -\omega_2\omega_3 \\ -\omega_3\omega_1 & -\omega_3\omega_2 & \omega_1^2 + \omega_2^2 \end{pmatrix} \\ &= \omega^2 (1 - \hat{\omega} \circ \hat{\omega}) \end{aligned}$$

with the essential property $(1 - \hat{\omega} \circ \hat{\omega})^2 = 1 - \hat{\omega} \circ \hat{\omega}$.

In the peculiar notation of Eq. (5.25), all three terms to the RHS are essentially projectors orthogonal to each other: with $P_1 \equiv P_\parallel \equiv \hat{\omega} \circ \hat{\omega}$, $P_2 \equiv P_{\perp 1} \equiv 1 - \hat{\omega} \circ \hat{\omega}$ and $P_3 \equiv P_{\perp 2} \equiv \hat{\omega}\times$, any rotation $\mathbf{R}(\vec{\omega} t)$ can be written as

$$\mathbf{R}(\vec{\omega} t) = P_\parallel + P_{\perp 1} \cos \omega t + P_{\perp 2} \sin \omega t$$

where $P_\parallel = \hat{\omega} \circ \hat{\omega}$ projects parallel to $\hat{\omega}$, while $P_{\perp 1} = 1 - \hat{\omega} \circ \hat{\omega}$ projects out the component normal to $\hat{\omega}$. $P_{\perp 2} = \hat{\omega}\times$ projects out the same part as $P_{\perp 1}$, but is rotated in addition around $\hat{\omega}$ by 90°. The cos and sin terms, finally, fix the rotational angle. The orthogonality of these projections is straightforwardly shown, since $P_\parallel \cdot P_{\perp 1} = (\hat{\omega} \circ \hat{\omega}) \cdot (1 - \hat{\omega} \circ \hat{\omega}) = \hat{\omega} \circ (\hat{\omega} - (\hat{\omega}\hat{\omega})\hat{\omega}) = 0$. Taking an arbitrary auxiliary

vector $\vec{b}$, it also follows that the projections $P_{\parallel}\vec{b}$ and $P_{\perp 2}\vec{b}$ as well as $P_{\perp 1}\vec{b}$ and $P_{\perp 2}\vec{b}$ are also orthogonal to each other: $\left(P_{\parallel}\vec{b}\right)\left(P_{\perp 2}\vec{b}\right) = \left(\hat{\omega}\vec{b}\right)\hat{\omega}\left(\hat{\omega}\times\vec{b}\right) = 0$ and also $\left(P_{\perp 1}\vec{b}\right)\left(P_{\perp 2}\vec{b}\right) = \left(\vec{b}-\left(\hat{\omega}\vec{b}\right)\hat{\omega}\right)\left(\hat{\omega}\times\vec{b}\right) = 0$. Note, however, that the product $P_{\perp 1}P_{\perp 2}$ itself is not equal to zero. When rotating a vector around itself only the first term in Eq. (5.25) contributes, in the sense that $\mathbf{R}(\vec{\omega}t)\cdot\vec{\omega} = \vec{\omega}$ leaves the vector unchanged as it must by construction. Finally, acting with $\mathbf{R}(\vec{\omega}t)$ on an arbitrary vector $\vec{b}$ and with $\gamma$ being the angle between $\vec{\omega}$ and $\vec{b}$, the length squared of the result is $\left(\mathbf{R}(\vec{\omega}t)\,\vec{b}\right)^2 = b^2\left((\sin\gamma\cos 2a)^2 + (\sin\gamma\sin 2a)^2 + (\cos\gamma)^2\right) = b^2$, i.e. it is preserved as expected.

As a short application of the rotation matrices above, the rotating frame of reference is considered used later in this chapter. In this system, space revolves around $\hat{\omega}$ with frequency $\omega t$. All vectors $\vec{v}$ are replaced by their rotating versions marked by a twiddle. $\vec{v}$ and $\tilde{v}$ are connected by the relationship $\vec{v}\equiv\mathbf{R}\tilde{v}$ where $\mathbf{R}\equiv e^{i\vec{\omega}\tilde{\mathbf{L}}\,t}$ describes the rotating frame. The effect on the first order derivatives is as follows: $\frac{d}{dt}\vec{r} = \frac{d}{dt}\left(\mathbf{R}\left(\mathbf{R}^{-1}r\right)\right) \equiv \frac{d}{dt}\left(\mathbf{R}\tilde{r}\right) = \mathbf{R}\frac{d}{dt}\tilde{r} + \left(\frac{d}{dt}\mathbf{R}\right)\tilde{r} = \mathbf{R}\frac{d}{dt}\tilde{r} - i\vec{\omega}\tilde{\mathbf{L}}\cdot\mathbf{R}\tilde{r} = \mathbf{R}\frac{d}{dt}\tilde{r} + \vec{\omega}\times\mathbf{R}\tilde{r}$. Note that here $\left[\mathbf{R},\vec{\omega}\tilde{\mathbf{L}}\right] = 0$ and therefore $\vec{\omega}\times\left(\mathbf{R}\tilde{r}\right) = \mathbf{R}\left(\vec{\omega}\times\tilde{r}\right)$. Use of this will be made shortly in the context of Rabi oscillations.

### 5.2.4 Rabi Oscillations in a Two–Level System

In the previous section the dynamics of a two–level system, mapped onto a spin system was discussed. Once an effective $\vec{B}$ is turned on and set constant, the pseudo spin precesses around the direction of the vector $\vec{B}$. This precession, however, preserves energy. This is easily seen, realizing the energy expectation value will not change while $|\psi\rangle$ is rotating around $\vec{B}$ since the projection of the Bloch vector onto $\vec{B}$ will remain the same and therefore according to Eq. (5.24), $\langle\psi|H|\psi\rangle = const.$

Rabi oscillations, however, do exactly the opposite, namely they change the energy in the system in a coherent fashion with the state $|\psi\rangle$ pumped periodically between the two eigenstates thus gaining and loosing energy periodically to and from the interacting environment. For this the system must be coupled to the exterior via an oscillating perturbation such as photons which are in resonance with the energy splitting of the two–level system in the sense that $\hbar\omega_{driving} \approx \varepsilon_2 - \varepsilon_1$.

Using the generic Hamiltonian $H = H_0 + V$ with $H_0 = \varepsilon_0 + \vec{h}_0\vec{\sigma}$ and the perturbation $V = V_0\cos\omega t \equiv \vec{v}_0\vec{\sigma}\cos\omega t \equiv \vec{v}(t)\,\vec{\sigma}$, the time evolution of the Bloch vector is described by Eq. (5.22)

$$\frac{d}{dt}\vec{r} = 2\left(\vec{h}_0 + \vec{v}(t)\right)\times\vec{r} \tag{5.26}$$

To eliminate the static $\vec{h}_0$ term, a rotating frame of reference is chosen. For this,

the following substitutions are made: every vector $\vec{v}$ is replaced by its rotating frame equivalent $\tilde{v}$, where $\vec{v} \equiv \mathbf{R}\tilde{v}$ with $\mathbf{R} \equiv e^{i\vec{\omega}\tilde{\mathbf{L}}t}$, and the first order derivatives $\frac{d}{dt}\vec{r}$ are replaced by $\frac{d}{dt}\tilde{r} + \vec{\omega} \times \tilde{r}$ as shown in the previous section. With this in mind and choosing $\vec{\omega} = 2\vec{h}_0$, Eq. (5.26) becomes

$$\begin{aligned} \frac{d}{dt}\tilde{r} + 2\vec{h}_0 \times \tilde{r} &= 2\left(\tilde{h}_0 + \tilde{v}\,(t)\right) \times \tilde{r} \\ \frac{d}{dt}\tilde{r} &= 2\,\tilde{v}\,(t) \times \tilde{r} \qquad (5.27a) \\ &= 2\,\left(e^{-i2t\vec{h}_0\tilde{\mathbf{L}}}\vec{v}\,(t)\right) \times \tilde{r} \qquad (5.27b) \end{aligned}$$

Note that $\tilde{h}_0 = \vec{h}_0$ and that the previously static direction of $\vec{v}\,(t)$ is now rotating around $\vec{h}_0$ in reverse direction with frequency $\omega = 2h_0$.

For illustration, the following explicit example is taken:

$$H_0 = \begin{pmatrix} \frac{\Delta}{2} & 0 \\ 0 & -\frac{\Delta}{2} \end{pmatrix} \equiv \vec{h}_0\vec{\sigma},\ V_0 = \begin{pmatrix} 0 & V \\ V & 0 \end{pmatrix} \equiv \vec{v}\vec{\sigma}$$

such that $\vec{h}_0 = \frac{\Delta}{2}(0,0,1)$ and $\vec{v} = V(1,0,0)$. Note that here the perturbation $\vec{v}$ is orthogonal to $\vec{h}_0$. With this and $\tilde{r} \equiv (\tilde{r}_x, \tilde{r}_y, \tilde{r}_z)$, Eq. (5.27b) becomes

$$\begin{aligned} \frac{d}{dt}\tilde{r} &= 2V\left(e^{-it\Delta\mathbf{L}_z}\begin{pmatrix}1\\0\\0\end{pmatrix}\cos\omega t\right) \times \tilde{r} = 2V\cos\omega t\begin{pmatrix}\cos\Delta t\\-\sin\Delta t\\0\end{pmatrix} \times \tilde{r} \\ &= 2V\cos\omega t\begin{pmatrix}0 & 0 & -\sin\Delta t\\ 0 & 0 & -\cos\Delta t\\ \sin\Delta t & \cos\Delta t & 0\end{pmatrix}\begin{pmatrix}\tilde{r}_x\\\tilde{r}_y\\\tilde{r}_z\end{pmatrix} \end{aligned}$$

The participating frequencies are extracted as follows $2\cos\omega t\sin\Delta t = \sin(\Delta+\omega)t + \sin(\Delta-\omega)t$ and $2\cos\omega t\cos\Delta t = \cos(\Delta+\omega)t + \cos(\Delta-\omega)$, therefore

$$\frac{d}{dt}\begin{pmatrix}\tilde{r}_x\\\tilde{r}_y\\\tilde{r}_z\end{pmatrix} = \mathrm{Re}\left[V\left[e^{i(\Delta+\omega)t} + e^{i(\Delta-\omega)t}\right]\begin{pmatrix}0 & 0 & i\\ 0 & 0 & -1\\ -i & 1 & 0\end{pmatrix}\right]\begin{pmatrix}\tilde{r}_x\\\tilde{r}_y\\\tilde{r}_z\end{pmatrix}$$

Thus the only participating frequencies are $e^{i(\Delta\pm\omega)t}$. The first term *oscillates at an*

*altogether different frequency so that its time averaged contribution* to $\tilde{r}$ is *negligible* [Yar68, p. 214].

Further, for the special case of when the perturbation is in exact resonance with the splitting $\Delta$, namely $\omega = \Delta$, this differential equation simplifies further to

$$\frac{d}{dt}\begin{pmatrix}\tilde{r}_x\\ \tilde{r}_y\\ \tilde{r}_z\end{pmatrix} = V\begin{pmatrix}0 & 0 & 0\\ 0 & 0 & -1\\ 0 & 1 & 0\end{pmatrix}\begin{pmatrix}\tilde{r}_x\\ \tilde{r}_y\\ \tilde{r}_z\end{pmatrix}$$

with the solution $\tilde{r}_x = const$ and for the $yz$–subspace

$$\begin{pmatrix}\tilde{r}_y\\ \tilde{r}_z\end{pmatrix} = A\begin{pmatrix}\cos(Vt+\varphi)\\ \sin(Vt+\varphi)\end{pmatrix}$$

The important point to notice is, that the major energy scale in $H$ is set by $H_0$ and its corresponding $\vec{h}_0 \equiv h_0\hat{z}$. Thus $\vec{r} = +\hat{z}$ $(-\hat{z})$ correspond to the excited (ground) state, respectively. Now with the perturbation $\vec{v}$ orthogonal to $\hat{z}$ and exactly in resonance with this splitting of the $\pm\hat{z}$ states, this small perturbation with amplitude $V$ drives the system up and down the two–level system in the $yz$ plane with frequency $V$, i.e. the intensity of the perturbation.

## 5.3 Hubbard Hamiltonian of $2 \times 2$ Network

A simple example for a network described by the Hubbard Hamiltonian given in Eq. (5.2) is shown in Fig. 5.1. With a given number of excess electrons on this type of array, the corresponding dynamics of this system is studied. Since at maximum two electrons are considered throughout, this simplifies the discussion insofar as the total wavefunction can be split into a product of spatial and spin contributions.

### 5.3.1 Two Identical Particles (Electrons)

For fermions as well as bosons, the correct statistics for particle exchange is taken care of systematically by the formalism of second quantization with its creation and annihilation operators. Quantum–mechanical particles are (anti)symmetric under particle exchange. Thus the physically correct quantum mechanical state acquires a factor of $\pm 1$ under particle exchange. In the case here for two electrons, for example, the states $c^+_{i\sigma}c^+_{j\sigma'}|0\rangle$ have this symmetry built into them by construction. Furthermore,

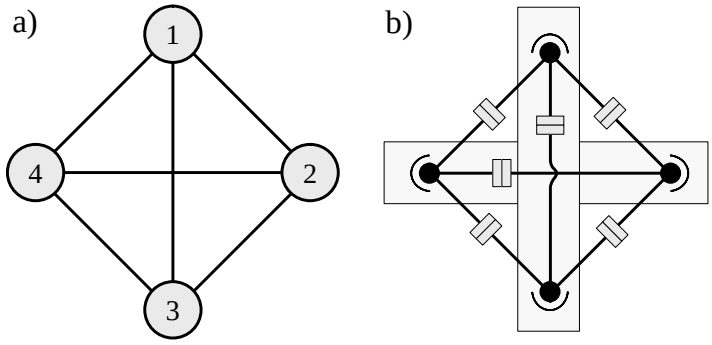


Figure 5.1: Setup of $2 \times 2$ array. (a) Arrangement of the four islands with mutual tunnel connection indicated by black lines. (b) Same as in (a) but shows explicitly tunneling junctions and capacitive coupling including the two voltage gates acting along the square diagonals. *Cross tunneling* (tunneling across the diagonals) is allowed and assumed to have the same tunneling amplitude $t$ as the nearest neighbor hopping along the outside of the array.

for two spin 1/2 particles one may change the basis to singlet and triplet states. The three triplet states are

$$c_{i\uparrow}^{+} c_{j\uparrow}^{+} \left|0\right\rangle , \; \frac{1}{\sqrt{2}} \left( c_{i\uparrow}^{+} c_{j\downarrow}^{+} + c_{i\downarrow}^{+} c_{j\uparrow}^{+} \right) \left|0\right\rangle , \; c_{i\downarrow}^{+} c_{j\downarrow}^{+} \left|0\right\rangle \tag{5.28a}$$

and exist only for the case $i \neq j$, which is enforced by the algebra of the creation (annihilation) operators. The one singlet state is

$$\frac{1}{\sqrt{2}} \left( c_{i\uparrow}^{+} c_{j\downarrow}^{+} - c_{i\downarrow}^{+} c_{j\uparrow}^{+} \right) \left|0\right\rangle \tag{5.28b}$$

for $i \neq j$ and $c_{i\downarrow}^{+} c_{i\uparrow}^{+} \left|0\right\rangle$ for $i = j$. This set of singlet and triplet states is eventually also motivated by spin–spin interaction ($\vec{s} \cdot \vec{s}$ coupling), since then the above set is the set of eigenstates for the system.

The singlet (triplet) states for a pair of particles are symmetric (antisymmetric) under particle exchange in the spatial part of the wave function, respectively. Since the total wave function is a product of the spatial wavefunction and the spin contribution, the spatial part alone can formally be interpreted as bosonic or fermionic, since the spin part can be used to make up for the overall correct final fermi statistics. Thus taking away the spin part of the wavefunction altogether, the triplet state has fermionic character

$$c_i^{+} c_j^{+} \left|0\right\rangle = -c_j^{+} c_i^{+} \left|0\right\rangle$$

since

$$c_{i\sigma}^{+}c_{j\sigma}^{+}\left|0\right\rangle = -c_{j\sigma}^{+}c_{i\sigma}^{+}\left|0\right\rangle \text{ and } \frac{1}{\sqrt{2}}\left(c_{i\uparrow}^{+}c_{j\downarrow}^{+}+c_{i\downarrow}^{+}c_{j\uparrow}^{+}\right)\left|0\right\rangle = -\frac{1}{\sqrt{2}}\left(c_{j\uparrow}^{+}c_{i\downarrow}^{+}+c_{j\downarrow}^{+}c_{i\uparrow}^{+}\right)\left|0\right\rangle$$

while the singlet state picks up bosonic character

$$c_{i}^{+}c_{j}^{+}\left|0\right\rangle \equiv \frac{1}{\sqrt{2}}\left(c_{i\uparrow}^{+}c_{j\downarrow}^{+}-c_{i\downarrow}^{+}c_{j\uparrow}^{+}\right)\left|0\right\rangle = +\frac{1}{\sqrt{2}}\left(-c_{j\downarrow}^{+}c_{i\uparrow}^{+}+c_{j\uparrow}^{+}c_{i\downarrow}^{+}\right)\left|0\right\rangle \equiv +c_{j}^{+}c_{i}^{+}\left|0\right\rangle .$$

Consequently, the correct (anti)commutator relationships for singlet and triplet states are

$$\begin{aligned} \left[c_i, c_j\right] = \left[c_i^{+}, c_j^{+}\right] = 0, \quad \left[c_i, c_j^{+}\right] = \delta_{ij} \quad \text{singlet states} \\ \left\{c_i, c_j\right\} = \left\{c_i^{+}, c_j^{+}\right\} = 0, \quad \left\{c_i, c_j^{+}\right\} = \delta_{ij} \quad \text{triplet states} \end{aligned} \tag{5.29}$$

Here, the index $i$ only refers to the spatial index (the site) and the spin index is dropped altogether. However, one must keep in mind the constraint of two electrons in the total system. Furthermore, since the singlet and triplet states are orthogonal to each other, their respective Hilbert spaces are decoupled from each other unless the Hamiltonian were to mix them (e.g. in the presence of spin–orbit effects) which is not the case here. Finally, care must be taken with respect to the correct normalization of the states in this notation. Specifically, the singlet state which describes double occupancy acquires a normalization factor $1/\sqrt{2}$ such that the correct state for double occupancy is $\frac{1}{\sqrt{2}}c_i^{+}c_i^{+}\left|0\right\rangle$.

### 5.3.2 Two Electron Matrix Hamiltonian

The matrix representation of the Hamiltonian for this configuration with a total of two electrons is extracted as follows. The off–diagonal elements of the Hamiltonian between singlet or triplet states are easily determined from the (anti)commutator relationships in Eq. (5.29). With the definition of the sign $s \equiv +1$ for singlet states and $s \equiv -1$ for triplet states based on the (anti)commutator relationships in Eq. (5.29), the off–diagonal elements are obtained as

$$\left\langle 12\right| H \left|13\right\rangle = -t \cdot \left\langle 0\right| c_2 c_1 \cdot c_i^{+} c_j \cdot c_1^{+} c_3^{+} \left|0\right\rangle = -t \cdot (1) = -t \tag{5.30a}$$

$$\left\langle 12\right| H \left|23\right\rangle = -t \cdot \left\langle 0\right| c_2 c_1 \cdot c_i^{+} c_j \cdot c_2^{+} c_3^{+} \left|0\right\rangle = -t \cdot (s) = -t\ s \tag{5.30b}$$

$$\left\langle 11\right| H \left|12\right\rangle = -t \cdot \left\langle 0\right| c_1 c_1 \frac{1}{\sqrt{2}} \cdot c_i^{+} c_j \cdot c_1^{+} c_2^{+} \left|0\right\rangle = -\sqrt{2}t\ \delta_s \tag{5.30c}$$

$$\left\langle 22\right| H \left|12\right\rangle = \left\langle 11\right| H \left|12\right\rangle = -\sqrt{2}t\ \delta_s \tag{5.30d}$$

where $\delta_s$ is defined such that $\delta_s = 1$ only if one is dealing with singlet states, and zero otherwise (note that by construction $|11\rangle$, $|22\rangle, \ldots$ are singlet states). These results are consistent with the evaluation of the off–diagonal elements in the full basis set including the spin index

$$\begin{aligned}
\langle 12|\, H\, |13\rangle &= -t \cdot \langle 0| \frac{1}{\sqrt{2}} \left(c_{2\downarrow} c_{1\uparrow} \pm c_{2\uparrow} c_{1\downarrow}\right) \cdot c^+_{i\sigma} c_{j\sigma} \cdot \frac{1}{\sqrt{2}} \left(c^+_{1\uparrow} c^+_{3\downarrow} \pm c^+_{1\downarrow} c^+_{3\uparrow}\right) |0\rangle \\
&= -\frac{t}{2} 2 = -t \\
\langle 12|\, H\, |23\rangle &= -t \cdot \langle 0| \frac{1}{\sqrt{2}} \left(c_{2\downarrow} c_{1\uparrow} \pm c_{2\uparrow} c_{1\downarrow}\right) \cdot c^+_{i\sigma} c_{j\sigma} \cdot \frac{1}{\sqrt{2}} \left(c^+_{2\uparrow} c^+_{3\downarrow} \pm c^+_{2\downarrow} c^+_{3\uparrow}\right) |0\rangle \\
&= \pm\frac{t}{2} 2 = \pm t \\
\langle 11|\, H\, |12\rangle &= -t \cdot \langle 0|\, c_{1\downarrow} c_{1\uparrow} \cdot c^+_{i\sigma} c_{j\sigma} \cdot \frac{1}{\sqrt{2}} \left(c^+_{1\uparrow} c^+_{2\downarrow} \pm c^+_{1\downarrow} c^+_{2\uparrow}\right) |0\rangle \\
&= -(1 \mp 1)\frac{t}{\sqrt{2}} \equiv -\sqrt{2} t \cdot \delta_s \\
\langle 22|\, H\, |12\rangle &= \langle 11|\, H\, |12\rangle = -\sqrt{2} t \cdot \delta_s
\end{aligned}$$

with $\delta_s$ as defined above.

The diagonal elements are the same for singlet and triplet states and are obtained similarly to the off–diagonal elements above. With no gate voltages applied these become

$$\begin{aligned}
\langle 13|\, H\, |13\rangle &= \langle 0|\, c_3 c_1 \cdot \frac{1}{2} V_{ij}\, n_i n_j \cdot c^+_1 c^+_3\, |0\rangle \\
&= \frac{1}{2}\left(V_{11} + V_{33} + V_{13} + V_{31}\right) \equiv \frac{1}{2} \vec{q}_{13} C^{-1}_{11} \vec{q}_{13} \equiv \varepsilon_1 \\
\langle 24|\, H\, |24\rangle &= \langle 13|\, H\, |13\rangle = \varepsilon_1
\end{aligned} \tag{5.32a}$$

$$\begin{aligned}
\langle 12|\, H\, |12\rangle &= \frac{1}{2}\left(V_{11} + V_{22} + V_{12} + V_{21}\right) \equiv \frac{1}{2} \vec{q}_{12} C^{-1}_{11} \vec{q}_{12} \equiv \varepsilon_2 \\
\langle 12|\, H\, |12\rangle &= \langle 23|\, H\, |23\rangle = \langle 34|\, H\, |34\rangle = \langle 41|\, H\, |41\rangle = \varepsilon_2
\end{aligned} \tag{5.32b}$$

$$\begin{aligned}
\langle 11|\, H\, |11\rangle &= \langle 0|\, c_1 c_1 \frac{1}{\sqrt{2}} \cdot \frac{1}{2} V_{ij}\, n_i n_j \cdot \frac{1}{\sqrt{2}} c^+_1 c^+_1\, |0\rangle \\
&= \frac{2}{2} \cdot \delta_s \cdot \frac{1}{2} 2 \cdot V_{11} \cdot 2 = \delta_s \cdot 2 V_{11} \equiv U \\
\langle 11|\, H\, |11\rangle &= \langle 22|\, H\, |22\rangle = \langle 33|\, H\, |33\rangle = \langle 44|\, H\, |44\rangle = U
\end{aligned} \tag{5.32c}$$

where $\vec{q}_{ij}$ is defined as the vector representing the classical charge distribution with one electron on site $i$ and the other electron on site $j$. Thus the diagonal terms represent

the Hartree energy which is equivalent to the classical electrostatic interaction energy of the charges on the network of quantum dots. The charge configuration on the $2 \times 2$ array at the lowest energy $\varepsilon_1$ consists of the two electrons sitting on opposite corners of the $2 \times 2$ array, namely on dots $(1,3)$ or $(2,4)$ as given in Eqs. (5.32a). The next higher energy state has the two electrons on nearest neighbor dots. The four equivalent configurations at energy $\varepsilon_2$ are given in Eqs. (5.32b). Finally, the states with highest energy are the states with double occupancy listed in Eqs. (5.32c). Their energy is typically referred to as the Hubbard $U$ as indicated.

To be reassured, above equations are shown to be equivalent to the full singlet–triplet basis set including the spin indices. For example,

$$\begin{aligned} \langle 13|\, H\, |13\rangle &= \langle 0|\, \frac{1}{\sqrt{2}}\left(c_{3\downarrow}c_{1\uparrow} \pm c_{3\uparrow}c_{1\downarrow}\right) \cdot \frac{1}{2} V_{ij}\, n_i n_j \cdot \frac{1}{\sqrt{2}}\left(c^+_{1\uparrow}c^+_{3\downarrow} \pm c^+_{1\downarrow}c^+_{3\uparrow}\right) |0\rangle \\ &= \frac{1}{2}\frac{2}{2}\left(V_{11} + V_{33} + V_{13} + V_{31}\right) \equiv \frac{1}{2}\vec{q}_{13} C^{-1} \vec{q}_{13} \equiv \varepsilon_1 \end{aligned}$$

where the cross–terms in the quantum mechanical operator expression in the first line do not contribute. Similarly,

$$\begin{aligned} \langle 11|\, H\, |11\rangle &= \langle 0|\, c_{1\downarrow}c_{1\uparrow} \cdot \frac{1}{2} V_{ij}\, n_i n_j \cdot c^+_{1\uparrow}c^+_{1\downarrow}\, |0\rangle \\ &= \frac{1}{2} 2 \cdot 2V_{11} = 2V_{11} \equiv U \end{aligned}$$

So again, the equivalence of the singlet–triplet representation with the (anti)commutator relationships in Eq. (5.29) becomes obvious.

In the Hubbard model as described, the Coulomb interaction enters in the diagonal terms; and by construction of the Hamiltonian, the quantum mechanical electrostatic potential in Fock space is equivalent to the classical electrostatic potential in terms of the inverse of the capacitance matrix

$$\begin{aligned} V_{pot} &= \frac{1}{2}\vec{q} C^{-1} \vec{q} = \frac{1}{2}\sum_{i,j} q_i C^{-1}_{ij} q_j = \frac{e^2}{2}\sum_{i,j} \hat{n}_i C^{-1}_{ij} \hat{n}_j \\ &\equiv \frac{1}{2}\sum_{i,j} \hat{n}_i V_{ij} \hat{n}_j \text{ with } V_{ij} \equiv e^2 C^{-1}_{ij} \end{aligned} \tag{5.34}$$

where the $i$–th component of $\vec{q}$ ($q_i \equiv e\,\hat{n}_i$) represents the total charge on site (island) $i$.

Finally, collecting all the terms, the resulting Hamiltonian for $2 \times 2$ network with

cross tunneling can be written down

$$H_{(2\times 2)} \equiv \tag{5.35}$$

| | $\|13\rangle$ | $\|24\rangle$ | $\|12\rangle$ | $\|23\rangle$ | $\|34\rangle$ | $\|14\rangle$ | $\|11\rangle$ | $\|22\rangle$ | $\|33\rangle$ | $\|44\rangle$ |
|---|---|---|---|---|---|---|---|---|---|---|
| $\|13\rangle$ | $\varepsilon_1$ | 0 | $-t$ | $-t$ | $\pm t$ | $-t$ | $-\sqrt{2}t\,\delta_s$ | 0 | $-\sqrt{2}t\,\delta_s$ | 0 |
| $\|24\rangle$ | | $\varepsilon_1$ | $\pm t$ | $-t$ | $-t$ | $-t$ | 0 | $-\sqrt{2}t\,\delta_s$ | 0 | $-\sqrt{2}t\,\delta_s$ |
| $\|12\rangle$ | | | $\varepsilon_2$ | $\pm t$ | 0 | $-t$ | $-\sqrt{2}t\,\delta_s$ | $-\sqrt{2}t\,\delta_s$ | 0 | 0 |
| $\|23\rangle$ | | | | $\varepsilon_2$ | $\pm t$ | 0 | 0 | $-\sqrt{2}t\,\delta_s$ | $-\sqrt{2}t\,\delta_s$ | 0 |
| $\|34\rangle$ | | | | | $\varepsilon_2$ | $-t$ | 0 | 0 | $-\sqrt{2}t\,\delta_s$ | $-\sqrt{2}t\,\delta_s$ |
| $\|14\rangle$ | | | | | | $\varepsilon_2$ | $-\sqrt{2}t\,\delta_s$ | 0 | 0 | $-\sqrt{2}t\,\delta_s$ |
| $\|11\rangle$ | | | | | | | $U$ | 0 | 0 | 0 |
| $\|22\rangle$ | | | | | | | | $U$ | 0 | 0 |
| $\|33\rangle$ | | | | | | | | | $U$ | 0 |
| $\|44\rangle$ | *h.c.* | | | | | | | | | $U$ |

where the lower triagonal is the hermitian conjugate (h.c.) of the upper triagonal due to the hermiticity of the Hamiltonian and where the top row and the left–most column of Eq. (5.35) indicate the two–particle basis states. The $-t$ ($+t$) refers to singlet (triplet) states, respectively, and states with double occupancy including the Hubbard $U$ only contribute to the singlet Hamiltonian.

The diagonal of the Hamiltonian above is now taken as $H_0$, and the off–diagonal part proportional to $t$ is considered the perturbation $V$, such that $H = H_0 + V$. With $t$ assumed to be small and $\varepsilon_1 < \varepsilon_2$ with $|\varepsilon_2 - \varepsilon_1| \ll t$, the states $|13\rangle$ and $|24\rangle$ can be considered the groundstates which are perturbed due to the presence of the tunneling.

## 5.4 On Singlet / Triplet Splittings

### 5.4.1 Effective Two–Level Hamiltonian for $2 \times 2$ Network

In order to obtain an estimate for the splitting in the ground state quantum two–level system (qu2LS), the Feshbach formalism is used to obtain an effective Hamiltonian for the qu2LS ($\mathcal{P}$ space) coupled to higher lying states ($\mathcal{Q}$ space, see Sec. 4, pp. 65). For simplicity, states of double occupancy are neglected, and so the Hamiltonian in Eq. (5.35) reduces to the six–dimensional matrix in the upper left block of Eq. (5.35)

including the basis states $|13\rangle$ to $|14\rangle$

$$H = \left(\begin{array}{cc|cccc} \varepsilon_1 & 0 & -t^* & -t & \pm t^* & -t \\ & \varepsilon_1 & \pm t & -t^* & -t & \pm t^* \\ \hline & & \varepsilon_2 & \pm|t| & 0 & \pm t \\ & & & \varepsilon_2 & \pm|t| & 0 \\ & & & & \varepsilon_2 & \pm|t| \\ h.c. & & & & & \varepsilon_2 \end{array}\right) \tag{5.36}$$

where $V_g = 0$ since here only the effect of the tunneling is discussed. With $t = 0$, the qu2LS grouped together in the upper left $2 \times 2$ block of the $H$ matrix is degenerate, while the intermediate states are split off $\Delta_0 \equiv \varepsilon_2 - \varepsilon_1$ which is the same for all of these intermediate states due to symmetry. Here, $\varepsilon_1$ and $\varepsilon_2$ are the overall diagonal contributions arising from the Coulomb interaction at $V_g = 0$.

The Hamiltonian in Eq. (5.36) can be diagonalized analytically. However, a perturbative approach provides explicit insights on the origins of the splitting due to exchange of otherwise degenerate states. Furthermore, the setup proves sufficiently simple to allow the complex sum to all orders over all possible histories in Hilbert space within the Feshbach formalism. The result consistently agrees with the analytical solution to the problem.

The possible network of transitions in the Hilbert space of the $2 \times 2$ network is shown in Fig. 5.2. For convenience, the qu2LS basis is written as $\mathcal{P} \equiv \{|13\rangle, |24\rangle\} \equiv \left\{|0\rangle_{qb}, |1\rangle_{qb}\right\} \equiv \{0,1\}_{qb}$, shown at the left and at the right of Fig. 5.2. The remaining intermediate states ($\mathcal{Q}$ space) form a ring topology where every node is linked to the $|0\rangle_{qb}$ and $|1\rangle_{qb}$ states. Note that there is no direct transition from $|0\rangle_{qb}$ to $|1\rangle_{qb}$, but one has to proceed through at least one of the intermediate states with an energy cost of $\Delta_0 \equiv \varepsilon_2 - \varepsilon_1$.

The lines in Fig. 5.2 indicate possible transitions between states due to one–particle tunneling of one of the two electrons. The dotted lines in blue indicate effectively an exchange of the two particles considered. Which transitions these are, can be read off directly from the Hamiltonian in Eq. (5.36), namely the ones that have an altered sign for the fermionic triplet states and thus come with the "±". Note however, that there is some arbitrariness in this, since the signs depend on the initially chosen basis set. A change in the basis of the sort $|i\rangle \rightarrow -|i\rangle$ for some of the basis vectors changes the picture of which transitions are related to particle exchange. This, however, should not affect the final physical results.

The effective 2D Hamiltonian for the qu2LS in the absence of a magnetic field and thus real $t$ follows from the Feshbach formalism as $H_{\mathit{eff}} = H_{PP} + \Sigma_{QQ}(E)$ as

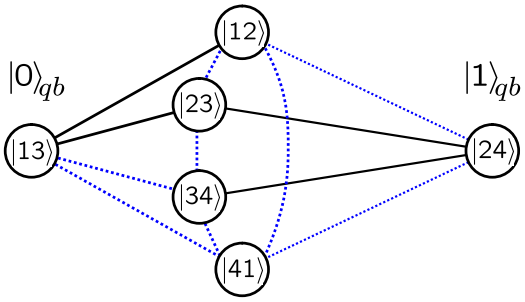


Figure 5.2: $2 \times 2$ array of quantum dots: network of states an transitions in between them where states with double occupancy are neglected. According to the basis chosen, certain triplet state transitions pick up a minus sign related to particle exchange. These transitions are indicated by the blue dashed line.

described in see Sec. 4, pp. 65. The tunneling is considered as the perturbation which mixes the $\mathcal{P}$ and the $\mathcal{Q}$ space. The matrix elements of the self–energy $(\Sigma)_{ij}$ with $i,j = \{0,1\}_{qb}$ are built from the sum over all possible paths that start in state $i$, immediately proceed to intermediate states $\mathcal{Q}$, and only in the final step come back to state $j$. The number of possible paths constructed in this manner for a total of $n$ steps is $S_n(i,j) \equiv 2^n$ with $n \geq 2$ since there are 4 possibilities to go from $|i\rangle$ to one of the intermediate states, then 2 possibilities of which way to go in the ring for each of the $n-2$ intermediate steps, and 1 choice left to finally leave the ring and go to state $|j\rangle$. Furthermore, for $n > 2$, exactly half of these paths include particle exchange, i.e. have an odd number of dashed lines in Fig. 5.2, and thus for the case of the triplet states cancel each other to zero. The underlying reason for this is the spatial $C_{4v}$ symmetry of the $2 \times 2$ setup which has two mirror symmetry planes perpendicular to the array. Therefore, for every path starting from $\{0,1\}_{qb}$ and ending in $\{1,0\}_{qb}$ has a mirrored counterpart where the particles are exchanged in the final state as compared to the first path. This is shown schematically in Fig. 5.3.

The case $n = 2$ needs separate consideration for the diagonal elements in $H_{\mathit{eff}}$. Since here the same step is taken twice, back and forth, the relative sign in $t$ does not matter. Therefore the triplet states have an $n = 2$ contribution in the diagonal. Putting all these pieces together, yields the matrix elements for the effective Hamiltonian which, for example, in case of the singlet states are

$$\begin{aligned} \langle i|\, H_{\mathit{eff}}\, |j\rangle_S &= \varepsilon_1 \delta_{ij} + \frac{(-2t)^2}{\omega - \varepsilon_2} \sum_{m=0}^{\infty} \left( \frac{-2t}{\omega - \varepsilon_2} \right)^m \\ &= \varepsilon_1 \delta_{ij} + \frac{(-2t)^2}{\omega - \varepsilon_2 + 2t} \equiv \varepsilon_1 \delta_{ij} + \Sigma_{ij}^S(\omega)\,, \end{aligned} \tag{5.37}$$

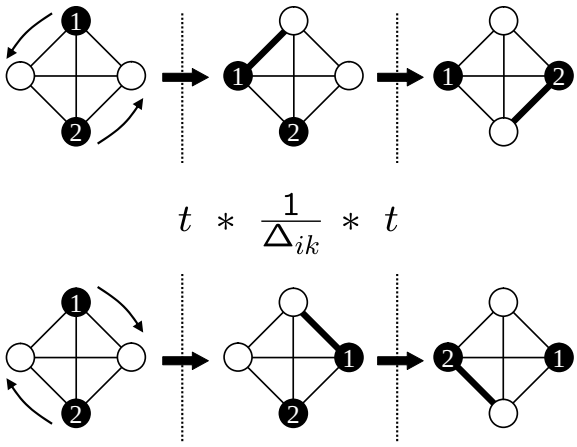


Figure 5.3: Demonstration of the effect of exchange in the perturbative Feshbach approach. Due to the $C_{4v}$ symmetry, for every path like in the first row there exists a second path mirrored along the vertical as shown in the second row making use of the intrinsic vertical mirror symmetry of $C_{4v}$. The essential difference is that the final state has its particles exchanged. The mathematical expressions in between describe the contribution to the self energy of the effective Hamiltonian within the Feshbach formalism where $t$ is the tunneling coefficient and $\Delta_{ik} \equiv \varepsilon_k - \varepsilon_i$ is the cost of energy for the intermediate state.

and together with the triplet states

$$H_{eff}^{singlet}(\omega) \equiv \begin{pmatrix} \varepsilon_1 & 0 \\ 0 & \varepsilon_1 \end{pmatrix} + \frac{4t^2}{\omega - \varepsilon_2 + 2t} \begin{pmatrix} 1 & 1 \\ 1 & 1 \end{pmatrix} \tag{5.38a}$$

$$H_{eff}^{triplet}(\omega) \equiv \begin{pmatrix} \varepsilon_1 & 0 \\ 0 & \varepsilon_1 \end{pmatrix} + \frac{4t^2}{\omega - \varepsilon_2} \begin{pmatrix} 1 & 0 \\ 0 & 1 \end{pmatrix}, \tag{5.38b}$$

where again for the triplet state only the paths with $n = 2$ contribute. It should be noted that for the sum in Eq. (5.37) to be defined, $\left|\frac{2t}{\omega - \varepsilon_2}\right|$ needs to be $< 1$, and therefore $\omega$ should not be closer than $2t$ to $\varepsilon_2$ since otherwise the geometrical sum is not defined. For that rather narrow interval of $|\omega - \varepsilon_2| < 2t$, however, Eq. (5.37) can be considered an analytic continuation. On the other hand, as an aside: for the Green's functions $G_0(\omega) = (\omega - H_0)^{-1}$ and $G(\omega) = (\omega - H)^{-1} = (\omega - H_0 - V)^{-1}$ the identity $G = G_0 + G_0 V G$ holds exactly, while the iterative series expansion of this identity $G = G_0 + G_0 V G = G_0 + G_0 V G_0 + G_0 V G_0 V G_0 + \ldots$ as used in the derivation of the Feshbach formalism does not necessarily converge. Yet it is this latter series expansion which has been summed up above.

The eigenstates for the qu2LS are now obtained from the nonlinear eigensystem $H_{\mathit{eff}}(\omega)|\psi\rangle = \omega|\psi\rangle$ where $|\psi\rangle$ is restricted to the 2D ground space. For simplicity, $\varepsilon_1$ is set to 0 which just corresponds to shifting the reference for energies to $\varepsilon_1$, and thus $\varepsilon_1$ is replaced by $\varepsilon_1 - \varepsilon_1 = 0$ and $\varepsilon_2$ is replaced by $\varepsilon_2 - \varepsilon_1 \equiv \Delta_0$. The effective triplet Hamiltonian $H_{\mathit{eff}}^{triplet}$ is still diagonal, and therefore the triplet states *do not mix* with each other, but are just shifted. This shift is determined by the eigenvalue equation using Eq. (5.38a) for the Hamiltonian, resulting in the nonlinear equation

$$\omega = \frac{4t^2}{\omega - \Delta_0}$$

which is easily solved for $\omega$

$$\omega = \frac{\Delta_0}{2} \pm \sqrt{\left(\frac{\Delta_0}{2}\right)^2 + 4t^2}$$

Since the shift is uniform for both eigenstates in the 2D subspace of the qu2LS, this is equivalent to four solutions; the first two solutions lie slightly below $\varepsilon_1 \equiv 0$, and consequently the triplet ground state qu2LS is lowered in energy by the tunneling perturbation

$$\begin{aligned} \omega_{min} &= \frac{\Delta_0}{2} - \sqrt{\left(\frac{\Delta_0}{2}\right)^2 + 4t^2} \\ &\approx -\Delta_0 \left(4\left(\frac{t}{\Delta_0}\right)^2 + \mathcal{O}\left(\left(\frac{t}{\Delta_0}\right)^4\right)\right) = -\frac{4t^2}{\Delta_0} + \mathcal{O}\left(t^4\right). \end{aligned} \tag{5.39}$$

The other two solutions have energy $\omega > \Delta_0$ with $\Delta_0$ the unperturbed lowest ground state excitation energy. Since the original Hamiltonian had dimension 6, there must be two more solutions that either coincide with the $\omega > \Delta_0$ solution or have no components at all in the subspace of the effective Hamiltonian.

For the case of the singlet state, the eigenvectors are $(1, \pm 1)/\sqrt{2}$, i.e. the symmetric and antisymmetric combinations of the original *unperturbed* eigenstates, and as a result the ground state degeneracy is lifted. The eigenvalue equation using Eq. (5.38a) leads to

$$\begin{aligned} \left(\frac{4t^2}{\omega - \Delta_0 + 2t} - \omega\right)^2 - \left(\frac{4t^2}{\omega - \Delta_0 + 2t}\right)^2 &= 0 \\ \omega^2 - 2\omega\frac{4t^2}{\omega - \Delta_0 + 2t} &= 0 \end{aligned}$$

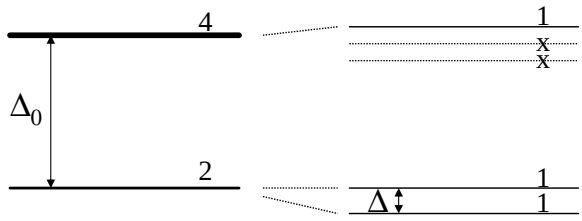


Figure 5.4: $2 \times 2$ network - level structure of effective Hamiltonian for ground state: left are shown the original unperturbed energy levels with their degeneracy indicated; right schematically shows the level structure resulting from the effective subspace of the ground states only.

with the simple antisymmetric solution $\omega = \varepsilon_1 \equiv 0$ and the remaining symmetric solutions $\omega = \frac{8t^2}{\omega - \Delta_0 + 2t}$, which is easily solved to

$$\omega = \frac{\Delta_0}{2} - t \pm \sqrt{\left(\frac{\Delta_0}{2} - t\right)^2 + 8t^2}$$

with

$$\begin{aligned} \omega_{min} &= \left(\frac{\Delta_0}{2} - t\right) - \sqrt{\left(\frac{\Delta_0}{2} - t\right)^2 + 8t^2} \\ &\approx -\Delta_0 \left(8\left(\frac{t}{\Delta_0}\right)^2 + \mathcal{O}\left(\left(\frac{t}{\Delta_0}\right)^3\right)\right) = -\frac{8t^2}{\Delta_0} + \mathcal{O}\left(t^3\right) \end{aligned} \tag{5.40}$$

So due to the non–linearity of the effective 2D Hamiltonian, it turns out that there are three eigenvalues. One is split off by about $\Delta_0$ and belongs to the $\mathcal{Q}$ space, while the originally degenerate ground state pair at $\omega = 0$ is now split by

$$\Delta \equiv 0 - \omega_{min} \approx \frac{8t^2}{\Delta_0} + \mathcal{O}\left(t^3\right) \tag{5.41}$$

This is schematically shown in Fig. 5.4. Note that due to the restriction to the 2D subspace not all the eigenstates are recovered by this procedure. To be precise, the only ones missing may coincide with the states already determined in the subspace with the same energies or, for different energies, must have components equal to zero in the subspace chosen for the effective Hamiltonian.

Comparing the new energy levels for singlet and triplet states from Eqs. (5.39) and

(5.41), the ground state clearly is the symmetric (bonding) singlet state; in between the two split singlet states, the degenerate triplet ground states reside, for small $t$ exactly in the middle.

The level splittings for the Hamiltonian given in Eq. (5.36) were double checked numerically. The double occupancy was neglected as in the previous discussion. The results are shown in Fig. 5.5. The exact result for the splitting of the singlet state is verified. The triplet ground state pair stays degenerate (up to numerical accuracy) as expected.

### 5.4.2 Extension to More Complex Networks with Isolated 2D Subspace

The above procedure can be generalized to more complex networks. Assume a network with two electrons and with initially no tunneling; further assume the system has two states degenerate and well separated from the rest of the states, e.g. a degenerate ground state pair labeled $|1\rangle$ and $|2\rangle$. The energy separation to the nearest state in the remaining spectrum is labeled $\Delta_0$. Now turning on tunneling with $t \ll \Delta_0$, also assume that there is one path of hops that *optimally connects* $|1\rangle$ *to* $|2\rangle$ in the sense, that it is the one with least cost in energy in the intermediate states and has fewest hops in that respect (note that if there are more paths that fulfill this criteria then interference effects can change the picture completely; one may pick a certain path though and look at its effective contribution). The number of hops for this optimal path is taken to be $n$.

For the singlet state configuration, analogously to Eq. (5.38a), an approximate effective Hamiltonian may be written down as follows

$$H^{2\times 2}_{\mathit{eff},S} \equiv \frac{c_1 t^2 + \mathcal{O}\left(t^3\right)}{\omega - \Delta_0} \begin{pmatrix} 1 & 0 \\ 0 & 1 \end{pmatrix} + \frac{c_2 t^n}{\left(\omega - \Delta_0\right)^{n-1}} \begin{pmatrix} 0 & 1 \\ 1 & 0 \end{pmatrix} \tag{5.42}$$

where $c_1$ and $c_2$ are some numbers of order 1 and $\Delta_0$ is some representative energy with respect to the energy separations of intermediate states. The energy reference again has been shifted to the initial eigenenergy of $|1\rangle$ and $|2\rangle$; therefore if one just looks for the effect of small $t$ on these states $|1\rangle$ and $|2\rangle$, then $|\omega| \ll \Delta_0$ is a valid assumption. The first term in Eq. (5.42) comes from simple hoping to neighboring sites and back immediately. The second term in Eq. (5.42), however, needs to connect the two states $|1\rangle$ and $|2\rangle$ by a path as described above and so it needs $n$ hops. Whatever the first term is, it will just contribute by shifting the energies; the splitting between the initially degenerate states $|1\rangle$ and $|2\rangle$ is determined by the off–diagonal elements in

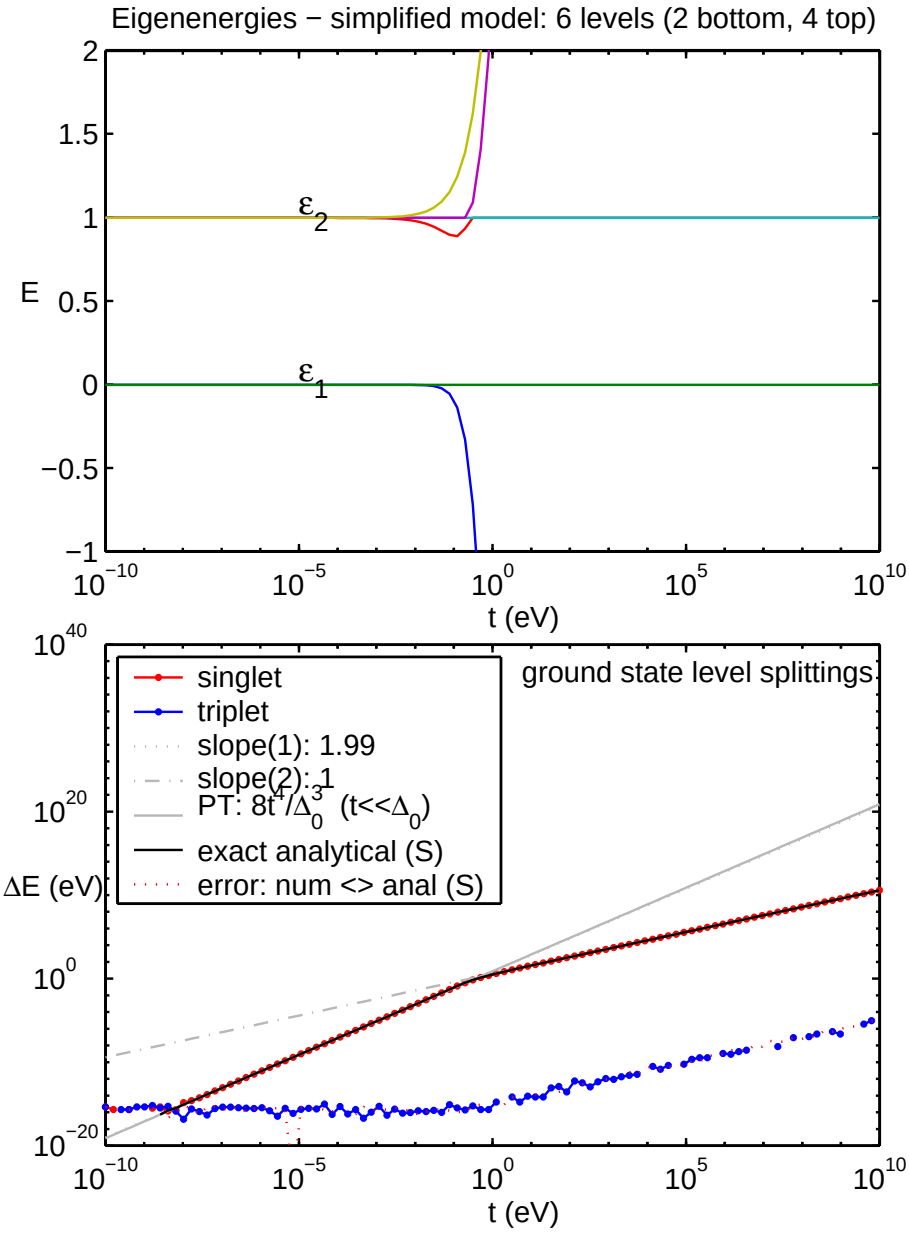


Figure 5.5: $2 \times 2$ network - numerical analysis of the level splitting of the groundstate for both singlet and triplet states respectively. The energy in the upper panel is shown relative to $\varepsilon_1$ and scaled to $\Delta_0 \equiv \varepsilon_2 - \varepsilon_1$. The energy splittings are shown in the lower panel. The noise data shown at the lower end of the data (note the log–log scale) thus just represents numerical roundoff error and is exactly zero otherwise.

the second term. Special care needs to be taken because of the non–linear structure of the effective Hamiltonian.

For readability, Eq. (5.42) is rewritten the following way

$$H_{eff,S}^{2\times 2} \equiv \begin{pmatrix} \alpha(\omega)\, t^2 & \beta(\omega)\, t^n \\ \beta(\omega)\, t^n & \alpha(\omega)\, t^2 \end{pmatrix} \tag{5.43}$$

where by comparison with Eq. (5.42) the functions $\alpha(\omega)$ and $\beta(\omega)$ are well–behaved functions for $|\omega| \ll \Delta_0$ (compare the terms in Eq. (5.42)). Thus the eigenvalue equation reads

$$\begin{aligned} &\left(\alpha\left(\omega\right)\, t^2 + \mathcal{O}\left(t^3\right) - \omega\right)^2 - \left(\beta\left(\omega\right)\, t^n\right)^2 = 0 \\ &\omega = \alpha\left(\omega\right)\, t^2 + \mathcal{O}\left(t^3\right) \pm \beta\left(\omega\right)\, t^n \end{aligned}$$

To lowest order in $\omega$ the splitting of the initially degenerate states $|1\rangle$ and $|2\rangle$ is given by

$$\Delta \approx 2\beta\left(0\right)\, t^n \equiv 2c_2 \frac{t^n}{\left(\Delta_0\right)^{n-1}} \tag{5.44}$$

where for $\beta\left(\omega\right)$ its original expression from Eq. (5.42) was substituted. As a result, the effect of turning on the tunneling goes like $t^n$ due to the $n$ hoppings, divided by the energy denominator for each propagating from one state to the other, for simplicity taken to be the same for all intermediate states. This is consistent with other approaches to perturbation theory.

## 5.5 Quantum Dots and Charge Qubits

Note: the content of this section mainly reflects the papers [WU03b, WU03a]

Quantum computation in its binary concept requires a set of two different quantum states, a *quantum two–level system* (qu2LS), that realizes the quantum bit physically [NC00]. Some physical systems are intrinsically qu2LSs such as the spin 1/2 of a fermion or the polarization of a photon. Spin 1/2 systems such as some nuclei of atoms or electrons are considered well–suited also because of the comparatively long spin decoherence times ($\sim$ ms to ns) [Lev01, GB58, KSSA97] which derives from the rather weak interaction of the spin with its environment. This long coherence also has the price that important processes in qubit operation are rather slow processes. On the other hand, decoherence times for charge based quantum systems are orders of magnitude shorter ($\sim$ ns) due to the comparatively strong Coulomb interaction

[HFC+03, SW03]. Yet, all quantum gates including interacting qubits can be expected to scale similarly in time and to allow for fast qubit operations well below the decoherence limits. Furthermore, final readout through single electron transistors (SET) or quantum point contacts (QPC) appears to be "straightforward" (i.e., implementable in principle) [GM01, DLJ+03, DS00].

In this section quantum bits (qubits) encoded in the spatial wave function of electrons embedded in condensed matter systems are discussed, and the emphasis is placed on whether it is possible to realize a qubit based solely on charge distribution (*charge qubit*) and capacitive coupling. For example, having a set of two quantum dots (qudots) close enough so that one electron can tunnel back and forth, one may envisage a qubit where the electron being on one quantum dot (qudot) represents one state, and being on another qudot the other state [HFC+03]. Other examples are the cellular automata setups with a $2 \times 2$ array of qudots with excess electrons [TL01, GSC+03]. These proposals are fundamentally based on the variability of the tunneling $t$. Yet there are many physical quantum systems where the handle on the tunneling is limited or non–existent, such as the case of metallic qudot structures where the tunneling barrier is determined by the thickness of oxide layers in the structure.

Quantum dot systems have been studied extensively in recent years. Quantum dots (qudots) typically contain from a few to a few hundreds of electrons and are manipulated from the exterior for example by voltage gates. Their behavior at low bias voltages can be well understood by looking at the energetically topmost electrons in the qudot [TAT+00]. For an even number of electrons, they may pair up such that the total spin is zero and the topmost two electrons essentially form a singlet, a system that has been proposed as a possible source for entangled electrons [SL03]. However, under special circumstances, the ground state may actually be a triplet even without the presence of an external magnetic field [FIE+03]. A straightforward explanation for this behavior can be given in terms of the exchange contribution to the energy from the two topmost electrons for the case of nearly degenerate single particle levels [TAT+00]. For an odd total number of electrons on a single qudot, the overall spin is typically found to be 1/2.

We consider an ensemble of qudots, typically an array of four up to nine interconnected and interacting qudots, like for example the symmetric $2\times2$ array similar to the typical cellular automata unit cell format [TL01, AOT+99, Len00, LCV+02, RCU04]. As long as there are at least a few tens of electrons on a single dot, the addition or subtraction of a single electron will not change the overall charge configuration, and in this sense, the classical capacitance matrix formalism still appears to be a valid procedure. In this sense, the interaction is modeled by the total capacitance matrix for the system. In the weak tunneling regime, the *regular* exchange energy

from the two–body interaction between electrons on different qudots is negligible. Moreover, residence of two excess electrons on the same qudot (double occupancy) is energetically unfavorable due to the comparatively large Coulomb charging energies.

The qudot arrays considered here with at most two operational excess electrons on it, are a particular implementation of a charge quantum bit (charge qubit). As shown in this chapter [WU03b], it is essential for the single qubit operations of such a charge qubit to have a non–local potential, tuneable tunneling amplitudes or an external magnetic field which provides a complex phase to the wavefunction. Since the *regular* exchange contribution with charges on different dots is clearly negligible, there are no non–local potential effects in the type of systems considered. Further, the tunneling amplitude is considered constant, fixed by the specific realization of the solid state qudot array, e.g. by the oxide barriers between metallic qudots, and are then basically unaltered by potential gates. In this context of a fixed geometry, the only way to implement full single qubit operations is by using an external magnetic field uniform over the array which can be controlled at will [WU03b].

Due to the geometrical symmetry of the qudot array, the ground state turns out to be exactly degenerate for the triplet states when no magnetic field and no gate voltages are applied. However, the spectrum exhibits a gap for the singlet states which is related to the distinct symmetry under particle exchange for the singlet and triplet states. Therefore, particle exchange does play an essential role, yet it is a higher order effect, similar to superexchange [JH96], as the exchange of two particles on the qudot array takes more than one tunneling step and explores virtual higher energy states.

This then suggests the question of whether there is a way that electrostatically controlled logical quantum gates (qugates) can realize the necessary single qubit operations and the tunability of interactions between them. In this context, it is important to clearly define what one means by a quantum bit encoded in a quantum two–level system (qu2LS) and what are the requirements for it. The following criteria are established for the usefulness of a qu2LS [NC00]:

A1. The qu2LS should include the ground state of the system in the *working–range* of the (tunable) parameters; this clearly facilitates the initialization process in an experiment and is much more reliable when compared to a qu2LS completely built on excited states.

A2. The qu2LS should be well separated in energy from the remaining states in the Hilbert space. This reduces the influence of the remaining Hilbert space, whose interference can be insofar interpreted as a source of *decoherence* and transitions to which may result in loss of probability in the primary system. This *lossy channel* for the qu2LS is considered in more detail below.

A3. The qu2LS must interact with a set of external gates in order to control single qubit states as well as the interaction between them without compromising the two–level system.

In the case of charge located on a set of well–defined quantum dots (a *qudot network*), the electrostatic interaction is clearly able to satisfy point (A3) where Coulomb blockade (or charging) effects introduce a high energy scale ($\gtrsim$ 1meV) in typical qudots. These structures localize the operating electrons and limit the unwanted fast decoherence times due to interaction with the surrounding condensed matter environment. Typical decoherence sources such as phonons or unstable impurities in the environment are regarded as frozen out or static, respectively, at the low temperatures required for operation of the qubit system. Consequently, the primary source of decoherence in this regime is in fact the reservoir of high–lying states, and its coherent interference with the qu2LS will be considered explicitly in our description.

The affect of the gates on the *reservoir* of high–lying states must be in the adiabatic regime. The time–dependent manipulation through gate action can be estimated in the following manner: the gates are considered to act in clearly specified time windows in a step like behavior: they are turned on and off at will. This switching, however, is always carried out with a maximum speed which introduces a characteristic frequency $\omega_{switch} = 2\pi/\tau_{switch}$, where $\tau_{switch}$ is the switching time itself. In order for the influence of the reservoir of higher lying states to be negligible, $\hbar\omega_{switch}$ must be much smaller than the energy difference to the closest coupled states in that bath; thus the switching must be done smoothly enough (adiabatically), so as to not admix higher states into the lower qubit states. Coherent quantum operation in the qu2LS, however, demands the switching to be done faster than $1/\delta$, where $\delta$ is the splitting of the qu2LS in question, and incorporated in criterion (A2).

With respect to criteria (A2) and (A3), an estimate of how much of the wave function may be lost for each gate operation can be obtained from the Feshbach formalism [Fes62] (see Sec. 4.3.4, pp. 89, specifically also Eq. 4.44). For the unperturbed low–energy state manifold $\mathcal{P}$ (in contrast to the remainder of the space $\mathcal{Q}$), an initial state $|\psi\rangle$ fully contained in $\mathcal{P}$ will acquire projections in $\mathcal{Q}$ due to a gate operation $V$ (assumed instantaneous), given by

$$\langle\psi_Q|\psi_Q\rangle = \langle\psi_P| H_{PQ} \frac{1}{E - H_{QQ}} \cdot \frac{1}{E - H_{QQ}} H_{QP} |\psi_P\rangle \ ,$$

where $H = H_0 + V$ and $H_{PQ} \equiv PHQ$ is a projection of the Hamiltonian, and with the other projections defined similarly (see Eq. (5.47) below). Space $\mathcal{Q}$ is considered to be at least an energy $\Delta_0$ separated from space $\mathcal{P}$ and the change in the matrix elements due to the gate operation $V$ is approximated by the splitting $\delta$ induced by that very

$V$ in the ground state pair in $\mathcal{P}$; with this, the equation above can be estimated as

$$\langle\psi_Q|\psi_Q\rangle \lesssim \langle\psi_P| \left(\frac{\delta}{\Delta_0}\right)^2 |\psi_P\rangle = \left(\frac{\delta}{\Delta_0}\right)^2 . \tag{5.45}$$

The gate operations considered are a sequence of steps in the external parameters, which implies that with every one of these steps a small probability fraction is lost from the ground qu2LS to the remaining higher lying states, and as such it can be considered as an additional channel for decoherence, even if the projection is nearly reversible in a gate cycle. Moreover, if the ground state can be considered sufficiently isolated ($\delta \ll \Delta$), the error drops quadratically with the ratio $\delta/\Delta$, so that if $\delta \simeq 0.03\Delta$, the probability lost per gate operation would be smaller than 0.1 %. However, the gate operations will never be performed instantaneously. Smoothening the transitions so that they take longer than $\Delta_0^{-1}$ but are faster than $\delta^{-1}$ clearly can be expected to reduce the probability loss to the $\mathcal{Q}$ space of excited states.

Thus with proper adiabatic design of the qugates with respect to the higher lying 'reservoir', the way to single qubit operations is open. However, how exactly these are realized still leaves plenty of possibilities, which one can imagine being flexible enough. Here the main emphasis is placed on capacitively coupled quantum gates and the question of whether they allow the necessary single qubit operations. Most surprisingly, the answer will turn out to be no. Despite the great degree of flexibility in geometry of electrostatic gates and system design, we will show below that it is not possible to implement fully operational qugates without compromising the robustness of the qubits.

### 5.5.1 Quantum Gates for Single Qubit Operation

By definition, quantum bits are physical (quasi) two–level systems. As such they are conveniently mapped into the spin 1/2 formalism using Pauli matrices [NC00, Bal99]. The system is described by a pseudospin which can be rotated in 3D space by applying perturbations which effectively act as magnetic field along different directions (note that there is no real magnetic field and that the real spin of the two electron system is taken care of by the singlet and triplet states). An arbitrary single qubit operation thus requires the realization of two distinct rotations in the 3D pseudo–spinor space. This translates to two linearly independent combinations of the three Pauli matrices $\sigma_{\{x,y,z\}}$ required to implement the necessary quantum gates, e.g. a $\sigma_x$ and a $\sigma_z$ gate, or in a more common notation in quantum computing, an X– and a Z–gate. In a more physical language, the most general Hamiltonian in 2D can also be written in terms of the Pauli spin matrices $H \equiv a1 + \vec{\mathcal{B}} \cdot \vec{\sigma}$, and as such it defines an effective equivalent of a magnetic field $\vec{\mathcal{B}} \equiv \vec{B}_{\mathit{eff}}$ (pseudo magnetic field). For full single qubit

operation then, the physical realization of two distinct effective magnetic fields is required where distinct is to be understood as pointing in different and optimally in orthogonal directions, such as a $\mathcal{B}_x$ and a $\mathcal{B}_z$ if the Hamiltonian is real ($\mathcal{B}_y = 0$).

### 5.5.2 Model System of 3×3 Array

The model network under consideration is a $3 \times 3$ array of qudots with a single state per site and spin included. The $3 \times 3$ array is considered large enough for theoretical purposes in order to contain and to illustrate the main physics. For an experiment in this area, however, it is likely more practical to choose an array with fewer dots and gates. For the analysis, the $3 \times 3$ array is flexible and manageable, and is used to illustrate the more general conclusions. Other geometries have been explored and yield similar results.

The $3 \times 3$ array of qudots has been already sketched earlier on together with the set of external gates in Fig. 2.1 (p. 7). As seen from panel (b) there, only nearest neighbor capacitances are taken into account as well as nearest neighbor tunneling between dots. Overall, four parameters enter the model: the capacitance from each dot to either one of the gates ($C_g = 45$aF ), the nearest–neighbor dot–dot capacitance ($C_{dd} = 45$aF), the dot self capacitance ($C_{d0} = 45$aF) and the nearest neighbor dot–dot tunneling ($t \sim 2\mu$eV). For these values, the energy cost for double occupancy (the Hubbard $U$) becomes $U = 1$ meV, a typically used value in this context. Including a dielectric constant of $\epsilon = 10$, these numbers represent a typical design where dots of size 200nm are separated by approximately also 200nm. These numbers can of course change depending on the detailed geometry and shapes of the dots. In that sense, the circles in Fig. 2.1a are just a symbolic representation of the dots. However, the capacitance values chosen correspond to relatively large nano–structures, and the resulting low energy and temperature requirements of few tens of mK may thus be lifted to some extent by going to smaller structures.

The $3 \times 3$ model introduced is representative for a network with $C_{4v}$ symmetry. As such it has a natural 2–fold degeneracy built into it. From the total capacitance matrix for the system, the single particle potential landscape for the array is calculated and shown in Fig. 2.3 (p. 9) and for comparison again in Fig. 5.6a. Now, the 90° symmetry of the potential can be broken by a peculiar voltage pattern such that it only effects the potential on the middle outer islands as shown in Fig. 5.6b.

The Hamiltonian used to describe this system is of the extended Hubbard type as given in Eq. (5.3) in Sec. 5.1 (pp. 95). For simplicity also with respect to the experiment, the electronic system of qudots is assumed to have a fixed number of two excess electrons ($2e$) on it which dynamically evolve over the array. Since in nanosystems, the individual energy levels for the electrons are well split due to spatial confinement

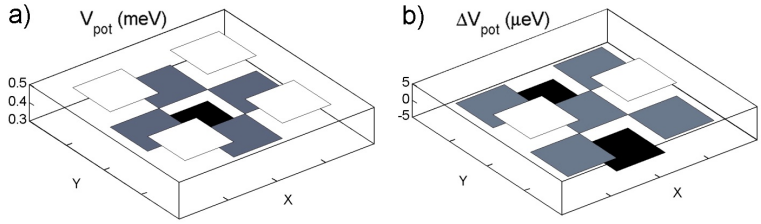


Figure 5.6: Potential landscape for array in Fig. 2.1. (a) Single particle potential on array with no gate voltages applied ($\mathbf{V}_g = 0$). (b) Change of single particle potential due to one specific set of applied gate voltages.

of the order of 1 meV (Hubbard $U$), the remaining electrons are considered to be tightly bound in the lower energy states they are in. Moreover, since spin flip processes occur on a comparatively long time scale [Lev01, GB58, KSSA97], they are neglected and thus the overall spin is considered constant.

### Numerical Simulations

The numerical simulations are done for a total of two operational charges on the array. The second charge when added to the $3 \times 3$ array leads to a competing effect of the potential well structure in Fig. 5.6a and the Coulomb repulsion. As already explained in the context of Fig. 2.3 (p. 9), this leads to the two fold degenerate classical ground state system with the charges arranged either vertically or horizontally as shown in right panel of Fig. 2.3b. These classical groundstates are also reflected in the quantum regime with weak coupling, and for the case of the triplet states, the spatial distribution of the quantum mechanical ground state system space is shown if Fig. 5.7d+e.

The eigenspectrum for the $3 \times 3$ system with two electrons and its dependence on the gate voltage pattern shown in Fig. 5.6b is plotted in Fig. 5.7a. The three different spin configurations for triplet states have exactly the same eigenspectrum. So looking at one specific triplet spin configuration, there is still an exact degeneracy in the ground state due to the spatial symmetry when no gate voltages are applied. The spatial configuration of this degenerate triplet groundstate pair is shown in Fig. 5.7d+e. For the singlet states, however, a gap opens up. This gap originates from the distinct exchange symmetry in the spatial part of the wave function when compared to the triplet states (see Sec. 5.4, p. 120). The ground state basis set for the singlet states is very similar in its spatial distribution to the triplet states shown in Fig. 5.7d+e. In the singlet subspace, however, this basis mixes into its symmetric and antisymmetric combinations (bonding/antibonding states) near the degeneracy point ($\mathbf{V}_g = 0$). The

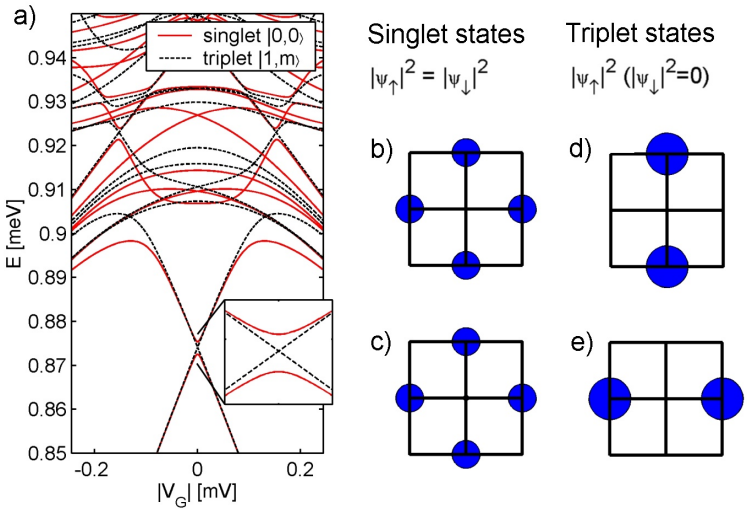


Figure 5.7: (a) Energy level spectrum of the $3 \times 3$ system and dependence of the symmetry breaking pattern of gate voltages in Fig. 5.6b. Singlet states $|s, s_z\rangle = |0, 0\rangle$ are shown in red, while triplet states $|s, s_z\rangle = |1, m = \{+1, 0, -1\}\rangle$ are shown in dashed black. (b) and (c) Probability distribution over the $3 \times 3$ array of the ground pair (qu2LS) for singlet states. Notice equal probability for spin up and spin down ($|\psi_\uparrow|^2 = |\psi_\downarrow|^2$). (d) and (e) Lowest triplet states. Case chosen ($s_z = +1$) has only a spin up component (note, however, that spatial probability distribution is the same for the sixfold degenerate triplet states).

gap in the singlet subspace is determined perturbatively using the Feshbach formalism (Sec. 5.4, p. 120) with the result

$$\delta \sim 32 \frac{t^4}{\Delta_0^3} \ , \tag{5.46}$$

where $\Delta_0$ is the energy gap to the excited manifold ($\Delta_0 \simeq 0.03$ meV in Fig. 3a). This result can be thought of visually as four hops ($t^4$) needed at the cost of about $\Delta_0$ for each of the three intermediate states ($\Delta_0^{-3}$). The prefactor gives the number of possible low energy paths from one basis state to the other including particle exchange symmetry.

A numerical simulation of the state evolution that makes use of the anticrossing of the singlet state is shown in Fig. 5.8. The state of the qu2LS is represented by a three dimensional vector in the Bloch sphere [NC00] where the (initial) eigenstates for $\mathbf{V}_g = 0$ are taken as the basis for this representation. Note that this is a slightly modified definition of the Bloch vector, insofar as there is a reservoir of higher lying states accessible to the system. Panels (a+b) show the *path* of the Bloch vector as three sequential qubit operations were performed: the first and the last operation

are based on the symmetry breaking gate voltage pattern shown in Fig. 5.6b, which rotate the Bloch vector around the $z$ axis, the horizontal circular path in panel (a). For demonstration purposes, the second operation is based on tunable tunneling (an effective $\sigma_x$ gate in the pseudo–spin space of the qubit, see below). This second operation rotates the Bloch vector around the $x$–axis and together with the first operation allows one to rotate the Bloch vector anywhere in the Bloch sphere as required for single qubit operations. Panel (c) shows the evolution of the real space probability distribution during the second operation. The two basis states in Fig. 5.7d+e are nicely rotated into each other over a time consistent with the nature of the Rabi oscillations. Typical rise–times for the voltage gate that do not mix in higher lying states are well below the 1 ps range, while if one were to tune the tunneling, the minimal rise–times for adiabatic switching would require times in the 100 ps range, in order to limit the admixing of higher lying states. The adiabatic regime considered here is clearly seen in the Bloch sphere representation of Fig. 5.8b by observing that the length of the Bloch vector is reduced to less than one in the intermediate gate operation. On return to the initial parameters, this amplitude temporarily lost to the bath is adiabatically regained.

### Rabi Oscillations and 2nd Quantum Gate

From the previous numerical analysis, it is clear that a $Z$ gate is easily implemented using the gate voltages. The asymmetrically applied voltage pattern in Fig. 5.6b raises and lowers the potential of the basis state configuration shown in Fig. 5.7d+e, and thus this is exactly what a $\sigma_z$ term in the effective 2D Hamiltonian does. But now, in contrast to the previous numerical analysis, where for demonstration purposes the tunneling $t$ was considered tunable, the tunneling is eventually considered constant, a choice motivated from the experimental point of view when thinking of lithographically grown qudot structures on the basis of Al/AlO. There the tunneling is determined by the thickness of the oxide layers which is fixed once and for all when growing the sample. So now with the tunneling fixed, one may ask, is it possible to obtain the second qugate by applying a peculiar pattern of capacitively coupled voltage gates only? The answer turns out to be no in the sense that either the second gate (X–gate) is orders of magnitude weaker than the first gate (Z–gate), or it compromises the two–level ground state system such that at least one initially well split off eigenstate comes within gap distance to the qubit encoding subspace.

As a way to illustrate this result in the $3 \times 3$ system of Fig. 2.1a, all six gate voltages were sampled randomly within their parameter space over a significant range of tunneling coefficient $t$ values. The results are shown in Fig. 5.9. Panel (a) shows the energy splitting in the ground state qu2LS ($\delta \equiv E_1 - E_0$) together with the energy

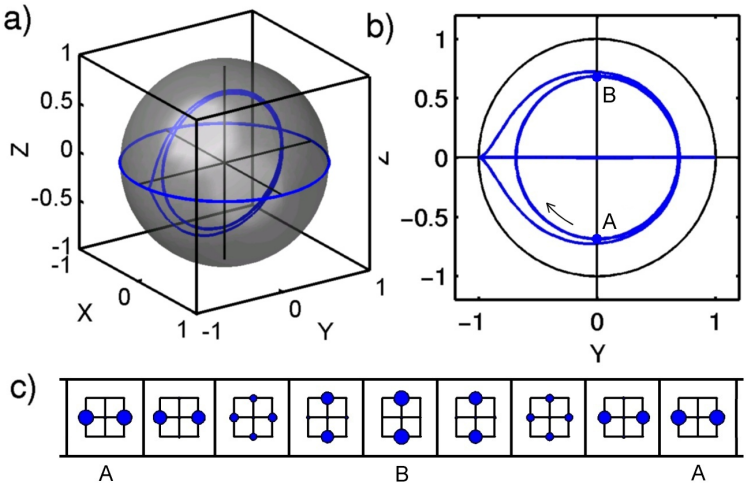


Figure 5.8: Coherent manipulation of the singlet state under gate action - (a) Evolution of the qubit in the Bloch sphere representation after projection onto the basis of the (initial) eigenspectrum at $\mathbf{V}_g = 0$. The Bloch sphere is shown in black, and the evolution of the Bloch vector in the qu2LS is shown in blue. (b) Same as panel (a), but side view, showing the slight size reduction due to the adiabatic interaction with the higher lying reservoir of states. (c) Coherent Rabi oscillations for the sequence $A \rightarrow B \rightarrow A$ in panel (b) in the direction indicated with $t = 10\mu$eV. The probability distribution in real space is shown for the $3 \times 3$ array over equally spaced time intervals in a total time window of 0.56ns which corresponds to one period for this tunneling based action.

splitting towards the higher lying states ($\Delta \equiv E_2 - E_1$). This clearly identifies the region of the intact qu2LS as the region where $\delta(V) \ll \Delta(V)$ and thus $t \leq 5\mu$eV. It is then clear that the condition $\delta(V) \gtrsim \Delta(V)$ invalidates the assumption of an energetically isolated qu2LS. Panel (b) to the right of Fig. 5.9 shows the statistics on the effective pseudo–magnetic field $\vec{\mathcal{B}}$ in dependence of the randomly sampled gate voltages. This effective equivalent of a magnetic field $\vec{\mathcal{B}} \equiv \vec{B}_{eff}$ is extracted from the effective Hamiltonian for the qu2LS, namely $H \equiv a1 + \vec{\mathcal{B}} \cdot \vec{\sigma}$. The Z–gate ($\mathcal{B}_z$) can clearly be turned on and off by the gate voltages and ranges from zero to the value limited by the applied voltages. Yet, $\mathcal{B}_x$ is overwhelmingly set by the tunneling $t$ and hardly responds to different applied voltages. In other words, although one has access to a variety of gate voltages and diverse ranges in the $3 \times 3$ system under consideration, the fixed $t$–value essentially also determines the strength of the X–gate. As $t$ cannot be varied, it negates the qubit control one needs over the entire Bloch sphere. The range of $\mathcal{B}_x$ values obtained by varying local voltages is so narrow that it is hardly visible in Fig. 5.9b. In order to see the difference between the maximum and minimum value of $\mathcal{B}_x$ achieved, their difference $|\Delta\mathcal{B}_x|$ is plotted separately: the first dip in this curve is related to a change in sign in $\Delta\mathcal{B}_x$, while the second kink

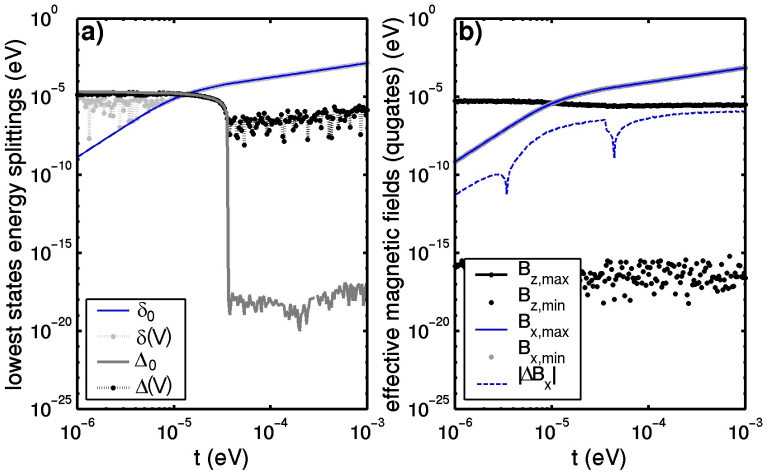


Figure 5.9: Numerical exploration of effective (pseudo–) magnetic fields from a random sequence of gate voltages (4096 configurations for every $t$ value). (a) Energy level splitting between the lowest two eigenstates (the qu2LS), $\delta$, as well as the level splitting between the 2nd and the 3rd eigenstate, $\Delta$, shown with and without gate voltages applied. A well behaved two level system exists for $t \lesssim 0.5 \times 10^{-5}$eV, while for larger $t$ higher lying states cross over. (b) Sampling the gate voltages randomly, the minimum and maximum pseudo–magnetic fields achieved are recorded ($H = a1 + \vec{\mathcal{B}}\vec{\sigma}$, and thus $\vec{\mathcal{B}}$ has units of energy). Since $\mathcal{B}_{x,min}$ and $\mathcal{B}_{x,max}$ are very similar, the difference $\Delta\mathcal{B}_x$ is shown explicitly by the blue dashed line. $\mathcal{B}_{z,min/max}$ values are clearly discernible. Note that the $\mathcal{B}_x$ is directly related to the gap in the ground state ($\delta_0$ in panel (a))

is already well beyond the qu2LS regime and originates in other higher lying states taking over the ground state.

The numerical results show that despite having access to a large set of voltage gates, the second qugate *cannot* be implemented electrostatically under the assumptions of constant tunneling and no real external magnetic field. One may argue, that this happens because of the peculiar geometry chosen and that there may be other geometries which would respond differently. That this is not the case will be shown in the following section.

### Electrostatic Interactions with Gates

From an analytical point of view, a set of general statements can be made with respect to the charge states considered above. If the total wavefunction of the system can be described by a single spatial wavefunction as is the case for two or less particles in total, the following two statements hold:

B1. Encoding the qubit in the charge and thus in the spatial wave function, demands

that the basis of the ground state pair is formed from two spatially separated wave functions.

B2. The attempt to implement an efficient second qugate via electrostatic means only with the tunneling $t$ kept constant and no real external magnetic field present, results in compromising the qu2LS with respect to the other states available to the system, and thus fails.

These two points are true in general, and as such consistent with the numerical simulation above.In order to show this, we will use the following further statements:

C1. The ground state of any of the considered states (single particle, singlet or triplet) for a real (not complex) Hamiltonian must be nodeless, where for the states with more than one particle one must consider only the restricted space $\Omega \equiv \vec{r}_1 < \vec{r}_2 < \ldots$ within some unique sorting scheme, where $\vec{r}_i$ points to the location of particle $i$ (this restriction is necessary since for example on the overall space, the triplet states have an intrinsic node due to the particle exchange symmetry).

C2. If a matrix element $\langle\psi_1| V |\psi_2\rangle$ is $\neq 0$ for a local potential, then for $\psi_1 \neq \psi_2$ at least one of the two wave functions must have a node within the space $\Omega$, and thus must be split off from the ground state itself.

The argument for statement (C1) is similar to one found in [SSK53]. The statement follows from the observation that any eigenstate $\psi(\vec{r}_1, \vec{r}_2)$ with a node within $\Omega$ has a counterpart $|\psi|$ which has the same energy expectation value $\int_\Omega |\psi| \cdot H \cdot |\psi| = E = \int_\Omega \psi H \psi$ and thus by the variational principle, the ground state must be always nodeless or, at least, can be chosen as such. Note that the kinks introduced in $|\psi|$ at the positions where $\psi$ changes sign, do not cause any problems with the Laplacian that appears in the Hamiltonian, as can be seen from the following simple consideration in 1D

$$\int_{-L}^{+L} dx \;\; |x| \frac{d^2}{dx^2} |x| = \int_{-L}^{-\varepsilon} dx \; x \frac{d^2}{dx^2} x + \underbrace{\int_{-\varepsilon}^{+\varepsilon} dx \;\; |x| \frac{d^2}{dx^2} |x|}_{\simeq 2\varepsilon\left(\varepsilon \frac{\varepsilon+\varepsilon-2\cdot 0}{\varepsilon^2}\right) \sim \varepsilon \to 0} + \int_{-L}^{-\varepsilon} dx \; x \frac{d^2}{dx^2} x$$

Statement (C2) is shown as follows: since $\int_\Omega \psi_1^*(\vec{r}_1, \vec{r}_2) V(\vec{r}_1, \vec{r}_2) \psi_2(\vec{r}_1, \vec{r}_2) \neq 0$ with the local potential $V(\vec{r}_1{}', \vec{r}_2{}'; \vec{r}_1, \vec{r}_2) \equiv V(\vec{r}_1, \vec{r}_2) \delta(\vec{r}_1{}' - \vec{r}_1) \delta(\vec{r}_2{}' - \vec{r}_2)$, there must be some region in space where both $\psi_1$ and $\psi_2$ are $\neq 0$ simultaneously. Yet, since $\psi_1$ and $\psi_2$ are orthogonal single–valued real functions, in order for $\langle\psi_1|\psi_2\rangle$ to

be $= 0$ there must be still another region in space with both $\psi_1$ and $\psi_2$ unequal to zero but with a different sign compared to the first region. Thus either $\psi_1$ or $\psi_2$ must switch sign from one region to the other.

With this, statement (B1) follows from the observation that for some specific set of parameters within the working–range of the qubit, the ground state is considered exactly degenerate. Thus utilizing statement (C1), both of these ground states must be nodeless. Yet, they must be also orthogonal to each other, and so as in statement (C2), $\psi_1$ and $\psi_2$ can be chosen such that $\psi_1$ is $= 0$ where $\psi_2 \neq 0$ and vice versa. This is what is meant by spatially separated wave functions. Moreover, since this ground state pair is supposed to be sufficiently decoupled from the remaining states, this situation only changes slightly during gate operations where for example an overlap is needed in order to rotate the system from one of the groundstates to the other.

Statement (B2) follows from the general structure of the Hamiltonian. From a perturbative point of view, the Feshbach formalism underlines this result. In matrix representation and in the notation of the Feshbach formalism (see Sec. 4, pp. 65), the Hamiltonian of the qubit system with an isolated subspace with index $\{1, 2\}$ is given by

$$
\begin{aligned}
H = & \left(\begin{array}{cc|ccc}
\varepsilon_1(\mathbf{V}_g) & 0 & \dots & H_{1k'}(t) & \dots \\
0 & \varepsilon_2(\mathbf{V}_g) & \dots & \dots & \dots \\
\hline
\vdots & \vdots & \ddots & \vdots & H_{kk'}(t) \\
H^*_{1k'}(t) & \vdots & \dots & \varepsilon_k(\mathbf{V}_g) & \dots \\
\vdots & \vdots & H^*_{kk'}(t) & \vdots & \ddots
\end{array}\right) \\
\equiv & \begin{pmatrix} H_{PP}(\mathbf{V}_g) & H_{PQ}(t) \\ H^+_{PQ}(t) & H_{QQ}(t, \mathbf{V}_g) \end{pmatrix}.
\end{aligned}
\tag{5.47}
$$

The potentials on the external voltage gates $\mathbf{V}_g$ only enter in the diagonal due to the fact that one is dealing with a local potential. The term $H_{PP}$ for example is the projection $PHP$ of the Hamiltonian onto the 2D ground state space $P$. Furthermore, with no gate voltages applied, the ground state is degenerate for $t = 0$, and therefore $\varepsilon_1 = \varepsilon_2$ for $\mathbf{V}_g = 0$. The Hamiltonian is diagonal when $t = 0$ and therefore $H_{PQ}(0) = 0$. Eventually, the coupling within $H_{PP}$ itself has to proceed through an intermediate state in $Q$ and therefore has to be mediated by $H_{PQ} \neq 0$. This is so because there is no direct mixing in $H_{PP}$, since it is diagonal.

From this structure of the Hamiltonian, the first qugate (Z–gate) is easily realized by choosing $\mathbf{V}_g$ such that $\varepsilon_1 \neq \varepsilon_2$, e.g. by breaking the 90° symmetry of the $3 \times 3$ array in the previous example. The second qugate (X–gate), however, can only be

realized through coupling to the remaining space $Q$. For simplicity but without restricting the case, a $\mathbf{V}_g$ is chosen such that it preserves $\varepsilon_1 = \varepsilon_2$, i.e. it has no Z–gate component. Now the effective two–level Hamiltonian constructed by the Feshbach formalism effectively folds the remaining Hilbert space into the reduced Hamiltonian $H_{PP}$ in the sense $H_{eff}^{P} \equiv H_{PP} + \Sigma_{QQ}$ and thus effects all elements in $H_{PP}$. The self–energy term $\Sigma_{QQ}$ due to the coupling of the $P$ space to the $Q$ space shifts the elements on the diagonal, but can also generate off–diagonal elements. The latter term is then straightforwardly related to the X–gate ($\sigma_x$) which gave rise to the splitting for the singlet qu2LS in Eq. (5.46). Thus by comparison, the effective second qugate for singlet states is approximated by

$$\mathcal{B}_x \approx 32 \frac{t^4}{\left[\Delta\left(\mathbf{V}_g\right)\right]^3}$$

where $\Delta(\mathbf{V}_g) \equiv \Delta_0 + \Delta\varepsilon(\vec{V}_g)$ is the gap $\Delta_0$ towards the higher lying states altered by the applied gate voltages $\mathbf{V}_g$. In order to keep the qu2LS well isolated from the remainder of the states, it must hold $|\Delta\varepsilon/\Delta_0| \ll 1$, so that the second gate is approximated by

$$\mathcal{B}_x \approx 32 \frac{t^4}{\Delta_0^3} \cdot \left(1 - \frac{3\Delta\varepsilon\left(\mathbf{V}_g\right)}{\Delta_0}\right) \tag{5.48}$$

This second qugate (X–gate) intrinsically has a much weaker dependence on the gate voltages since it must be mediated by the coupling $t$, while the first qugate (Z–gate) is directly sensitive to the gate voltages as $\Delta\varepsilon(\mathbf{V}_g)$. In summary, for the qu2LS to be well–defined in the sense that it is sufficiently decoupled from the rest of the system, it must hold that $t/\Delta_0 \ll 1$ (weak tunneling by construction of the qu2LS) and now also $|\Delta\varepsilon/\Delta_0| \ll 1$ in order for the gate operation to not interfere with the higher lying states. The consequence is that the initial splitting for the singlet states is small and the effect of the second qugate only changes this splitting by a fraction which is an order of magnitude smaller. In order to get a significant contribution, the second condition $|\Delta\varepsilon/\Delta_0| \ll 1$ would have to be lifted with the obvious consequence that it sacrifices the notion of an isolated qu2LS altogether. This proves statement (B2).

Local electrostatic interaction of voltage gates with a charge qubit system is therefore not sufficient for a full set of single qubit rotations. However, revision of the arguments above clearly leaves two ways out of this dilemma: first, the gap ($\mathcal{B}_x$) is controlled by the tunneling. Thus a tunable tunneling would allow for the second qugate needed as is well–known [GSC+03] but this was explicitly excluded from an experimental point of view. Second, the system was assumed to be described by one single and real spatial wavefunction, since the Hamiltonian was assumed to be real and the maximum number of particles considered was two. The argument of

a nodeless ground state wave function very much relies on that fact since for a real wave function a sign change is only possible via a transition through zero while for example in the complex case this is no longer required. With this, statement (B1) becomes irrelevant, and the freedom on $\langle\psi_1| V |\psi_2\rangle \neq 0$ is greatly increased. Specifically, an external magnetic field which makes the Hamiltonian complex, will in fact not increase the initially existent (but constant!) X–gate for singlet states, but it can reduce it to zero as will be shown in the next section. In a sense then, this is again equivalent to an effectively tunable tunneling even though the interdot site tunneling amplitude $|t|$ remains constant throughout.

The other door that is left open, is considering more than two operative electrons on the array. There are clearly cases then, where the total wavefunction of the system cannot be described anymore by a simple product of a single spatial wavefunction and a spin part anymore, but by a sum over such products of spatial and spin terms. This again, eliminates the requirement of a nodeless wavefunction in the ground state. However, the clear separation of a groundstate qu2LS from the remainder of the states does not appear to be that efficient, or, from a practical point of view clearly complicates the experimental setup if one were to think for example about three electrons on a ring with six dots which again has a natural qu2LS for weak tunneling. Systems like the latter one, however, still behave exactly the same as the $2e$ systems discussed here, but where in addition their more complex experimental setup eventually makes it even more unlikely to be realized some day given the rather strict complications already existent for very simple systems. In this sense also, the $3 \times 3$ array considered above has been studied only for theoretical purposes in order to see the explore the model characteristics. However, its dynamics is very similar to the much simpler $2 \times 2$ array which will be considered with respect to a real magnetic field in the remainder of this discussion.

### 5.5.3 Magnetic Gate with Application on $2 \times 2$ Array

As shown in the previous section, a purely electrostatic realization of full single charge qubit operation is not possible. For the necessary second quantum gate a real external magnetic field is introduced in the following discussion. The tunneling is kept at the same amplitude, but it picks up a complex phase. The behavior of the singlet and triplet states are then determined by the two external parameters, the asymmetrically applied gate voltage $V_g$, which breaks the 90° symmetry and realizes the Z–gate as shown earlier, and the magnetic field $B$ perpendicular to the array. Careful control of the magnetic flux through the system allows one to construct a fully operational X–gate in the sense that this X–gate can be turned on and off completely at will. The maximum strength of this X–gate is eventually determined by the tunneling

amplitude. Together, the voltage gates and the magnetic field allow full quantum manipulation of the charge qubit.

The analysis of the numerical results again follows the Feshbach formalism (Sec. 4, pp. 65). This approach provides insights on the nature of the system dependence on fields, and explains the ability of the magnetic field to complete the set of necessary single qubit operations.

The model network under consideration here is a $2 \times 2$ array of qudots with a single spatial state per site plus spin. The system has been already sketched in Fig. 5.1a (p. 116). As explicitly outlined in panel (b) of that figure, tunneling is allowed between any pair of dots, where every tunnel junction also carries capacitance. The parameters which enter the model are: the dot–gate capacitance ($C_g = 25$aF), the dot–dot capacitances ($C_{dd} = 25$aF for nearest neighbor dots and 17aF for dots connected through the diagonal of the array), the dot self–capacitance ($C_{d0} = 25$aF) and the dot–dot tunneling amplitude ($t = 2\mu$eV). Similar to the $3\times3$ array earlier, the parameters have been chosen such that the energy cost for double occupancy of a dot (standard Hubbard $U$) is about 1meV which corresponds to typical dot dimensions of 100nm. Note that the tunneling amplitude $t$ is chosen fairly small, which is essential to ensure a good quality of the qu2LS in the groundstate that is the higher lying states are well split off compared to the dynamic splitting due to $t$ in the groundstate system.

The Hamiltonian used to describe this system is again given by Eq. (5.3) described in Sec. 5.1 (pp. 95). The uniform magnetic field perpendicular to the network of qudots affects the tunneling as already mentioned by giving it a complex phase in the Peierls sense (see Sec. 5.6, pp. 150, Eq. 5.50). The phases are determined by the path integral of the vector potential $\vec{A}$ describing the applied magnetic field, $\vec{B} = \vec{\nabla} \times \vec{A}$. Using a symmetric gauge, the acquisition of phase in the $2 \times 2$ array of qudots is indicated in Fig. 5.10 panel (a). The phase *flows* clockwise on the outer connections while the diagonal connections still remain phaseless. The ring structure leads to an Aharonov–Bohm (AB) phase [AB59] for a single particle moving around the ring. Note, however, that the second particle is essential for the necessary ground state qu2LS needed in the qubit setup. For lithographic setups on the scale of 200nm, the required magnetic field for an AB phase cycle on the whole array is around 100mT which is still rather small. At these fields the local wave functions in the individual quantum dots do not change much, and the tunneling amplitude $|t|$ can be considered constant.

In Fig. 5.10b, the two–particle Hilbert space and the allowed tunnel transitions are shown for the $2 \times 2$ system. For simplicity, states of double occupancy are safely neglected due to their much larger energy scale compared to the lowest energy processes considered here. The blue dashed lines in Fig. 5.10b are related to particle exchange

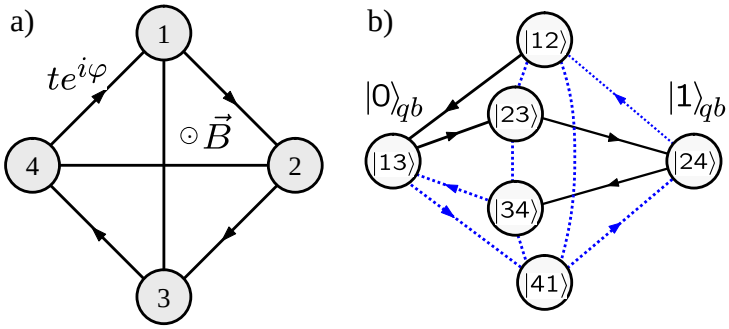


Figure 5.10: $2 \times 2$ qudot array. (a) Array with a perpendicular magnetic field applied. (b) Schematic network of Hilbert space states with the tunneling transitions indicated by connecting lines (no double occupancy). The arrows indicate the flow of complex phase acquired by the tunnelling $|t|\, e^{i\varphi}$. The dashed blue lines indicate paths of particle exchange (see text). $|0\rangle_{qb} \equiv |13\rangle$ and $|1\rangle_{qb} \equiv |24\rangle$ are the qubit states with $|ij\rangle$ being a state with one electron on dot $i$ and the other on dot $j$.

in the sense that the off–diagonal element in the corresponding triplet Hamiltonian has an extra minus sign due to its fermionic character, as it can also be seen directly from the basis chosen. For example, the transition $|12\rangle$ to $|23\rangle$ can be thought of as the two–step process of one hopping and one exchange, $|12\rangle \rightarrow |32\rangle \rightarrow -|23\rangle$. Thus any path in this Hilbert space network of Fig. 5.10b in the sense of the Feshbach formalism with an odd number of dashed segments has an extra minus sign associated with it. Moreover, if the path is closed, then an odd number of dashed segments refers to an effective exchange of the two electrons. More on this later.

### Analysis

Using the Hamiltonian in Eq. (5.3), the eigenspectrum for the $2 \times 2$ array is shown in Fig. 5.11 panel (a) as function of an asymmetric gate voltage drag $V_g$, with no magnetic field applied ($B = 0$). For small $V_g$, the singlet (triplet) qu2LS in the groundstate is well separated from the remaining singlet (triplet) spectrum. In contrast to the singlet set, however, which has an anticrossing at $V_g = 0$, the triplet set is degenerate there. Panel (b) then shows the eigenspectrum as function of the magnetic field when there are no gate voltages applied ($V_g = 0$). The tunneling has been chosen relatively large ($|t| = 5\mu$eV) such that the energy splitting $\delta$ due to the tunneling in the low–energy singlet set (the qu2LS we will focus on) reaches about 1/10 of the distance to the nearest higher lying states, $\Delta$. This is still a good qubit configuration, as the coherent state manipulation in the qu2LS can be performed

without significant admixture of the higher lying states. However, the gates must be switched smoothly enough for the evolution to be adiabatic with respect to the higher lying states, as will be seen later from the numerical analysis.

The energy spectrum in Fig. 5.11b is periodic in the magnetic field in the usual AB sense. Since $\varphi$ is the phase between two dots on the outer loop of the $2 \times 2$ array, it relates to one quarter of the phase on the entire outer loop, this means that with every $\Delta\varphi = 2\pi/4$ one additional flux quantum enters or leaves the cross–sectional area of the array. This is seen for example in the splitting of the singlet which opens and closes with a period $\Delta\varphi = 2\pi/4$. The exact period of the system, however, is $\Delta\varphi = \pi$. Note, that this is not because of the usual $t \to -t$ symmetry which does not hold here because of the diagonal cross link in the array shown in Fig. 5.10a. Instead, it can be formally related to changing the sign in both basis states of the qu2LS where an additional overall phase on a basis state is irrelevant to the physics. This is easily seen for $\varphi = \pi$ from Fig. 5.10b by considering $|0\rangle_{qb} \equiv |13\rangle = -|31\rangle$ and dropping all the arrows shown.

Now the essential effect of the magnetic field is that it allows one to close the gap in the singlet qu2LS while at the same time it opens a gap in the triplet qu2LS (at fixed $S_z$). The smallest magnetic field where this happens is at $\varphi \equiv \varphi_0 = 0.286\ \pi$, indicated by the arrow in Fig. 5.11b. The important consequence of tuning the magnetic field to $\varphi \to \varphi_0$ is that the charge qubit can be held *frozen* in its state when also $V_g = 0$ (see below).

Figure 5.11c and d show the singlet ground state configuration and its two *spatially distinct* basis states, respectively. Note that in order to have a (close to) degenerate groundstate qu2LS, there must exist a basis representation that is spatially complementary as argued in Sec. 5.5.2 (pp. 138), in agreement with what is shown in panel (d).

For the charge qubit encoded in the $2 \times 2$ array with the basis states as shown in Fig. 5.11d, the physical quantum gates are now as follows: the asymmetrically applied gate voltage (see Fig. 5.1b) only drags apart the potentials of the two qubit basis states in Fig. 5.11d and thus represents the Z–gate ($\sigma_z$). On the other hand, the singlet gap or anticrossing can be related to a real off–diagonal element in the 2D pseudospin Hamiltonian which can be tuned down to exactly zero by a magnetic field as shown above. Thus this is referred to as the X–gate ($\sigma_x$). Together, the two physical qugates introduced can be utilized to generate arbitrary rotations of the Bloch vector and thus to construct arbitrary qugates for the qu2LS. Also, since both of the qugates can be turned off completely by setting $V_g = 0$ and turning on a specified magnetic field, this allows to freeze the qu2LS in any arbitrary state at any time.

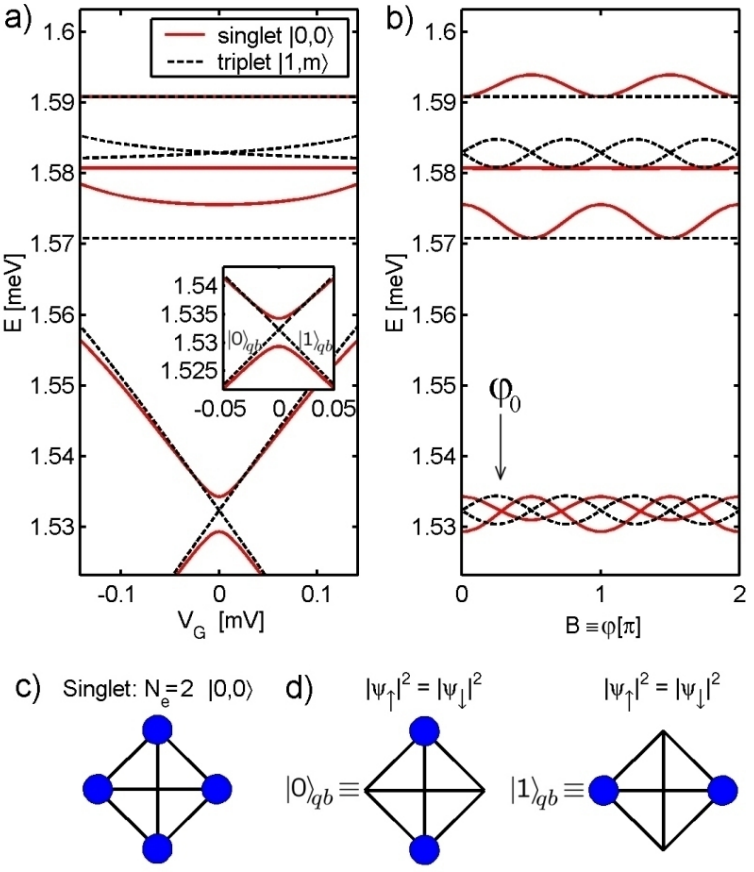


Figure 5.11: Energy spectra for the qu2LS of the $2 \times 2$ qudot system together with a few higher lying states for singlet and triplet states ($|S,\ S_z\rangle = |0,0\rangle$ and $|S,\ S_z\rangle = |1, m = -1, 0, 1\rangle$ respectively). (a) Energy spectrum vs. asymmetrically applied gate voltage, $V_G \equiv V_{g_1} = -V_{g_2}$. The doubly occupied states lie about 1meV higher in energy (outside figure) and therefore have negligible influence. The inset shows a closeup of the (anti)crossing in the qu2LS. (b) Energy spectrum vs. uniform external magnetic field perpendicular to the array expressed through the phase in $t = |t|\, e^{i\varphi}$. The initial singlet anticrossing at $\varphi = 0$ is completely closed for $\varphi = \varphi_0 = 0.286\ \pi$, indicated by the arrow in panel (b), while at the same time the triplet levels show a pronounced anticrossing. (c) Singlet ground state probability distribution over the $2 \times 2$ array. This state is a symmetric combination of the basis states shown in panel (d): Probability distribution of the basis states of the singlet qu2LS labeled $|0\rangle_{qb}$ and $|1\rangle_{qb}$ with equal probability to find spin up or spin down, $|\psi_\uparrow|^2 = |\psi_\downarrow|^2$.

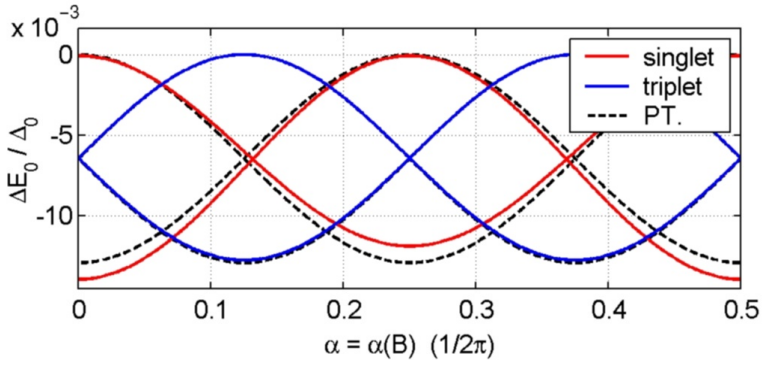


Figure 5.12: Energy splitting in the qu2LS for the system of Eq. 5.36 in dependence of the magnetic field for singlet (red) and triplet states (blue). The splitting is shown in units of $\Delta_0 = \varepsilon_2 - \varepsilon_1$, namely the separation of the qu2LS from the remaining Hilbert space. The dashed black line is the result of the lowest order Feshbach analysis, Eq. (5.49).

### Splitting due to Exchange Energy

The opening and closing of the gap in the qu2LS can be understood in a more picturesque way using the Feshbach formalism which provides further insight into the origin of these splittings. With no magnetic field, this has already been done in Sec. 5.4 (pp. 120). With no gate voltages applied the triplet ground state qu2LS is lowered by $-\frac{4t^2}{\Delta_0} + \mathcal{O}(t^3)$ with $\Delta_0 = \varepsilon_2 - \varepsilon_1$, but the qu2LS is still degenerate. On the other hand, the singlet qu2LS splits up into a bonding state lowered by $-\frac{8t^2}{\Delta_0} + \mathcal{O}(t^3)$ in energy which is thus the ground state, and an antibonding state not shifted at all in energy.

### Effect of External Magnetic Field

In analogy to the splitting without a magnetic field analyzed above, the Feshbach formalism can be applied again for the case of an external magnetic field where the tunneling coefficient acquires complex phases indicated by the arrows in Fig. 5.10b. Note that these phases affect only the first and last step in each path of the Hilbert space network of Fig. 5.10b, while transitions between intermediate states remain unaltered by the presence of the magnetic field. This follows from the observation that transitions between intermediate states correspond to transitions through the diagonal of the array in Fig. 5.10a which does not acquire any magnetic phase in the symmetric gauge for the magnetic vector potential.

The paths can be summed up similarly. For simplicity, however, only the contribution to lowest order in $t$ for the effective Hamiltonian will be given. The denominator $\omega - \varepsilon_2$ is then replaced by $\varepsilon_1 - \varepsilon_2 = -\Delta_0$, and so the lowest order contribution to the

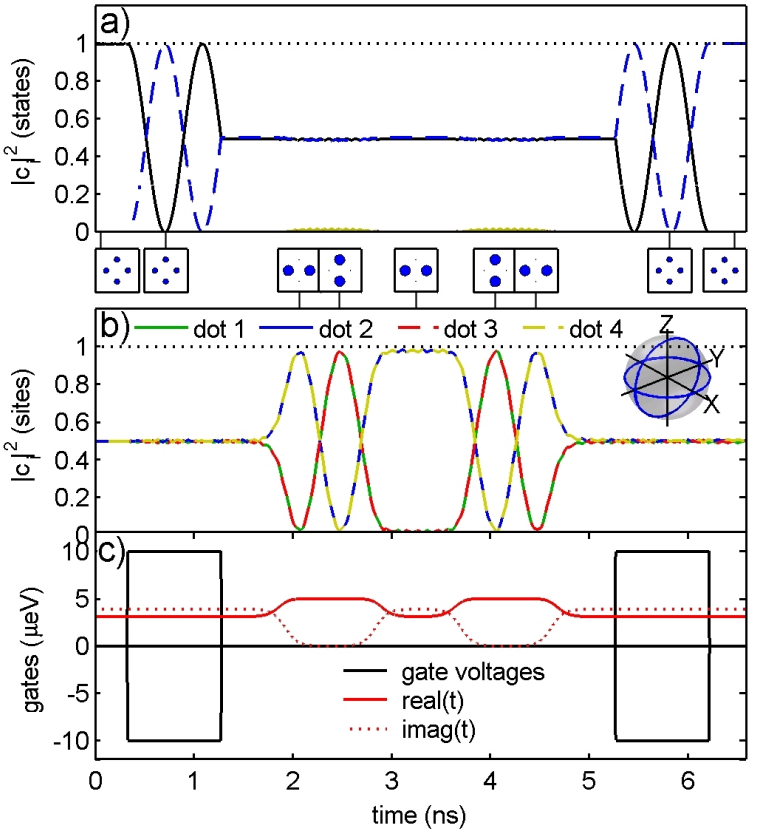


Figure 5.13: Time evolution and control of the singlet qu2LS on the $2 \times 2$ array. (a) Time evolution of the state occupancy with respect to the qubit basis $|0\rangle_{qb}$ and $|1\rangle_{qb}$ (see Fig. 5.11d). (b) Time evolution of the site occupancy $\left|\langle c_i^+ c_i\rangle\right|^2 \equiv \left|\langle\psi\left|c_i^+ c_i\right|\psi\rangle\right|^2$. The square panels in between panels (a) and (b) show snapshots of the charge distribution on the array at the times indicated either towards panel (a) or panel (b). The inset in panel (b) shows the time evolution of the qubit in Bloch sphere representation. (c) Time–dependence of the voltage gates (black) and the magnetic field expressed through Re (t) and Im (t) (red lines) where Abs (t) is kept constant. The time constant for rise and fall time of the gate voltages was chosen as $\tau_V \equiv 0.658$ ps while for the tunneling the considerably longer $\tau_\varphi \equiv 100 \cdot \tau_V = 65.8$ ps was used out of adiabatic purposes with respect to the higher lying states.

self energy term is

$$\Sigma_{eff}^{singlet}(\omega,\varphi) = -\frac{4t^2}{\Delta_0}\begin{pmatrix} 1 & \cos 2\varphi \\ \cos 2\varphi & 1 \end{pmatrix} + \mathcal{O}\left(t^3\right) \tag{5.49a}$$

$$\Sigma_{eff}^{triplet}(\omega,\varphi) = -\frac{4t^2}{\Delta_0}\begin{pmatrix} 1 & i\sin 2\varphi \\ -i\sin 2\varphi & 1 \end{pmatrix} + \mathcal{O}\left(t^3\right). \tag{5.49b}$$

Comparing this with the last terms in Eqs. (5.38), the effect of the external magnetic field is obvious. With increasing $\varphi$ the singlet splitting can be reduced down to zero ($\cos 2\varphi = 0$), while simultaneously a comparable gap opens in the triplet states, in agreement with the numerical data for the full $2 \times 2$ system in Fig. 5.11b. Consequently, the effect of the magnetic field on the singlet (triplet) states is that of an X (Y) gate, respectively, and thus clearly provides the necessary second quantum gate for single qubit operation. Figure 5.12 compares the exact numerical results of the Hamiltonian in Eq. (5.36) with above lowest order perturbative approach for the splitting in the qu2LS. The lowest order contribution in the Feshbach formalism already provides an excellent approximation.

### Numerical Qubit Dynamic

The time evolution of the $2 \times 2$ qudot array is studied numerically for the singlet state under the action of the Z–gate (voltage) and the X–gate (magnetic field). Note that here the X–gate is considered non–active when a magnetic field is tuned to the phase $\varphi = \varphi_0$ indicated by the arrow in Fig. 5.11b, while the gate is considered active when the magnetic field is turned off ($\varphi = 0$). In this sense, with none of the two gates applied, the system is *static* since the singlet states are degenerate.

Typical time dynamics data is shown in Fig. 5.13 over a range of a few nanoseconds. Starting in the singlet ground state (Bloch vector $\vec{r}_b = +\hat{x}$), the system is static at $t = 0$. The following Z–gate (voltage) rotates this state around the $\hat{z}$ axis by 450°, leaving the system in $\vec{r}_b = +\hat{y}$. After a short time interval the X–gate (magnetic) is activated at $t = 1.6$ ns which rotates $\vec{r}_b$ around the $\hat{x}$–axis by again 450°, leaving the system in the $+\hat{z}$ state where it is stalled again now being in the central region on the time axis in figure Fig. 5.13b. Since $\pm\hat{z}$ corresponds to the basis states of the qubit, the charge distribution equals the $|1\rangle_{qb}$ state in Fig. 5.11d as can be seen by the snapshots shown along the time evolution in between panels (a) and (b) in Fig. 5.13. After another X–gate of the same duration, the system is in the $-\hat{y}$ state at $t = 4.8$ ns. When finally a (-X)–gate is applied, the qubit is rotated by $-450°$ around the $\hat{z}$–axis and the system is left in the $-\hat{x}$ configuration at $t = 6.2$ ns. The time evolution of the Bloch vector in this whole process sweeps two grand circles in the Bloch sphere, as shown in the inset of panel (b).

The numerical data shown in Fig. 5.13 confirms the previous analysis in the sense that the qubit can be placed into any state by applying appropriate magnetic field and gate voltages to the system, yielding full control of the qubit as desired.

## 5.6 Appendix: Effect of Magnetic Field on Tunneling Amplitude

An external magnetic field perpendicular to a network of qudots effects the system insofar as spatial propagation can be associated with the pickup of complex phase. In this sense, in the weak tunneling regime the $t_{ij}$ become complex [Pei33]

$$t_{ij} = t_{ji}^* = |t_{ij}|\, e^{i\varphi_{ij}} \text{ with } \varphi_{ij} \equiv \frac{e}{\hbar} \int_{x_i}^{x_j} \vec{A} \cdot d\vec{\ell} \tag{5.50}$$

where $\vec{A}$ is the vector potential for the magnetic field with $\vec{B} = \vec{\nabla} \times \vec{A}$. A short justification for Eq. (5.50) will be given in the following section.

The acquisition of phase of the tunneling coefficients as in Eq. (5.50) introduces a *flow* of phase which is conveniently indicated by arrows on the tunnel connections (see for example Fig. 5.1, p. 116). For closed loops of qudots, the phase *flows* clockwise or counter–clockwise around the loop depending on the direction of the magnetic field. The apparent ring structure leads to an Aharonov–Bohm (AB) phase [AB59] for a single particle moving around the ring. The overall phase in this ring is calculated using Eq. (5.50)

$$\varphi_{loop} = \frac{e}{\hbar} \oint \vec{A} \cdot d\vec{\ell} = \frac{e}{\hbar} \int \underbrace{\left(\vec{\nabla} \times \vec{A}\right)}_{=\vec{B}} d\vec{S} \equiv \frac{e}{\hbar}\phi \equiv 2\pi \frac{\phi}{\phi_0}$$

with the total magnetic flux threaded through the loop given as $\phi$. When $\varphi_{loop}$ changes by a total of $2\pi$, this is related to a change of the total flux $\phi$ by one flux quantum $\phi_0 \equiv \frac{h}{e} = 4.135 \cdot 10^{-15}\ \mathrm{Tm}^2 = 4.135\,\mathrm{mT}\,\mu\mathrm{m}^2$ that entered or left the ring and the physics is expected to be the same for both values of the magnetic field. For typical lithographic setups on the scale of 200 nm the required magnetic field for one AB phase cycle on the whole array is rather small, namely about 100 mT ($4.135 \cdot 10^{-15}\ \mathrm{Tm}^2 / (200 \cdot 10^{-9}\ \ \mathrm{m})^2 = \frac{4.135}{4} \cdot 10^{-1}\ \mathrm{T} \approx 100\ \mathrm{mT}$). With this, the local wave functions in the individual quantum dots are assumed to approximately remain the same such that the absolute value of the tunneling $|t|$ is considered constant.

### The Quantum–Mechanical Treatment of a Magnetic Field

The origin of Eq. (5.50) stems from the usual substitution of the momentum operator in the presence of a magnetic field $\vec{p} \to \vec{p} - \frac{q}{c}\vec{A}$ in CGI units [Bal99, p. 308], or

equivalently in SI units

$$\vec{p} \to \tilde{p} \equiv \vec{p} - q\vec{A} \tag{5.51a}$$

with $\vec{p}$ the canonical momentum and $q = -e$ for the case of an electron. This substitution is derived from the classical Lagrangian for a particle with charge $q$ in the presence of a magnetic field $\vec{B} = \vec{\nabla} \times \vec{A}$ [Bal99]. Moreover, Eq. (5.51a) is equivalent to the following unitary transformation of the momentum operator

$$\vec{p} \to \tilde{p} = e^{-i\frac{q}{\hbar}\int^{x}\vec{A}(x')d\vec{x}'}\vec{p}e^{i\frac{q}{\hbar}\int^{x}\vec{A}(x')d\vec{x}'} \equiv e^{-i\alpha(x)}\ \vec{p}\ e^{i\alpha(x)} \tag{5.51b}$$

with

$$\alpha\left(x\right) \equiv \frac{q}{\hbar}\int^{x}\vec{A}\left(x'\right)d\vec{x}' \tag{5.51c}$$

since

$$e^{-i\alpha(x)}\vec{p}e^{i\alpha(x)} = 1\cdot\vec{p} - e^{-i\frac{q}{\hbar}\int^{x}\vec{A}(x')d\vec{x}'}\left(\frac{\hbar}{i}\vec{\nabla}e^{i\frac{q}{\hbar}\int^{x}\vec{A}(x')d\vec{x}'}\right) = \vec{p} - q\vec{A}\left(\vec{x}\right)$$

For a free particle with the Hamiltonian $H = \frac{p^2}{2m}$ the Hamiltonian is transformed similarly, $\tilde{H} = e^{-i\alpha(x)}\frac{p^2}{2m}e^{i\alpha(x)}$. Together with the complimentary unitary transformation of the wave function

$$\psi\left(x\right) \to \tilde{\psi}\left(x\right) \equiv e^{-i\alpha(x)}\psi\left(x\right)$$

it follows

$$\tilde{H}\left|\tilde{\psi}\right\rangle = e^{-i\alpha(x)}\frac{p^2}{2m}e^{i\alpha(x)}\cdot e^{-i\alpha(x)}\left|\psi\right\rangle = e^{-i\alpha(x)}\frac{p^2}{2m}\left|\psi\right\rangle$$

such that for any eigensolution of the initial problem $H\left|\psi\right\rangle = E\left|\psi\right\rangle$, the transformed $\left|\tilde{\psi}\right\rangle$ is the solution for the Hamiltonian including the magnetic field $\tilde{H}$ and it has the same eigenenergy $E$ as the original free particle without the magnetic field

$$\tilde{H}\left|\tilde{\psi}\right\rangle = e^{i\alpha(x)}E\left|\psi\right\rangle = E\left|\tilde{\psi}\right\rangle$$

In the presence of a potential $V\left(x\right)$, this one must be also transformed similarly to Eq. (5.51b) since

$$\tilde{H} = e^{-i\alpha(x)}\frac{p^2}{2m}e^{i\alpha(x)} + V\left(x\right) = e^{-i\alpha(x)}\left(\frac{p^2}{2m} + \tilde{V}\left(x\right)\right)e^{i\alpha(x)}$$

with the resulting transformed potential

$$\tilde{V}\left(x\right) \equiv e^{i\alpha(x)}V\left(x\right)e^{-i\alpha(x)}$$

The eigenvalues of the new Hamiltonian $\tilde{H}$ are therefore unlikely to be same compared to the initial eigenvalues without the magnetic field.

It is interesting to notice that the function $\alpha(x) = \frac{q}{\hbar}\int^x \vec{A}(x')\,d\vec{x}'$ can actually be altered arbitrarily by a vector potential obeying $\vec{A} = \vec{\nabla}\alpha$ ($\vec{A}$ is then just the related vector field to some potential $\alpha(x)$). This type of local phase $\alpha(x)$ added to a wave function $|\psi\rangle$ does not change the physics since $|\psi|^2$ still is the same. Hence if $\alpha(x)$ is a unique single valued function in the sense that $\alpha(x) = q\int^x \vec{A}(x')\,d\vec{x}'$ is independent of the path chosen (thus $\vec{\nabla}\times\vec{A} = \vec{B} = 0$ !), the Hamiltonian should be insensitive under this local phase transformation of $\psi(x)$

$$\psi(x) \to e^{ia(x)}\psi(x) \tag{5.52}$$

Note that this makes perfect sense since any $\alpha(x)$ with $\vec{A} = \frac{\hbar}{q}\vec{\nabla}\alpha$ only relates to a physically irrelevant gauge transformation well known in classical electrodynamics [Jac99, p. 240]

$$\vec{A} \to \vec{A} + \vec{\nabla}\chi \quad \text{and} \quad \phi \to \phi - \frac{\partial}{\partial t}\chi$$

with the arbitrary and non–physical gauge contribution $\chi$. This simply follows from the observation that the physical magnetic field $\vec{B} = \vec{\nabla}\times\vec{A} = \vec{\nabla}\times\left(\frac{\hbar}{q}\vec{\nabla}\alpha\right) = 0$. In order to have the Hamiltonian invariant under the transformation Eq. (5.52), the second term on the RHS of

$$\frac{\hbar}{i}\vec{\nabla}\cdot e^{ia(x)}\psi(x) = e^{ia(x)}\cdot\frac{\hbar}{i}\vec{\nabla}\psi(x) + \hbar\left(\vec{\nabla}\alpha\right)e^{ia(x)}\psi(x)$$

must be cancelled. The simplest fashion to do so is to subtract it on both sides

$$\underbrace{\left(\frac{\hbar}{i}\vec{\nabla} - \hbar\left(\vec{\nabla}\alpha\right)\right)}_{=\vec{p}-q\vec{A}}e^{-ia(x)}\psi(x) = e^{ia(x)}\cdot\frac{\hbar}{i}\vec{\nabla}\psi(x)$$

where now the operator on the LHS cancels the effect of the local phase $\alpha(x)$. This is exactly consistent with the operator in Eq. (5.51a) derived from the classical Lagrangian to the problem at the first place.

For a physical field, the phase $\alpha(x)$ is not a simple single valued function anymore in the sense that $\alpha(x) = q\int^x \vec{A}(x')\,d\vec{x}'$ depends on the path chosen for the integral. And the Hamiltonian is sensitive to exactly this type of a physically relevant vector potential with $\vec{A}$ with $\vec{\nabla}\times\vec{A} = \vec{B} \neq 0$.

In the case of localized quantum dots with weak tunneling along fixed paths, such as in Fig. 5.1, p. 116, it is then plausible to assume that for the tunneling coefficient $t_{ij} \equiv \langle i|\,H\,|j\rangle$ which could be chosen real in the case without a magnetic field, now

picks up a phase according to the previous discussion, namely $\alpha(x) \equiv \frac{q}{\hbar}\int^{x} \vec{A}(x')\,d\vec{x}'$ in agreement with the initial statement in Eq. (5.50). A more rigorous treatment to the root of the problem can be found in [Pei33].

# Chapter 6

# Conclusions

Nanoscale electrostatics plays an essential role in calculating the dominant system energy parameters. Since nanoscale *electronic* systems are embedded into electronic circuits, they are necessarily connected via leads to the macroscopic external world, and as a consequence the interplay between the very large (e.g. the leads) and the very small (e.g. the quantum dots) is unavoidable and must be accounted for. For well distinguishable and thus localized nanoscale systems, the capacitance matrix formalism is a very convenient tool in that respect. For weak tunneling between islands and a few tens of mobile electrons on each island, the capacitive description provides an excellent approach to estimate the systems energetics.

In the field of nanoscopic electrostatics several physical effects of different origin determine the major system characteristics. Conducting surfaces from macroscopic objects such as leads directly respond to nearby charges and in return also affect the dynamics of these charges. The related screening effects are of crucial importance. Moreover, localized static background charges if present in the system must be included in the analysis. If these are just impurities, they may not play that important a role since at low temperatures they provide a static potential landscape. On the other hand, with samples becoming cleaner and better these impurities may eventually become negligible. More importantly, systematic charging effects such as resulting from the dangling bonds on the sample surface must be taken into account adequately. At room temperature mobile and equilibrated, these states can be considered well–localized at low temperatures so that they become frozen and thus static during a cooling process. The resulting charge densities can drag the whole system characteristics as was shown in this work for the depleted ring structure.

Any model to describe electrostatic nano–systems must include appropriately these types of effects. Likewise, due to the complexity of real geometries, intuitive guesses can turn out to be quite wrong, and so a numerical model at least to double check one's intuition is of great use. The numerical relaxation algorithm presented in

this work solves a wide variety of electrostatic problems on a grid and is clearly apt to incorporate many of the major effects described above. The higher order algorithm generalized to 3D was equipped with a large set of different boundary conditions, some of which were developed along the way such as for example the local update algorithm for the 2DEG or the constraint on the overall charge of an island through the direct access to the charge density anywhere in the simulated system. The emerging numerical tool then allowed us to tackle highly interesting and experimentally relevant nanoscale geometries.

Quantum bits encoded in the electronic states of double quantum dots with one operative electron constitute the simplest charge qubit one can imagine. The mutual screened Coulomb interaction between two such qubits is well described by classical means. The effective interaction encoded in double–qudots can be understood as strongly screened dipole–dipole interaction. With respect to quantum computation, it is crucial to have the possibility of instantaneous control of the qubit pair interaction essential for the realization of basic quantum gates operating on pairs of qudots. The question that immediately arises is, can one screen the qubit interaction in an efficient and controlled *dynamical* manner. The interaction was studied in dependence of qubit distance. The resulting energy scales and distance dependence is a very useful information, yet it is clearly not something that can be done dynamically in current systems. Alternative approaches would clearly be an interesting issue to be explored in further detail.

In the remainder of the work charge qubits encoded in qubit arrays were addressed in general with respect to quantum computation. A network of quantum dots was modeled by a Hubbard Hamiltonian with one spatial state per site and including spin. Here the qudot interaction was simplified via capacitance parameters for nearest neighbor coupling. We focused on systems with at most two operative electrons. A set of general statements could be formulated and shown to clearly limit the possible geometries of a final realization of this type of charge qubits. Having constructed an energetically isolated two–level system including the ground state, the next step was to look for possible single qubit operations. With a fixed tunneling, as is the case in metallic islands separated by oxide layers, the first trial to have the necessary two quantum gates for full single qubit operation based on capacitively coupled gates alone failed halfway in the sense that it is straightforward to create one quantum gate through capacitively coupled gates. Yet, the second quantum operation only comes at the cost of compromising the isolated quantum two level system by bringing in a third state into the qubit energy space, in clear contradiction with the notion of a well isolated quantum bit.

In consequence, what is needed is *more quantum mechanics* in the sense that pure capacitive coupling turns out to be *too classical*. For the type of systems analyzed in

this work, it follows straight from earlier arguments, that one must be able to either alter the tunneling coefficient or to have a complex Hamiltonian, e.g. by applying an external magnetic field. Interestingly, the magnetic field which applies a complex phase to the tunneling eventually creates an effective tunneling coefficient which is tunable in amplitude by the magnetic field, such that this case is very similar to really changing the tunneling amplitude in the first place. With the resulting effective localization of the electrons on the dots due the external magnetic field, the second quantum gate for single qubit operation was successfully constructed. Full single quantum bit operation was demonstrated and dynamic numerical simulations were performed and underlined the previous discussion.

The realization of the second quantum gate using a uniform external magnetic gate has the clear experimental drawback that it is hard to address a sole qubit while leaving all the others unaffected. Therefore it is clearly desirable to replace the magnetic field by electronic means. In semiconductor quantum dots based on depleted 2DEG systems, this clearly appears to be feasible by varying the tunneling for example for the simplified dot–dot system as discussed in Sec. 3.2.6. Alternatively, it may be possible to achieve full single–qubit operations by temporarily employing a subset of the higher lying states, e.g. by bringing in a third state. This was looked at and appears possible, yet also has its drawbacks. Most importantly, for most of the qubit operations the qubit may reside in the second and third state but not in the ground state which makes relaxation into the groundstate a very important channel of decoherence.

In terms of decoherence, most emphasis in this work is put on the effect of the higher lying states and their adiabatic evolution. Other sources of decoherence are clearly present. The coupling to phonons is neglected by assuming low enough temperatures. However, there are other intrinsic effects which are independent of temperature. First of all, the quantum bit is controlled dynamically from the exterior. The leads have a certain resistance and thus a finite response time to changes in potentials. Taking the extreme case where the leads only have one full quantum channel and a capacitive coupling to the qubit system of typical 30 aF, then the time constant $\tau = RC = 0.39\,\mathrm{ps}$ is much smaller than the typical gate operations employed in this work. It appears to be safe to assume instantaneous gate operation and thus that the decoherence effect of the gates is small. On the other hand, the state of the quantum bit has to be read out at some point in time. The suggested detectors sensitive to single electron rearrangements are QPCs or SETs. Maximized sensitivity corresponds to maximum back action onto the quantum system itself. Thus keeping the sensitivity to a minimum during the computational process is absolutely necessary. Still, the presence of close–by single–electron detectors must be considered carefully and extensive research is done by many other groups in that respect.

*To learn to appreciate is not just to register one's desires. It is to educate one's desires; to believe that judgments based on these at any given time can be improved; that one goes on learning, and that there is always likely to be a gap between what one appreciates here and now and what would be full appreciation.*

Dorothy Emmet

# Appendix A

# Notes on C(++) Projects and Sources

Along the Ph.D. project several distinct numerical projects emerged and were coded in C with increasing extensions to C++ classes and function templates. All programming was done on an Alpha Linux machine or equivalent with 1GB of RAM. The main math library linked into the programs was the *Compaq Extended Math Library* (CXML) which includes all the standard BLAS and LAPACK routines, but has additional routines such as the three dimensional fast Fourier transform algorithm used in the EST3D project. The fact that CXML is a Fortran library does not cause any troubles, except that one has to be aware of some peculiarities such as additional trailing underscores in the function names, or that the matrix storage in Fortran is by column in contrast to C(++) where it is by row. Consequently, in fact the transpose of a matrix is handed over to the CXML routines. Wrapper functions were written to take care of these minute but important differences.

The basic C++ classes which were used extensively, were coded from scratch such that maximum transparency was guaranteed. Especially for example for the dynamic matrices in 2D as well as in 3D, it is essential that the whole data block is a continuous sequence in memory space when used with external libraries such as the CXML Fortran library mentioned above. Furthermore, the vector and the 2D and 3D matrix classes provide very convenient object spaces in terms of program coding. However, one must be aware of the extra overhead these classes can produce, and so especially for small portions of the programs which heavily operate in certain matrices for example, pointer variables were defined and referenced into these matrix structures in order to operate on the pure C level. Nevertheless, the C++ classes provide a very compact and convenient access to data which is also handed over easily to subroutines.

An extensive library of standard user routines was developed for data I/O from

and to files as well as to the standard output (terminal). All programs were written to produce detailed and readable logging with adjustable logging depth and direct reference into the source code when warnings or errors occurred (source file and line number). The program input was provided through two major paths: for simple parameters, environmental variables on the UNIX level were used and set through UNIX shell scripts which also started the program itself. For more complex data such as input arrays, ASCII data files in standard MatLab notation were used (*.m files) so they also could be loaded straightforwardly into MatLab itself for further analysis. With respect to the program output, all larger sized data was written into binary format files and compatible with the binary MatLab I/O format (*.mat files, version 5). Since there was no API available for Alpha Linux systems, this interface was written from scratch with the .mat format available from the official MatLab web site (MathWorks, Inc.). The resulting binary output files (MAT files) ensured exact floating point data transfer to MatLab without any loss in precision, and in addition kept the data files at a manageable size. This was especially valuable, as all the data analysis and visualization was done in MatLab. The binary data files easily were of the size of a few megabyte (MB). For example, for a rather small $64 \times 64 \times 64$ array sampling 3D space, the corresponding float space (real*4) is about 1MB. The corresponding ASCII data file would be at least more than a factor 2 larger in size. In practice, many variables and matrices were saved in a single MAT file including their variable name which simplified their later reference and analysis considerably. Yet the overall data size easily piles up in a single program run, not to mention then many runs for different configurations. In that sense, the running MAT file interface was really appreciated and absolutely worth all the time getting it to work.

In coarse summary, the total source code output is as follows

- Electrodynamics in 3D (8400 lines) - classical dynamics of a well isolated single charge confined to a very dilute 2DEG interacting with a periodic array of metallic islands in a plane offset by a small distance ( nm scale). The results to this work are found in [WU02].

- Electrostatic simulation of nanoscale geometries (EST3D, 5000 lines). The results are presented in Chap. 3 (pp. 31).

- Quantum mechanical Hubbard dynamics in fully parameterized Hilbert space (5200 lines). The results are presented in Chap. 5 (pp. 95).

- my own library files, including C++ classes and extensive I/O and logging routines (10800 lines).

From the size of these source codes it is clear, that high modularity and readability is a very important issue, as it is in general, and it has been taken care off throughout the whole programming process.

# Appendix B

# Papers & Conferences

Papers published, conferences attended and talks given as part of my Ph.D. studies:

## Papers

- *Screening in quantum dots formed by depletion*, A. Weichselbaum and S. E. Ulloa (to be submitted)
- *Aharonov–Bohm phase as quantum gate in two–electron charge qubits*, A. Weichselbaum and S. E. Ulloa (submitted to PRB)
- *Charge qubits and limitations of electrostatic quantum gates*, A. Weichselbaum and S. E. Ulloa (submitted to PRA)
- *Potential landscapes and induced charges near metallic islands in three dimensions*, A. Weichselbaum and S. E. Ulloa, PRE **68**, 056707 (2003), also selected by the Virtual Journal of Nanoscale Science & Technology, **8**, 23 (2003)
- *Electron dynamics near a metallic island array*, A. Weichselbaum, S.E. Ulloa, Physica Stat. Sol. B, **230**, 325-330 (2002)

## Conferences & Talks

- *QCA Qubits and Electrostatic Limitations on Single Qubit Operations*, A. Weichselbaum and S. Ulloa, contributed talk given at the APS March meeting 2004 (Montreal, Mar 22-26, 04)
- *Numerical Electrostatics in 3D from Dielectric Interfaces to 2DEG*, A. Weichselbaum and S. Ulloa, contributed talk given at the APS March meeting 2004 (Montreal, Mar 22-26, 04)

- *Electric and magnetic manipulation of 2e charge qubit systems*, A. Weichselbaum and S. Ulloa, contributed talk given at the APS Ohio Sectional Fall meeting 2003 (Cleveland, Oct 17-18, 03)

- *Manipulating few electrons in a 2D SET array*, A. Weichselbaum and S. Ulloa, contributed talk given at the APS March meeting 2003 (Austin, Mar 3-7, 03)

- *Manipulating few electrons in a 2D Hubbard array*, A. Weichselbaum and S. Ulloa, poster presented at the 50th Midwest Solid State Conference (Urbana Champaign, Illinois, Oct 18-20, 2002

- *Point Charge Interaction With Array of Metallic Islands: 3D Potentials And Self–Consistent Outer–Boundary Conditions*, A. Weichselbaum and S. Ulloa, poster presented at the Gordon Research Conference (GRC) on Correlated Electrons (Colby College, Waterville, ME, Jun 29 - Jul 03, 2002)

- *Influence of a periodic metallic island structure onto the motion of an electric charge in 2D nano–geometry*, A. Weichselbaum and S. Ulloa, contributed talk given at the APS March meeting 2002 (Indianapolis, Mar 18-22, 02)

- *Electronic Solitons Near a Periodic Metallic Island Array*, A.Weichselbaum, S.Ulloa, poster presented at the summer seminar Nano–Physics & Bio–Electronics - A new Odyssey (MPI Dresden, Germany, Aug 06-31, 2001); the poster was also presented at the PASI conference (Pan–American Advanced Studies Institute) on Physics and Technology at the Nanometer Scale (Jun 25 - Jul 03, 2001) and at CLACSA–X (Congreso Latinoamericano de Ciencias de Superficies y sus Aplicaciones, Jul 3-7, 2001), both in San Jose, Costa Rica

This work has been supported by NSF / NIRT 0103034.

# References

[AB59] Y. Aharonov and D. Bohm, *Significance of electromagnetic potentials in the quantum theory*, Phys. Rev. **115** (1959), 485.

[AOT+99] I. Amlani, A. Orlov, G. Toth, G. Bernstein, C. Lent, and G. Snider, *Digital logic gate using quantum–dot cellular automata*, Science **284** (1999), 289.

[Bal99] L. Ballentine, *Quantum mechanics - a modern development*, World Scientific, 1999.

[Bec80] T. Beck, *Real–space mesh techniques in density–functional theory*, Rev. Mod. Phys. **72** (1041-1080), 1041–1080.

[BIM97] T. Beck, K. Iyer, and M. Merrick, *Multigrid methods in density functional theory*, J. Quant. Chem. **61** (1997), 341–348.

[Coa80] T. Coalson, *Numerical methods for solving poisson and poisson–boltzmann type equations*, Encyclopedia of Comp. Chem. (Wiley) **3** (2080), 1998.

[Dem97] James W. Demmel, *Applied numerical linear algebra*, SIAM, Philadelphia, 1997.

[DLJ+03] L. DiCarlo, H. J. Lynch, A. C. Johnson, L. I. Childress, K. Crockett, and C. M. Marcus, *Differential charge sensing and charge delocalization in a tunable double quantum dot*, cond-mat/0311308, 2003.

[DM91] M. Davis and J. McCammon, *Dielectric boundary smoothing in finite difference solutions of the poisson equation: An approach to improve accuracy and convergence*, J. Comp. Chem. **12** (1991), 909–912.

[DS00] M. Devoret and R. Schoelkopf, *Amplifying quantum signals with the single electron transistor*, Nature **406** (2000), 1039.

[Fes62] H. Feshbach, *A unified theory of nuclear reactions, ii*, Annals of Physics (NY) **19** (1962), 287.

[Fey59] Richard Feynman, *Plenty of room at the bottom*, talk given at APS meeting, CalTech, Dec 1959.

[FIE+03] Andreas Fuhrer, Thomas Ihn, Klaus Ensslin, W. Wegscheider, and M. Bichler, *Singlet–triplet transition tuned by asymmetric gate voltages in a quantum ring*, PRL **91** (2003), 206802.

[GB58] J. Gordon and K. Bowers, *Microwave spin echoes from donor electrons in silicon*, PRL **1** (1958), 368.

[GM01] H. Goan and G. Milburn, *Dynamics of mesoscopic charge quantum bit under continuous quantum measurement*, PRB **64** (2001), 235307.

[GSC+03] S. Gardelis, C. G. Smith, J. Cooper, D. A. Ritchie, E. H. Linfield, and Y. Jin, *Evidence for transfer of polarization in a quantum dot cellular automata cell consisting of semiconductor quantum dots*, PRB **67** (2003), 033302.

[Har79] W. Harrison, *Solid state theory*, Dover Publications, New York, 1979.

[HE88] R. Hockney and J. Eastwood, *Computer simulations using particles*, Adam Hilger, Philadelphia, 1988.

[Hew93] A. Hewson, *The kondo problem to heavy fermions*, Cambridge University Press, New York, 1993.

[HFC+03] T. Hayashi, T. Fujisawa, H. D. Cheong, Y. H. Jeong, and Y. Hirayama, *Coherent manipulation of electronic states in a double quantum dot*, PRL **91** (2003), 226804.

[HKSW98] James R. Heath, Philip J. Kuekes, Gregory S. Snider, and R. Stanley Williams, *A defect–tolerant computer architecture: Opportunities for nanotechnology*, Science **280** (1998), 1716.

[HS93] M. Holst and F. Saied, *Multigrid solution of the poisson–boltzmann equation*, J. Comp. Chem. **14** (1993), 105–113.

[HVH+98] R. Held, T. Vancura, T. Heinzel, K. Ensslin, M. Holland, and W. Wegscheider, *In–plane gates and nanostructures fabricated by direct oxidation of semiconductor heterostructures with an atomic force microscope*, Appl. Phys. Lett. **73** (1998), 262.

[Jac99] J. D. Jackson, *Classical electrodynamics, 3rd ed.*, Wiley, New York, 1999.

[JH96] J. Jefferson and W. Häusler, *Effective charge–spin models for quantum dots*, PRB **54** (1996), 4936.

[KHF+86] I. Klapper, R. Hagstrom, R. Fine, K. Sharp, and B. Honig, *Focusing of electric field in the active site of $cu-zn$ superoxide dismutase: Effects of ionic strength and amino–acid modification*, Proteins **01** (1986), 47–59.

[KSSA97] J. Kikkawa, I. Smorchkova, N. Samarth, and D. Awschalom, *Room–temperature spin memory in two–dimensional electron gases*, Science **277** (1997), 1284.

[LCV+02] M. Lieberman, S. Chellamma, B. Varughese, Y. Wang, C. Lent, G. Bernstein, G. Snider, and F. Peiris, *Quantum–dot cellular automata at a molecular scale*, Ann. NY. Acad. Sci. **960** (2002), 225.

[Len00] C. Lent, *Bypassing the transistor paradigm*, Science **288** (2000), 1597.

[Lev01] J. Levy, *Quantum–information processing with ferroelectrically coupled quantum dots*, PRA **64** (2001), 052306.

[Lik99] K. Likharev, *Single–electron devices and their applications*, Proc. IEEE **87** (1999), 606–632.

[Mah00] Gerald D. Mahan, *Many–particle physics, 3rd ed.*, Kluwer Academic Plenum Publishers, New York, 2000.

[Mat76] R. Mattuck, *A guide to feynman diagrams in the many–body problem, 2nd ed., reprinted 1992*, Dover Publications, 1976.

[Moo65] Gordon E. Moore, co–founder of Intel, *Cramming more components onto integrated circuits*, Electronics **38** (1965), 8.

[MW98] G. Mahler and V. A. Weberruß, *Quantum networks, dynamics of open nanostructures, 2nd ed.*, Springer, New York, 1998.

[MWL91] Yigal Meir, Ned S. Wingreen, and Patrick A. Lee, *Transport through a strongly interacting electron system: Theory of periodic conductance oscillations*, PRL **66** (1991), 3048.

[MYS67] N. H. March, W. H. Young, and S. Sampanthar, *The many–body problem in quantum mechanics*, Cambridge University Press, New York, 1967.

[NC00] M. Nielsen and I. Chuang, *Quantum computation and quantum information*, Cambridge University Press, 2000.

[Pei33] R. Peierls, *Zur theorie des diamagnetismus von leitungselelektronen*, Z. Phys. **80** (1933), 763.

[PM01] H. Pastawski and E. Medina, *Tight binding' methods in quantum transport through molecules and small devices: From the coherent to the decoherent description*, cond-mat/0103219, 2001.

[RCU04] F. Rojas, E. Cota, and S.E. Ulloa, *Magnetic field and dissipation effects on the charge polarization in quantum cellular automata*, to appear in IEEE Transactions on Nanotechnology (2004), 2004.

[SFI+03a] M. Sigrist, A. Fuhrer, T. Ihn, K. Ensslin, Sergio E. Ulloa, W. Wegscheider, and M. Bichler, *Magnetic field dependent transmission phase of a double dot system in a quantum ring*, cond-mat/0308223, 2003.

[SFI+03b] M. Sigrist, A. Fuhrer, T. Ihn, K. Ensslin, W. Wegscheider, and M. Bichler, *Transmission phase through two quantum dots embedded in a four–terminal quantum ring*, cond-mat/0307269, 2003.

[SKKL01] V. Sverdlov, D. Kaplan, A. Korotkov, and K. Likharev, *Single–electron soliton avalanches in tunnel–junction arrays*, PRB **64** (2001), 041302.

[SL03] D. Saraga and D. Loss, *Spin–entangled currents created by a triple quantum dot*, PRL **90** (2003), 166803.

[So02] Woonyoung So, *A study of heavy ion collision*, unpublished (seminar), 2002.

[SSK53] J. Slater, H. Statz, and G. Koster, *A two–electron example of ferromagnetism*, Phys. Rev. **91** (1953), 1323.

[SW03] M. Storcz and F. Wilhelm, *Decoherence and gate performance of coupled solid–state qubits*, PRA **67** (2003), 042319.

[TAT+00] S. Tarucha, D. Austing, Y. Tokura, W. van der Wiel, and L. Kouwenhoven, *Direct coulomb and exchange interaction in artificial atoms*, PRL **84** (2000), 2485.

[TL01] G. Toth and C. S. Lent, *Quantum computing with quantum dot cellular automata*, PRA **63** (2001), 052315.

[TVPF93] S. Teukolsky, W. Vetterling, W. Press, and B. Flannery, *Numerical recipes in c (2nd ed.)*, Cambridge University Press, New York, 1993.

[VKI+03] T. Vančura, S. Kičin, T. Ihn, K. Ensslin, M. Bichler, and W. Wegscheider, *Kelvin probe spectroscopy of a two–dimensional electron gas below* $300mk$, Appl. Phys. Lett. **83** (2003), 2602.

[WRM+91] D. Weiss, M. Roukes, A. Menschig, P. Grambow, K. von Klitzing, and G. Weimann, *Electron pinball and commensurate orbits in a periodic array of scatterers*, PRL **66** (1991), 2790.

[WU02] Andreas Weichselbaum and Sergio E. Ulloa, *Electron dynamics near a metallic island array*, Phys. Stat. Sol. B **230** (2002), 325.

[WU03a] ———, *Aharonov–bohm phase as quantum gate in two–electron charge qubits*, condmat/0403120 (submitted to PRB), 2003.

[WU03b] ———, *Charge qubits and limitations of electrostatic quantum gates*, cond-mat/0401106 (submitted to PRA), 2003.

[WU03c] ———, *Potential landscapes and induced charges near metallic islands in three dimensions*, PRE **68** (2003), 056707.

[Yar68] A. Yariv, *Quantum electronics (2nd corrected printing)*, Wiley, New York, 1968.